THE INTERACTION OF HELIUM-3 IONS WITH SAMARIUM ISOTOPES

by

ROBERT W. EAGLE

A Thesis submitted to the Faculty of Natural Sciences of the University of London for the degree of Doctor of Philosophy

Bedford College, London

January 1975

A B S T R A C T

The experimental process for measuring the elastic and inelastic differential cross-sections for the scattering of helium-3 ions from 148, 150, 152 and 154 Samarium isotopes at 53 MeV is described. These results complement the data taken with helium-3 on ^{144}Sm, and with protons and deuterons on all the even Samarium isotopes at the same energy. The properties of the Samarium isotopes permit a study of the sensitivity of optical and collective model analyses on nuclei, whose characteristics change from spherical and vibrational (A = 144) to the region of permanent deformation where the nucleus is rotational (A = 154). These data are used to investigate the isotopic dependence of the optical model, particularly the recent folding models where an effective two-body interaction is folded in with the nucleonic density distribution.

The data are also used to test the nucleus-nucleus model or "double folding" model, where an effective interaction is first folded with the target density and then with the projectile density. The scattering of the incident projectiles, ^{3}He, ^{4}He, ^{12}C and ^{16}O, from Samarium isotopes is tested with this theory. The importance of using an effective interaction with the correct "saturation" properties is also shown. D.W.B.A. and S.C.A. analyses of the data are performed, and the need for coupling low lying states to the elastic scattering is shown.

To my parents

and my sister

....'If I believe that there is no such thing as God and that my mental processes are determined solely by the motions of atoms in my brain, I have no reason to suppose that my beliefs are true...hence I have no reason to suppose my brain to be composed of atoms.'

J.B.S.Haldane (paraphrase)

....'hence every theory which makes the human mind the result of irrational causes is inadmissible, for it would be a proof that there are no such things as proofs.'

C.S.Lewis

CONTENTS

DIAGRAMS

5.1 The 'two proton' contribution to the nuclear potential form factor of the ^{3}He-3 parameter model.

5.2 Real potentials obtained from the ^{3}He-3 parameter model.

5.3 Imaginary potentials obtained from the ^{3}He-3 parameter model.

5.4 Comparison of the real potential shapes for various models.

5.5 Comparison of imaginary potential shapes for various models.

5.6 Fits obtained using the ^{3}He-3 parameter model.

5.7 A plot of $\log_e\left\{\frac{Vo}{f(r)} - 1\right\}$ against nuclear radius - r. for the microscopic form factor f(r) for ^{144}Sm.

5.8 Comparison of microscopic form factor and Saxon-Woods shape which best represents the microscopic form factor shape.

5.9 Fit to the ^{144}Sm(^{3}He,^{3}He) data using the Saxon-Woods shape best representing the microscopic form factor produced by the ^{3}He-3 parameter model.

5.10 Fit to the ^{144}Sm(^{3}He,^{3}He) data using the Saxon-Woods shape best representing the microscopic form factor produced by the ^{3}He-3 parameter model, and allowing the imaginary depth to vary.

5.11 Fit to the ^{144}Sm(^{3}He,^{3}He) data using the Saxon-Woods shape best representing the microscopic form factor produced by the ^{3}He-3 parameter model, and allowing the real geometry parameters to vary.

5.12 Fit to the ^{144}Sm(^{3}He,^{3}He) data using the Saxon-Woods shape best representing the microscopic form factor produced by the ^{3}He-3 parameter model, and allowing the real diffuseness and the imaginary geometry to vary.

5.13 Effect of fitting the data using a Saxon-Woods representation of the microscopic real potential and allowing the geometry parameters to vary.

CHAPTER 1

Introduction

1.1 Comments on Nuclear Structure Model Concepts

In the absence of any comprehensive theory of nuclear structure, there have been many attempts at providing various models which describe the general features of the nucleus, and which reproduce its nuclear properties and structural characteristics. Most models reduce the many-body problem of individual nucleons within the nucleus to a two-body problem where the nucleus is represented by a single potential. This idea of a central potential in which the nucleons are contained leads to the Independent Particle Shell Model, which by inclusion of a spin-orbit potential, successfully predicts the closed shells and those levels which have strong single particle characteristics. The liquid drop model reduces the nucleus to a one-body problem and describes all the static properties of nuclei. This model can be extended to deformed drops, as in the collective model which describes the vibrational and rotational aspects of nuclear structure. Combination of the essential features of the deformed liquid drop model and the independent particle model gives the Unified Model, where the nucleons are assumed to move in a common non-spherical potential. Excitations of individual nucleons and collective motions of the nucleus as a whole are considered.

The collective model (Bo 11) follows the assumptions of the shell model in that the nucleons fill the energy levels of the potential. However, the closed shells form a nuclear core which Rainwater (Ra 01) used to offer an explanation of the large observed static quadrupole moments of odd-mass nuclei by suggesting that there was a polarising

effect on the remainder of the nucleus by the odd nucleon, and that this effect could give rise to a collective distortion of the shape of the nucleus.

The Optical Model, which is a development of the Independent Particle Model, deals with the effect of the central potential on the scattering and reaction of particle beams. It reduces to a two-body problem but in common with the other models introduces the central potential on an 'ad hoc' basis. This major criticism of the nuclear models has been partially resolved by the reformulation of the optical model in which the central potential is derived from the nuclear density distribution and an effective nucleon-nucleon interaction. This approach which goes some way towards removing the criticism of all previous models (i.e. that of a potential in which the particles move being produced by the particles themselves) has already been widely successful in explaining proton scattering (Gr 08). The extension of this approach to composite particle interactions shows in a dramatic way the limitation of the usual perturbation approximations and points out the areas where further development is needed. Light ion interactions play a crucial role in the development of nuclear reaction theories which should cover the range from nucleon-nucleon to heavy ion-heavy ion cases. The examination of the limitations of the reformulated versions of the optical model using composite ion interactions is of prime importance in the development of our understanding of nuclear structure.

1.2 The interaction of medium energy light ions with nuclei

The optical model has been used in recent years to fit angular

distributions of the elastic scattering of light ions from a complete range of elements throughout the periodic table with great success (Ho 04) (Ho 05). This model, which treats the nuclear potential well as complex to account for elastic and inelastic scattering and nuclear reactions, also introduces a spin-orbit potential. Real, volume and surface imaginary and spin orbit Saxon-Woods shape potentials make up the phenomenological optical model potential, which also includes a Coulomb term. Energy dependence, (N-Z) dependence and A dependence has also been included by linear dependence of the depth of the potential based on the work of Perey (Pe 02).

Until recently, however, there have been some questions concerning inherent ambiguities in the optical model and the energy and isotopic dependence of the optical model potentials. Some ambiguities arise due to the large number of parameters in the simple optical model, such that they lose their simple intuitive meaning. Many results for proton scattering from a wide range of nuclei have been recorded in references already given in this section and Green et al (Gr 07).

The optical model analyses of deuteron scattering from various isotopes has been of particular importance in determining the spin-orbit force, since the deuteron has a ground state spin of 1.

The composite particle scattering optical model analyses have provided considerably more scope for study of the nuclear physics. Alpha particle and helium-3 scattering analyses have led to many ambiguities. The need for a surface term as opposed to a volume absorption term has been discussed (Wo 06).

Isospin and asymmetry dependence has been a feature of much interest for all incident projectiles. Thomas (Th 11) investigated

the isospin dependence for proton scattering from a range of isotopes. However, his analysis compared the respective real central depths. Sinha (Si 09) showed that the change in volume integral was a better guide to any isospin or asymmetry dependence. Urone (Ur 01) (Ur 02) performed analyses for asymmetry dependence using data of helium-3 and triton scattering from a range of isotopes.

Discrete and continuous ambiguities in the real central part of the optical model potential for composite particle scattering have been discussed (Ca 01). The problem of the continuous or valley ambiguities caused by the inability to determine unique values of the real central potential parameters has led to the concept of the constancy of the volume integral per particle pair. The discrete ambiguity is caused by the phenomenological equivalence of discrete potentials, i.e. the asymptotic wave functions generated by equivalent potentials are identical, although the wave functions in the interior region may differ in the number of nodes for different potential strengths (Dr 01). These ambiguities should be eliminated (Go 04) (Si 08) by measuring differential cross-sections at "sufficiently" high energies and "sufficiently" large scattering angles. Recently, the optical model family ambiguities have been resolved by analysis of data at high energies and extending to backward angles (Fu 09) (We 02) (Fu 07).

The energy dependence of the optical model has been investigated (We 03) (Ma 02) (Fu 09) with the conclusion that an energy dependent geometry in the phenomenological optical model was required. The energy dependence arises mainly from the exchange term, i.e. anti-symmetrisation of incident nucleons with respect to the nucleons in the target. This decreases with increasing energy.

The depth of the spin-orbit potential is yet to be established for helium-3 scattering, although Fulmer (Fu 08) by analysing helium-3 scattering from a wide range of isotopes concludes that a spin-orbit depth of $\sim$2 MeV is necessary.

The optical model for heavy ion scattering where the Coulomb effect is predominant is less well understood. The cross-sections can be fitted with many potential depths but the idea that the real central depth is approximately equal to the nucleon scattering central depth multiplied by the mass number A of the incident projectile is shown to be false. Parametrised phase shifts are sometimes used as an alternative to optical model potentials.

Meson-nucleus (Wi 04) and pion-nucleus (Si 17) optical models have recently been introduced where the need for energy dependent parameters has been stressed.

The value of using different types of incident projectile is that they each show us a different region of nuclear structure. The optical model works very well for protons. Deuterons, with a large spin, have enabled many polarisation experiments to be performed. However, they are loosely bound and phenomenological models do not work too well. Alpha particles are very tightly bound and have no spin. They do not test the present models, any more than do protons (Ho 07). Helium-3 particles are the lightest complex particles. With sufficient energy they cause direct interactions to predominate. With heavier ions the complexity of the interaction mechanisms and the predominance of the Coulomb interaction makes the interpretation of their cross-sections more difficult.

1.3 Motivations for Present Work

With the high intensity ^{3}He beam of the Variable Energy Cyclotron, Harwell, and the high resolution of the Oak Ridge Isochronous Cyclotron Spectrograph it is possible to study ^{3}He elastic and inelastic scattering on the Samarium isotopes at an energy sufficient to give a reasonable amount of structure to the cross-sections, and over a wide angular range, allowing unambiguous optical model analyses.

The present work seeks to extend the range of data available on the Samarium isotopes and to apply it to the study of the effect of deformation on current nuclear model predictions. Samarium isotopes occupy a unique place in the periodic table of elements ranging from a closed neutron shell (N = 82) for ^{144}Sm which is a spherical and vibrational nucleus to the deformed rotational nucleus, ^{154}Sm, having ten neutrons outside the closed shell. The deformation increases with increasing mass of these nuclei. The particularly interesting quality that has been the subject of much study is the transition from vibrational to rotational nuclei at A = 150. The Samarium isotopes are the only suitable range of isotopes since ^{144}Sm, ^{148}Sm, ^{150}Sm, ^{152}Sm and ^{154}Sm are all stable. Few or none of the isotopes of neodymium (Z = 60), promethium (Z = 61), europium (Z = 63) or gadolinium (Z = 64) are stable.

The energy levels of the stable Samarium isotopes are shown in fig. 1.1 (Nu 03).

Apart from the deformation properties of the Samarium isotopes, they also provide an opportunity to investigate A and N - Z dependence in the optical model.

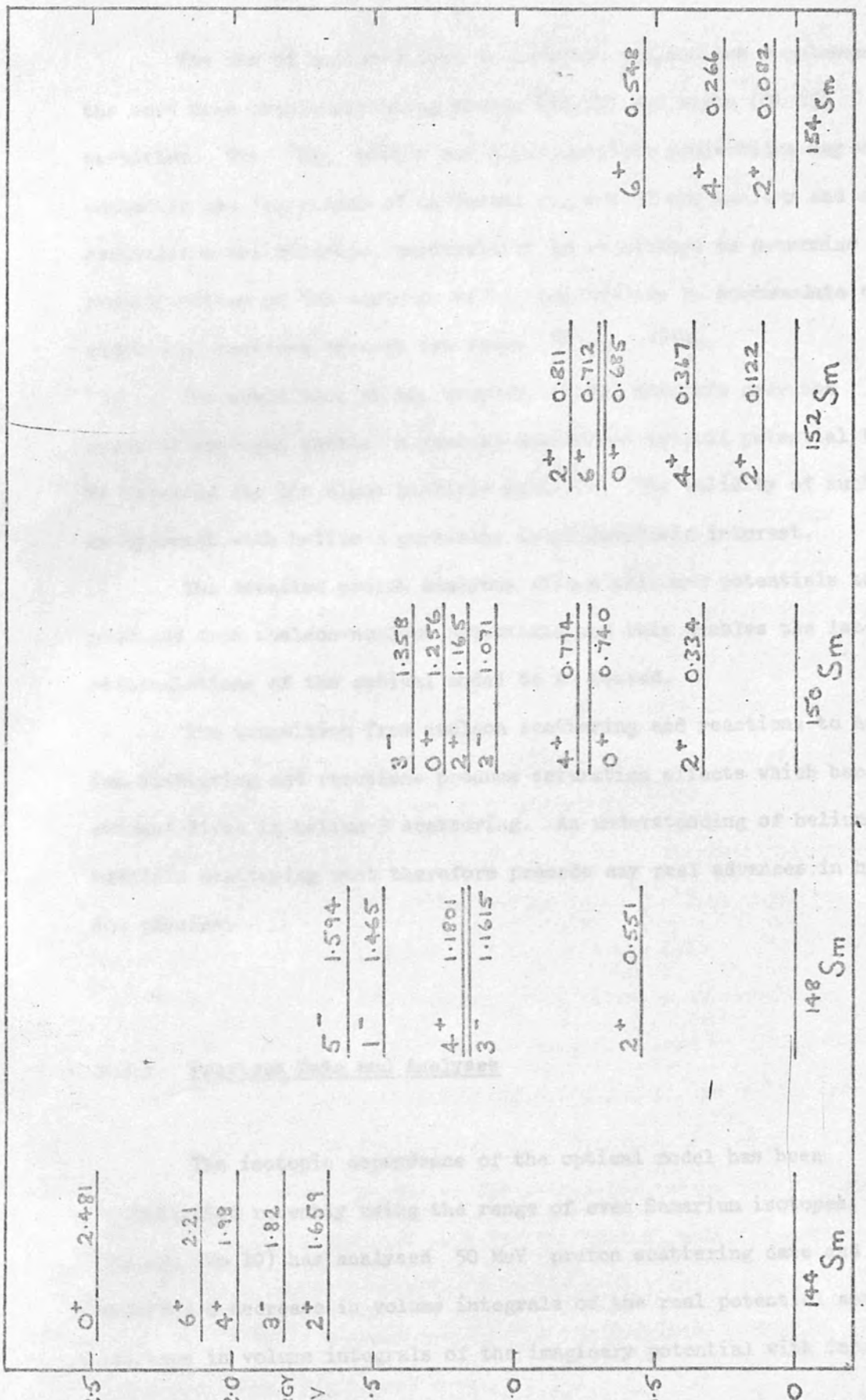

Fig 1.1 Energy Level Diagram for Samarium Isotopes

The use of helium-3 ions as incident projectiles complements the work done previously using proton (Wo 10) and alpha (Gl 03) particles. The ^{3}He, proton and alpha particle projectiles may well emphasize the importance of different regions of the nucleus and so comparisons are valuable, particularly in an attempt to determine the redistribution of the nucleons within the nucleus to accommodate the additional neutrons through the range ^{144}Sm - ^{154}Sm.

The comparison of the coupled channel analysis over the range of isotopes enabled a general undeformed optical potential to be obtained for the alpha particle analysis. The validity of such an approach with helium-3 particles is of intrinsic interest.

The detailed proton analyses allows helium-3 potentials to be produced from nucleon-nucleus potentials and this enables the latest reformulations of the optical model to be tested.

The transition from nucleon scattering and reactions to heavy ion scattering and reactions produce saturation effects which become evident first in helium-3 scattering. An understanding of helium-3 particle scattering must therefore precede any real advances in heavy ion physics.

1.3.1 Previous Data and Analyses

The isotopic dependence of the optical model has been investigated recently using the range of even Samarium isotopes. Woollam (Wo 10) has analysed 50 MeV proton scattering data and observed a decrease in volume integrals of the real potential and an increase in volume integrals of the imaginary potential with increasing

target mass. Trends in the geometrical parameters were observed with the diffuseness terms increasing with neutron number of the target, although the radius parameters remained constant.

Measurements have been reported for elastic and inelastic scattering of protons at 16 MeV (St 19) and 30 MeV (La 02) and deuterons at 12 MeV (Ze 01) (Ch 04). However, these angular distributions, because of their low energies, lack sufficient structure in their angular distributions to facilitate a complete analysis.

Analyses were also performed by Glendenning et al (Gl 03) for alpha particle scattering from the Samarium isotopes. The optical model parameters show a dramatic decrease in real potential from ^{148}Sm to ^{154}Sm, and an accompanied increase in the diffuseness parameters. They found that contributions of strong collective states to the optical potential were removed by treating them explicitly in the SCA formalism. Thus it was possible to describe alpha scattering from all the isotopes with the same optical potential, providing the deformation parameters were suitably adjusted.

Woollam (Wo 09) has measured the elastic and inelastic scattering of helium-3 ions from ^{144}Sm and analysed the data using the regular and reformulated models and the DWBA and SCA.

Carbon, ^{12}C, and oxygen, ^{16}O, elastic scattering at 130 MeV from ^{152}Sm and ^{154}Sm has been performed by Friedman (Fr 05). The data for ^{16}O elastic scattering which extends to 50^{o} is fitted using optical model parameters showing a decrease in real potential and increase in radius parameter for increasing target mass. Similar effects are seen in the same work for the optical model parameters fitting ^{16}O elastic scattering from the Neodymium isotopes ^{144}Nd, ^{146}Nd and ^{148}Nd, where a decrease in the imaginary potential also occurs for increasing target mass.

1.4 Thesis Summary

This thesis describes the measurement and analysis of elastic and inelastic scattering of 50 MeV helium-3 scattering from Samarium isotopes. Chapter one covers the general problems in the field and the motivation for the research.

Chapter two describes the theoretical considerations of the nuclear structure models, particularly the optical model and the collective models, and shows in a simple way the steps which enable the folding model, the D.W.B.A., and the coupled channels approach to be derived.

Chapter three describes the measurement of the elastic and inelastic differential cross-sections of helium-3 scattering from ^{148}Sm and ^{150}Sm at 53.4 MeV on the variable energy cyclotron at Harwell, and helium-3 scattering from ^{152}Sm and ^{154}Sm at 53.1 MeV on the Oak Ridge Isochronous Cyclotron, Oak Ridge, Tennessee. The design of the experiment is discussed with particular reference to the absolute and relative errors.

The analyses of the elastic and inelastic scattering angular distributions are discussed in chapter four. The simple optical model parameters are obtained for helium-3 scattering from Samarium isotopes. An attempt is made in the reformulated model of Greenlees (Gr 08) to obtain the mean square radii of the two-body force (Yukawa) and the matter distribution uniquely. The fits to the inelastic scattering using the D.W.B.A. are shown and the corresponding deformation parameters are obtained. A coupled channels analysis is performed, coupling all the levels which have had data extracted for each isotope. A comparison of D.W.B.A. and coupled channels analysis is discussed.

The more recent reformulations of the optical model (Th 12) (Si 15) (Si 13) are discussed in chapter five, and the limitations of

these models are investigated, particularly with respect to the nuclear density used for the folding process and the subsequent shapes of the real and imaginary form factors. In particular, two models; the ^{3}He - 3 parameter model and the nucleus-nucleus model are discussed, and the nucleus-nucleus model is also used to determine the microscopic real and imaginary form factors produced for alpha, ^{12}C and ^{16}O particle scattering from Samarium isotopes.

The conclusions of this work, concerning the additional information obtained about the nuclear structure of Samarium isotopes, the effect of (N-Z) dependence in the optical model, various models' ability to cope with helium-3 scattering from both vibrational and rotational isotopes, and the first really critical tests of the recent reformulated models are discussed in chapter six.

CHAPTER 2

Theoretical Considerations

Introduction

In this chapter the stages of the theoretical bases for the current nuclear structure models will be derived. The history of the optical model and its limitations will first be shown. By considering the stages from the time independent Schrodinger equation, the Lippman-Schwinger equation, and the 'T' matrix, the basis of the present reformulated and folding models will be presented. The essential features of the reformulated optical model is the replacement of the empirical potential by a summation of nucleon-nucleon forces over the whole nucleus. This has been done in terms of the density distribution in the nucleus and an effective nucleon-nucleon interaction. The extension of the folding models to composite particles will also be considered.

The cross-sections for the process of inelastic scattering may be calculated by a perturbation theory expression. In some cases, however, perturbation theory is not sufficiently accurate, especially when there is strong coupling between the elastic and inelastic channels. The coupled equations for the wave functions in all reaction channels will be derived, and the perturbation theory will be shown to be a weak-coupling limit in which the transition amplitude is proportional to the radial derivative of the optical potential causing elastic scattering. The deformation parameter, β , will be derived from this proportionality.

2.1 The Simple Optical Model

The main feature of the optical model is that the many-body problem of scattering of a nucleon or group of nucleons from a complex nucleus can be approximated by a two-body problem where the basic interaction between the incident particle and target nucleus is represented by a potential which depends only upon the distance separating the centres of the two bodies.

The Schrodinger time independent non-relativistic equation is then given by

$$\nabla^2\psi + \frac{2\mu}{\hbar^2}(E - V(r))\psi = 0 \qquad 2.1.1$$

where E is the centre of mass energy, μ is the reduced mass and $V(r)$ is the optical potential.

The following brief historical outline shows the development of the phenomenological local optical potential:

Bethe (Be 06) replaced target nucleus by real potential well.

Ostrofsky, Breit and Johnson (Os 01) considered a complex potential to account for absorption of incident nucleons.

Bethe (Be 08) showed the single particle approach was valid at higher energies.

Le Levier and Saxon (Le 04) employed a complex square well.

Chase and Rohrlich (Ch 02) showed square well gave too much scattering.

Woods and Saxon (Wo 05) proposed a complex potential well with a diffuse edge which took the form

$$V(r) = -(U + iW)\left\{\frac{1}{1 + \exp(r-R_R)/a)}\right\} . \qquad 2.1.2$$

Fermi (Fe 02) suggested a non-central spin-orbit potential.

The surface component of the imaginary potential was achieved by taking the first derivative of a volume form factor. At low energies, less than 10 MeV , the absorption is expected to be low due to the Pauli principle, and at high energies, greater than 100 MeV , the absorption is expected to be low because of the short wavelength. The maximum absorption occurs at energies $\sim$ 50 MeV where the centre of the nucleus is black.

A coulomb scattering term must be added to the nuclear scattering terms to obtain the total scattering potential. The shape of this potential has been determined by electron scattering measurements (Ac 02), but most analyses have used the relation $R_c = 1.25A^{1/3}\text{fm}$ to give

$$V_c(r) = \frac{Zze^2}{2R_c}\left(3 - \frac{r^2}{R_c^2}\right) \quad r \leq R_c \qquad 2.1.3$$

$$V_c(r) = \frac{Zze^2}{r} \qquad r > R_c$$

where Ze and ze are the charges on the target nucleus and incident particle respectively.

Thus the phenomenological optical model was written as

$$U(r) = V_c(r) - V_R f_R(r) - iW_V f_I(r) + 4ia_I W_D \frac{df_I(r)}{dr}$$

$$+ V_s\left(\frac{\hbar}{m_\pi c}\right)^2 \frac{1}{r}\frac{df_s(r)}{dr}\,\underline{\ell}.\underline{\sigma} \qquad 2.1.4$$

where

$$f_i = \left[1 + \exp\frac{(r_1 - R_i)}{a_i}\right]^{-1}$$

and

$$R_i = r_i A^{\frac{1}{3}} .$$

It is necessary to describe mathematically an incident beam together with outgoing particles. The wave function describing an incident beam of spinless neutral particles is the plane wave,

$$\phi_K(r) = \exp i\underline{k}.\underline{r} . \qquad 2.1.5$$

The wave function describing the elastically scattered particles is the spherical wave,

$$\phi_s = f(\theta,\phi) \frac{\exp(ikr)}{r} \qquad 2.1.6$$

where the cross-section is related to $f(\theta,\phi)$ by

$$\sigma(\theta,\phi) = |f(\theta\ \phi)|^2 . \qquad 2.1.7$$

At large distances the nuclear potential will be negligible, and since the total wave function $\overline{\psi}$ satisfying the Schrodinger equation (2.1.1) must describe both freely moving incident particles and freely moving scattered particles we expect the boundary condition that,

$$\overline{\psi}(r) \sim \exp(i\underline{k}.\underline{r}) + f(\theta,\phi) \frac{\exp(ikr)}{r} . \qquad 2.1.8$$

The quantity $f(\theta,\phi)$ is called the scattering amplitude. Putting $U = 2\mu V/\hbar^2$ and $E = \hbar^2k^2/2\mu$ and assuming that $U = U(r)$ only then the Schrodinger equation becomes

$$(\nabla^2 + k^2 - U)\,\bar{\psi} = 0 \quad . \qquad 2.1.9$$

Assuming independence of ϕ (axial symmetry around beam) then it is reasonable to look for a set of solutions $\bar{\psi} = \bar{\psi}(r,\cos\theta)$ since θ runs from 0 to π in spherical polar coordinates, hence given $\cos\theta$, θ is determined uniquely. Thus a complete set of Legendre polynomials may be obtained

$$\bar{\psi} = \bar{\psi}(r,\cos\theta) = \sum_{\ell=0}^{\infty} A_\ell(r)\, P_\ell(\cos\theta)$$

$$= \sum_{\ell=0}^{\infty} C_\ell \frac{1}{r} F_\ell(r)\, P_\ell(\cos\theta) \qquad 2.1.10$$

where C_ℓ are as yet undetermined numbers

F_ℓ are as yet undetermined functions.

Using the Laplacian operator

$$\nabla^2 = \frac{\partial^2}{\partial r^2} + \frac{2}{r}\frac{\partial}{\partial r} + \frac{1}{r^2}\Lambda \qquad 2.1.11$$

where

$$\Lambda = \frac{\partial^2}{\partial\theta^2} + \cot\theta \frac{\partial}{\partial\theta} + \frac{1}{\sin^2\theta}\frac{\partial^2}{\partial\phi^2} \quad .$$

Then substituting (2.1.10) into (2.1.9),

$$\left(\frac{\partial^2}{\partial r^2} + \frac{2}{r}\frac{\partial}{\partial r} + \frac{1}{r^2}\Lambda + k^2 - U\right) \sum_{\ell=0}^{\infty} C_\ell \frac{1}{r} F_\ell(r)\, P_\ell(\cos\theta) = 0 \qquad 2.1.12$$

hence

$$\Lambda P_\ell(\cos\theta) = \left[\frac{\partial^2}{\partial\theta^2} + \cot\theta \frac{\partial}{\partial\theta}\right] P_\ell(\cos\theta) \qquad 2.1.13$$

$$= \frac{1}{\sin\theta}(\sin\theta \frac{\partial^2}{\partial\theta^2} + \cos\theta \frac{\partial}{\partial\theta})P_\ell(\cos\theta) \qquad 2.1.14$$

$$= \{\frac{1}{\sin\theta}(\frac{\partial}{\partial\theta}\left[\sin\theta \frac{\partial}{\partial\theta}\right])\}P_\ell(\cos\theta) \qquad 2.1.15$$

$$= (\frac{1}{\sin\theta}\frac{\partial}{\partial\theta}\sin^2\theta \frac{\partial}{\sin\theta\,\partial\theta})P_\ell(\cos\theta) \quad . \qquad 2.1.16$$

Putting $x = \cos\theta$

$$\Lambda P_\ell(\cos\theta) = (\frac{d}{dx}(1 - x^2)\frac{d}{dx})P_\ell(x) \qquad 2.1.17$$

$$= (1 - x^2)P''_\ell(x) - 2xP'_\ell(x) \qquad 2.1.18$$

which is similar to Legendre's equation of order ν

$$(1 - x^2)\frac{d^2y}{dx^2} - 2x\frac{dy}{dx} + \nu(\nu+1)y = 0 \; . \qquad 2.1.19$$

Hence

$$\Lambda P_\ell(\cos\theta) = -\ell(\ell + 1) P_\ell(\cos\theta) \; . \qquad 2.1.20$$

Thus from (2.1.12)

$$\sum_{\ell=0}^{\infty} C_\ell(\frac{\partial^2}{\partial r^2} + \frac{2}{r}\frac{\partial}{\partial r} - \frac{\ell(\ell+1)}{r^2} + K^2 - U)\frac{1}{r}F_\ell(r)\,P_\ell(\cos\theta) = 0. \qquad 2.1.21$$

Since this is true for all θ, coefficients of each P_ℓ can be equated to zero

$$\left[\frac{\partial^2}{\partial r^2} + \frac{2}{r}\frac{\partial}{\partial r} - \frac{\ell(\ell+1)}{r^2} + K^2 - U\right]\frac{1}{r}F_\ell(r) = 0 \qquad 2.1.22$$

hence

$$\left[\frac{\partial^2}{\partial r^2} - \frac{\ell(\ell+1)}{r^2} - U + K^2\right]F_\ell(r) = 0 \ . \qquad 2.1.23$$

This is the radial wave equation, usually written

$$\frac{d^2U_L(r)}{dr^2} + \{\frac{2\mu}{\hbar^2}(E - V(r)) - \frac{L(L+1)}{r^2}\}U_L(r) = 0 \qquad 2.1.24$$

where $V(r)$ is the optical potential, at present ignoring Coulomb and spin terms, and the $L(L+1)/r^2$ term is called the centrifugal barrier.

Quantum mechanics requires a particle to only occupy certain energy levels when bound in a potential well. This means that to find a solution of (2.123) $V(r)$ must be known, but it is also what we are trying to find.

The problem is solved by

a) Solving the equation at large distances analytically (where the nuclear force is zero). The Coulomb potential is included for large distances as it has an infinite range.

b) Integrating outwards from the origin using a trial value of $V(r)$.

The two resulting values are then compared at some point in the region of the nuclear surface called the matching radius. The degree of mismatch enables a better $V(r)$ to be calculated in the next iteration.

For each L value there can be several different solutions of the radial wave equation (2.123). This causes an ambiguity in the possible values of V.

From the radial wave equation the amplitude for partial waves neglecting Coulomb and spin terms is (Ho 06)

$$f(\theta) = \frac{1}{2iK} \sum_{L=0}^{\infty} (2L + 1)(e^{2i\delta_L} - 1) P_L(\cos\theta)$$

where the physical information is carried in the phase shift term δ_L due to the nuclear potential.

A scattering matrix element is defined

$$S_L = e^{2i\delta_L}$$

and the absorption coefficient η is $\eta_L = |S_L|^2$.

When the incident particle is charged there is a Coulomb term in the optical potential $V(r)$, and the analytical solution of the radial equation in the external region contains regular and irregular Coulomb functions.

When the incident particle has a spin >0 , then the optical potential $V(r)$ contains a spin orbit term. The spin of the incident particle can couple in two ways with the orbital angular momentum L , and hence the corresponding radial wave equations give two solutions U_L^+ and U_L^- for the two-spin orientations. The equations may be solved to give scattering matrix elements S^+ and S^- for each L value.

The differential cross-section depends on the spin independent and spin flip scattering ampltidues

$$A(\theta) = f_c(\theta) + \frac{1}{2iK} \sum_{L} \{(L+1)S_L^+ + LS_L^- - (2L+1)\}e^{2i\sigma_L} P_L(\cos\theta)$$

$$B(\theta) = \frac{1}{2iK} \sum_{L=1}^{\infty} (S_L^+ - S_L^-) e^{2i\sigma_L} P_L^1(\cos\theta)$$

where f_c is the Coulomb amplitude and σ_L the Coulomb phase shifts. The differential cross-section is then given by

$$\frac{d\sigma}{d\Omega} = |A|^2 + |B|^2$$

and the total reaction cross-section is given by

$$\left(\frac{d\sigma}{d\Omega}\right)_R = \frac{\pi}{k^2} \sum_L \{(L+1)(1-|S_L^+|^2) + L(1-|S_L^-|^2)\} .$$

2.1.1 The Experimental Analysis

Numerical values for the parameters are inserted into the simple optical model equation (2.1.2) and the theoretical cross-sections computed. These parameter values are then systematically varied to find a set which minimises the quantity

$$\Delta_{pp}^2 = \frac{1}{N} \sum \left(\frac{\sigma_{exp} - \sigma_{th}}{\delta\sigma_{exp}}\right)^2 .$$

where $\sigma_{exp} \pm \delta\sigma_{exp}$ is the experimental cross-section and σ_{th} the theoretical cross-section.

The philosophy of the optical model requires a smooth variation of the parameters obtained with nuclear mass and incident energy, although this is often not the case. This can often be explained by intrinsic ambiguities between the various parameters.

When iterating over a set of parameters it is important to start with physically reasonable potentials (taken from a previous analysis) and associated geometries.

The first stage of the analysis is to normalise the elastic scattering cross-sections by assuming that all forward scattering is due to Coulomb scattering.

The central real potential is then adjusted to optimise the fit to the differential cross-sections. The parameters are then varied to obtain a well-defined minimum in Δ^2_{pp}. This in itself can present many problems because of the many localised minima in the multi-parameter space. There is an additional difficulty in location of all the local minima, which is the problem of ambiguities in the potential (see section 2.1.2). A search routine for parameter optimisation has been developed for electronic computation (Me 05).

2.1.2 Ambiguities in the Optical Model

In many cases, even with large quantities of experimental data, the optical model is unable to uniquely define a set of parameters. The valley, or continuous ambiguities, can be defined by the $V_R r_R^n$ = constant relation. The physical interpretation is that although the individual depth and radius parameters of the real potential are not entirely independent, there is an overall volume integral of the potential which remains approximately constant. i.e. the following analytical expressions are derived for the volume integral and mean square radius of a Saxon-Woods potential,

$$J_R = \frac{4}{3}\pi V_R R_R^3 \left[1 + \left(\frac{\pi a_R}{R_R}\right)^2\right]$$

$$\langle r^2\rangle_R = \frac{3}{5} R_R^2 \left[1 + \frac{7}{3}\left(\frac{\pi a_R}{R_R}\right)^2\right].$$

Also ambiguous, for composite particle scattering, is the choice between volume and surface absorption shapes.

Characteristic of strongly absorbed particles is an ambiguity in potential well depth (Gr 07). These discrete ambiguities give in helium-3 scattering sets of real central potentials varying from 50 MeV up to several hundred MeV, in steps of 40 MeV , which all give similar fits for elastic scattering. These ambiguities occur because scattering of strongly absorbed particles is insensitive to the interior of the nucleus. The scattering is determined by only a few partial waves and the addition of multiples of 2π to these few phase shifts produces similar scattering angular distributions. As the energy and angular range of data is increased the increasing importance of a range of partial waves removes these ambiguities.

2.1.3 Limitations of the Optical Model

The model is really only applicable to large nuclei, $A > 30$. In fact, however, the model has been applied to much smaller nuclei with quite successful results. The model describes gross features of series of nuclei, and so it is expected to have a smooth variation of parameters with A and E , and not to accommodate peculiarities of individual nuclei. Analyses, using the optical model, have been performed in an attempt to extract some systematic scheme of the variation of optical parameters with nuclear mass, incident energy, isospin and asymmetry.

The model describes non-spherical nuclei in an average way. Nuclei with large distortions show a tendency to small radii and large diffuseness.

As further refinements were added to the model by the inclusion of additional parameters, its utility for describing reactions has been impeded and the physical interpretation of the meaning of the parameters has become less valuable.

2.2 Folding Models

It has been shown that the asymptotic form of the wave function in nuclear scattering is a plane wave and a scattered wave combination, viz.

$$< \psi^+ > \; = e^{i\underline{k}.\underline{r}} + f(\theta) \frac{e^{ikr}}{r} \quad . \qquad 2.2.1$$

Schrodinger's equation may be given as the eigenvalue equation

$$H|\psi^+ > \; = \; E|\psi^+ > \qquad 2.2.2$$

where E is the total energy of the system and H is the Hamiltonian

$$H = H_N + K_0 + V \qquad 2.2.3$$

H_N: nuclear internal states of nuclei

K_0: incident particles kinetic energy

$$= H_0 + V$$

H_0: unperturbed nuclear and projectile Hamiltonian.

Lippman Schwinger (Li 05) showed that this could be used to derive

$$|\psi^+> = |n,K> + \frac{1}{E-H_0+i\varepsilon} V |\psi^+> \qquad 2.2.4$$

where for $|n> = |0>$ nucleus is in its ground state and where $|n> = \psi_n(r_1,r_2 \ldots r_A)$ and $|K> = e^{i\underline{k}.\underline{r}_0}$.

If we define

$$T|0,K> = V|\psi^+> \qquad 2.2.5$$

then the T matrix equation follows, whereby

$$T = V + VGT \qquad 2.2.6$$

where $G = \frac{1}{E - H_0 + i\varepsilon}$ a Green's function.

Quantum mechanically, the maxtrix elements of T are thus

$$<n,K'|T|0,K> = <n,K'|V|0,K> + \sum_{i,p} <n,K'|V|ip> \frac{1}{E-E_{inc}-E_n+i\varepsilon} <ip|V|0,K> \qquad 2.2.7$$

where the first term on the right-hand side of equation 2.2.7 represents the direct transition from the ground state to an excited state (n > 0) or ground state (n = 0). This term contains the information about elastic scattering events

$$<0,K'|U|0,K> = <K'|<0|U|0>|K> \qquad 2.2.8$$

OPTICAL
POTENTIAL

If V is replaced by $\sum_i t_e(r_0,r_i)$, an effective interaction, then

$$U_{opt} = \langle 0| \sum_i t_e(r_0,r_i) |0\rangle \quad . \qquad 2.2.9$$

Hence

$$U_{opt}(r_0) = \int \psi_0^*(r_1-r_A)\ t_e(r_0,r_i)\ \psi_0(r_1-r_A) d\vec{r}_1, d\vec{r}_2 \ldots d^3 r_A$$

$$= \int \rho(r_1)\ t_e(r_0,r_1)\ d\vec{r}_1 \quad . \qquad 2.2.10$$

Hence t_e is an effective interaction based on the bare nucleon-nucleon interaction, and is a simplification of the nucleon-nucleon t-matrix.

2.2.1 First Reformulation

This model was proposed by Greenlees, Pyle and Tang (Gr 08), in which the real part of the optical potential was obtained from nuclear matter distributions and the nucleon-nucleon force. In order to calculate the interaction between the incident nucleon and the target nucleus they made two approximations:-

1) The wave function with respect to the exchange of the incident nucleon with a nucleon in the target nucleus was not anti-symmetrised.

2) The effects of polarisation of the target nucleus by incident nucleons was ignored.

Kerman, McManus and Thaler (Ke 01) had shown that the real part of the optical potential may be written as

$$V(r) = A \int \bar{t}\,(|\underline{r} - \underline{r}'|)\rho(r')\,d\underline{r}' \qquad 2.2.11$$

where A - number of target nucleons

$\rho(r')$ - matter density of nucleus

$\bar{t}(r)$ - spin-isospin average of the real part of the two nucleon effective interaction.

Using this potential in the reformulated optical model, Greenlees et al showed that it was possible to derive such quantities as the mean square radii $\langle r^2 \rangle_m$ and $\langle r^2 \rangle_d$ of the nuclear matter distribution, and the effective interaction,

$$\langle r^2 \rangle_R = \langle r^2 \rangle_m + \langle r^2 \rangle_d \,. \qquad 2.2.12$$

The density distributions in this model were generated from the Saxon-Woods shape,

$$\rho_m(r) = \left[1 + \exp\left(\frac{r - r_m A^{\frac{1}{3}}}{a_m}\right) \right]^{-1} . \qquad 2.2.13$$

The effective interaction was taken to be a Yukawa.

The optical potential then was based upon the nucleon-nucleon potential having direct U_D, isospin U_τ and spin orbit $U_{L.S}$ contributions, hence

$$U_{opt} = U_D + U_\tau + U_{L.S} + U_{IMAG} \qquad 2.2.14$$

$$U_D = \int \rho_p\, u_{pp} + \int \rho_n\, u_{np}$$

$$= \int (\rho_p + \rho_n)\left(\frac{u_{pp} + u_{nn}}{2}\right) + \int (\rho_p - \rho_n)\left(\frac{u_{pp} - u_{nn}}{2}\right)$$

$$U_D = \int \rho_m(r)\, u_d\,(|r - r_0|\, dr \qquad 2.2.15$$

$$U_\tau = \{\int [\rho_p(r) - \rho_n(r)]\, u_\tau(|r - r_0|)dr\}\, \tau_{0z}$$

$$U_{L.S} = \{ -\frac{1}{\hbar} \sum_{n=1}^{\infty} \frac{4\pi}{(2n+1)!} \frac{2n}{r_0} \frac{d}{dr_0} \left[\frac{2(n-1)}{r_0} \frac{d^{2n-3}}{dr_0^{2n-3}} \rho_m + \frac{d^{2n-3}}{dr_0^{2n-2}} \rho_m \right] \times \int_0^{\infty} u_{LS}(\eta)\, \eta^{2n+2}\, d\eta \}\, \underline{\ell}_0 \cdot \underline{\sigma}_0$$

where u_d, u_τ and u_{LS} contribute to the two-body interaction u_{0i} between the incident nucleon and a nucleon i in the target nucleus. Here the density distributions are related by,

$$\rho_m(r) = \rho_p(r) + \rho_n(r) \; . \qquad 2.2.16$$

The incoming particle coordinate is $\underline{r}_0$ and its isospin component is τ_{03}.

$u_\tau(r)$ was $\dfrac{u_d(r)}{\xi}$ where $\xi = -0.48$.

The imaginary term U_{IMAG} was calculated phenomenologically using a Saxon-Woods form factor.

This reformulation is of advantage in so far that ρ_p is determined from electron scattering; u_d can be obtained from bound state calculations. Hence the potential only has 8 instead of 12 parameters. These can be reduced to 3 parameters if the imaginary potential is derived from the real potential as described in section 2.2.2.

2.2.2 The Proton Reformulated Optical Model

The motivation of this work has been the desire to obtain a real part, and later an imaginary part of the optical potential for proton and composite particle-nucleus interactions from the nucleon-nucleon force. Hamada and Johnston (Ha 01) described an energy independent nucleon-nucleon potential comprising a central, tensor, linear and quadratic potential, and they assumed the presence of hard cores in all states, i.e. the potential increases to infinity as the internucleon distance tends to zero. They showed that their potential model represented both p - p and n - p data below 315 MeV .

The t-matrix for the two nucleon interaction is

$$t = v + vgv \qquad 2.2.17$$

where g may be the free Green's function, the scattering Green's function or the bound state Green's function

$$g_{free} = \frac{1}{E - K_1 - K_0 + i\varepsilon} \qquad 2.2.18$$

$$g_{scatt} = \frac{1}{E - H_N - K_0 + i\varepsilon} \qquad 2.2.19$$

$$g_{bound} = \frac{1}{E - (K_1+V_1) - (K_0+V_0) + i\varepsilon} \; . \qquad 2.2.20$$

The value of V is then a function of the summation of t_{scatt} which can be approximated (Ke 01) to

$$V = \sum_{i=1}^{A} t_{free}(r_0, r_1) \qquad 2.2.21$$

which is known as the impulse approximation.

Thomas, Sinha and Duggan (Th 12) developed a six-parameter optical model in which the real central part was calculated by folding several effective nucleon-nucleon interactions into matter distributions. They used the effective interactions due to Negele (Ne 01), Pandharipande (Pa 01) and Green (Gr 06) for proton scattering from a range of nuclei, and later Sinha and Duggan (Si 10) used the Kuo-Brown effective interaction (Ku 04).

The feature in the Kuo-Brown effective interaction of being able to distinguish the first and second order optical potentials makes this interaction popular when generating composite particle optical potentials self-consistently from the nucleon-nucleus optical potential.

The Kuo-Brown Effective Interaction

Kuo and Brown (Ku 04) evaluated the G-matrix of equation 2.2.6 using the Hamada and Johnston free nucleon-nucleon potential

$$V = V_C + V_T S_{12} + V_{LS}(\underline{L}.\underline{S}) + V_{LL} L_{12} . \qquad 2.2.22$$

For the even states of the Kuo-Brown force, the separation distance method was used (Mo 06) whereby the potential was divided into two parts, the short-range and the long-range parts. This enabled them to get round the problem of an infinitely repulsive core by choosing a separation distance so that the effect of the attractive part of the short-range potential balanced the effect of the repulsive core. Then what remained was essentially the long-range part of the potential.

The singlet even and triplet even states of the Kuo-Brown force were then evaluated from

$$V_{SE}^{KB}(r) = V_{L}^{HJ}(r) = 0.08(\tfrac{1}{3}\mu)(\tau_1.\tau_2)(\sigma_1.\sigma_2)Y(r)\left[1 + a_{cs}Y(r) + b_{cs}Y^2(r)\right] \qquad 2.2.23$$

$$V_{TE}^{KB}(r) = V_{L}^{HJ}(r) - \frac{8}{240}V_{TL}^2(r)$$

$$= 0.08(\tfrac{1}{3}\mu)(\tau_1.\tau_2)(\sigma_1.\sigma_2)Y(r)\left[1 + a_{ct}Y(r) + b_{ct}Y^2(r)\right]$$

$$- \frac{8}{240}\left[0.08(\tfrac{1}{3}\mu)(\tau_1.\tau_2)Z(r)\left[1 + a_tY(r) + b_tY^2(r)\right]\right]^2 \qquad 2.2.24$$

where μ = 139.4 MeV = pion mass

$a_{cs} = 8.7$, $b_{cs} = 10.7$, $a_{ct} = 6.0$, $b_{ct} = -1.0$

$a_t = -0.5$, $b_t = 0.2$

$$Z(r) = (1 + \frac{3}{r} + \frac{3}{r^2})Y(r) \text{ and } Y(r) = \frac{e^{-r}}{r} \qquad 2.2.25$$

V_{LT} is the Hamada and Johnston long-range tensor term. The hard core radius was $0.343\ \frac{\hbar}{\mu c}$.

The singlet odd and triplet odd states were calculated using the reference spectrum method, since these states are never attractive so the separation method cannot be used (Be 09).

Slanina and McManus (Sl 18) calculated the real parts of the central and spin orbit optical potential to first-order for proton scattering using the Kuo-Brown interaction. To

first-order in the effective two-nucleon interaction, the real part was written (Ke 01)

$$V(r) = A\int \bar{t}\,(|\underline{r} - \underline{r}'|)\,\rho(r')\,d\underline{r}' \qquad 2.2.26$$

where A - number of nucleons in the target

$\rho(r')$ - the matter point density

$\bar{t}(r)$ - spin-isospin average of the real part of the two-nucleon effective interaction.

From the Kuo-Brown force they assumed

$$t_{pp}(r) = \frac{1}{4} V_{SE}(r)$$

$$t_{np}(r) = \frac{1}{8}(V_{SE}(r) + 3V_{TE}(r)) \; . \qquad 2.2.27$$

Because they neglected exchange terms the direct term gave very little energy dependence.

The direct term of the reformulated proton optical model $V_d(r)$ was calculated by folding the proton-proton and proton-neutron effective interactions into the proton and neutron point-density distributions respectively, giving

$$V_d(r) = \int \rho_p(r') t^d_{pp}(|r - r'|) d^3r' + \int \rho_n(r') t^d_{pn}(|r - r'|) d^3r' \qquad 2.2.28$$

where in general

$$t^d_{pp}(r) = \frac{1}{4} V_{SE}(r) + \frac{3}{4} V_{TO}(r)$$

$$t^d_{pn}(r) = \frac{1}{8} V_{SE}(r) + \frac{3}{8} V_{TE}(r) + \frac{1}{8} V_{SO}(r) + \frac{3}{8} V_{TO}(r) \; .$$

A non-local exchange term was introduced, which arises from the antisymmetrization of the coordinates of the incident nucleon with those of the target nucleons (Ow 02)

$$V_e(\underline{r},\underline{r}') = \int \left[\rho_p(\underline{r},\underline{r}')t^e_{pp}(|\underline{r} - \underline{r}'|) + \rho_n(\underline{r},\underline{r}')t^e_{pn}(|\underline{r} - \underline{r}'|)\right] \times j_0(Kr)d^3\underline{r}_2 \qquad 2.2.29$$

where

$$t^e_{pp} = \frac{1}{4} V_{SE}(r) - \frac{3}{4} V_{TO}(r)$$

$$t^e_{pn} = \frac{1}{8} V_{SE}(r) + \frac{3}{8} V_{TE}(r) - \frac{1}{8} V_{SO}(r) - \frac{3}{8} V_{TO}(r) .$$

A Blin Stoyle prescription (Bl 10) was used for the spin orbit term, and the imaginary potential was calculated phenomenologically.

Sinha (Si 11) calculated the second-order nucleon-nucleus optical potential using a second-order perturbation formalism. He showed that the previous methods of simulating the second-order effect by using density dependent forces and approximate estimations were inaccurate for scattering, and that the second-order term was not negligible. The second-order term can be seen to come from equation 2.2.6, which may be re-written

$$T = V + VGV + VGVGV + ... \qquad 2.2.30$$

where the second term is the second-order term hitherto approximated assuming G to be a constant energy denominator usually referred to as the "closure approximation". Using the impulse approximation, 2.2.21, it is seen that

$$t_{free} = v + v g_{free} v \qquad 2.2.31$$

where using a constant energy denominator and the long-range part of the Kuo-Brown interaction

$$t_{free} = V_L + \frac{V_L^2}{240} \qquad 2.2.32$$

which is essentially the procedure taken to obtain 2.2.24, and the effective interaction from 2.2.22 is written as density dependent

$$t_{free} \simeq t_{eff} = V_L + \frac{8V_{TL}^2}{240}\left(1 - \alpha\left(\frac{\rho}{\rho_0}\right)^{2/3}\right) \quad . \qquad 2.2.33$$

Now

$$G = \frac{1}{E - H + i\varepsilon} \qquad 2.2.34$$

$$= P\left(\frac{1}{E - H}\right) + i\pi\delta(E - H)$$

so T may be written

$$T = V + V\left(P\left(\frac{1}{E - H}\right) + i\pi\delta\right)V \quad . \quad . \qquad 2.2.35$$

1st order real — 2nd order real — imaginary

Tedder and Sinha (Te 03) have calculated the imaginary term by taking the imaginary part of the second-order term of the nuclear T-matrix and evaluating the imaginary part of G using a plane wave approximation. Sinha and Duggan (Si 10) (Si 11) have calculated the

imaginary part of the optical potential using the Kuo-Brown effective interaction, assuming that the absorption arises entirely from the forward scattering amplitude (sometimes referred to as the frivolous model). The two-body effective interaction used to calculate the imaginary potential has a finite range. The nucleus in this model is usually described by a Fermi gas model, and the local Fermi momentum is calculated using the Thomas-Fermi approximation.

The first-order optical potential within the framework of the impulse approximation in coordinate space may be written (Ke 01)

$$U_{opt}(\underline{r}_1) = \frac{\hbar^2}{2\pi^2 m} \int d^3\underline{q}\; M(\underline{q})\; F(\underline{q})\; \exp(i\; \underline{q}\; .\; \underline{r}_1) \qquad 2.2.36$$

where $\underline{q}$ is the momentum transfer in the centre of mass system, $M(\underline{q})$ the free two-nucleon scattering amplitude and $F(\underline{q})$ the Fourier transform of the nucleonic distribution $\rho(r)$. The imaginary potential is assumed to arise from the imaginary part of the forward scattering amplitude, $M(0)$.

Then the imaginary potential $W(r_1)$ becomes

$$\begin{aligned} W(r_1) &= \text{Im}\; U_{opt}(\underline{r}_1) \\ &= \frac{-\hbar^2}{2\pi^2 m}\, \text{Im}\{M(0)\} \left[\frac{\int d^3\underline{q}\; M(\underline{q})\; F(\underline{q})\; \exp(i\underline{q}.\underline{r}_1)}{\text{Re}\{M(0)\}} \right] \end{aligned} \qquad 2.2.37$$

since the imaginary part of $M(0)$ is small compared to the real part. Hence Sinha and Duggan show that the imaginary potential can be expressed

$$W(r_1) = -\frac{4\pi\hbar^2}{m}\; \text{Im}\{M(0)\}\rho_{eff}(r_1) \qquad 2.2.38$$

where

$$\rho_{eff}(r_1) = UR(r_1) / J_f \ .$$

$UR(r_1)$ is the real part of the optical potential and J_f is the volume integral of the effective interaction.

Generalising the definition of the effective density to recognise the neutrons and protons separately one obtains

$$W(r_1) = \frac{1}{2} \hbar V_p \sum_{i=p,n} \rho^i_{eff}(r_1) \langle\sigma\rangle_{pi} \qquad 2.2.39$$

using the optical theorem. $\langle\sigma\rangle_{pi}$ being the average total nucleon-nucleon cross-section inside the nucleus, and V_p the velocity of the protons inside the nucleus.

Summary

The 3-parameter Kuo-Brown proton optical potential can be formulated as

$$U^{KB}_{opt} = S_R U_R(r) + i S_I W_I(r) + S_{SO} U_{SO}(r)$$

where S_R, S_I and S_{SO} are three normalisation parameters, and U_R is given by

$$U_R(r) = V_d(r) + V_e(\underline{r},\underline{r}')$$

as given by equations 2.2.28 and 2.2.29. The direct and exchange parts of the real potential consists of a sum of first-order terms (singlet

even) and second-order terms (triplet even and tensor forces). The exchange term contains the energy dependence term $j_0(Kr)$ where K is the projectiles momentum in the nucleus.

W_I is given by equation 2.2.37, and U_{SO} is the Blin Stoyle prescription for the spin orbit potential (Bl 10)

$$U_{SO}(r) = V_{SO} \left(\frac{\hbar}{m_\pi c}\right)^2 f_{SO}(r) \, \underline{\ell}.\underline{\sigma} \quad .$$

2.2.3 The ^{3}He Reformulated Optical Model

The approximate composite optical potential used in earlier analyses has been taken to be a value of $A \times V_p$, where A is the number of nucleons in the incident projectile, and V_p the real central depth of the proton potential. The derivation of the helium-3 optical potential from the proton and neutron optical potentials,

$$U_{^3He} = 2U_p + U_N$$

lacks the correct emphasis on the second-order term, which becomes increasingly important as A increases. However, the Kuo-Brown effective interaction allows the second-order term to be considered in the ^{3}He reformulation.

Samaddar et al (Sa 01) have calculated the optical potential for composite particles in terms of the optical potentials of neutrons and protons forming the projectile. The total Hamiltonian of a system consisting of helium-3 is

$$H = H_T + T_1 + T_2 + T_3 + v_{12} + v_{23} + v_{31} + V_1 + V_2 + V_3$$

2.2.40

where v_{ij} is the interaction between the ith and jth particles of the projectile, $V_i = \Sigma_{\ell=1}^{N} v_{i\ell}$ is the interaction between the ith particle of the projectile and the target consiting of N nucleons and T_i the kinetic energy operator of the ith particle.

This may be written,

$$H = H_T + \left[- \frac{\hbar^2}{2\mu_1} \nabla_R^2 - \frac{\hbar^2}{2\mu_2} \nabla_\rho^2 - \frac{\hbar^2}{2\mu_3} \nabla_r^2 \right] + V_{pp} + 2V_{pn} + V_n + 2V_p$$

2.2.41

where $\underline{R} = \frac{1}{3}(r_1 + r_2 + r_3)$

$\underline{r} = r_1 - r_2$

$\underline{\rho} = r_3 - \frac{1}{2}(r_1 + r_2)$

and r_1, r_2 and r_3 are the radial coordinates of the three nucleons constituting helium-3.

Sinha et al (Si 15) have used this approach in the development of a three-parameter optical model for helium-3 particles. Using the Feshbach formalism (Fe 03) (Fe 04) they developed the optical potential,

$$U_{opt}(R,E) = PVP + PVQ(E^+ - QHQ)^{-1} QVP \qquad 2.2.42$$

where $V = V_n + 2V_p$ and P is the projection operator such that

$$P\underline{\Psi} = \phi_0 \chi_0 \qquad 2.2.43$$

where $\underline{\Psi}$ is the eigenfunction of H and ϕ_0 and χ_0 are the ground state wave functions of the target and helium-3 respectively.

$Q = 1 - P$ is given by

$$Q\bar{\Psi} = \sum_{n\neq o}^{\infty} \phi_n \chi_n \qquad 2.2.44$$

The first term of equation 2.2.42 is

$$PVP = \langle \phi_0 \chi_0 | 2V_p + V_n | \chi_0 \phi_0 \rangle \quad . \qquad 2.2.45$$

Defining

$$G_H(E) = Q(E^+ - QHQ)^{-1}Q$$

$$G_{p,n}(E) = Q_{p,n}(E^+ - Q_{p,n} H_{p,n} Q_{p,n})^{-1}Q_{p,n}$$

where $H_{p,n}$ are the appropriate Hamiltonians for the proton and neutron target system. $Q_{p,n}$ are the corresponding projection operators. So

$$G_H(E) = \sum_{i=2p,n} G_i(E - T_j - T_k) + \sum_{i=2p,n} G_i(E - T_j - T_k) \left[V_j + V_k + v_{pp} + 2v_{pn}\right] GH(E) \quad . \qquad 2.2.46$$

Thus

$$PVG_H(E)VP = \langle \phi_0\chi_0 | \sum_{i=2p,n} V_i G_i(E_{eff}) \left[2V_p + V_n\right] + \sum_{i=2,n} V_i G_i(E_{eff}) \{V_j + V_k + v_{pp} + 2v_{pn}\} G_H(E) \left[2V_p + V_n\right] | \phi_0 \chi_0 \rangle \qquad 2.2.47$$

where $E_{eff} = E - T_j - T_k$.

Samaddar et al (Sa 01) considered the second term of this equation to be small. Thus equations 2.2.45 and 2.2.47 constitute the total helium-3 optical potential. The one-body real potential is generated by folding in a Kuo-Brown effective interaction with the target nucleus density.

The ^{3}He optical potential in terms of the optical potential of the constituent nucleons of ^{3}He is given by

$$U_{opt}^{^3He}(R,E) = \langle X_0\phi_0 | V_{p_1} + V_{p_2} + V_n | \phi X_0 \rangle$$

$$+ \sum_{i=p_1,p_2,n} \langle X_0\phi_0 | V_i G_i(E_{eff}) V | \phi_0 X_0 \rangle \ .$$

The motivation for using the Kuo-Brown interaction is that it is possible to distinguish between the first and second-order optical potential for the Kuo-Brown interaction which in turn makes it possible to generate composite particle optical potentials self-consistently from a nucleon-nucleus optical potential. The accuracy of this second-order term may also be critically tested.

2.2.4 The Nucleus-Nucleus Model

The nucleus-nucleus models hitherto derived by folding a phenomenological nucleon-nucleus optical potential with the projectile density have neglected the saturation properties which prevent the nuclear density from increasing beyond a certain magnitude. The simple folding models used in previous work can be represented by

$$U = \int < \chi_i | G\rho_t | \chi_f > \qquad 2.2.48$$

i.e. folding a Gaussian interaction, G , into a target density, and hence into the incident particle wave function

$$U = \int G\, \rho_t\, \rho_i \qquad 2.2.49$$

where ρ_i was also taken to be a Gaussian shape. Hence the optical potential was written in terms of another Gaussian interaction which took into account the incident projectile density

$$U = \int G'\, \rho_t \quad . \qquad 2.2.50$$

In this model the nucleon-nucleus optical potential is calculated by folding in a density-dependent two-body effective interaction, which takes into account saturation properties, with the target density. This potential is then folded in with the projectile density (Si 13) (Si 16).

The one-body optical potential at a point $\underline{t}$ relative to the centre of the target is

$$U_1(t) = \sum_{i=p,n} \int p_1^i(\underline{\xi}) V_{KK}^i(|\underline{s}|) \alpha^i \left[1 - \beta^i \{ \rho_{m1}(\underline{x}) + \rho_{m2}(\underline{\xi}_2 + \frac{\underline{s}}{2}) \right] d^3\xi_1 \qquad 2.2.51$$

neglecting all exchange terms.

V_{KK} is Kallio-Koltveit interaction (La 01) with associated parameters α^i and β^i .

ρ_1^i is the nucleon-density distribution measured from its centre, $\underline{\xi}_1$;

ρ_{m1} is the target matter density evaluated at $\underline{x} = \frac{1}{2}(\underline{t} + \underline{\xi}_1)$.

ρ_{m2} is the projectile matter density evaluated at $(\underline{\xi}_2 + \underline{s}/2)$ where $\underline{\xi}_2$ is the internal coordinate of the projectile and

$$|\underline{s}| = |\underline{t} - \underline{\xi}_1| \ .$$

Expanding ρ_{m2} gives

$$\rho_{m2}(\underline{\xi}_2 + \frac{\underline{s}}{2}) \simeq \rho_{m2}(\underline{\xi}_2) + \frac{s^2}{24} \nabla^2 \rho_{m2}(\underline{\xi}_2) \ . \qquad 2.2.52$$

$U_1(t)$ now has three components

$$U_1(t) = U_{11}(t) + \rho_{m2}(\underline{\xi}_2)\, U_{12}(t) + \nabla^2 \rho_{m2}(\underline{\xi}_2)\, U_{13}(t) \qquad 2.2.53$$

where

$$U_{11}(t) = \mathbf{V} \left[1 - \beta^i \rho_{m1}(x)\right] d^3 \xi_1$$

$$- \rho_{m2}(\underline{\xi}_2)\, U_{12}(t) = - \rho_{m2}(\underline{\xi}_2) \mathbf{V} \beta^i \, d^3 \xi_1$$

$$- \nabla^2 \rho_{m2}(\underline{\xi}_2)\, U_{13}(t) = - \nabla^2 \rho_{m2}(\xi) \mathbf{V} \beta^i \frac{s^2}{24} \, d^3 \xi_1$$

and $$\mathbf{V} = \sum_{i=p,n} \int \rho_1^i(\xi_1)\, V_{KK}(|s|) \alpha^i \ . \qquad 2.2.54$$

The first term contains no incident projectile density and so is similar to the simple folding model equation 2.2.50 using a two-body interaction instead of a Gaussian. The second term is repulsive, indicating the reduction in the one-body optical potential arising from the density-dependent part of the two-body interaction. Folding these equations with the projectile density the nucleus-nucleus

optical potential as a function of $\underline{R}$, the distance between the centres of the two nuclei becomes

$$U_{NN}(\underline{R}) = \int \rho_{m2}(\underline{\xi}_2)\, U_{11}|\underline{R} - \underline{\xi}_2|\, d^3\xi_2 - \int \rho_{m2}^2(\underline{\xi}_2)\, U_{12}|\underline{R} - \underline{\xi}_2|$$

$$d^3\xi_2 - \int \rho_{m2}(\underline{\xi}_2)\nabla^2\rho_{m2}\, U_{13}|\underline{R} - \underline{\xi}_2|\, d^3\xi_2 \,. \qquad 2.2.55$$

One of the advantages of this model is that U_{11}, U_{12}, U_{13} can be evaluated for a particular target without referring to any particular projectile.

This nucleus-nucleus potential allows any composite particle optical potential to be calculated, and hence enables the proton, helium-3, alpha and heavy ion data to be compared. This model does not include exchange effects and so it is expected to be more accurate for higher energy data.

The character of elastic scattering changes as one goes to heavier ions, where extremely peripheral nuclear effects predominate and there is no penetration due to saturation effects. These effects are expected to be seen to a small extent in ^{3}He scattering data.

2.3 The Collective Model

The collective model was introduced as an extension of the liquid drop model to explain the band structure of some nuclear states which demonstrated that not only do nucleons behave like single nucleons producing single particle states, but that they can act collectively to produce excited states of the nuclear core with vibrational and rotational characteristics.

This model makes provision for the deformation of the nucleus into a spheroidal shape. The shape of the surface in terms of radius R referring to an equilibrium radius $\bar{R}$ employ spherical harmonic expansions, which for space-fixed coordinate axes may be written

$$R = \bar{R}\left[1 + \sum_{\lambda\mu} \alpha_{\lambda\mu} Y_{\lambda\mu}(\theta,\phi)\right] \qquad 2.3.1$$

or for body-fixed coordinate axes

$$R = \bar{R}\left[1 + \sum_{\lambda\mu'} a_{\lambda\mu'} Y_{\lambda\mu'}(\theta',\phi')\right] \qquad 2.3.2$$

where μ or μ' range in integral steps from $-\lambda$ to $+\lambda$, and are zero for axial symmetry in the z direction (polar axis). So if the nucleus maintains a permanent non-spherical shape while rotating, then $\alpha_{\lambda\mu}$ vary with time even though the shape is fixed (i.e. $a_{\lambda\mu'}$ constant).

For ellipsoidal nuclei with quadrupole deformations ($\lambda = 2$) there are two values a_{22} and a_{20} related to the deformation parameters β_D and γ_D as,

$$a_{22} = \frac{1}{\sqrt{2}} \beta_D \sin \gamma_D \qquad 2.3.3$$

$$a_{20} = \beta_D \cos \gamma_D \qquad 2.3.4$$

hence

$$\beta_D^2 = (a_{20})^2 + 2(a_{22})^2. \qquad 2.3.5$$

Assuming the axis of rotation to be the z axis in the body-fixed system such that $\mu' = 0$ then

$$\beta_D = a_{20} \qquad 2.3.6$$

and

$$R = \bar{R}\left[1 + \beta_D Y_{20}(\theta')\right] = \bar{R}\left[1+(\frac{5}{4\pi})^{\frac{1}{2}}\beta_D P_2(\cos\theta')\right] \qquad 2.3.7$$

thus the departure from sphericity may be written

$$\Delta R \equiv R - \bar{R} = \bar{R}\, a_{20}\, Y_{20}(\theta') \,. \qquad 2.3.8$$

The β_D parameter measures the net deformation of the nucleus, and the γ_D parameter dictates the type of resultant deformed shape, e.g. $\gamma_D = 0$ gives a prolate spheroid, while $\gamma_D = \pi$ gives an oblate spheroid.

A Nilsson ellipticity parameter (Ni 02) was introduced,

$$\delta_D \equiv \frac{a - b}{\bar{R}} = 2\,\frac{a - b}{a + b} \qquad 2.3.9$$

for an ellipsoidal nucleus with major semiaxis a and minor semiaxis b with mean radius $\bar{R}$.

From 2.3.7

$$a = \bar{R}\left[1 + \beta_D(\frac{5}{4\pi})^{\frac{1}{2}}\right] \text{ and } b = \bar{R}\left[1 - \frac{1}{2}\beta_D(\frac{5}{4\pi})^{\frac{1}{2}}\right] \qquad 2.3.10$$

and hence,

$$\beta_D = \frac{4}{3}(\frac{\pi}{5})^{\frac{1}{2}}\,\delta_D = \frac{8}{3}(\frac{\pi}{5})^{\frac{1}{2}}\,\frac{a - b}{a + b} \,. \qquad 2.3.11$$

The magnitude of the electric quadrupole moment, determined spectroscopically, gives an indication of the shape and extent of asymmetry. The quadrupole moment of a homogeneously charged ellipsoid is .

$$Q_0 = \frac{2}{5} Ze(a^2 - b^2) = \frac{4}{5} \bar{R}^2 Ze \, \delta_D \qquad 2.3.12$$

or substituting equation 2.3.10, the second-order term is obtained

$$Q_0 = \frac{3}{(5\pi)^{\frac{1}{2}}} \bar{R}^2 Ze \, \beta_D \left[1 + \left(\frac{5}{64\pi}\right)^{\frac{1}{2}} \beta_D \right] . \qquad 2.3.13$$

Q_0 in this expression constitutes the intrinsic quadrupole moment, assuming the symmetry axis is aligned in the direction of the nuclear spin $\underline{J}$. Its relation to the actually measured Q is (Ma 04)

$$Q = \frac{[3K^2 - J(J+1)]}{(J+1)(2J+3)} Q_0 \qquad 2.3.14$$

with $J = K, K+1 \ldots,$ where the ground state quadrupole moment is given by setting $K = J$

$$Q_{gs} = \frac{J(2J-1)}{(J+1)(2J+3)} Q_0 . \qquad 2.3.15$$

The value of Q_0 may also be derived from the probability for E2 transitions within a rotational band, where the reduced transition probability

$$B(E2, 0^+ \rightarrow 2^+) = \frac{5}{16\pi} e^2 Q_0^2 . \qquad 2.3.16$$

Equations 2.3.11, 2.3.12 and 2.3.16 relate B(E2), Q_0, β_D and δ_D such that

$$B(E2) = \frac{1}{5\pi} \overline{R}^4 Z^2 (0.946 \beta_D)^2 \quad . \qquad 2.3.17$$

2.3.1 Rotational and Vibrational Nuclei

The reason for some nuclei being spherical and vibrational, whilst others are deformed and rotational, can be seen by considering the possible ways that the nucleons can couple, and the resulting equilibrium shapes favoured by the coupling schemes. The first is favoured by the short-range inter-nucleon forces which tend to couple nucleons in pairs to $J = 0$ configurations to produce a spherical equilibrium shape. The second is favoured by a tendency of each nucleon to align its orbit with the average field produced by all the other nucleons to produce a deformed equilibrium shape.

For a closed-shell nucleus, all j-shells of single particle orbitals are either fully occupied or completely vacant, and the density distribution is spherical. The aligned coupling scheme now says that if nucleons are added to the next empty j-shell the density distribution will be concentrated in the equatorial plane or the polar axis, depending on whether the first nucleon was put into the $m = j$ or $m = \frac{1}{2}$ orbit, i.e. whether the j of the nucleon has a maximum or minimum projection on the symmetry axis. This non-spherical field attracts other nucleons to align their orbital planes with the equator or polar axis, in as much as they are allowed by the Pauli principle producing oblate or prolate spheroids, respectively. When the field becomes deformed, the total angular momentum, j, of a nucleon

ceases to be a good quantum number, and the wave functions spread over a number of j- orbitals. In this way the effect of the Pauli principle can be minimized and very large deformations established as in rare earth nuclei. The aligned coupling scheme makes no attempt to ensure that the total angular momentum of the system should be a good quantum number, and it does not, therefore, describe a stationary state of the nucleus. Thus, the deformed nucleus must rotate in such a manner that its rotational angular momentum couples with the intrinsic angular momentum.

The field producing forces make no provision for spherical nuclei, other than those with doubly closed shells. A simple explanation for the stable spherical shape found in many nuclei is given in terms of the short-range interaction. Two particles assumed to be moving in time reversed orbits approach each other twice in every orbit. If there is a strong short-range interaction between them, they frequently scatter into new time reversed orbits. Thus, they rapidly spread over all angular space to provide a spherical density distribution. In even-even nuclei the ground state is invariably $J = 0$. The Pauli principle, however, prevents more than two particles coming very close together. Thus, a number of particles must be coupled pairwise to $J = 0$. The spherical equilibrium shape for vibrational motion may be represented by the dynamic deformation parameter α_μ such that

$$R(\theta) = R_0\left(1 + \sum_\mu \alpha_\mu Y_{20}(\theta)\right) .$$

The nucleus may be considered to have one or more vibrational quanta, or phonons, of energy $\hbar\omega_\lambda$, angular momentum $\lambda\hbar$, and parity

$(-1)^{\lambda}$. The lowest level is caused by a $\lambda = 2$ (quadrupole) phonon. Vibrations with $\lambda = 0$, and $\lambda = 1$ are due to density oscillations of the spherical nucleus, and motions of the centre of mass of the nucleus, respectively.

2.4 The Application of the Collective Model in Inelastic Scattering

D.W.B.A. predictions in the framework of the collective model enable values of the deformation parameter β and angular momentum J to be found. The assumption here is that the collective states are only weakly coupled to the elastic scattering channel, so that the incoming and outgoing waves are distorted by the same potentials as the elastic scattering interaction, the latter being unaffected by the inelastic scattering process.

However, this is not always a good assumption, indeed the successes of the D.W.B.A. with its over simplifications are often quite surprising. Pickup (Gr 09) and stripping (Sh 07) (We 01) reactions with incident ^{3}He particles have been found to be inadequately described by the D.W.B.A.

It is often necessary to explicitly include dominant inelastic channels in the calculations. This technique, known as the strong coupling approximation (SCA), couples highly excited states to the elastic channel resulting in a series of coupled radial equations being derived from the Schrodinger equation.

The coupled equations' formalism will be shown in 2.4.1., and the D.W.B.A. special case of coupled equations will be illustrated in 2.4.2.

2.4.1 The S.C.A. Approach

In D.W.B.A. the distorted wavefunctions for the incoming and outgoing particles are generated using the optical potential which describes elastic scattering, and the effect of the non-elastic channels is taken into account through the imaginary part of the optical potential. If, however, one or more inelastic channels are strongly coupled to the elastic channel, it is not sufficiently accurate to take them into account through the D.W.B.A.

In S.C.A. the elastic scattering and the reaction channels under consideration are treated explicitly, while the remaining reaction channels are taken into account by an imaginary potential, as in the simple optical model. Treatment of a collective 2^+ level was described by Buck (Bu 14). Extensions of the calculations to higher excited states have been made by Buck (Bu 13), Buck et al (Bu 14) and Tamura (Ta 01).

The Schrodinger equation for an interaction between an incident projectile and target nucleus is

$$T - V(\underline{r},\xi) + H(\xi)\,\overline{\psi}(\underline{r},\xi) = E\,\overline{\psi}(\underline{r},\xi) \qquad 2.4.1$$

where the nuclear states $\chi_\alpha(\xi)$ are defined by

$$H(\xi)\chi_\alpha(\xi) = \varepsilon_\alpha \chi_\alpha(\xi) \ . \qquad 2.4.2$$

The $\chi_\alpha(\xi)$ form a complete orthonormal set so that the total wavefunction of the system may be expanded to give the sum of the wavefunctions for each channel

$$\overline{\Psi}(\underline{r},\xi) = \sum_{\alpha} \psi_{\alpha}(\underline{r})\chi_{\alpha}(\xi) \quad . \qquad 2.4.3$$

Using these equations and integrating over the nuclear coordinates ξ gives

$$(T-E+\varepsilon_{\alpha})\ \psi_{\alpha}(\underline{r}) = \sum_{\alpha=1}^{N} V_{\alpha\alpha'}(\underline{r})\ \psi_{\alpha'}(\underline{r}) \qquad 2.4.4$$

where

$$V_{\alpha\alpha'}(\underline{r}) = \int \chi_{\alpha}^{*}(\xi)\ V(\underline{r},\xi)\ \chi_{\alpha'}(\xi)\ d\xi \quad . \qquad 2.4.5$$

The angular coordinates may be removed from these equations by the usual partial-wave expansion

$$\psi_{\alpha}(r) = \sum_{LM} \frac{\phi_{\alpha}(r)}{r}\ Y_{L}^{M}(\theta,\phi) \quad . \qquad 2.4.6$$

Equations 2.4.4 and 2.4.6 yield

$$\{\frac{d^2}{dr^2} - \frac{L(L+1)}{r^2} + K_{\alpha}^2 - W_{\alpha\alpha}(r)\}\ \phi_{\alpha}(r) = \sum_{\alpha'\neq\alpha} W_{\alpha\alpha'}(r)\phi_{\alpha'}(r)$$

$$2.4.7$$

where

$$W_{\alpha\alpha'}(r) = \frac{2m}{\hbar^2} \sum_{LM} Y_{L'}^{M'*}(\theta,\phi)V_{\alpha\alpha'}(\underline{r})Y_{L}^{M}(\theta,\phi)d\Omega \qquad 2.4.8$$

where the relations 2.4.7 constitute a set of coupled equations for the wavefunctions in the elastic and all the inelastic channels in the reaction under consideration. In practice, these equations are truncated, and to allow for the effect of all channels not taken

into account explicitly by letting $V(\underline{r},\xi)$ be complex.

2.4.2. The D.W.B.A. Approach

The D.W.B.A. theory has been well documented elsewhere (Gl 02), (Ba 03), (Ki 02), (Ja 01) and by Hodgson (Ho 06) whose treatment of the D.W.B.A. will be illustrated here.

Considering the reaction in which particles are incident in channel α, and outgoing in channels α', as well as the incident channel, the matrix element $S_{\alpha\alpha'}$ is defined as the amplitude of the outgoing wave in channel α' when a wave of unit amplitude is incident in channel α. Thus the asymptotic forms of the waves are

$$\phi^{\alpha}_{\alpha}(r) \sim e^{-i(Kr-\frac{1}{2}L\pi)} - S_{\alpha\alpha}\, e^{i(Kr-\frac{1}{2}L\pi)} \qquad 2.4.9$$

and

$$\phi^{\alpha}_{\alpha'}(r) \sim -S_{\alpha\alpha'}\, e^{i(Kr-\frac{1}{2}L\pi)} \qquad 2.4.10$$

where the radial wave function $\phi^{\alpha}_{\alpha}(r)$ satisfies the radial wave equation obtained from coupled channels theory

$$\left\{ \frac{d^2}{dr^2} - \frac{L(L+1)}{r^2} + K^2_{\alpha} - W^{\alpha}_{\alpha\alpha}(r) \right\} \phi^{\alpha}_{\alpha}(r) = \sum_{\alpha\neq\alpha'} W^{\alpha}_{\alpha\alpha}(r)\phi^{\alpha}_{\alpha'}(r). \qquad 2.4.11$$

Now, consider the reaction when particles are incident in channel β. Then,

$$\left\{ \frac{d^2}{dr^2} - \frac{L(L+1)}{r^2} + K^2_{\alpha} - W^{\beta}_{\alpha\alpha}(r) \right\} \phi^{\beta}_{\alpha}(r) = \sum_{\alpha=\alpha'} W^{\beta}_{\alpha\alpha}(r)\phi^{\beta}_{\alpha'}(r). \qquad 2.4.12$$

These equations may be rearranged to give

$$\{ \frac{d^2}{dr^2} - \frac{L(L+1)}{r^2} + K_\alpha^2 - W_{\alpha\alpha}^{\alpha}(r) \} \phi_\alpha^\alpha(r) - \sum_{\alpha'=\alpha,\beta} W_{\alpha\alpha'}^{\alpha}(r)\phi_{\alpha'}^{\alpha}(r)$$

$$= W_{\alpha\beta}^{\alpha}(r)\phi_\beta^\alpha(r) \qquad 2.4.13$$

and

$$\{ \frac{d^2}{dr^2} - \frac{L(L+1)}{r^2} + K_\alpha^2 - W_{\alpha\alpha}^{\beta}(r) \} \phi_\alpha^\beta(r) - \sum_{\alpha'=\alpha,\beta} W_{\alpha\alpha'}^{\beta}(r)\phi_{\alpha'}^{\beta}(r)$$

$$= W_{\alpha\beta}^{\beta}(r)\phi_\beta^\beta(r) \ . \qquad 2.4.14$$

Hence

$$\phi_\alpha^\beta(r) \frac{d^2}{dr^2} \phi_\alpha^\alpha(r) - \phi_\alpha^\alpha(r) \frac{d^2}{dr^2} \phi_\alpha^\beta(r)$$

$$= \phi_\alpha^\beta(r)\, W_{\alpha\beta}^{\alpha}(r)\, \phi_\beta^\alpha(r) \ - \ \phi_\alpha^\alpha(r)\, W_{\alpha\beta}^{\beta}(r)\, \phi_\beta^\beta(r) \qquad 2.4.15$$

assuming

$$\phi_\alpha^\beta(r) \sum_{\alpha'} W_{\alpha\alpha'}^{\alpha}(r)\, \phi_{\alpha'}^{\alpha}(r) \ = \ \phi_\alpha^\alpha(r) \sum_{\alpha'} W_{\alpha\alpha'}^{\beta}(r)\, \phi_{\alpha'}^{\beta}(r) \ . \qquad 2.4.16$$

Integrating from 0 to ∞ and using the asymptotic forms 2.4.1 and 2.4.2 for the radial wave equation gives for 2.4.7. L.H.S.

$$\left[\phi_\alpha^\beta(r) \frac{d^2}{dr^2} \phi_\alpha^\alpha(r) - \phi_\alpha^\alpha(r) \frac{d^2}{dr^2} \phi_\alpha^\beta(r) \right]_0^\infty$$

$$= - S_{\beta\alpha} e^{+X}(ike^{-X} - ikS_{\alpha\alpha} e^{+X}) - (e^{-X} - S_{\alpha\alpha} e^{+X})(-ik) S_{\beta\alpha} e^{+X}$$

$$= 2ikS_{\beta\alpha} \qquad 2.4.17$$

where

$$X = i(Kr - \tfrac{1}{2}L\pi) .$$

Now for 2.4.7 R.H.S. it is assumed that the inelastic channels are weakly coupled to the elastic channel so that $\phi_\alpha^\beta(r) << \phi_\alpha^\alpha(r)$. Thus

$$S_{\beta\alpha} = \frac{-1}{2ik} \int_0^\infty \phi_\alpha^\alpha(r)\, W_{\alpha\beta}^\alpha(r)\, \phi_\beta^\beta(r)\, dr . \qquad 2.4.18$$

And since this is true for all channels β ,

$$S_{\alpha\alpha'}^{LM} = - \frac{1}{2ik} \int_0^\infty \phi_\alpha^{\alpha'}(r)\, W_{\alpha'\alpha}(r)\, \phi_\alpha^\alpha(r)\, dr \qquad 2.4.19$$

where L + M show that matrix element refer to a particular partial wave. The total inelastic cross-section is now given by

$$\sigma_{\alpha\alpha'} = \frac{4\pi}{k^2} |S_{\alpha\alpha'}|^2 . \qquad 2.4.20$$

From 2.4.5, 2.4.6, and 2.4.14

$$S_{\alpha\alpha'} = - \frac{2m}{\hbar^2} \frac{1}{2ik} \int \psi_{\alpha'}(r)\, V_{\alpha\alpha'}(r)\, \psi_\alpha(r)\, dr . \qquad 2.4.21$$

The correlated modes of motion of the nucleons produce a static deformation of the nucleus which is parameterized in terms of the radius

$$R(\theta,\phi) = R_0(1 + \sum_{LM} \beta_L Y_L^M(\theta,\phi)) . \qquad 2.4.22$$

The deformed potential $V(R(\theta,\phi))$ expanded about $r = R_0$ gives

$$V(r-R(\theta,\phi)) = V(r-R_0) - \frac{d}{dr} V(r-R_0)\delta R + \frac{1}{2}\frac{d^2}{dr^2} V(r-R_0)\delta R^2 \ldots$$

where $$\delta R = R_0(\sum_{LM} \beta_L Y_L^M(\theta,\phi)) \ . \qquad 2.4.23$$

The first term in the expansion is the undeformed optical potential giving rise to the elastic scattering. To first-order the inelastic transitions arise from the second term.

2.5 Forms of Analysis

The data for helium-3 elastic scattering from the Samarium isotopes was analysed using the regular optical model and reformulations of it, and the data for the helium-3 inelastic scattering was analysed using the collective model, both D.W.B.A. and Strong Coupling Approximation (SCA).

The regular and reformulated optical model due to Greenlees (Gr 08) analysis was performed using the computer code RAROMP (Py 04). This programme enables both depths and geometry parameters to be searched upon to obtain the best X^2 minimum fit of the theoretical curve to the elastic scattering data. The programme has facilities for coulomb, real, surface and volume imaginary, and spin orbit depths and associated geometries. For the reformulated optical model analysis, the matter distribution or the neutron and proton density distributions may be parameterised to give a Saxon-Woods shape density. There are facilities for using either a Gaussian or a Yukawa interaction as the effective two-body interaction, and the mean square radius of this interaction can be specified. When using the regular optical model analysis the ambiguity between the real depth and real radius parameters, namely that

$$V_R \, r_R^n = \text{const} \qquad 2.5.1$$

in effect means that these two parameters cannot be varied simultaneously. There is also an ambiguity problem in the family of parameters which best fit the angular distributions. The particular family of parameters which will give the best fit is largely determined by the starting parameters.

The D.W.B.A. analysis was performed using the computer code DWUCK (Ku 03). The distorted waves are generated from the optical potential obtained using the optical model parameters from the simple optical model analysis. For inelastic scattering the form factor for the transfer of angular momentum L is represented by the derivative of the optical potential. The fits to the inelastic scattering data of the cross-sections generated by DWUCK determine the deformation parameters for the nucleus according to the relation (Jo 02)

$$\frac{d\sigma}{d\Omega} = C \sum_L \beta_L^2 \, \sigma_L(\theta) \qquad 2.5.2$$

where σ_L is the cross-section calculated by DWUCK and C is a normalisation factor.

The S.C.A. analysis was performed using the computer code JUPITOR (Ta 01) (Ta 02) which was modified by H. Rebel and G. W. Schweimer at Karlsruhe (Sc 05) (Re 02). This programme included a parameter search routine with an improved treatment of the rotational model.

The microscopic optical model analyses were performed using programmes written by Sinha (Si 14) and arranged by the author.

CHAPTER 3

The Measurement of Helium-3 Scattering Cross-sections from Samarium Isotopes at 53 MeV

Introduction

This chapter will describe the experiments performed on the Variable Energy Cyclotron, Harwell, and the Oak Ridge Isochronous Cyclotron. Brief descriptions of these machines and their major facilities will be included, and the design of a nuclear physics experiment will be discussed.

The electronics will be described together with the calibration and setting up procedures.

The methods of data taking and data reduction will also be discussed in detail here, and the analysis of these data will follow in subsequent chapters.

3.1 AVF or Isochronous Cyclotrons

The AVF or Isochronous Cyclotrons were introduced to overcome the difficulties due to relativistic and focussing problems with the original cyclotron and the low intensity limitation of the synchrocyclotron.

The isochronous cyclotron was developed possessing an azimuthally varying magnetic field, so that particles traverse regions of field which are alternatively greater than and less than the mean field. Thus the radius of trajectory changes in these regions becomes respectively greater than and less than the mean radius. In the Harwell Variable Energy Cyclotron the ridge between high and low fields

is deliberately set at a constant angle to the particle motion. The axially deflecting forces are strong and the ridges spiral from the centre to the outer edge of the magnet gap. Thus the angle at which the particle approaches the edge oscillates, i.e. first positive and then negative with respect to normal. The resultant effect of this varying field is focussing.

3.2 The VEC at AERE Harwell

The VEC belongs to a family of machines known as 'sector focussed cyclotrons', of which there are approximately forty operational in the world. This particular machine is extremely versatile, being capable of accelerating many different ions to an energy which can be varied over a wide range by changing the machine parameters. The VEC machine is capable of producing beam currents for helium-3 beams of up to 2μA on target, which facilitated the data taking at backward angles where the cross-sections for helium-3 elastic scattering from Samarium were very small. The plan diagram of the VEC is shown in fig 3.1(La 03).

The magnet ridges are in a spiral shape to give an azimuthal variation adequate to provide focussing for 50 MeV protons. The frequency is varied by moving the shorted end of the radio frequency cavity to an appropriate position (Al 05).

Ions of the type required are produced in the arc discharge at the centre of the magnet gap. They are accelerated to the required energy by an alternating radio-frequency electric field being constrained to move in spiral paths by the magnetic field. When they achieve the desired energy they are pulled out by an electrostatic

Fig 3.1 Photograph of the general layout of the V.E.C.

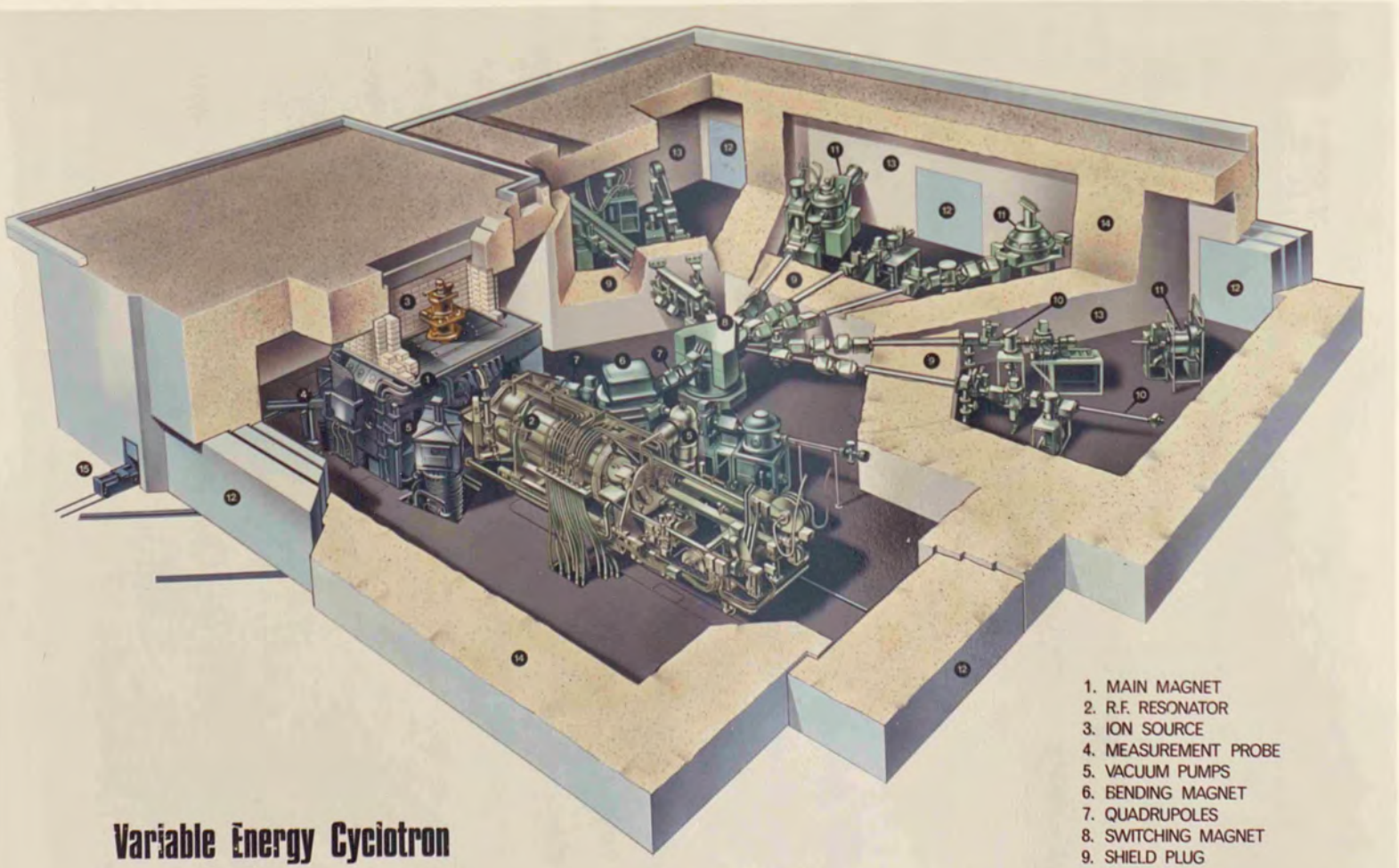

Variable Energy Cyclotron

1. MAIN MAGNET
2. R.F. RESONATOR
3. ION SOURCE
4. MEASUREMENT PROBE
5. VACUUM PUMPS
6. BENDING MAGNET
7. QUADRUPOLES
8. SWITCHING MAGNET
9. SHIELD PLUG
10. FLIGHT TUBES
11. USERS EXPERIMENTS
12. SHIELDING DOORS
13. TARGET ROOMS
14. CONCRETE SHIELDING
15. TARGET TRANSPORTER

extractor after which they travel down evacuated pipes, through bending and focussing magnets in the beam optics system and into one of the target rooms.

The variable energy cyclotron has magnet poles of 70 inch diameter with twenty-one independent 'trim' coils. The mean magnetic field at maximum energy is 17 kilogauss and the maximum power dissipated in the magnet and trim coils is 600 KW. The machine has facilities for varying the RF frequency range from 7.6 - 23 MHz with a maximum RF power of 200 KW. The machine operates at an internal pressure of 2×10^{-6} mm Hg, and vacuum trips are installed in the event of any vacuum leaks, especially in the scattering chamber of the user.

The cyclotron has the capacity for producing 50 MeV protons and other ions with a maximum energy of $86Q^2/A$ MeV (atomic weight A, charge Q).

The particular quality of this machine is its ability to produce 1800n A of ^3He beam at 53.4 MeV on target, thus enabling back angle data to be taken efficiently. However, the resolution required for ^3He scattering from the rotational nuclei of the Samarium isotopes in order to separate out the first excited state precluded its use for these experiments.

3.3 Beam Extraction and Transport

As the circulating beam approached the outer radius it passed a septum. The final beam intensity obtained was limited by the power dissipation on the septum. The turn separation at the extraction radius is ~0.75 mm, hence the cyclotron extractor intercepts several

orbits of the internal beam. Thus the unanalysed beam contained particle energies over a small energy range. This was reduced by magnetically analysing the beam with the bending magnet and separating the particles of different momenta with the analysing slit sb B.

Beyond the separator was a high radial electrostatic field and magnetic channel which deflected the beam out into the beam pipe.

The Beam Transport of the Variable Energy Cyclotron is shown in fig. 3.2. After extraction from the cyclotron the beam passed through a steering magnet which corrected the alignment of the extracted beam. Two short focal length quadrupoles Q_1 and Q_2 produced horizontal and vertical focussing of the beam onto the entrance slit (slit box A) of the bending magnet. The beam then passed through the exit slit (slit box B). Slit box A and slit box B had slits of width 0.04 and 0.06 inches, respectively.

Quadrupoles Q_3 and Q_4 were left unconnected since it had been shown that these focussed the beam onto the switching magnet, thus reversing the dispersive effect of the bending magnet and worsening resolution. The switching magnet directed the beam along beam line 5 through two more quadrupoles, Q_5 and Q_6, which focussed the beam onto slit box 1. Further quadrupoles, Q_7 and Q_8, and a steering magnet which adjusted vertical and horizontal directions of the beam, focussed the beam onto slit box 2 and hence through the antiscattering baffle. The beam then entered the scattering chamber and interacted with the target. The main Faraday cup monitored the quantity of beam current through the target.

Beam probes were used to monitor the beam in the cyclotron, and slit boxes along the beam line were used to monitor the beam

Fig 3.2 Beam Transport System of the V.E.C.
(not to scale)

b a	Two back angle detector ports
b m	Bending magnet
d p	Diffusion pump
f a	Forward angle detector range
f c	Faraday cup
g v	Shut-off gate valve
i c	internal collimator
q	quadrupoles
s b	slit box
s c	scattering chamber
st m	steering magnet
sw m	switching magnet

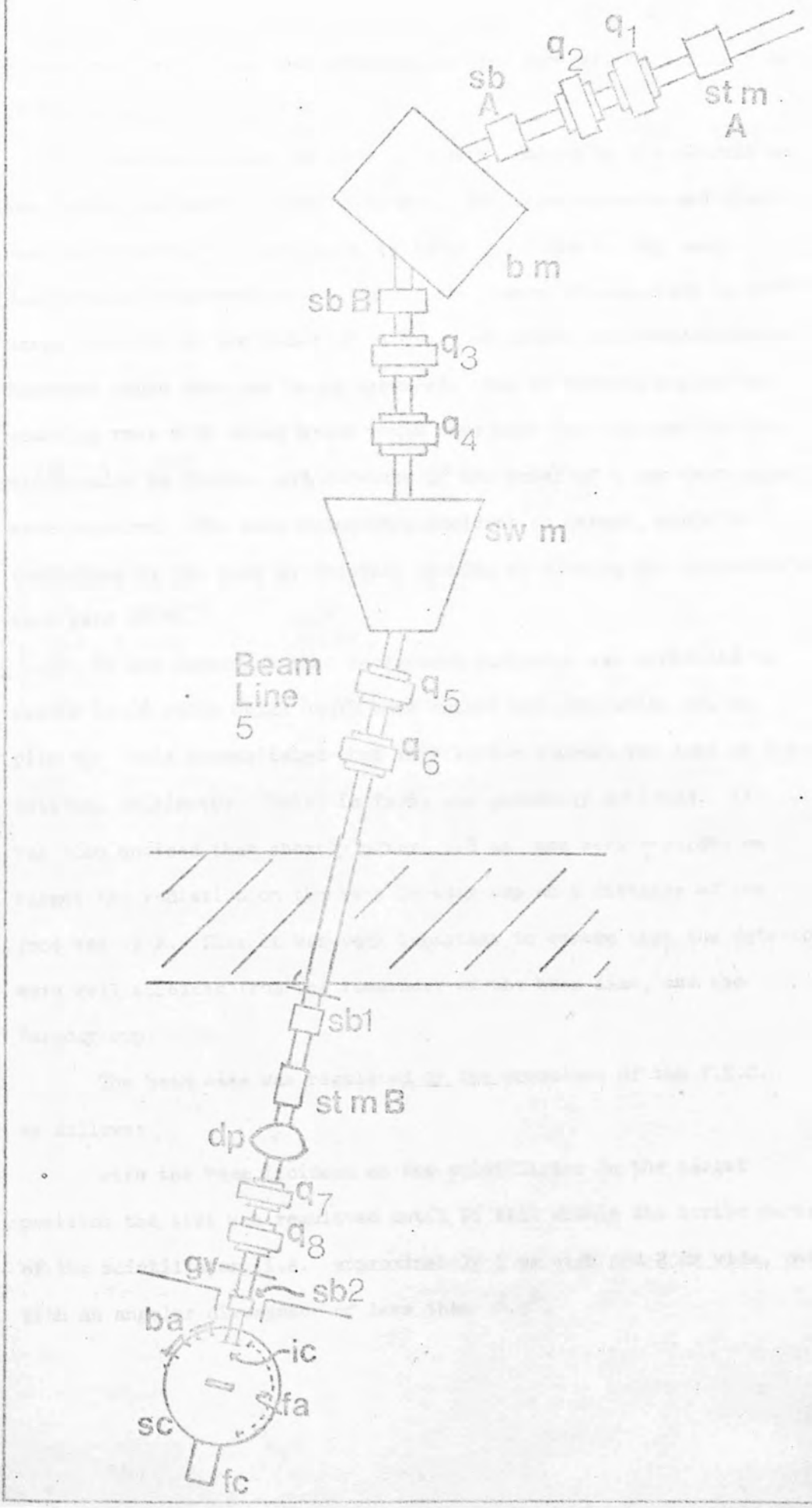
q1
q2
sb A
st m A
b m
sb B
q3
q4
sw m
Beam Line 5
q5
q6
sb1
st m B
dp
q7
q8
gv
sb2
ba
ic
fa
sc
fc

current and centre the beam by measuring the currents on either side of the slits.

A maximum current of 1800 nano amps limited by the current on the septum was recorded on the target. The beam currents and transmission recorded then are shown in Table 3.1. Due to the large decrease in cross-section with angle (12 orders of magnitude in 150°) large currents of the order of 1.8 μA on target were required when backward angle data was being measured. But at forward angles the counting rate with these beams would have been far too much for the electronics to handle, and currents of the order of a few nano amps were required. The beam intensity, incident on target, could be controlled by the user by remotely opening or closing the cyclotron's exit gate slits.

It was important that background radiation was minimised to reduce count ratio which would have caused bad resolution due to pile up. This necessitated that very little current was lost on the internal collimator. This, in fact, was generally achieved. It was also noticed that shortly after 1.8 μA had been recorded on target the radiation on the main Faraday cup at a distance of one foot was 1 R. Thus it was very important to ensure that the detectors were well shielded from the remainder of the beam line, and the Faraday cup.

The beam size was regulated by the operators of the V.E.C. as follows:

with the beam incident on the scintillator in the target position the size was regulated until it fell within the scribe marks of the scintillator, i.e. approximately 5 mm high and 2 mm wide, and with an angular divergence of less than 0.3°.

Beam Position	Current (μA)	Efficiency (%)
Extracted Beam	36	
Beam transmitted through septum	18	50
Beam transmitted through slit A (0.04 inches)	9	50
Beam transmitted through slit B (0.06 inches)	2	22.2
Beam transmitted through collimator	1.4	70

Table 3.1

Beam currents along beam line when 1400 n amps was recorded on target.

The beam transport was set up initially with an analogue computer simulating beam profiles. The beam line conditions were predicted using a computer program to scale up the focussing currents to the energy and rigidity of the 53.4 MeV helium-3 beam. Only final small adjustments to maximise the transmission were required afterwards.

3.4 Experimental Design

3.4.1 The Scattering Chamber and Detection Systems

The beam was transported to a 66 cm diameter scattering chamber, fig. 3.3, which was a fixed chamber with a rotateable lid on which two of the detector telescopes were mounted. The lid could be rotated using a variable speed motor and the angle measured to 0.05^{o}. The precision position of the portholes around the chamber enabled the initial detector angle setting to be measured accurately using an optical theodolyte. The chamber could be evacuated using two six-inch diffusion pumps and a supplementary pump located before quadrupole Q_7. The maximum working pressure of the chamber was about 2×10^{-4} torr, but the pressure was generally about 10^{-5} torr and this pressure could generally be achieved in 40 minutes starting from atmospheric pressure. Diffusion pumps were used with liquid nitrogen baffles to stop back-streaming and condensation of oil on cold detectors.

Fig 3.3 Photograph of the A.E.R.E. Variable Energy Cyclotron - Beam Line 5.

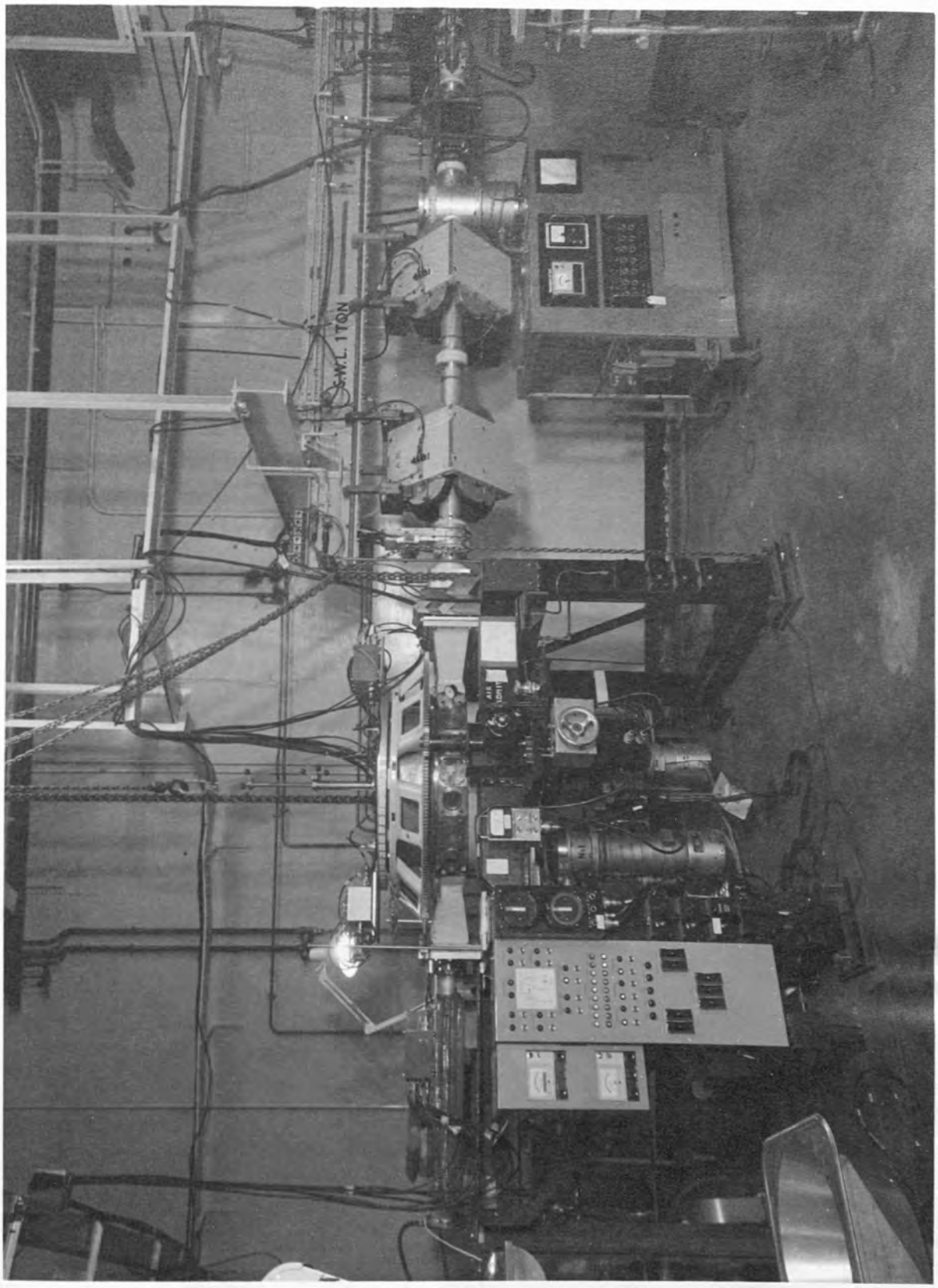
S.W.L. 1TON

3.4.2 The Detector Locations

In view of the large decrease in cross-section with angle, it was calculated that some backward angle data runs would require long counting times (~10 hours) to achieve a satisfactory number of counts. It was therefore decided to have, permanently placed at backward angles in two back angle ports, two detectors (which will hereafter be denoted as back angle detectors) each capable of being set at three different angles, such that the angles from 125° - 150° could be measured in approximately 5° steps. These detectors were located in two backward angle portholes, but they could be moved to forward angle portholes at the beginning of the experiment when the mass function generator was being set.

The two detector telescopes which were mounted on the lid of the chamber, see fig. 3.4, (hereafter called forward angle detectors) were capable of being moved through the complete angular range. When measuring the angular distributions, these detectors were moved around to the opposite side of the beam to the back angle detectors, thus avoiding collisions.

A diagram of the back angle detector positions is shown in fig 3.5, and the actual apparatus used to achieve this is shown in fig 3.6. The port at 115° enabled the connections from the detectors to be fed through the side of the chamber.

The back angle detectors and their preamplifiers had been designed to operate at room temperatures, and even with 1000 volts on the E detectors, their leakage currents remained below 10μ amps. However, the forward angle detectors and their Harwell preamplifiers were found to work better in a cryogenic state. This was in fact necessary to prevent enormous leakage currents from the detectors. Thus the

Fig 3.4 Forward Angle Detector System and Housing showing Cooling Pipes.

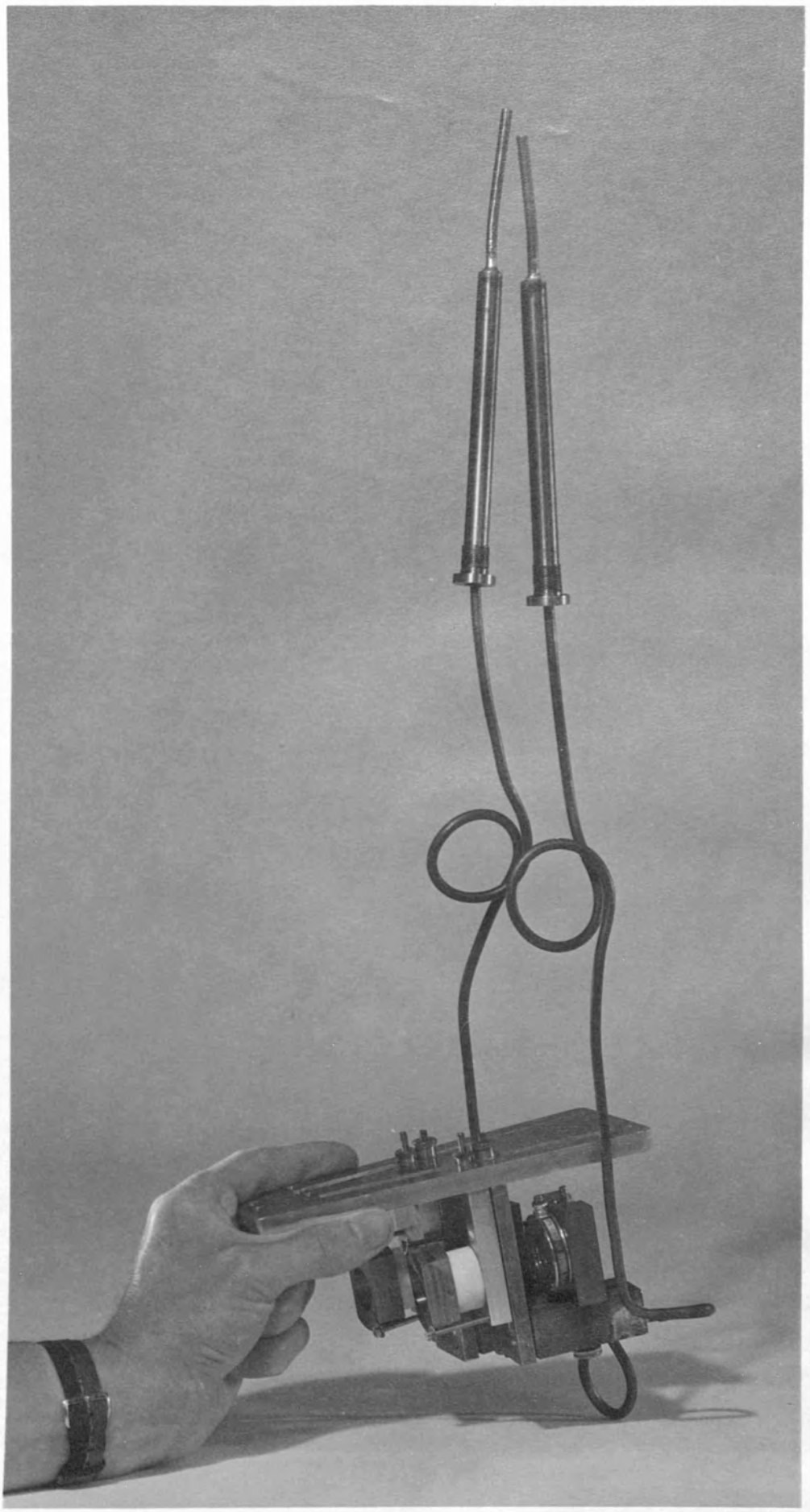

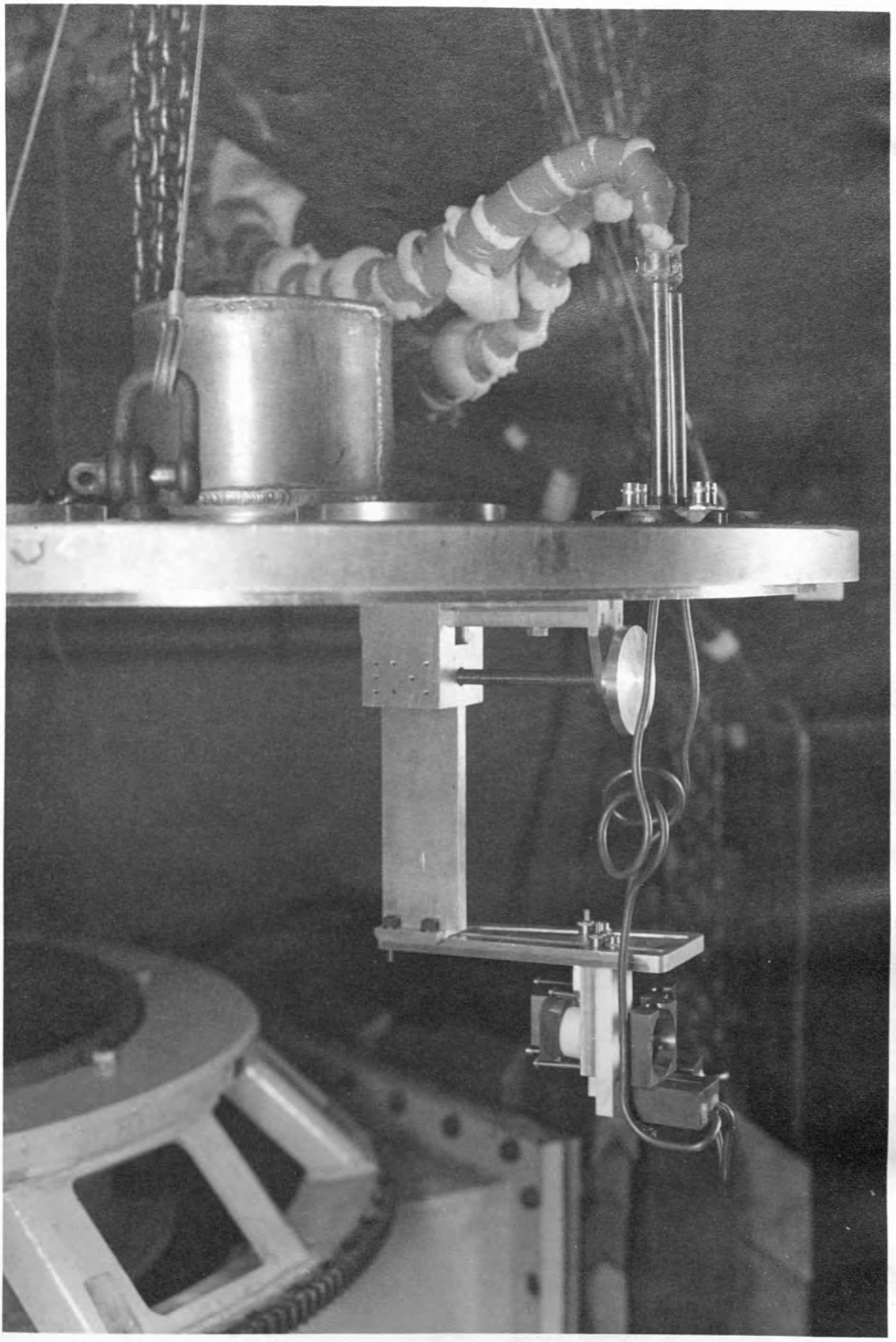

Fig 3.5 Photograph to illustrate the three positions of the backward angle detectors.

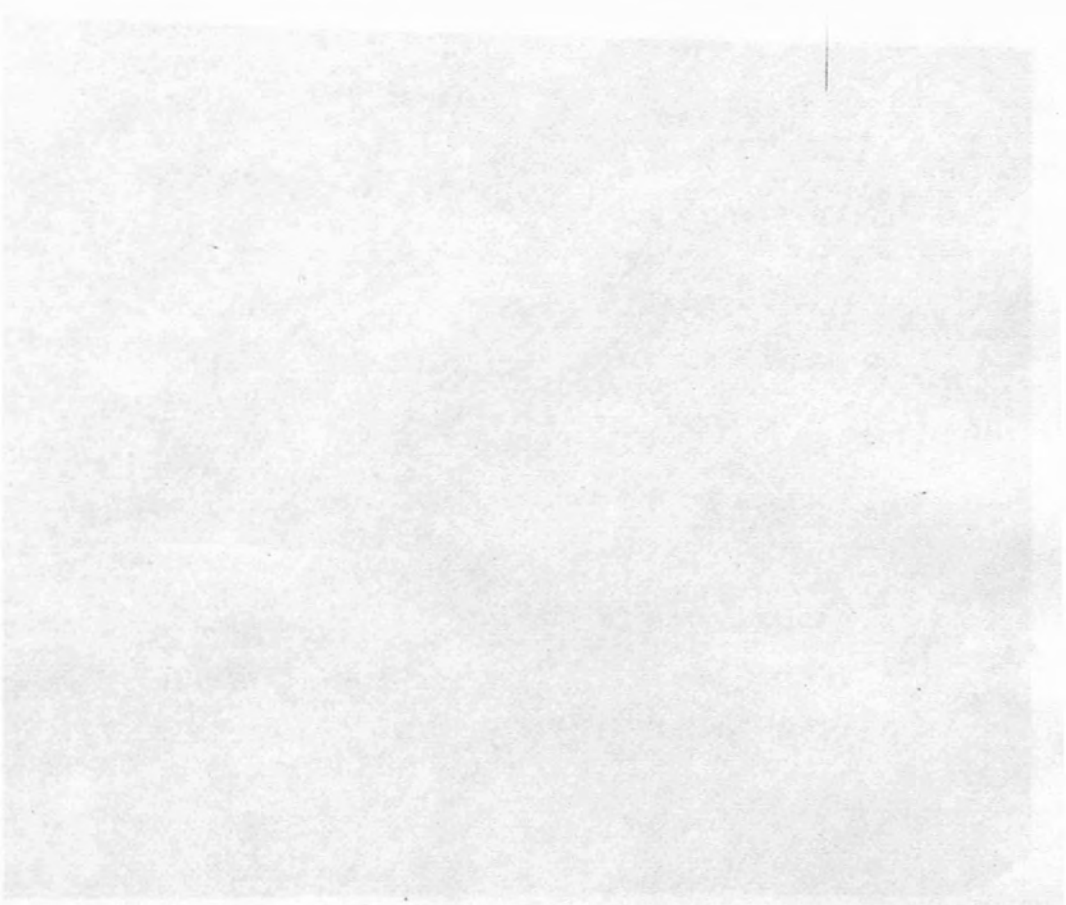

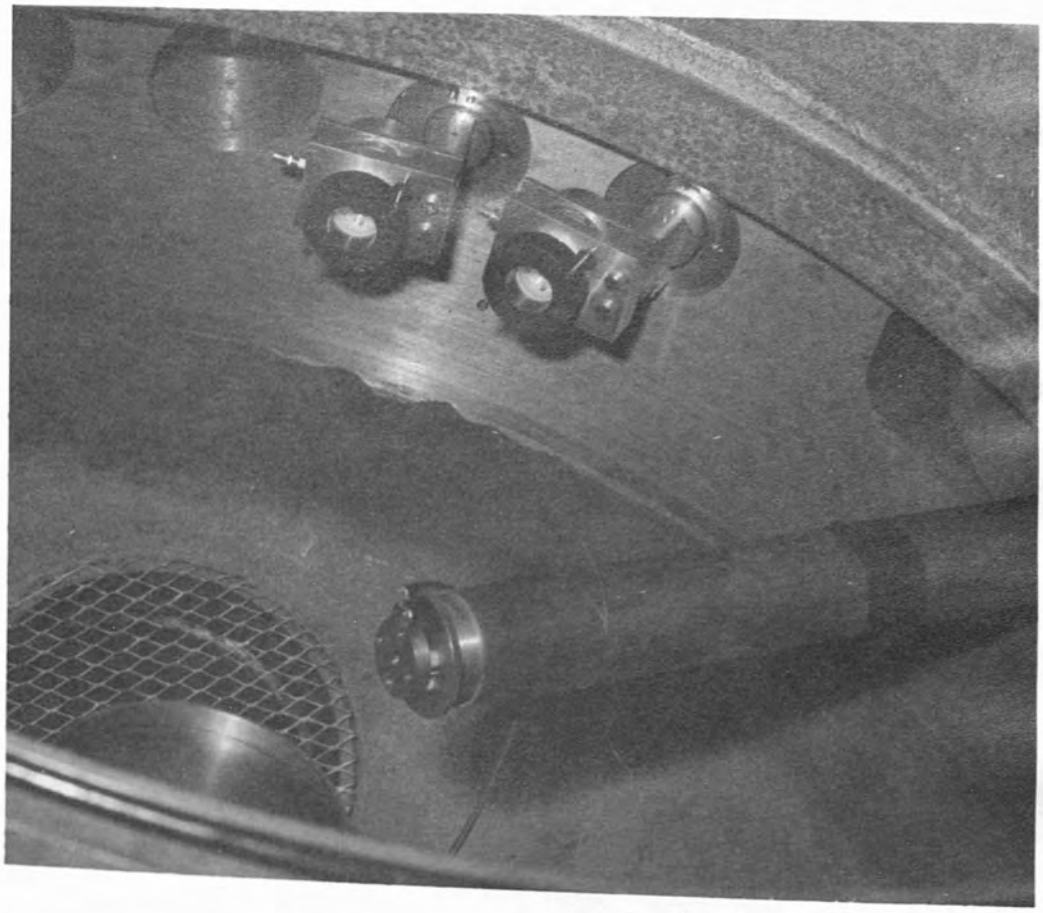

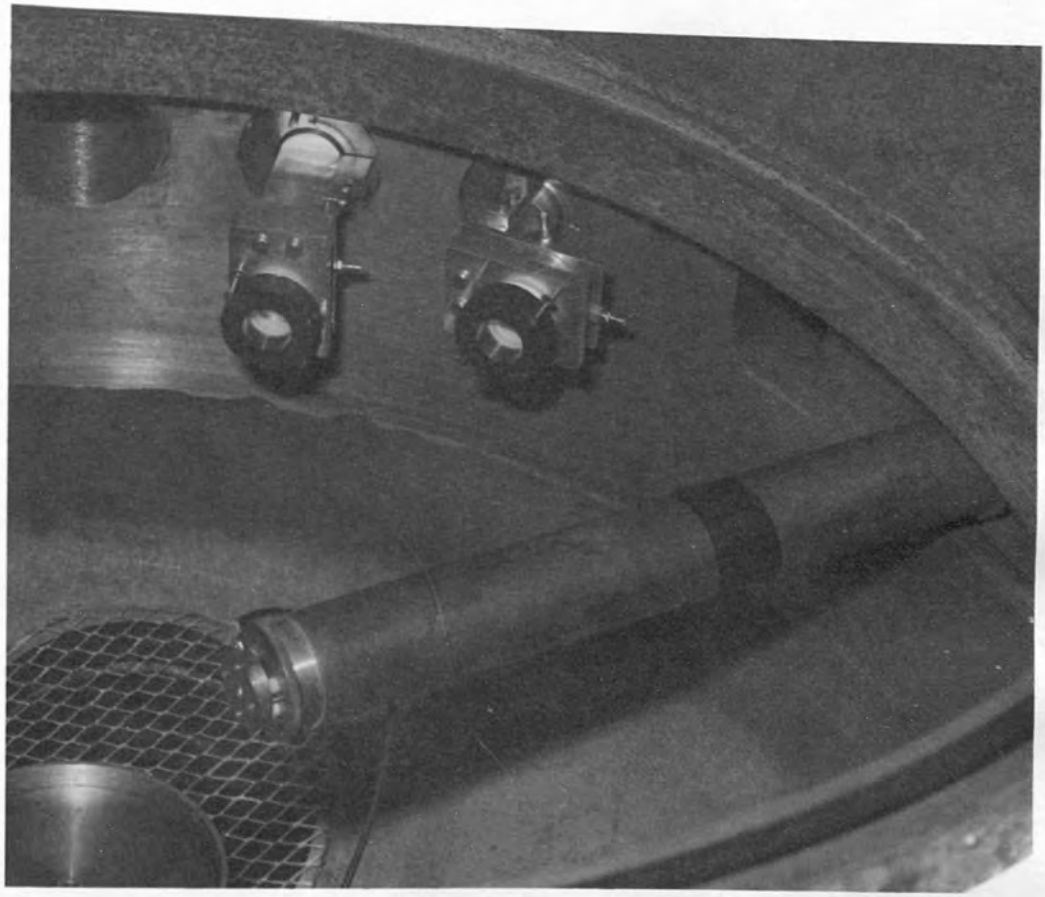

Fig 3.6 Backward Angle Detector Mounting System

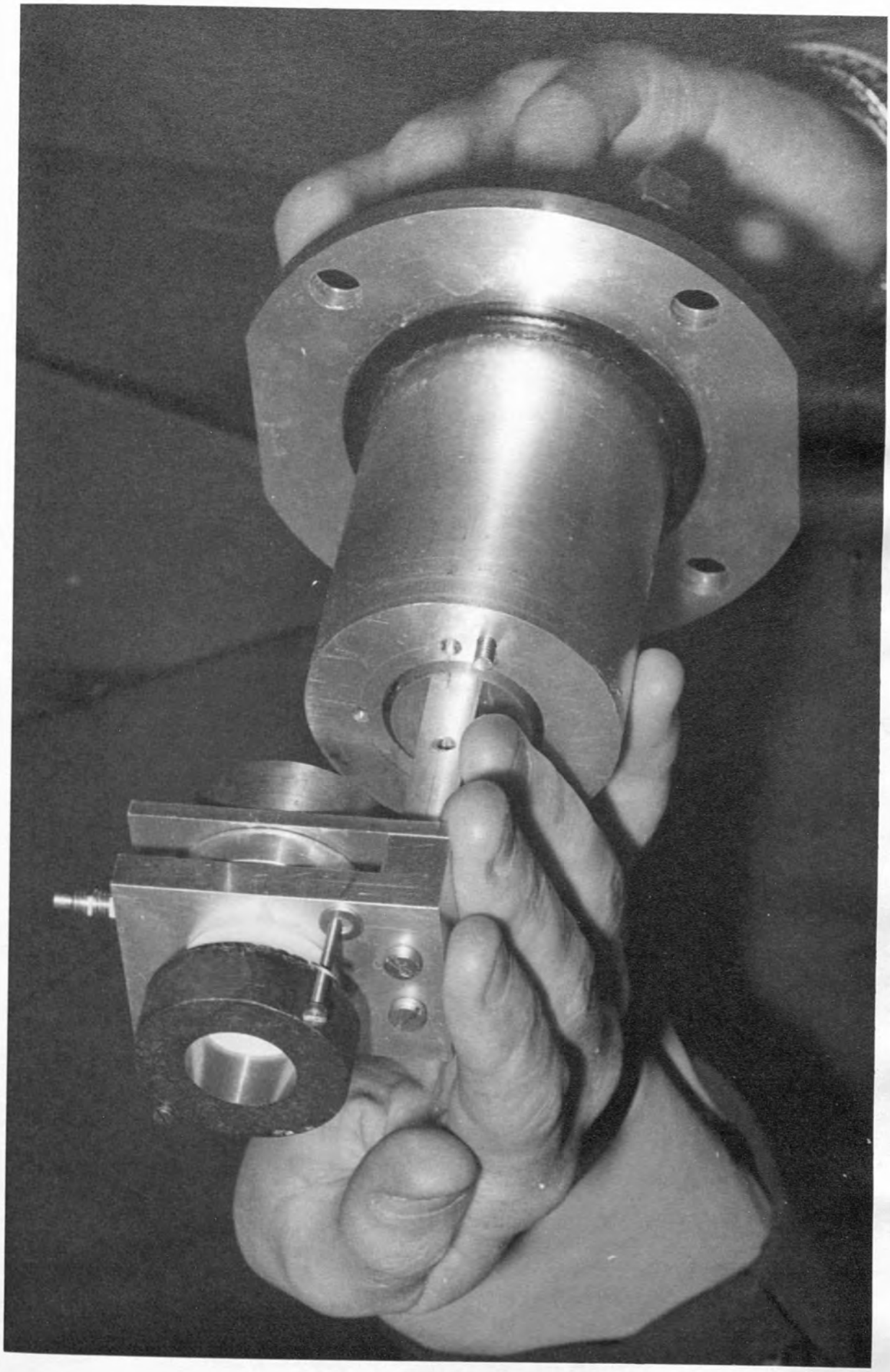

detectors were cooled using refrigerated coolants. The detector telescopes were mounted on copper blocks which were cooled from room temperature to about $-50^{\circ}C$ in approximately 30 minutes by the circulation of the coolant methyl alcohol, which has a low viscosity at low temperatures, through well-lagged nylon pipes around the copper blocks and back to a heat exchanger where a eutectic mixture of ethyl alcohol and dry ice cooled the methyl alcohol to $-60^{\circ}C$ (Ze 02). The detectors could be brought back to room temperature by circulating hot alcohol round the detectors using the heating system shown in fig. 3.7. This procedure usually took about 20 minutes. It was necessary always to remove the biases on the detectors and warm them up to room temperature before allowing air into the chamber, otherwise water vapour would condense and freeze on the actual detectors themselves.

Two monitor counters were placed $14^{\circ} \pm 0.17^{\circ}$ on either side of the beam, and these were used to detect beam wander during the long runs at backward angles, i.e. only runs without beam wander were accepted. One of these counters was also used to determine ADC dead time. One output from the amplifier was connected directly, while the other was connected to the "busy" output of the ADC so that the ratio of the two countrates gave the percentage dead time.

3.4.3 The Detector Telescopes

The forward angle detector system consisted of two telescopes separated by an angular displacement of 9.4167° relative to the centre of the scattering chamber. Each telescope consisted of a

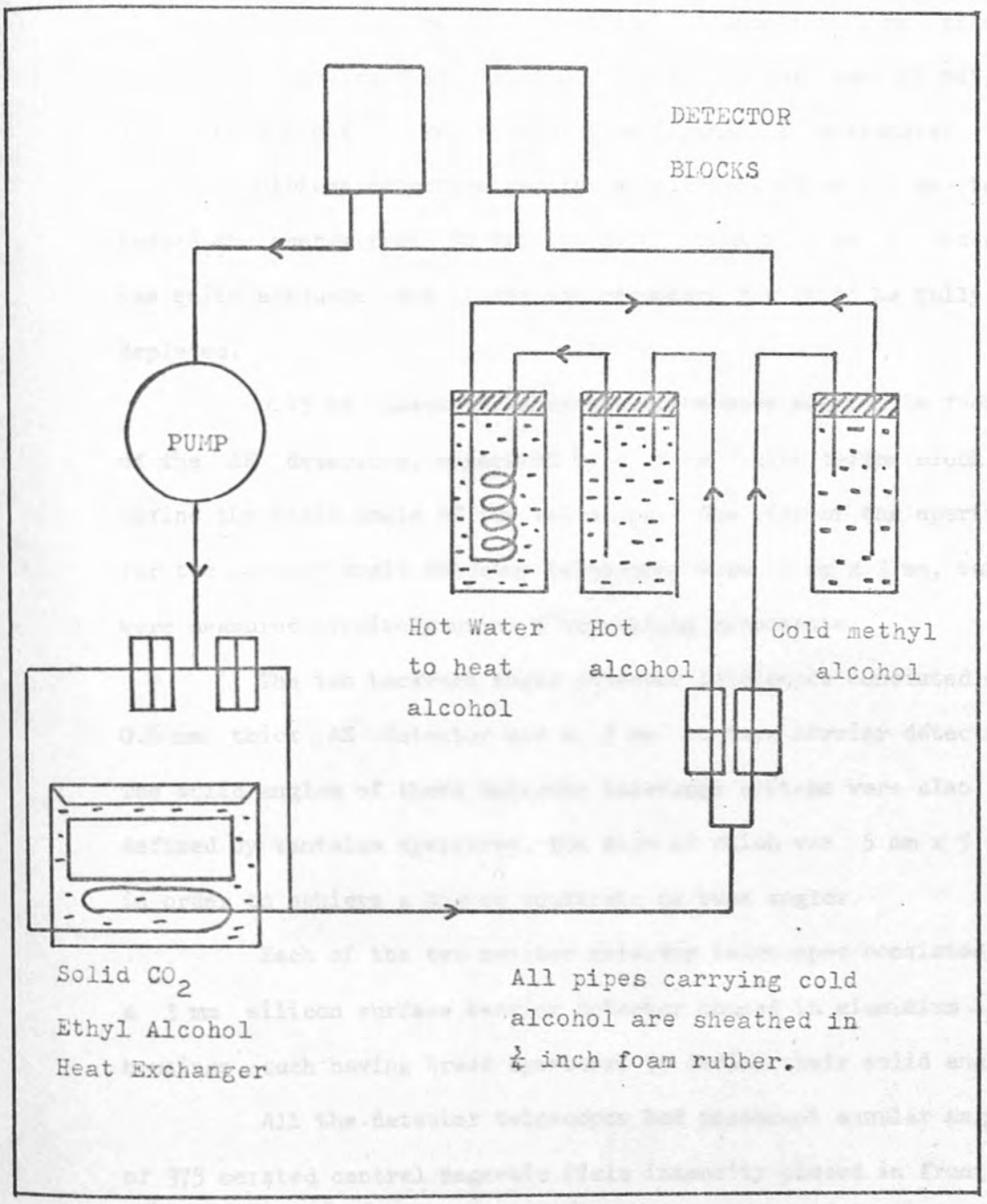

Fig 3.7 The principle of the cooling and heating system.

thin ΔE and a thick E silicon lithium drifted detector. Since the mass function generator in this experiment gave better discrimination with an energy loss of about 20% in the ΔE detector, the ΔE detector was 0.4 mm thick and the E detector 2 mm thick. The stopping power of silicon for ^{3}He at 50 MeV was 25 MeV/mm, hence there was a 10 MeV energy loss in the ΔE detectors.

Silicon detectors require a thickness of ~ 1.3 mm to reduce the energy from 50 MeV to zero. Thus a 2 mm E detector was quite adequate, and it was not necessary for it to be fully depleted.

0.15 cm thick tantalum apertures were mounted in front of the ΔE detectors, separated by a 1 cm thick teflon block, to define the solid angle of the telescope. The size of the apertures for the forward angle detector telescopes were 5 mm x 3 mm, but were measured precisely using a travelling microscope.

The two backward angle detector telescopes consisted of a 0.6 mm thick ΔE detector and a 3 mm surface barrier detector. The solid angles of these detector telescope systems were also defined by tantalum apertures, the size of which was 5 mm x 5 mm, in order to achieve a higher countrate at back angles.

Each of the two monitor detector telescopes consisted of a 3 mm silicon surface barrier detector housed in aluminium alloy housings, each having brass apertures to define their solid angles.

All the detector telescopes had permanent annular magnets of 375 oersted central magnetic field intensity placed in front of the telescopes to suppress any secondary electrons and low energy background charged particles.

3.4.4 Targets

The targets were fixed to steel frames mounted on a target ladder fixed at the centre of the scattering chamber. This ladder could be rotated by hand to various target angle positions to an accuracy of $\pm 0.1^{\circ}$. The ladder had ten target positions and could be moved vertically to enable the correct target to be moved into position. Whenever target or detector positions were changed remotely, the small Faraday cup located next to slit box 1 was always inserted in the beam to prevent any beam scatter off the target ladder itself, and also to eliminate the possibility of running a detector through the beam. The targets which had been sent under vacuum were assembled in their positions on the target ladder in less than 5 minutes of exposure to air.

The energy levels of the first excited states of the Samarium 148 and 150 isotopes required that the energy resolution of the beam should be better than 300 KeV. Calculations were performed to find the optimum target angle and thickness for the optimum resolution. Typical results shown in table 3.2 show that a 1.0 mg target is much better than a 2.0 mg target for resolution purposes.

Target Angle = 45° (transmission)

θ	1.0 mg	2.0 mg
30°	44.5 KeV	67 KeV
60°	44 KeV	66 KeV
90°	44.5 KeV	64 KeV
120°	155 KeV	314 KeV

Target Angle = -45° (reflection)

θ	1.0 mg	2.0 mg
90	160 KeV	325 KeV
120	137 KeV	275 KeV
150	137 KeV	274 KeV

TABLE 3.2 ENERGY SPREAD IN TARGETS OF SAMARIUM 148

Fig. 3.8 shows the energy spread in the target for various target angles over the entire angular range.

The targets were prepared by the Oak Ridge National Laboratory Nuclear Isotope Division and were better than 95% isotopically pure (see Table 3.3).

The percentage of other rare earth elements present in the targets was less than 0.5%.

3.5 Beam Integration

The large Faraday cup was a 1.12 metre graphite cylinder subtending an angle of 3.2° at the target centre. The beam current was fed into a standard 100% feedback Miller integrator which had four charge capacity ranges, nominally 10^{-6}, 10^{-7}, 10^{-8} and 10^{-9} coulombs/cycle sensitivity. Each capacitor was calibrated prior to and following each run. The calibrations were performed using a Harwell 1688A current generator (Ae 04).

Currents produced by a standard cell were fed into the beam integrator and the number of cycles per second were determined to less

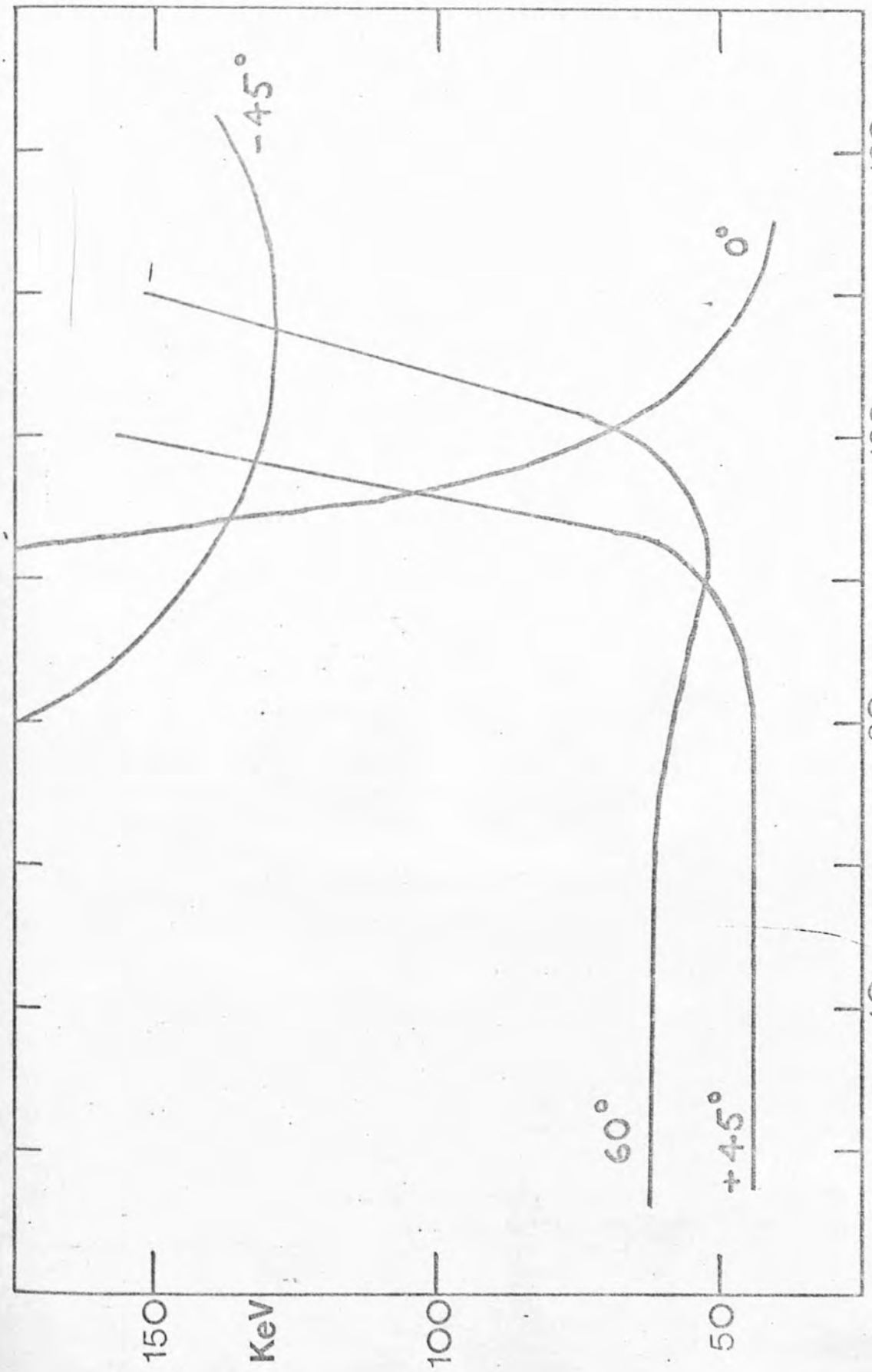

Fig 3.8 Energy Spread in Target for Various Target Angles

Target 1 ^{150}Sm 1.05 mg/cm^2

ISOTOPE	ATOMIC PERCENTAGE	PRECISION
144	0.05	± 0.02
147	0.39	± 0.03
148	0.47	± 0.03
149	1.70	± 0.05
150	95.48	± 0.10
152	1.46	± 0.05
154	0.45	± 0.04

Target 2 ^{148}Sm 1.04 mg/cm^2

ISOTOPE	ATOMIC PERCENTAGE	PRECISION
144	0.04	± 0.01
147	1.30	± 0.05
148	96.40	± 0.10
149	1.46	± 0.05
150	0.25	± 0.02
152	0.37	± 0.02
154	0.20	± 0.02

Table 3.3 Isotopic analysis of Samarium isotopes.

than 0.1%. The method of calibration was as follows:- the precise current $8.0 \pm 0.016 \times 10^{-7}$ amps supplied from the current generator was used to calibrate the 10^{-6} and 10^{-7} coulombs/cycle ranges of the current integrator using the formula,

$$q = \frac{I \times t}{N}$$

where I is current in amps, t time in seconds and N number of cycles. However, due to the discharge cycle of the integrator, each capacitor had a dead time of 100 ± 1 μ sec. Thus the corrected number of cycles was

$$N = N_0\left(1 - \frac{N\tau}{T}\right)^{-1} .$$

The 10^{-7} range was then used to determine the exact value of the current nominally equal to 8×10^{-8} amps. This current was then used to calibrate the 10^{-8} range which in turn was used to determine the current nominally equal to 8×10^{-9} amps. This current was then used to calibrate the 10^{-9} range. The errors, accumulated by this method, were always less than the error due to the calibration current, which was 0.2%. With the Faraday cup connected the leakage current was determined using the 10^{-9} range and was found to be extremely small, $\sim 2 \times 10^{-12}$ amps.

3.6 Absolute and Relative Errors

The uncertainties in determining cross-sections are due to absolute and relative errors. Absolute errors affect the normalisation

of the angular distribution and are due to errors in measuring the solid angle and the calibration of the Faraday cup storage capacitor. The error in measuring the target thickness will also affect the absolute error, and since for the Samarium isotopes the targets were not punched, the absolute errors were corrected after the cross-sections had been obtained by normalising the forward angle data to Coulomb scattering. Wollam (Wo 06) showed that the experimental cross-sections followed the shape of the Coulomb cross-sections out to 30°.

The error in calibrating the storage capacitor was less than the 0.2% error of the current used to calibrate the ranges on the capacitor.

The correction factor for the leakage current was

$$1 - \frac{L.T}{N.FC}$$

L = leakage current, and N = number of Faraday cup cycles. However, this error was estimated at approximately 0.002%.

The error in measuring the laboratory scattering angle would affect the position of the minima in the cross-sections. This angle was measured to an accuracy of $\pm 0.1^{\circ}$. The zero position was checked in both runs by the asymmetry scattering on opposite sides of the beam.

The effects of relative errors is to change the shape of the angular distribution. These cannot be corrected for by normalising the data, they must be known precisely.

The counting statistics, both the statistical error in the number of peak counts and the uncertainty of the number of counts in each peak, contribute to the relative error. These errors depend on peak separation in each spectrum and the relative peak sizes.

The lost number of Faraday cup cycles due to the integrator dead time was corrected for at each data point. This corrected figure was given by

$$N_{CORR} = N\left(1 - \frac{N\tau}{T}\right)^{-1} ,$$

where τ is the dead time and N the number of counts measured in time T.

The target angle was measured relative to its position normal to the beam axis. The change in target thickness due to the target angle was corrected for by the scaling factor equation

$$S = \frac{N_S^2 \cdot FC^1}{N_S^1 \cdot FC^2} ,$$

where N_S^1 is the number of peak counts in the normal target position counted for FC^1 Faraday cup cycles, and N_S^2 is the number of peak counts counted at target angle α for FC^2 Faraday cup cycles.

The left and right hand monitor counters were used to check and correct for beam wander. However, this proved to be negligibly small during the helium-3 run.

Corrections to the horizontal scattering by the vertical height of the solid angle aperture was taken into account by

$$d = \cos^{-1}\left(\cos\left(\theta_{lab}\right)\cos\rho\right) - \frac{\theta_{lab}}{2}$$

where ρ is the vertical angle subtended at the target. This correction was never more than 0.2° at forward angles.

The smearing angle (Fa 01) was calculated to be 1.53° for this experiment.

The final relative error was due to the number of counts lost

due to the ADC dead time. This was corrected for by multiplying the number of peak counts by (N_1/N_2) where N_1 is the number of counts recorded in the right-hand monitor and N_2 the number of counts in the right-hand monitor inhibit. The errors may be summarised as follows:-

Absolute Errors

Primary	Normalisation to Coulomb	± 0.05% at 15°
Secondary	Solid angle aperture	± 0.05%
	Solid angle radius	± 0.06%
	Integrator calibration	± 0.2%

Relative Errors

Angle settings	± 0.1°
Zero error of angle	0.425°
Integrator dead time	± 100μ sec
Integrator leakage	± 0.002%
ADC dead time	± 1.8% at 20° < 0.01% at angles >100°
Angular smearing	1.53°
Beam spot size geometry	± 0.06%
Target position changes	± 0.01%
Statistics in peaks	(θ=0 to 60°) ± 3% (θ=60 to 150°) ± 3 - 100%

3.7 Electronic Systems

The outline plans of the two electronic systems used to handle the four detector telescopes are shown in figs. 3.9 and 3.10.

Events satisfying coincidence and particle identification requirements were recorded on pulse height analysers. The particle identification was achieved using mass function generators which took up the majority of the time at the beginning of the experiment for setting up.

The forward angle detector systems and the backward angle detector systems used separate electronic systems, but these were generally similar and the following descriptions apply to both systems. Any major differences in the two systems will be described.

3.7.1 Analogue and Coincidence

Four preamplifiers (Ae 03) from the two forward angle detector telescopes and four preamplifiers (Te 08) (Te 10) from the two backward angle detector telescopes, situated in the experimental area each feed pulses to a main amplifier (Te 04) which produces two immediate bipolar pulses and two baseline restored unipolar pulses delayed by 2μs . This delay allows logic to be performed on the bipolar pulses. The bipolar output from a ΔE detector triggers a crossover pick-off (Te 05) set at a low threshold value. After 100ns delay this provides a strobe to a Timing Single Channel Analyser (Te 06) (TSCA). Meanwhile the E pulse associated with the ΔE is fed to the input of the TSCA set on the crossover discriminate mode. The crossover pickoff must strobe the TSCA within 200ns from the E crossover point to produce an output signal. This is subject to

Fig 3.9 Electronics for Forward Angle Detectors

and

Fig 3.10 Electronics for Backward Angle Detectors

ATT	Attenuator or Mass Match
BA	Biased Amplifier
COP	Cross over Pickoff
DA	Delay Amplifier
LG	Linear Gate
LI	Linear Interface
MA	Main Amplifier
MFG	Mass Function Generator
PA	Pre-Amplifier
SCA3	Single Channel Analyser set for ^{3}He particles
SCA4	Single Channel Analyser set for ^{4}He particles
ST	Stretcher
TSCA	Timing Single Channel Analyser

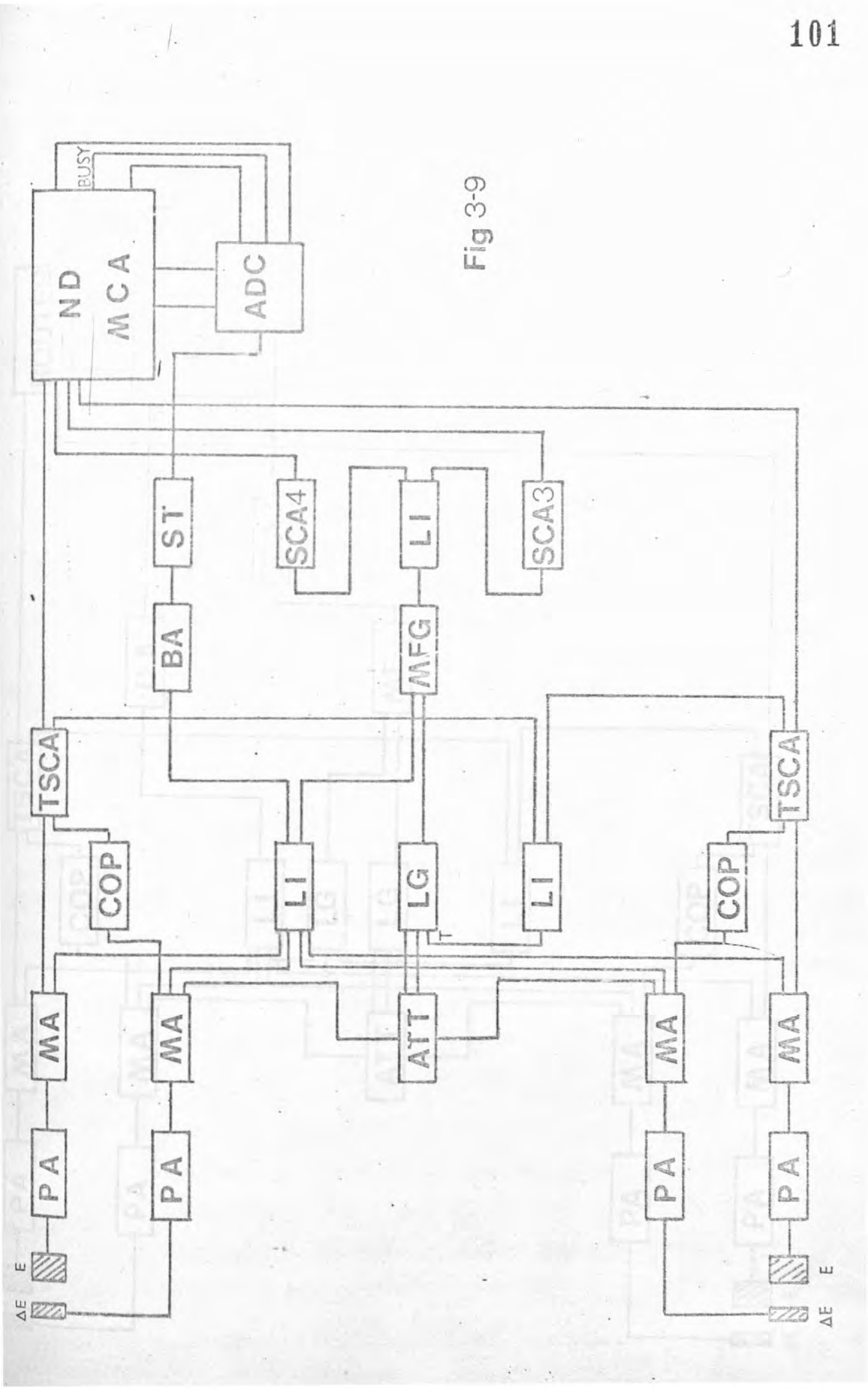
ND
MCA
BUSY
ADC
ST
SCA4
LI
SCA3
BA
MFG
TSCA
COP
LI
LG
LI
COP
TSCA
MA
MA
ATT
MA
MA
PA
PA
PA
PA
E
ΔE
ΔE
E

Fig 3-9

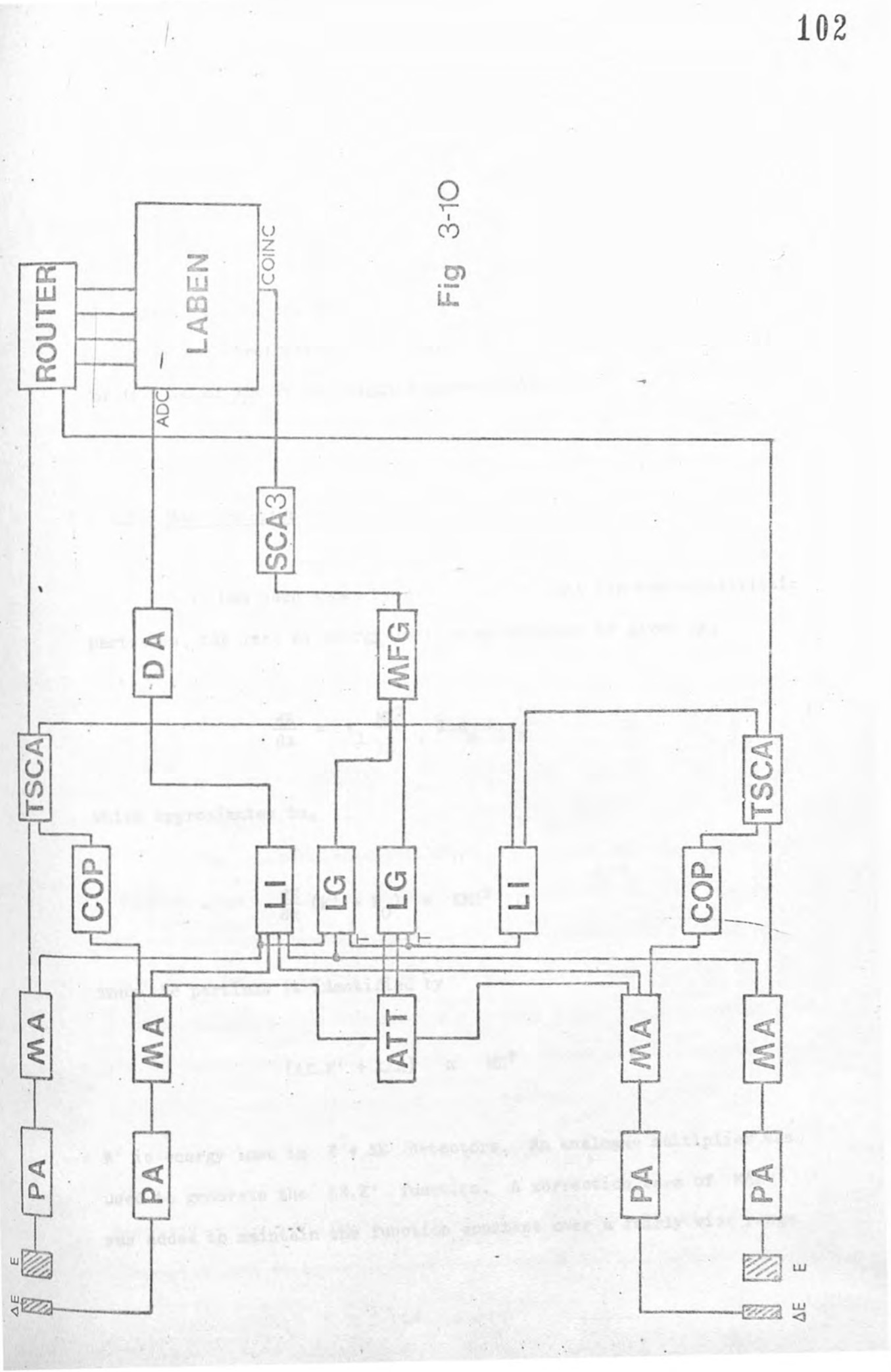
ROUTER
LABEN
COINC
ADC
SCA3
DA
MFG
TSCA
COP
LI
LG
LG
LI
COP
TSCA
MA
MA
ATT
MA
MA
PA
PA
PA
PA
E
ΔE
ΔE
E

Fig 3-10

the E pulse crossing the threshold level. Thus the ΔE - E coincidence is achieved.

One output of the TSCA triggers the linear gate and adder which receives baseline restored unipolar pulses from the ΔE and E amplifiers. The summed energy E + ΔE passed to a mixer accepting pulses from either telescope and subsequently to a biased amplifier and stretcher (Te 07). This produces an output pulse used for the ADC of the Pulse Height Analyser PHA(Nu 04).

3.7.2 Mass Function

It has been shown by Bethe (Be 07) that for non-relativistic particles, the rate of energy loss in an absorber is given by,

$$\frac{dE}{dx} = K_1 \frac{MZ^2}{E'} \log_e K_2 \frac{E'}{M}$$

which approximates to,

$$\frac{dE}{dx}(E' + E_0) = KMZ^2 \quad .$$

Thus the particle is identified by

$$(\Delta E.E' + K\Delta E) \quad \alpha \quad MZ^2$$

E' is energy lost in E + ΔE detectors. An analogue multiplier was used to generate the ΔE.E' function. A correction term of KΔE was added to maintain the function constant over a fairly wide range

of energies. It was found that multiplying the ΔE pulse by 2 provided better mass discrimination. One mass function generator was used for the two detector telescope systems.

A two-dimensional plot of $E + \Delta E$ against MFG output on the PHA was used to obtain a linear dependence on energy by adjusting the correction term. Typical mass spectra obtained are shown in fig. 3.11.

The outputs of the mass function generator for the forward angle detector system were fed to two SCA's, one selecting He^3 and the other He^4. The outputs of the mass function generator for the backward angle detector system were fed to only one SCA set for helium-3 pulses.

Thus an analogue input is only analysed if a pulse of the correct height is received from the MFG.

3.7.3 Pulse Height Analyser

The analyser used for the forward angle detector system was a Nuclear Data 2000 series multi-channel analyser, (Nu 05) (Nu 06), and for the backward angle detectors a Laben multi-channel-analyser (Rh 03). Fast pulses from a TSCA were stretched and inverted to provide routing pulses for the PHA. Summed routing pulses passed to a mixer-rejector unit which accepted or rejected analogue input pulses according to whether routing pulses overlapped. Thus the PHA only analysed when a valid MFG output signal and a valid $E - \Delta E$ coincidence signal coincided. The Nuclear Data 2000 series multi-channel-analyser was divided into 4×512 channels. This represented the two detector telescope systems, each containing a He^3 and He^4 spectrum.

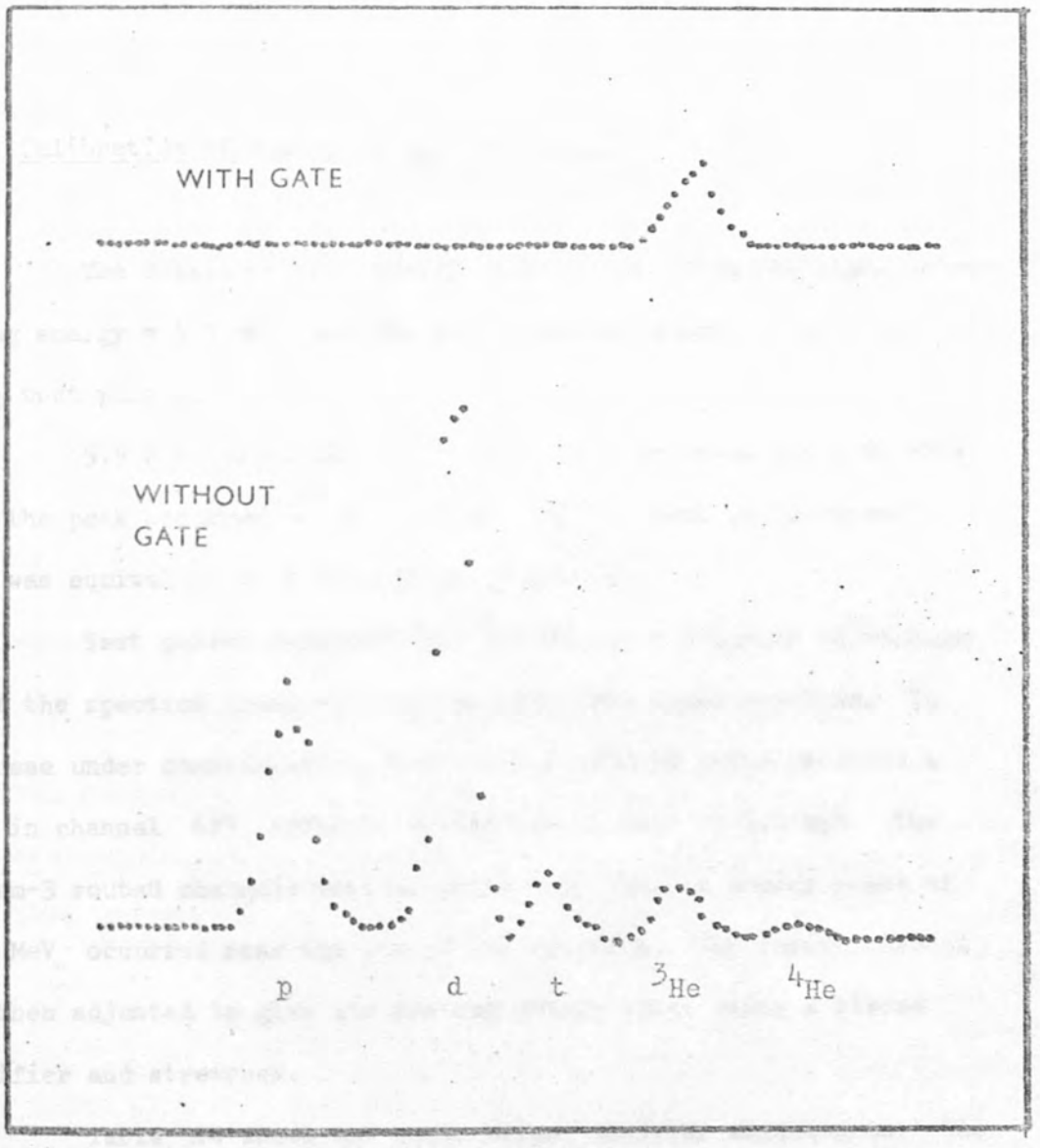

Fig 3.11 Typical Mass Spectra showing

a) Mass function generator - ungated

b) Mass function generator - gated for ^{3}He ions.

The Laben pulse height analyser was divided into 2 x 256 channels. This represented the two detector telescope systems, each containing a He^3 spectrum only.

The pulse height analysers had facilities for data integration and peak checking. The data was punched out on 8 hole paper tape.

3.8 Calibration of Apparatus and Data Taking

The detectors were tested using an Americium 241 alpha source having energy = 5.5 MeV, and the multi-channel analysers were set up using test pulses.

5.5 MeV alpha particles produced a spectrum where in this case the peak occurred in channel 627 with a fwhm of 10 channels. This was equivalent to a resolution of 100 KeV.

Test pulses injected into the PHA were adjusted in voltage until the spectrum produced coincided with the alpha spectrum. In the case under consideration, test pulses of 0.69 volts produced a peak in channel 627 with the result that 1 volt $\simeq$ 8.2 MeV. The helium-3 routed channels were adjusted such that an energy pulse of $\sim$54 MeV occurred near the end of the spectrum. The lowest channel was then adjusted to give the desired energy range using a biased amplifier and stretcher.

Table 3.4 shows the pulse height analyser adjustments. The detector amplifiers were adjusted using the two E and ΔE detectors, and setting the DC height of the 5.5 MeV alpha pulses on a cathode ray oscilloscope to 0.55 volts. The gains of the amplifiers were adjusted until all the peaks of the 5.5 MeV alpha pulses occurred in the same channel on the pulse height analyser. Table 3.5 shows the

MULTI CHANNEL ANALYSER SETTINGS

Gate Input - Positive going pulse 0 to 5 volts

Conversion gain	2048
Zero suppresion	1280
Zero Course	6.6
Bottom channel	45 MeV
Top channel	67 MeV
Routing	4 x 512
Test pulses	1 volt = 20 MeV

LABEN PULSE HEIGHT ANALYSER SETTINGS

Gate Input - Negative going pulse 0 to -6 volts D.C.

Bottom channel	43 MeV
Top channel	54 MeV
Routing	2 x 256
Test pulses	1 volt = 8.2 MeV

Table 3.4 Settings on the data collecting devices

FORWARD ANGLE DETECTORS

DETECTOR	PEAK CHANNEL ON M.C.A.	F.W.H.M. (KeV)	AMPLIFIER GAIN
E 1	506	80	13.41
E 2	509	100	13.14
E 3	508	150	14.4
E 4	506	90	11.3

BACK ANGLE DETECTORS

DETECTOR	PEAK CHANNEL ON LABEN	F.W.H.M. (KeV)	AMPLIFIER GAIN
E 5	627	99.9	3.285
E 6	627	61	3.25
E 7	627	120	3.89
E 8	627	80	3.07

Table 3.5 Detector resolution using a ^{241}Am alpha source.

results obtained.

Before data taking began the He^3 beam was scattered from an Fe^{56} target. This has a well-determined first excited state of 0.85 MeV. The resolution was calculated to be 235 KeV. The beam line parameters are shown in table 3.6. Checks were occasionally made using the scintillator to ensure that there was no beam spot wander.

The Faraday cup cycles and monitor detector counts were recorded on scalers and their values were automatically printed out at the end of each run. Events which satisfied the mass and energy coincidence requirements were recorded on the PHA's.

Data was taken using the four detector telescopes. Data for some angles was taken using two different detector telescopes. This overlapping procedure enabled a cross calibration between two detector telescopes to be established. The angular distribution of the ^{148}Sm isotope was measured completely, and then the ^{150}Sm angular distribution was measured. The data at the end of each run was then punched out on eight hole paper tape.

It was important to determine the zero angle of the beam since the cross-sections in this experiment fall off very rapidly with increasing angle. The forward angle detector systems were used to measure to a high degree of accuracy the cross-sections at points at about 20° on either side of the beam, see fig. 3.12. A zero error was determined to be 0.425°.

		Current (amps)
Steering Magnet	Horiz.	155
	Vert.	27
Quadrupoles	1	-221
	2	+195
	3	-
	4	-
	5	-3.75
	6	+3.1
	7	+5.0
	8	-5.5
Bending Magnet		-26.8
Steering Magnet		+78.5

Table 3.6 Beam line parameters.

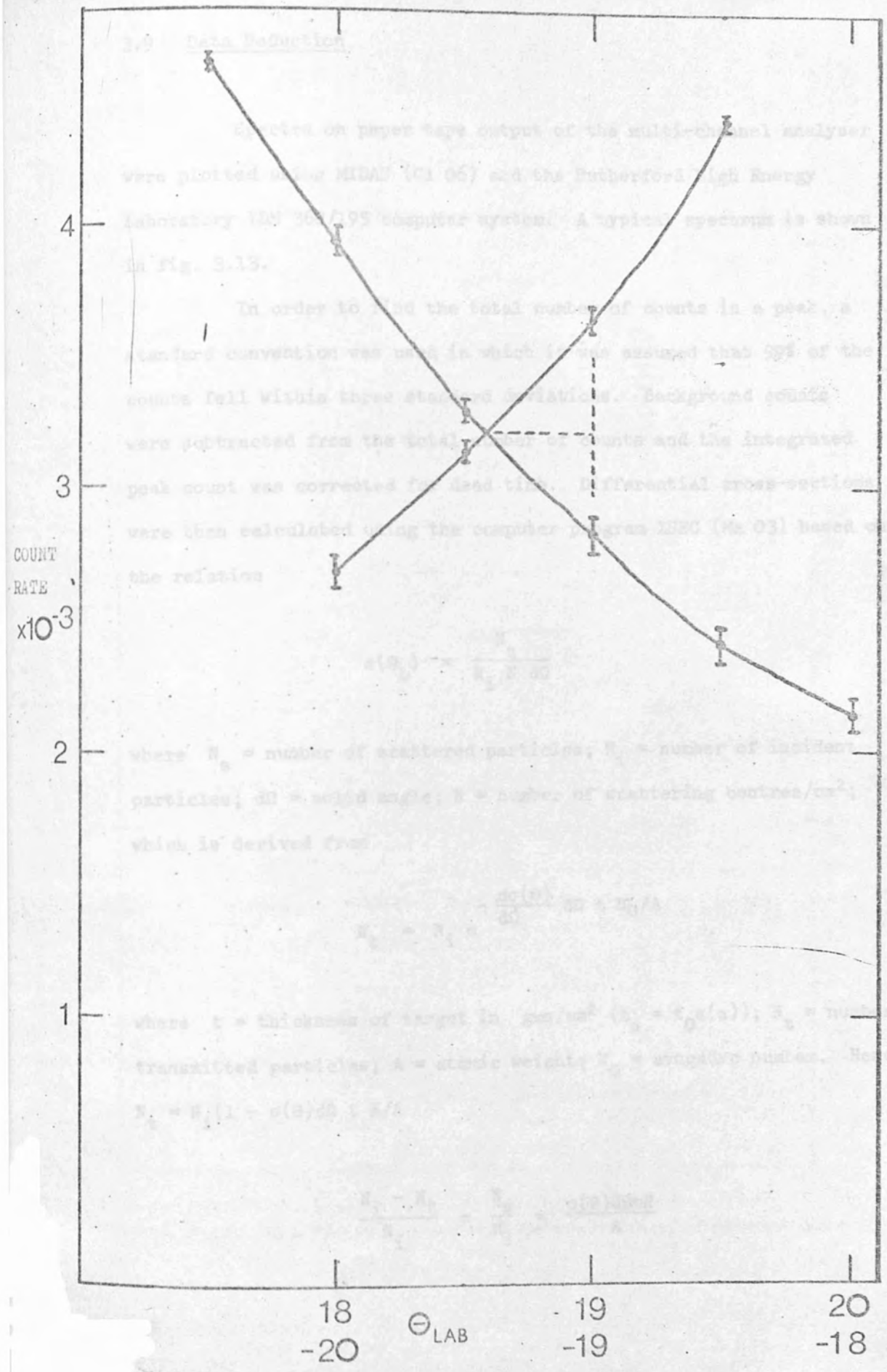

Fig 3.12 Graph to determine the true zero angle of the beam

3.9 Data Reduction

Spectra on paper tape output of the multi-channel analyser were plotted using MIDAS (C1 06) and the Rutherford High Energy Laboratory IBM 360/195 computer system. A typical spectrum is shown in fig. 3.13.

In order to find the total number of counts in a peak, a standard convention was used in which it was assumed that 99% of the counts fell within three standard deviations. Background counts were subtracted from the total number of counts and the integrated peak count was corrected for dead time. Differential cross-sections were then calculated using the computer program XSEC (Ma 03) based on the relation

$$\sigma(\theta_L) = \frac{N_s}{N_i N \, d\Omega}$$

where N_s = number of scattered particles; N_i = number of incident particles; $d\Omega$ = solid angle; N = number of scattering centres/cm^2; which is derived from

$$N_t = N_i \, e^{-\frac{d\sigma(\theta)}{d\Omega} d\Omega \, t \, N_0/A}$$

where t = thickness of target in gms/cm^2 ($t_\alpha = t_0 s(\alpha)$); N_t = number of transmitted particles; A = atomic weight; N_0 = avogadro number. Hence

$$N_t = N_i(1 - \sigma(\theta) d\Omega \, t \, N/A$$

$$\frac{N_i - N_t}{N_i} = \frac{N_s}{N_i} = \frac{\sigma(\theta) d\Omega t N}{A}$$

or

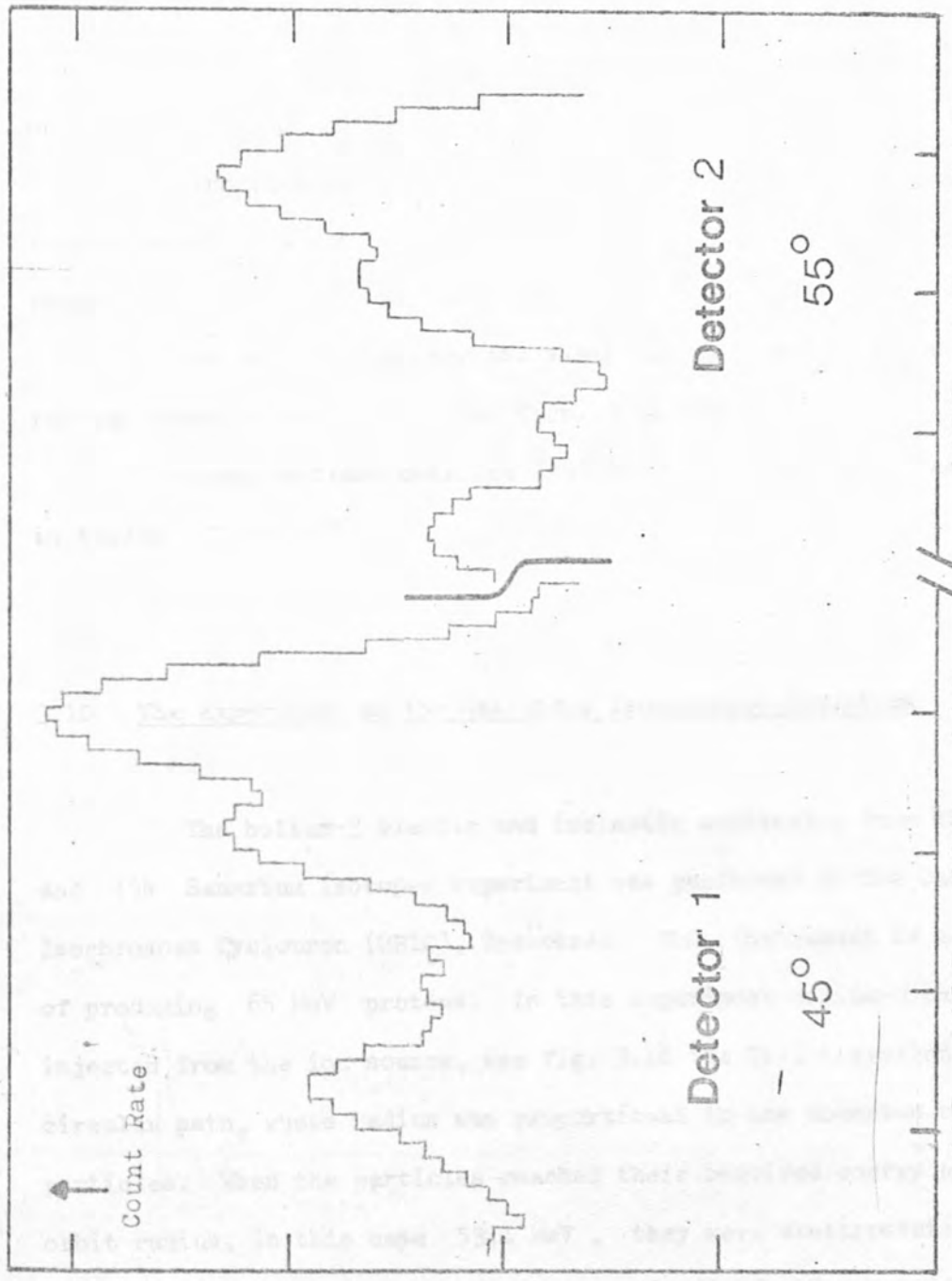

Fig 3.13 Typical spectrum of ^{3}He scattering from ^{150}Sm from the two forward angle detectors.

$$\frac{d\sigma(\theta)}{d\Omega} = \frac{N_s \; A \; z \; 1.602 \times 10^{-19}}{c d\Omega \; t_0 s(\alpha) \; N} \qquad 3.1$$

where z = charge on incident particle; $s(\alpha)$ = target scale factor for appropriate angle α; c = total charge collected corrected for dead time, leakage current and error in the range selecting capacitor of the Faraday cup system.

Normalisation of the data was achieved by normalising the forward angle data out to 35° to coulomb scattering in the same range.

The value of N for the Samarium 148 and Samarium 150 run was found to be 0.78 . See figs. 3.14 and 3.15.

Cross-sections obtained from this experiment are presented in tables 3.7 to 3.17

3.10 The Experiment at the Oak Ridge Isochronous Cyclotron

The helium-3 elastic and inelastic scattering from the 152 and 154 Samarium isotopes experiment was performed at the Oak Ridge Isochronous Cyclotron (ORIC), Tennessee. This instrument is capable of producing 65 MeV protons. In this experiment helium-3 particles injected from the ion source, see fig. 3.16 (Ba 01), travelled in a circular path, whose radius was proportional to the momentum of the particles. When the particles reached their required energy and orbit radius, in this case 53.1 MeV , they were electrostatically deflected into a region of reduced magnetic field which permitted them to escape the influence of the magnet and travel through the evacuated beam pipe to a target. The 153° analysing magnet enabled the required beam resolution of 80 KeV to be achieved.

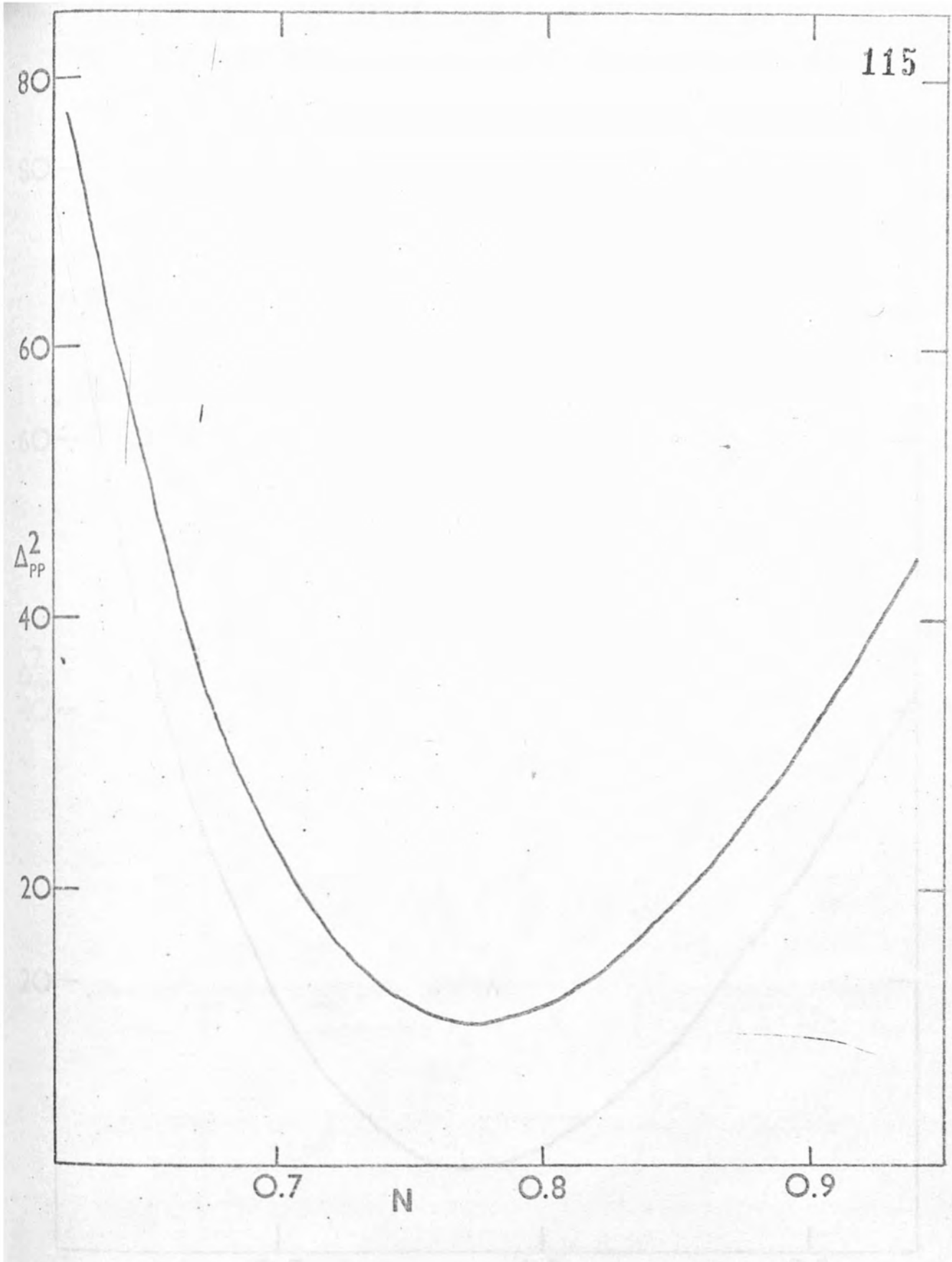

Fig 3.14 Normalisation graph for ^{148}Sm at 53.4 MeV

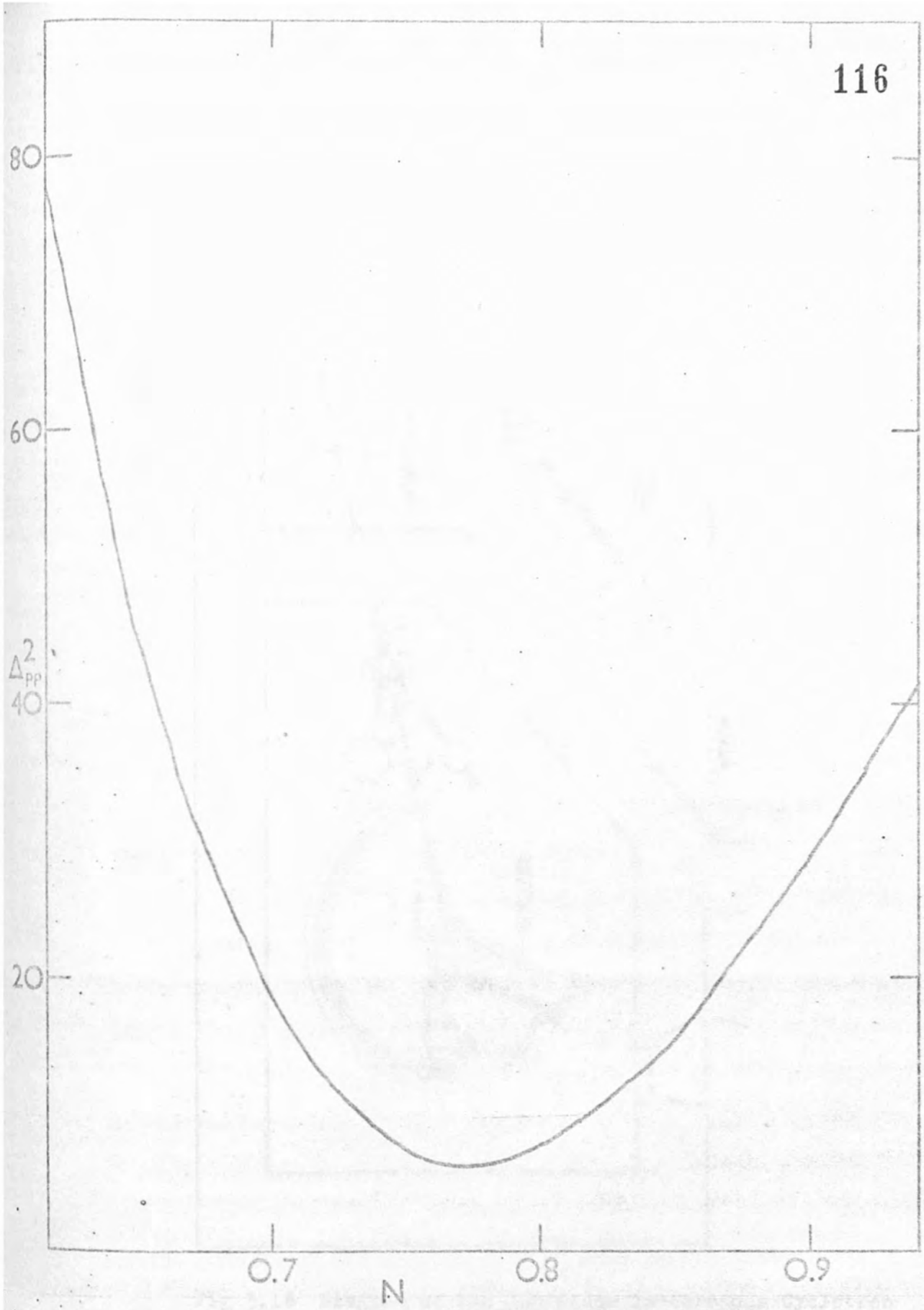

Fig 3.15 Normalisation graph for ^{150}Sm at 53.4 MeV

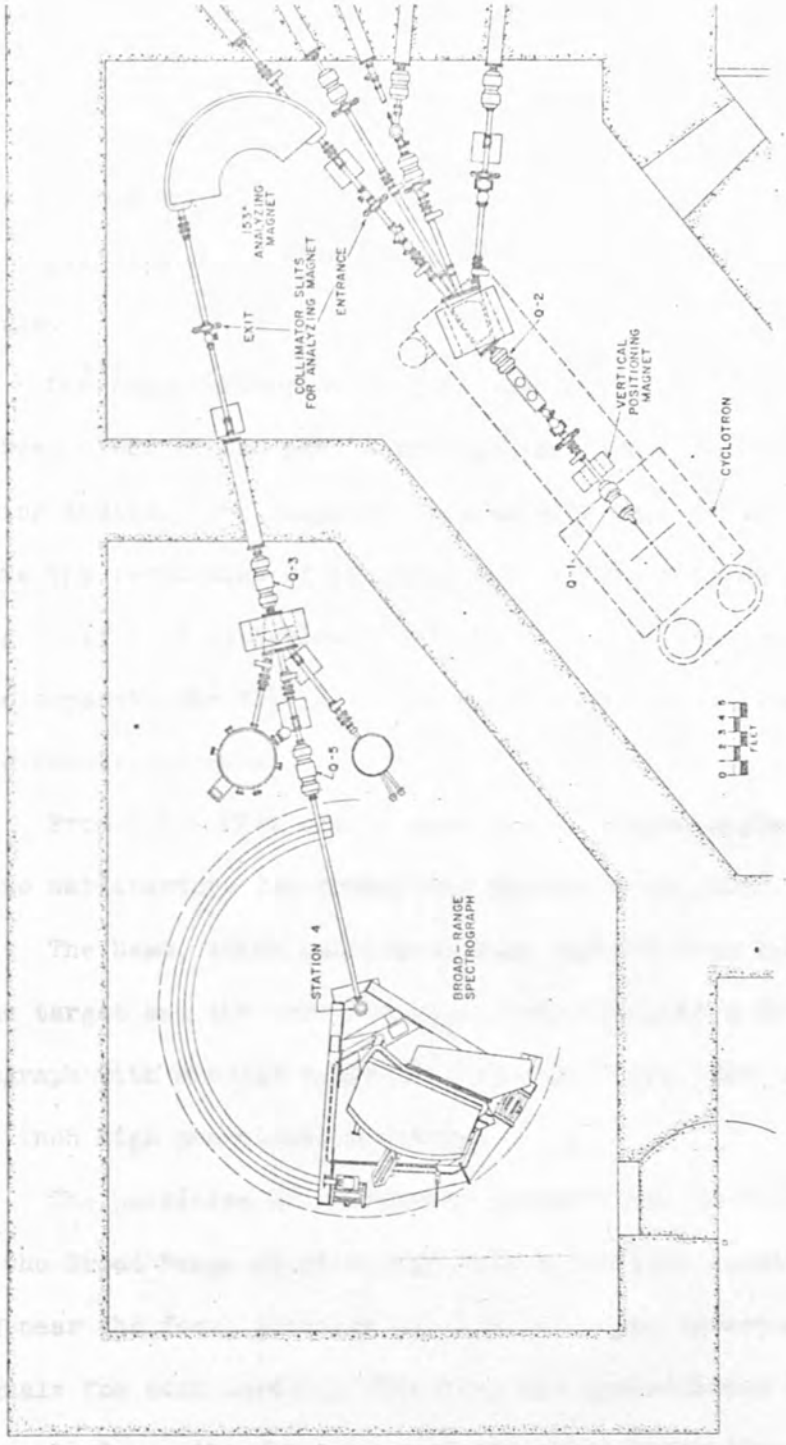

Fig 3.16 Diagram of the Oak Ridge Isochronous Cyclotron

The targets were produced by the Oak Ridge National Laboratory, Isotope Division to the high purity specification required. The Samarium-152 target was approximately $2mg/cm^2$ and the Samarium-154 target was approximately $1mg/cm^2$. These targets were considered too valuable to punch in order to find the thickness, hence the data had to be normalised by normalising the forward angle data out to 30° to the Coulomb scattering in the same range.

One major criterion in this experiment was the resolution of the beam after it had passed through the target for various scattering angles. The computer program HPRP (Hp 08) was used to calculate the resolution of the beam for different target angles. (See fig. 3.17.) A criterion of 82 KeV f.w.h.m. was necessary in order to separate the first 2^+ level of Samarium-154 from the eleastic scattering peak.

From fig 3.17 it can be seen that a target angle of 45° was quite satisfactory for scattering angles up to 103°.

The beam, after passing through various beam optics, interacts with the target and the emergent particles pass into a Broad Range Spectrograph with a solid angle of 1.3×10^{-4} sr. for 1° full width and 1 inch high acceptance aperture.

The particles are deflected proportional to their momentum around the Broad Range Spectrograph onto a position sensitive detector located near the focal position of 179 cms. The detector produces two signals for each particle detected; one proportional to the position of the particle on the detector, and the other proportional to the loss in energy (ΔE) as the particle passes through the detector.

A bias of 200 volts was placed on the position sensitive detector couplet SPHX-7-50-800 (015) and SSR-7-50-1000 (016) which

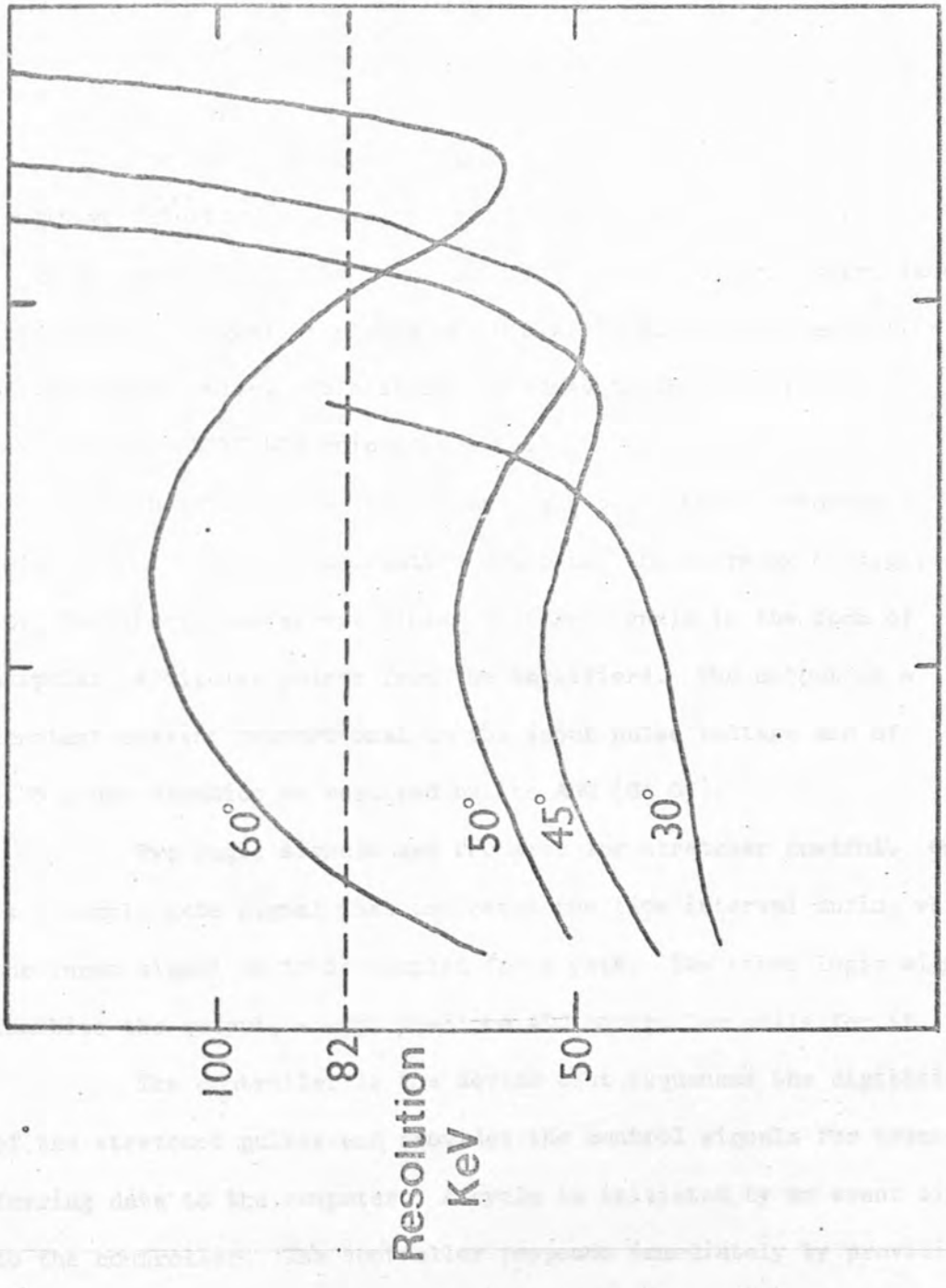

Fig 3.17 Resolution of elastically scattered Helium-3
for various target angles.
N.B. A resolution of 82KeV must be achieved.

although 1000μ thick was only 800μ fully depleted.

Information from this detector was collected and compiled in a computer SEL840A.

3.10.1 Electronics Systems at O.R.I.C.

The position (energy) and ΔE(mass) pulses from the position sensitive detector were amplified using a TC133 pre-amplifier and a TC200 amplifier. (See fig. 3.18.) The "event" (or "start data acquisition") signal came from the S.C.A. looking at the amplifier of the energy pulse. This signal is added to the scaler-switch level in the ORTEC 418 coincidence box.

The stretchers provide analogue pulse height storage to hold the pulse height information until the ADC is ready to digitise it. The stretchers accept linear voltage signals in the form of unipolar or bipolar pulses from the amplifiers. The output is a constant current proportional to the input pulse voltage and of 4.75 μ sec duration as required by the ADC (Go 05).

Two logic signals are required for stretcher control. One is a sample gate signal that indicates the time interval during which the input signal is to be sampled for a peak. The other logic signal inhibits the output, except when the ADC controller calls for it.

The controller is the device that sequences the digitising of the stretched pulses and provides the control signals for transferring data to the computer. A cycle is initiated by an event signal to the controller. The controller responds immediately by providing a sample gate pulse of adjustable duration for the stretchers. At the end of the gate pulse the analogue data are stored in the stretchers

Fig 3.18 Block diagram of electronics associated with the Detector Couplet SPHX-7-50-800 and the computer S.E.L. 840 A.

ADC	Analogue to Digital Converter (TC 501)
CO	Coincidence Unit (Ortec 418)
COM	Computer (S.E.L. 840 A)
DA	Delay Amplifier (TC 215)
DET	Detector Couplet SPHX-7-50-800
FC	Faraday Cup
IA	Inverting Amplifier
MA	Main Amplifier
MC	Multiplexer Control
PA	Pre-amplifier (TC 133)
PAPS	Pre-amplifier power supply
PG	Pulse Generator
PHA	Pulse Height Analyser
PS	Power Supply 150v DC
RB	Ring Bias
S	Scaler
ST	Stretcher (TC 620)
TSCA	Timing Single Channel Analyser (TC 420)

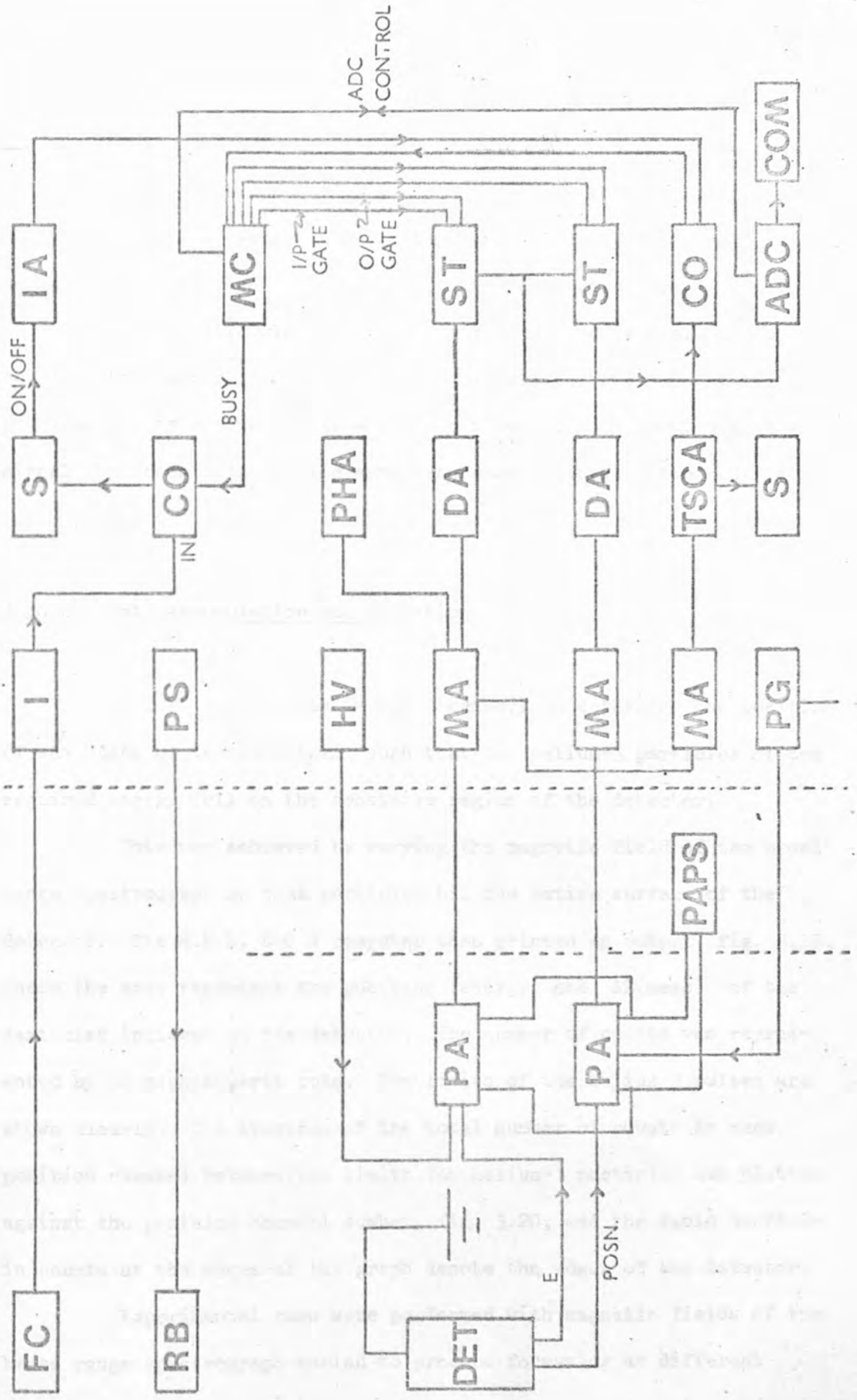
ADC CONTROL
COM
I/P GATE
O/P GATE
IA
MC
ST
ST
CO
ADC
ON/OFF
BUSY
S
CO
PHA
DA
DA
TSCA
S
IN
I
PS
HV
MA
MA
MA
PG
PAPS
PA
PA
E
POSN.
FC
RB
DET

and the controller goes into a digitising and data transfer cycle. When an output is required from a stretcher, its inhibit is removed and the ADC is commanded to initiate a conversion. When the conversion is complete, the controller signals the computer that a data word is available. When the computer signals back that it has accepted the word, the cycle goes on to the next stretcher.

The counting loss due to system dead time is evaluated by counting the number of unaccepted event signals. This eliminates the problems of inferring the true loss from dead time evaluated from a signal that does not have the same time correlations as the real data.

3.10.2 Data Accumulation and Reduction

Before taking data it was necessary to determine the position of the edges of the detectors, such that the helium-3 particles of the required energy fell on the sensitive region of the detector.

This was achieved by varying the magnetic field of the broad range spectrograph so that particles hit the entire surface of the detector. The S.E.L. 840 A computer then printed an output, fig. 3.19, where the axes represent the position (energy) and ΔE(mass) of the particles incident on the detector. The number of counts was represented by an alphanumeric code. The limits of the helium-3 pulses are shown clearly. The spectrum of the total number of counts in each position channel between the limits for helium-3 particles was plotted against the position channel number, fig. 3.20, and the rapid decrease in counts at the edges of the graph denote the edges of the detector.

Experimental runs were performed with magnetic fields of the broad range spectrograph varied to produce focussing at different

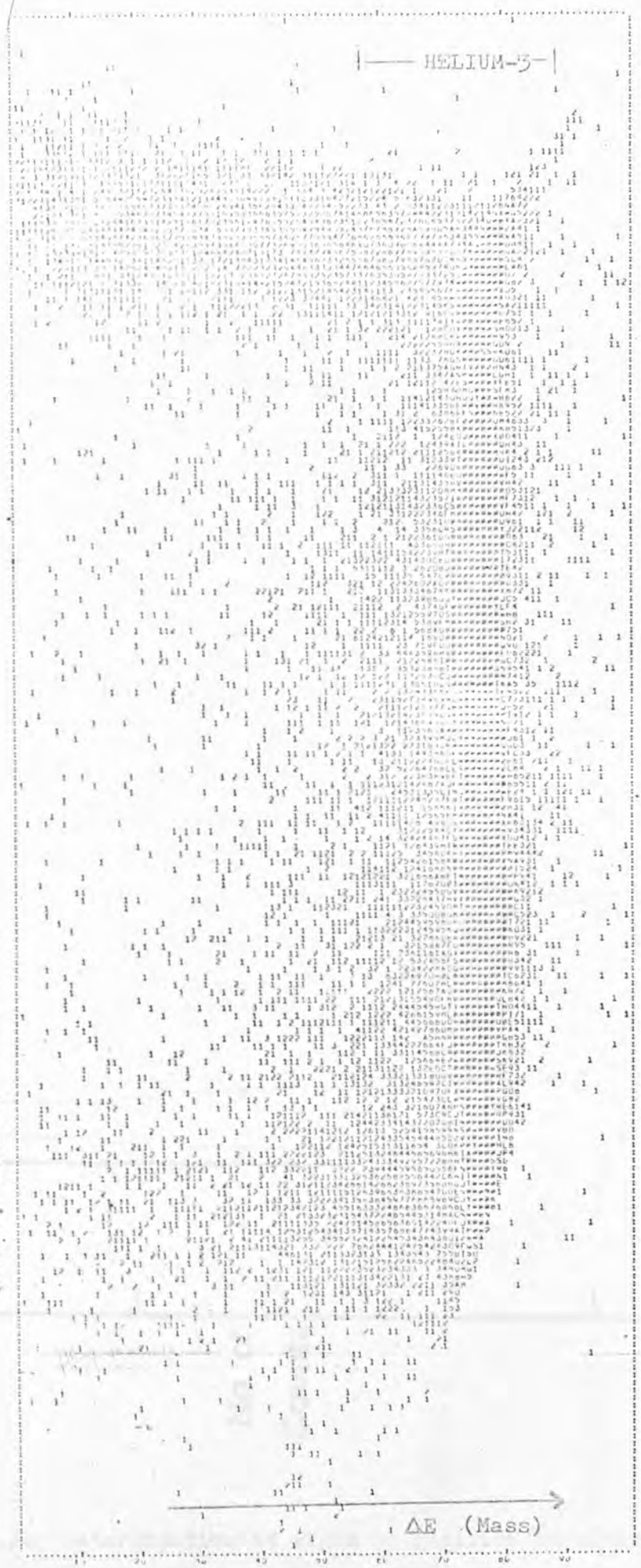

Fig 3.19 Output from Position Sensitive Detector

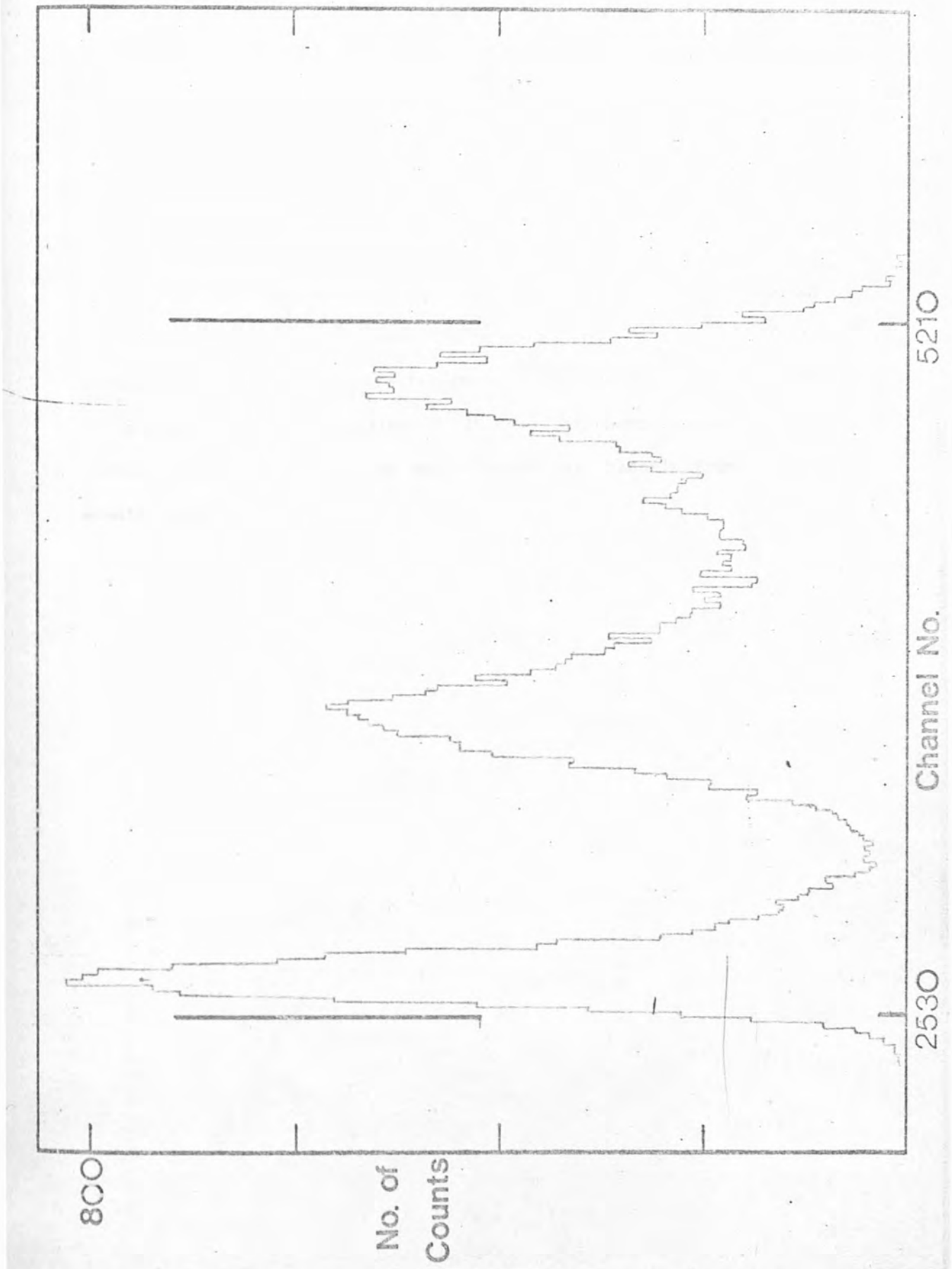

Fig 3.20 Determination of edges of position sensitive detctor

positions on the focal plane, calculated using the computer program HPRP (Hp 08). A graph of the peak channel in each case against the calculated focal point is shown in fig. 3.21. This enabled the number of channels per millimetre to be determined.

The data acquisition was facilitated by the use of the on-line computer which printed graphs of position of detected pulses against the mass of the pulses for each run, and then a graph of the total number of counts in the helium-3 limits against the energy of the pulses. With a resolution of 10 KeV per channel, the 2^+ level on the ^{154}Sm data was approximately $8\frac{1}{2}$ channels from the elastic peak.

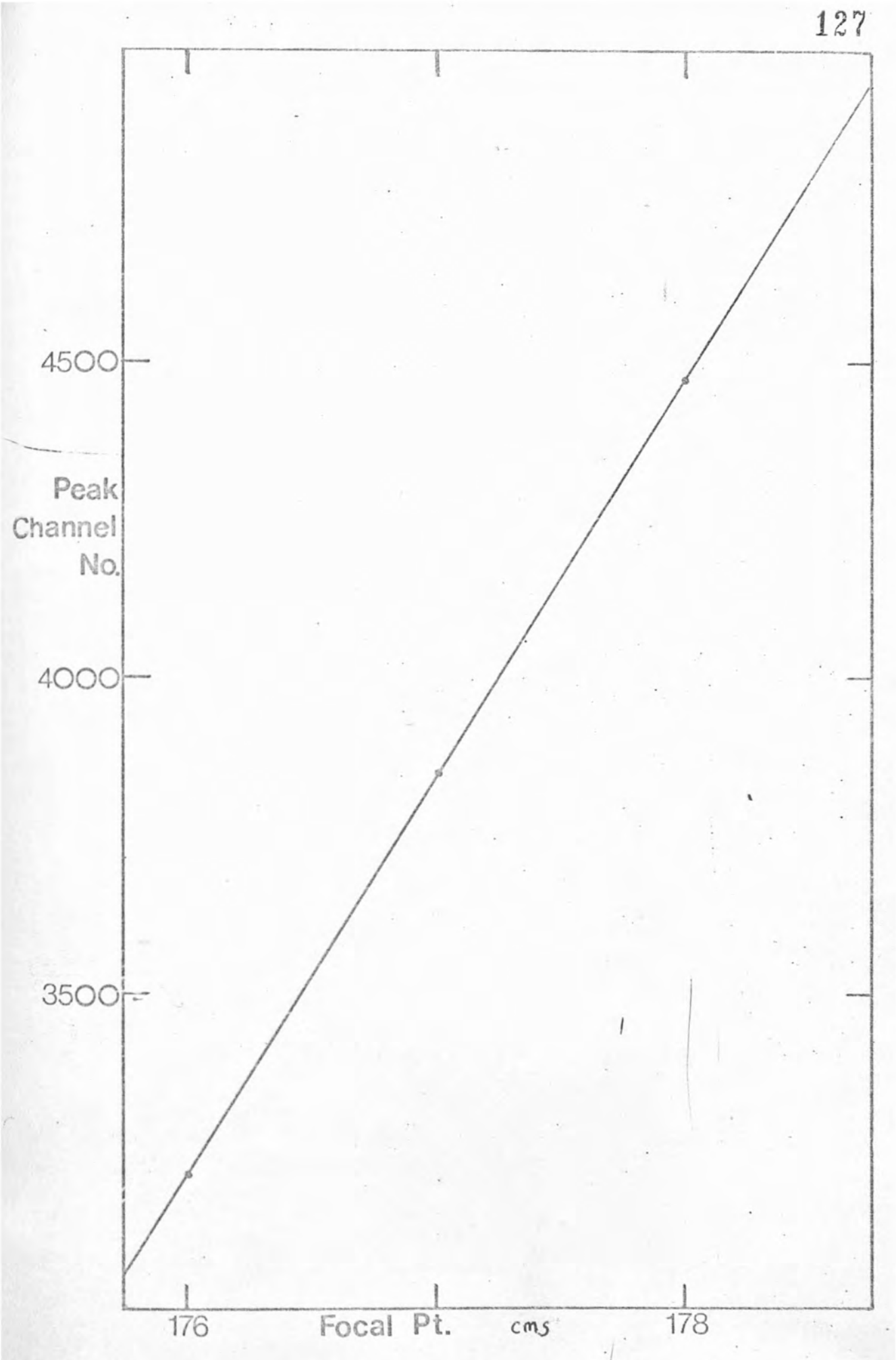

Fig 3.21 Graph to determine the calibration of the P.S.D.

TABLE : 3.7

CROSS-SECTIONS FOR ELASTIC SCATTERING

148 SM(H,H)

INCIDENT ENERGY : 53.4 MEV (LAB)

N = 0·78

ANGLE (CM)	CROSS-SECTION (MB/SR)	ERROR (MB/SR)
8.38	3.34E+05	4.88E+03
10.91	1.30E+05	1.90E+03
13.65	5.18E+04	7.59E+02
16.29	2.41E+04	2.62E+02
18.19	9.86E+03	1.06E+02
18.33	1.11E+04	1.86E+02
18.74	8.39E+03	8.83E+01
18.92	9.75E+03	1.08E+02
19.22	7.07E+03	7.68E+01
19.73	5.96E+03	5.29E+01
20.24	5.10E+03	5.55E+01
20.75	4.31E+03	4.71E+01
20.97	4.91E+03	8.43E+01
21.34	3.86E+03	4.26E+01
21.55	4.32E+03	4.75E+01
23.60	2.59E+03	4.43E+01
26.81	1.06E+03	1.16E+01
28.06	6.12E+02	9.54E+00
28.57	6.39E+02	8.22E+00
28.86	6.32E+02	9.50E+00
29.10	4.89E+02	7.97E+00
29.61	4.36E+02	5.79E+00
30.13	3.95E+02	6.27E+00
30.64	3.52E+02	5.61E+00
31.17	3.24E+02	5.40E+00
31.49	3.64E+02	4.93E+00
32.06	3.03E+02	3.35E+00
34.68	1.61E+02	1.79E+00
36.73	1.08E+02	1.42E+00
37.30	9.00E+01	9.89E-01
39.91	5.47E+01	5.04E-01
41.95	4.05E+01	5.18E-01
42.52	2.81E+01	3.07E-01
44.56	2.09E+01	2.75E-01
47.16	1.31E+01	1.61E-01
49.76	9.14E+00	1.13E-01
52.35	4.87E+00	5.72E-02
52.90	4.13E+00	4.74E-02
55.49	2.17E+00	2.63E-02
58.06	1.50E+00	1.91E-02

TABLE : 3.7 (CONT.)

ANGLE (CM)	CROSS-SECTION (MB/SR)	ERROR (MB/SR)
60.64	1.15E+00	1.53E-02
62.67	8.23E-01	1.13E-02
63.21	7.23E-01	1.05E-02
65.23	4.63E-01	7.31E-03
67.79	2.86E-01	5.22E-03
70.35	1.94E-01	4.06E-03
72.89	1.42E-01	3.36E-03
73.42	1.16E-01	2.21E-03
75.96	8.02E-02	2.14E-03
78.50	4.95E-02	1.63E-03
81.03	2.66E-02	9.20E-04
83.02	1.99E-02	7.40E-04
85.54	1.76E-02	8.90E-04
90.56	7.93E-03	4.60E-04
93.53	3.21E-03	2.20E-04
98.55	2.54E-03	2.20E-04
101.03	2.26E-03	1.80E-04
103.51	1.57E-03	1.40E-04
105.46	7.50E-04	1.10E-04
107.92	3.30E-04	7.00E-05
110.38	4.40E-04	8.00E-05
113.34	2.80E-04	6.00E-05
125.55	7.72E-05	2.33E-05
127.94	9.00E-05	3.00E-05
130.49	1.41E-05	1.41E-05
132.78	2.00E-05	1.00E-05
135.42	1.41E-05	9.99E-06
140.34	2.38E-05	1.38E-05
142.38	2.00E-05	1.00E-05
145.26	4.78E-05	1.95E-05
150.18	1.60E-05	1.13E-05

TABLE : 3.8

CROSS-SECTIONS FOR INELASTIC SCATTERING

148 SM(H,H*) TO 2+ LEVEL AT 0.5502 MEV

INCIDENT ENERGY : 53.4 MEV (LAB)

N = 0·78

ANGLE (CM)	CROSS-SECTION (MB/SR)	ERROR (MB/SR)
8.38	4.84E+03	9.56E+01
18.19	1.52E+02	4.01E+00
18.33	4.99E+01	6.37E+00
18.74	1.27E+02	2.72E+00
19.22	1.41E+02	3.83E+00
19.73	1.13E+02	2.33E+00
20.24	1.02E+02	2.81E+00
20.75	6.27E+01	2.38E+00
21.34	7.56E+01	2.33E+00
21.55	9.90E+01	2.00E+00
26.61	2.58E+01	5.14E-01
28.06	1.28E+01	1.02E+00
28.57	1.05E+01	6.53E-01
29.10	9.28E+00	5.63E-01
29.61	9.08E+00	5.44E-01
30.13	7.81E+00	6.82E-01
30.64	7.14E+00	6.19E-01
31.17	6.42E+00	6.07E-01
31.49	8.39E+00	4.74E-01
32.06	9.75E+00	1.84E-01
34.68	6.81E+00	1.22E-01
36.73	4.83E+00	1.84E-01
37.30	4.90E+00	7.42E-02
39.91	2.57E+00	4.24E-02
41.95	1.76E+00	6.33E-02
44.56	1.54E+00	4.67E-02
47.16	1.07E+00	2.57E-02
47.29	9.03E-01	1.36E-02
47.72	7.79E-01	1.27E-02
49.76	5.84E-01	1.57E-02
52.90	4.14E-01	7.00E-03
55.49	3.01E-01	5.63E-03
57.01	2.30E-01	5.26E-03
57.52	1.89E-01	4.88E-03
58.06	2.01E-01	4.35E-03
60.64	1.41E-01	3.51E-03
62.67	1.22E-01	3.06E-03
63.21	1.21E-01	3.21E-03

TABLE : 3.8 (CONT.)

ANGLE (CM)	CROSS-SECTION (MB/SR)	ERROR (MB/SR)
65.23	7.67E-02	2.35E-03
67.79	4.43E-02	1.74E-03
70.35	3.81E-02	1.60E-03
72.89	3.42E-02	1.52E-03
73.42	2.69E-02	9.30E-04
75.96	1.67E-02	9.10E-04
78.50	1.00E-02	7.00E-04
81.03	6.64E-03	4.40E-04
83.02	6.46E-03	4.10E-04
85.54	5.34E-03	4.80E-04
88.05	2.87E-03	3.50E-04
90.56	2.81E-03	2.70E-04
93.53	1.87E-03	1.70E-04
96.07	1.30E-03	1.50E-04
98.55	1.10E-03	1.40E-04
101.03	7.80E-04	1.10E-04
103.51	5.20E-04	6.00E-05
107.92	3.90E-04	8.00E-05
110.38	2.90E-04	5.00E-05
113.34	1.90E-04	5.00E-05
125.55	3.51E-05	1.57E-05
130.49	7.04E-05	3.15E-05
135.42	2.82E-05	1.41E-05
140.34	2.38E-05	1.38E-05
145.26	1.59E-05	1.13E-05
150.18	3.19E-05	1.60E-05

TABLE : 3.9

CROSS-SECTIONS FOR INELASTIC SCATTERING

148 SM(H,H*) TO 3- LEVEL AT 1.1615 MEV

INCIDENT ENERGY : 53.4 MEV (LAB)

N= 0·78

ANGLE (CM)	CROSS-SECTION (MB/SR)	ERROR (MB/SR)
8.38	2.74E+03	5.38E+01
18.19	8.46E+01	2.89E+00
18.74	7.63E+01	2.01E+00
19.22	6.85E+01	2.57E+00
19.73	6.14E+01	1.61E+00
20.24	5.48E+01	1.99E+00
20.75	4.74E+01	1.75E+00
21.34	4.52E+01	1.76E+00
21.55	5.45E+01	1.39E+00
26.81	1.25E+01	3.31E-01
28.06	4.06E+00	5.68E-01
28.57	4.86E+00	4.41E-01
29.10	5.28E+00	5.49E-01
29.61	4.99E+00	4.01E-01
30.13	5.55E+00	5.74E-01
30.64	4.66E+00	4.98E-01
31.17	4.26E+00	4.93E-01
31.49	5.03E+00	3.64E-01
32.06	6.93E+00	1.47E-01
34.68	3.33E+00	7.72E-02
36.73	2.07E+00	1.18E-01
37.30	2.66E+00	4.80E-02
39.91	2.26E+00	3.86E-02
41.95	1.55E+00	5.91E-02
42.52	1.13E+00	1.75E-02
44.56	9.56E-01	3.60E-02
47.16	7.57E-01	2.10E-02
47.29	6.36E-01	1.06E-02
47.72	5.46E-01	9.93E-03
49.76	6.26E-01	1.64E-02
52.35	3.42E-01	7.48E-03
52.90	3.40E-01	6.11E-03
55.49	2.44E-01	4.92E-03
57.01	2.04E-01	4.89E-03
57.52	1.79E-01	4.73E-03
58.06	1.85E-01	4.13E-03
60.64	1.25E-01	3.27E-03
62.67	1.01E-01	2.73E-03
63.21	9.10E-02	2.73E-03

TABLE : 3.9 (CONT.)

ANGLE (CM)	CROSS-SECTION (MB/SR)	ERROR (MB/SR)
65.23	8.59E-02	2.50E-03
67.79	6.49E-02	2.14E-03
70.35	3.60E-02	1.56E-03
72.89	2.61E-02	1.32E-03
73.42	2.05E-02	8.00E-04
75.96	2.17E-02	1.05E-03
78.50	1.40E-02	8.30E-04
81.03	1.06E-02	5.60E-04
83.02	6.22E-03	4.00E-04
85.54	4.53E-03	4.40E-04
88.05	4.54E-03	4.40E-04
90.56	3.61E-03	3.10E-04
93.53	2.00E-03	1.70E-04
96.07	1.46E-03	1.60E-04
98.55	9.20E-04	1.30E-04
101.03	9.20E-04	1.20E-04
105.46	1.06E-03	1.30E-04
107.92	4.10E-04	8.00E-05
110.38	2.90E-04	6.00E-05
113.34	1.80E-04	5.00E-05
125.55	2.11E-05	1.22E-05
130.49	2.82E-05	1.99E-05
135.42	4.24E-05	1.73E-05
140.34	7.94E-06	7.94E-06
150.18	2.39E-05	1.38E-05

TABLE : 3.10

CROSS-SECTIONS FOR ELASTIC SCATTERING

150 SM(H,H)

INCIDENT ENERGY : 53.4 MEV (LAB)

N = 0·78

ANGLE (CM)	CROSS-SECTION (MB/SR)	ERROR (MB/SR)
8.38	3.18E+05	4.65E+03
11.01	1.27E+05	1.86E+03
13.65	4.65E+04	6.82E+02
16.28	2.12E+04	3.11E+02
18.32	1.04E+04	1.73E+02
18.92	8.82E+03	1.30E+02
20.96	4.71E+03	8.05E+01
23.59	2.38E+03	4.07E+01
26.22	1.14E+03	1.92E+01
28.85	5.73E+02	1.01E+01
32.05	2.70E+02	2.99E+00
34.67	1.23E+02	1.41E+00
37.29	8.07E+01	9.60E-01
39.90	5.13E+01	6.07E-01
41.94	3.54E+01	4.56E-01
44.54	1.56E+01	2.39E-01
47.15	1.20E+01	1.97E-01
49.75	8.88E+00	1.38E-01
52.89	3.98E+00	5.34E-02
55.46	2.11E+00	2.55E-02
57.00	1.42E+00	2.06E-02
57.51	1.45E+00	2.01E-02
62.65	7.54E-01	1.54E-02
65.22	4.37E-01	6.83E-03
68.31	1.87E-01	2.99E-03
73.41	9.08E-02	1.83E-03
75.95	6.10E-02	1.43E-03
77.96	4.30E-02	1.10E-03
81.01	1.92E-02	7.40E-04
83.01	1.30E-02	5.70E-04
85.53	1.27E-02	5.60E-04
88.56	9.34E-03	4.30E-04
90.54	7.08E-03	4.10E-04
93.51	2.60E-03	1.90E-04
96.05	1.72E-03	1.50E-04
98.54	1.69E-03	1.70E-04
101.02	1.44E-03	1.30E-04
103.49	6.80E-04	9.00E-05
105.44	3.80E-04	7.00E-05
108.41	1.80E-04	4.00E-05

TABLE : 3.10 (CONT.)

ANGLE (CM)	CROSS-SECTION (MB/SR)	ERROR (MB/SR)
110.36	2.90E-04	5.00E-05
113.33	3.10E-04	5.00E-05
117.70	6.00E-05	2.00E-05
122.57	3.00E-05	1.00E-05
125.54	1.16E-04	2.02E-05
127.93	6.00E-05	2.00E-05
130.48	7.63E-05	1.50E-05
132.77	5.00E-05	3.00E-05
135.41	5.39E-05	1.13E-05
137.05	1.00E-05	1.00E-05
140.33	5.94E-05	1.54E-05
145.25	3.44E-05	9.52E-06
150.17	2.12E-05	6.39E-06

TABLE : 3.11

CROSS-SECTIONS FOR INELASTIC SCATTERING

150 SM(H,H*) TO 2+ LEVEL AT 0.3340 MEV

INCIDENT ENERGY : 53.4 MEV (LAB)

N = 0·78

ANGLE (CM)	CROSS-SECTION (MB/SR)	ERROR (MB/SR)
8.38	4.19E+03	8.47E+01
11.01	1.80E+03	3.85E+01
13.65	5.81E+02	1.41E+01
16.28	2.17E+02	5.52E+00
18.32	7.02E+01	7.25E+00
18.92	1.34E+02	3.56E+00
20.96	3.50E+01	3.74E+00
23.59	2.28E+01	2.14E+00
26.22	2.40E+01	1.46E+00
28.85	1.64E+01	1.01E+00
32.05	1.19E+01	2.04E-01
34.67	7.31E+00	1.48E-01
37.29	7.32E+00	1.48E-01
39.90	4.01E+00	8.37E-02
41.94	2.59E+00	7.53E-02
44.54	2.18E+00	5.84E-02
46.71	1.37E+00	2.08E-02
47.15	1.25E+00	1.85E-02
49.75	9.85E-01	3.51E-02
52.89	6.66E-01	1.50E-02
55.46	5.11E-01	7.94E-03
57.00	3.35E-01	7.96E-03
57.51	2.51E-01	5.99E-03
62.65	1.73E-01	6.58E-03
65.22	1.14E-01	2.84E-03
68.31	6.75E-02	1.51E-03
73.41	4.13E-02	1.13E-03
75.95	2.11E-02	7.80E-04
77.96	1.46E-02	6.00E-04
81.01	1.26E-02	5.90E-04
83.01	1.25E-02	5.60E-04
85.53	6.45E-03	3.90E-04
88.56	2.53E-03	2.20E-04
90.54	3.03E-03	2.70E-04
93.51	2.13E-03	1.70E-04
96.05	1.72E-03	1.50E-04
98.54	1.13E-03	1.40E-04
101.02	6.60E-04	9.00E-05

TABLE : 3.11 (CONT.)

ANGLE (CM)	CROSS-SECTION (MB/SR)	ERROR (MB/SR)
103.49	6.30E-04	9.00E-05
105.44	4.70E-04	8.00E-05
108.41	4.40E-04	7.00E-05
110.36	2.80E-04	5.00E-05
113.33	1.40E-04	3.00E-05
117.70	5.00E-05	2.00E-05
122.57	3.00E-05	1.00E-05
125.54	8.40E-05	1.72E-05
127.93	1.00E-05	1.00E-05
130.48	5.57E-05	1.28E-05
135.41	3.05E-05	8.46E-06
137.05	2.00E-05	1.00E-05
140.33	4.75E-05	1.37E-05
145.25	2.38E-05	7.95E-06
150.17	2.12E-05	7.48E-06

TABLE : 3.12

CROSS-SECTIONS FOR INELASTIC SCATTERING

150 SM(H,H*) TO 3- LEVEL AT 1.0710 MEV

INCIDENT ENERGY : 53.4 MEV (LAB)

N = 0.78

ANGLE (CM)	CROSS-SECTION (MB/SR)	ERROR (MB/SR)
8.38	1.68E+03	4.80E+01
11.01	7.19E+02	2.07E+01
13.65	3.01E+02	9.25E+00
16.28	1.28E+02	3.96E+00
18.92	6.26E+01	2.23E+00
20.96	2.21E+01	2.96E+00
23.59	5.33E+00	1.03E+00
26.22	4.04E+00	5.85E-01
28.85	5.41E+00	5.70E-01
32.05	4.67E+00	1.12E-01
34.67	2.15E+00	7.18E-02
37.29	2.02E+00	6.94E-02
39.90	1.74E+00	5.09E-02
41.94	1.21E+00	4.96E-02
44.54	6.58E-01	3.60E-02
46.71	5.90E-01	1.18E-02
47.15	5.01E-01	9.67E-03
49.75	5.77E-01	2.64E-02
52.89	3.01E-01	9.41E-03
55.46	2.14E-01	4.38E-03
57.00	1.69E-01	5.39E-03
57.51	1.58E-01	4.58E-03
58.05	6.63E-02	2.19E-03
62.65	6.68E-02	4.57E-03
65.22	8.05E-02	2.32E-03
67.78	1.91E-02	1.07E-03
68.31	3.34E-02	1.00E-03
73.41	1.70E-02	6.90E-04
75.95	1.37E-02	5.20E-04
77.96	1.47E-02	6.10E-04
81.01	6.06E-03	4.10E-04
83.01	3.74E-03	3.00E-04
85.53	4.10E-03	3.10E-04
88.56	3.32E-03	2.50E-04
90.54	2.94E-03	2.60E-04
93.51	1.11E-03	1.20E-04
96.05	6.40E-04	9.00E-05
98.54	6.80E-04	1.10E-04

TABLE : 3.12 (CONT.)

ANGLE (CM)	CROSS-SECTION (MB/SR)	ERROR (MB/SR)
101.02	8.40E-04	1.00E-04
103.49	4.60E-04	7.00E-05
105.44	5.30E-04	8.00E-05
108.41	1.50E-04	4.00E-05
110.36	1.70E-04	4.00E-05
113.33	1.10E-04	3.00E-05
117.70	1.50E-04	4.00E-05
122.57	5.00E-05	2.00E-05
125.54	1.19E-04	2.04E-05
127.93	2.00E-05	1.00E-05
130.48	6.75E-05	1.41E-05
135.41	5.85E-05	1.17E-05
137.05	1.00E-05	1.00E-05
140.33	1.15E-04	2.13E-05
145.25	6.35E-05	1.30E-05
150.17	2.64E-05	8.39E-06

TABLE : 3.13

CROSS-SECTIONS FOR INELASTIC SCATTERING

150 SM(H,H*) TO 0+ LEVEL AT 0.7405 MEV

INCIDENT ENERGY : 53.4 MEV (LAB)

N = 0·78

ANGLE (CM)	CROSS-SECTION (MB/SR)	ERROR (MB/SR)
8.38	1.89E+03	4.82E+01
11.01	6.68E+02	1.97E+01
13.65	3.36E+02	9.91E+00
16.28	1.44E+02	4.25E+00
18.32	2.57E+01	4.36E+00
18.92	6.43E+01	2.27E+00
20.96	4.02E+00	1.26E+00
23.59	3.08E+00	7.78E-01
26.22	2.15E+00	4.26E-01
28.85	1.78E+00	3.25E-01
32.05	2.35E+00	7.53E-02
34.67	1.20E+00	5.23E-02
37.29	8.89E-01	4.47E-02
39.90	5.88E-01	2.82E-02
41.94	3.89E-01	2.75E-02
44.54	1.16E-01	1.49E-02
46.71	1.79E-01	5.88E-03
47.15	1.96E-01	5.46E-03
47.15	1.20E-01	1.52E-02
49.75	1.18E-01	1.17E-02
52.89	8.72E-02	4.85E-03
55.46	5.80E-02	2.04E-03
57.00	3.97E-02	2.51E-03
57.51	3.61E-02	2.07E-03
58.05	2.55E-02	1.32E-03
62.65	1.85E-02	2.07E-03
65.22	1.73E-02	1.02E-03
67.78	7.29E-03	6.50E-04
68.31	1.39E-02	5.20E-04
73.41	7.82E-03	4.60E-04
75.95	5.17E-03	3.70E-04
77.96	3.92E-03	3.00E-04
81.01	2.62E-03	2.60E-04
83.01	2.64E-03	2.50E-04
85.53	1.57E-03	1.90E-04
88.56	1.16E-03	1.50E-04
90.54	9.90E-04	1.50E-04
93.51	6.40E-04	9.00E-05

TABLE : 3.13 (CONT.)

ANGLE (CM)	CROSS-SECTION (MB/SR)	ERROR (MB/SR)
96.05	4.80E-04	8.00E-05
98.54	3.00E-04	7.00E-05
101.02	2.50E-04	5.00E-05
103.49	2.40E-04	5.00E-05
105.44	1.30E-04	4.00E-05
108.41	1.20E-04	4.00E-05
110.36	1.50E-04	4.00E-05
113.33	8.00E-05	2.00E-05
117.70	6.00E-05	2.00E-05
122.57	4.00E-05	1.00E-05

TABLE : 3.14

CROSS-SECTIONS FOR ELASTIC SCATTERING

152 SM(H,H)

INCIDENT ENERGY : 53.1 MEV (LAB)

N = 1·3

ANGLE (CM)	CROSS-SECTION (MB/SR)	ERROR (MB/SR)
16.30	1.24E+04	3.92E+01
20.40	3.15E+03	9.92E+00
24.50	1.05E+03	8.17E+00
28.50	2.87E+02	3.73E+00
32.60	1.32E+02	2.05E+00
36.70	5.29E+01	9.13E-01
40.70	2.31E+01	4.16E-01
44.80	8.17E+00	2.26E-01
48.90	4.30E+00	1.17E-01
52.90	2.02E+00	8.03E-02
57.00	6.80E-01	3.32E-02
61.00	4.26E-01	2.53E-02
65.00	2.42E-01	1.89E-02
69.10	6.06E-02	9.70E-03
75.10	2.40E-02	4.51E-03
81.10	8.10E-03	2.25E-03
83.10	5.80E-03	1.37E-03
88.90	3.10E-03	9.80E-04
93.20	3.00E-04	3.00E-04
97.20	3.00E-04	3.00E-04

TABLE : 3.15

CROSS-SECTIONS FOR INELASTIC SCATTERING

152 SM(H,H*) TO 2+ LEVEL AT 0.1218 MEV

INCIDENT ENERGY : 53.1 MEV (LAB)

N = 1·3

ANGLE (CM)	CROSS-SECTION (MB/SR)	ERROR (MB/SR)
16.30	4.59E+02	1.09E+01
20.40	1.00E+02	1.80E+00
24.50	7.47E+01	3.03E+00
28.50	4.82E+01	1.77E+00
32.60	2.32E+01	8.64E-01
36.70	1.10E+01	5.89E-01
40.70	6.58E+00	3.34E-01
44.80	3.64E+00	1.52E-01
48.90	2.41E+00	1.26E-01
52.90	1.38E+00	6.82E-02
57.00	4.78E-01	3.88E-02
61.00	2.52E-01	2.69E-02
65.00	1.34E-01	2.11E-02
69.10	8.62E-02	1.89E-02
75.10	1.13E-02	4.92E-03
81.10	8.60E-03	3.33E-03
83.10	1.08E-02	1.85E-03
88.90	3.20E-03	1.43E-03
93.20	1.30E-03	9.19E-04
97.20	7.00E-04	7.00E-04

TABLE : 3.16

CROSS-SECTIONS FOR ELASTIC SCATTERING

154 SM(H,H)

INCIDENT ENERGY : 53.1 MEV (LAB)

N = 1·36

ANGLE (CM)	CROSS-SECTION (MB/SR)	ERROR (MB/SR)
16.30	1.22E+04	5.64E+01
20.40	3.00E+03	9.86E+00
24.50	9.67E+02	1.09E+01
28.50	3.33E+02	4.64E-01
32.60	1.16E+02	1.93E+00
36.70	4.52E+01	1.20E+00
40.70	2.04E+01	5.87E-01
44.80	8.07E+00	2.26E-01
48.90	2.79E+00	1.36E-01
52.90	1.38E+00	6.80E-02
57.00	5.10E-01	4.01E-02
61.00	2.20E-01	2.51E-02
65.00	8.85E-02	1.72E-02
69.10	5.39E-02	1.29E-02
75.10	3.07E-02	8.12E-03
81.10	5.00E-03	2.50E-03
83.10	5.80E-03	1.37E-03
88.90	3.80E-03	1.55E-03
93.20	1.30E-03	9.19E-04
97.20	7.00E-04	7.00E-04

TABLE : 3.17

CROSS-SECTIONS FOR INELASTIC SCATTERING

154 SM(H,H*) TO 2+ LEVEL AT 0.0820 MEV

INCIDENT ENERGY : 53.1 MEV (LAB)

N = 1·36

ANGLE (CM)	CROSS-SECTION (MB/SR)	ERROR (MB/SR)
16.30	4.19E+02	7.21E+00
20.40	1.30E+02	2.01E-01
24.50	5.30E+01	1.82E+00
28.50	2.77E+01	1.31E+00
32.60	1.85E+01	7.66E-01
36.70	9.76E+00	3.92E-01
40.70	4.77E+00	1.88E-01
44.80	3.84E+00	1.68E-01
48.90	1.23E+00	1.99E-01
52.90	9.95E-01	5.63E-02
57.00	4.70E-01	2.76E-02
61.00	2.17E-01	1.81E-02
65.00	6.64E-02	9.94E-03
69.10	9.45E-02	1.21E-02
75.10	4.40E-02	5.83E-03
81.10	1.18E-02	2.71E-03
83.10	1.08E-02	1.85E-03
88.90	2.50E-03	8.84E-04
93.20	9.00E-04	5.20E-04
97.20	3.00E-04	3.00E-04

CHAPTER 4

Analysis of Elastic and Inelastic Scattering Angular Distributions

Introduction

The data obtained from ^{3}He scattering from the Samarium isotopes are analysed in terms of basically two nuclear structure models in this chapter.

The elastic scattering data are analysed in terms of the regular and reformulated optical models. The real discrete ambiguity problem in the former, and the ability to obtain unique values for the mean square radius of the matter distribution, and the mean square radius of the two-body effective interaction in the latter are discussed.

The inelastic elastic scattering data are analysed in terms of the collective model.

The Distorted Wave Born Approximation, in which the potential producing inelastic scattering is treated as a perturbation of the potential producing elastic scattering, is used to predict scattering to the 2^+ and in some cases 3^- levels of the nuclei, and these predictions are compared with experimental results. The Strong Coupling Approximation, in which the coupling of the low lying levels of the nucleus to the elastic scattering channel is taken into account explicitly, is also used to describe the elastic and inelastic scattering of helium-3 from Samarium isotopes.

4.1 Simple Optical Model Analysis

The ^{3}He data shown in figs. 4.1 and 4.2 are interesting in so far that the cross-sections are so similar for all the isotopes, the

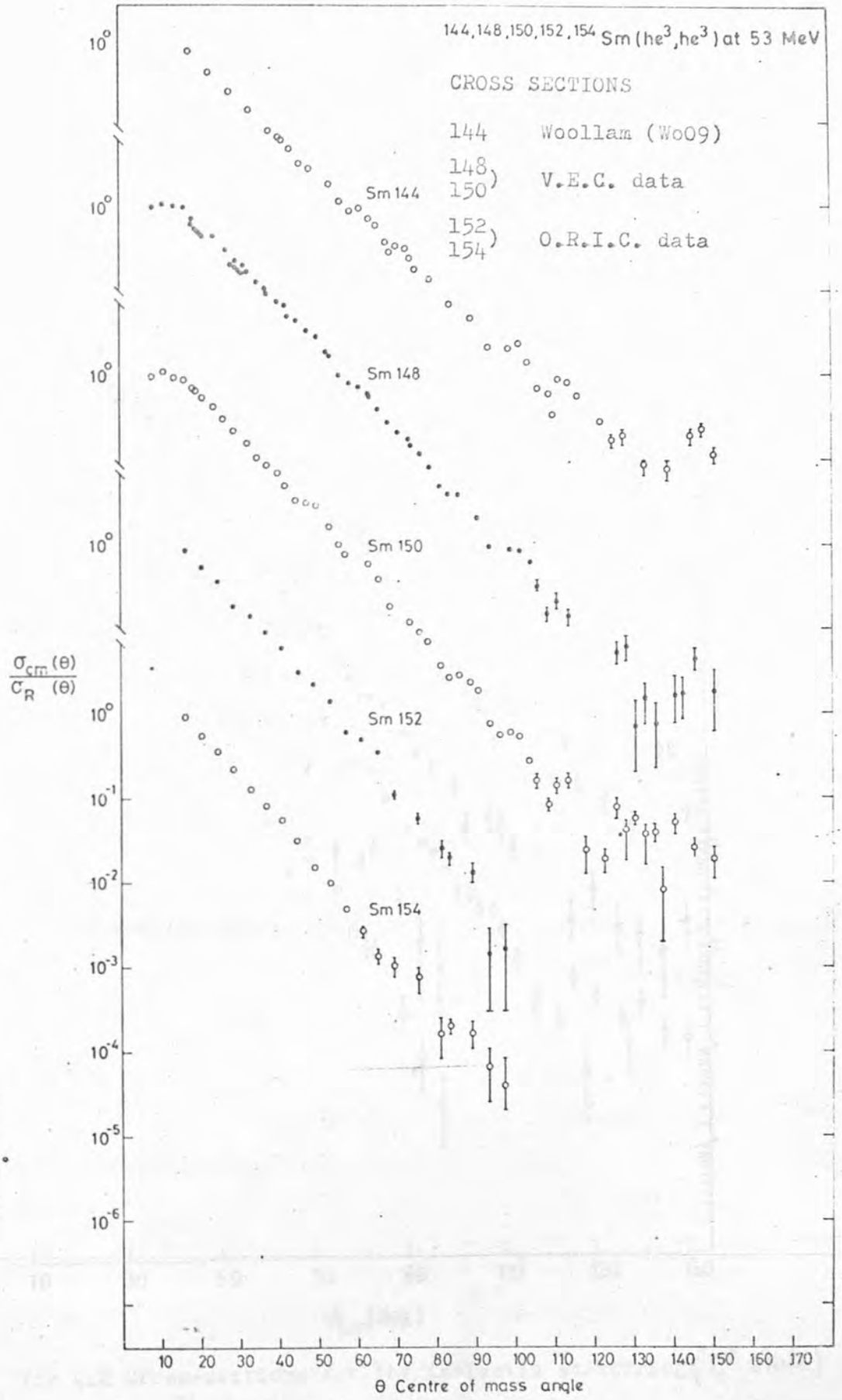

Fig 4.1 Cross-Sections for the elastic scattering of ^{3}He from Samarium isotopes

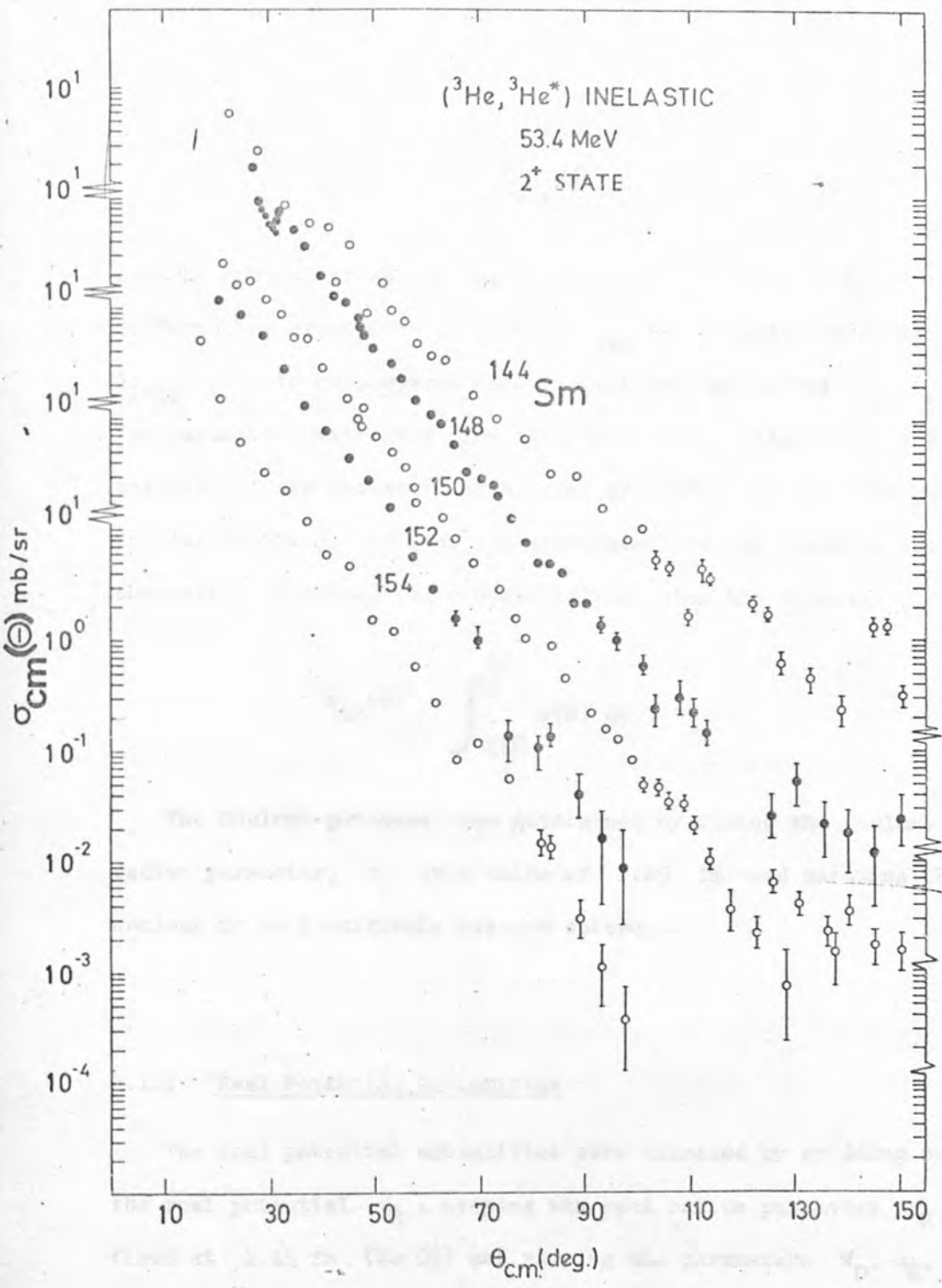

Fig 4.2 Cross-Sections for the inelastic scattering (2^+ state) of ^{3}He from Samarium isotopes.

largest difference being between ^{144}Sm and ^{148}Sm . The envelope of the cross-sections plotted as a ratio to the Rutherford cross-sections show an exponential decrease with angle.

The computer code RAROMP (Py 04) used for the simple and reformulated optical model analysis minimised the quantity

$$\Delta = \frac{1}{N} \sum_{i=1}^{N} \{ \frac{\sigma_{th}(\theta_i) - \sigma_{exp}(\theta_i)}{\Delta\sigma_{exp}(\theta_i)} \}^2$$

for the optical potential equation 2.1.4. N is the number of differential cross-section points $\sigma_{exp}(\theta_i)$, each with error $\Delta\sigma_{exp}(\theta_i)$, to be compared with the theoretical values $\sigma_{th}(\theta_i)$. The parameters extracted from this model were suitable for a D.W.B.A. analysis of the inelastic data. The programme corrects for the angular smearing, $\Delta\theta$, of the cross-sections, by smearing the theoretical differential cross-sections using the formula

$$\bar{\sigma}_{th}(\theta) = \int_{\frac{-\Delta\theta}{2}}^{\frac{\Delta\theta}{2}} \sigma(\theta)\, d\theta \, .$$

The Coulomb potential was determined by fixing the Coulomb radius parameter, r_c to a value of 1.25 fm and assuming the nucleus to be a uniformly charged sphere.

4.1.1 Real Potential Ambiguities

The real potential ambiguities were examined by gridding over the real potential V_R , keeping the real radius parameter r_R fixed at 1.13 fm (Wo 09) and varying the parameters W_D, a_R, r_I, a_I until some convergence was reached. A typical grid over V_R for

^{150}Sm is shown in fig. 4.3.

From these grids four potentials were extracted corresponding to real volume integrals of J_R/A_iA_t of 240, 300, 400 and 480 MeV fm^3 $nucl^{-2}$. These families corresponded to values in V_R initially of about 95, 135, 170 and 200 MeV.

Using these approximate values of V_R , each isotope was analysed by varying all the parameters to convergence. Initially no spin orbit potential was used, and the imaginary potential was just a derivative term which has been widely used in ^3He scattering analysis. The search sequence was simply V_R, W_D, r_I, a_R, a_I until convergence was reached. The fits obtained are shown in figs. 4.4 and 4.5 . Visibly all potential sets fit the data very well out to 90^o, but then the strength of oscillations for one isotope increases as the potential becomes deeper. The shape of the Samarium 154 oscillations is very peculiar, but considerable difficulty was experienced in fitting the Samarium 154 data due to its lack of structure and limited angular range.

The parameters which were used to obtain these best fits are listed in table 4.1, which also lists the parameters obtained by Woollam (Wo 06) for the Samarium 144 analysis.

Measurements of alpha particle scattering (Gl 03) (Ba 02) and proton scattering (St 20) (Fu 6) for the even Samarium isotopes at 50 MeV have been reported.

The alpha particle elastic scattering cross-sections were shown to be qualitatively different even for such close neighbours as ^{148}Sm (spherical) and ^{154}Sm (deformed). The slope became steeper and the amplitude of the oscillations smaller for more deformed nuclei. This difference was explained by the stronger coupling to

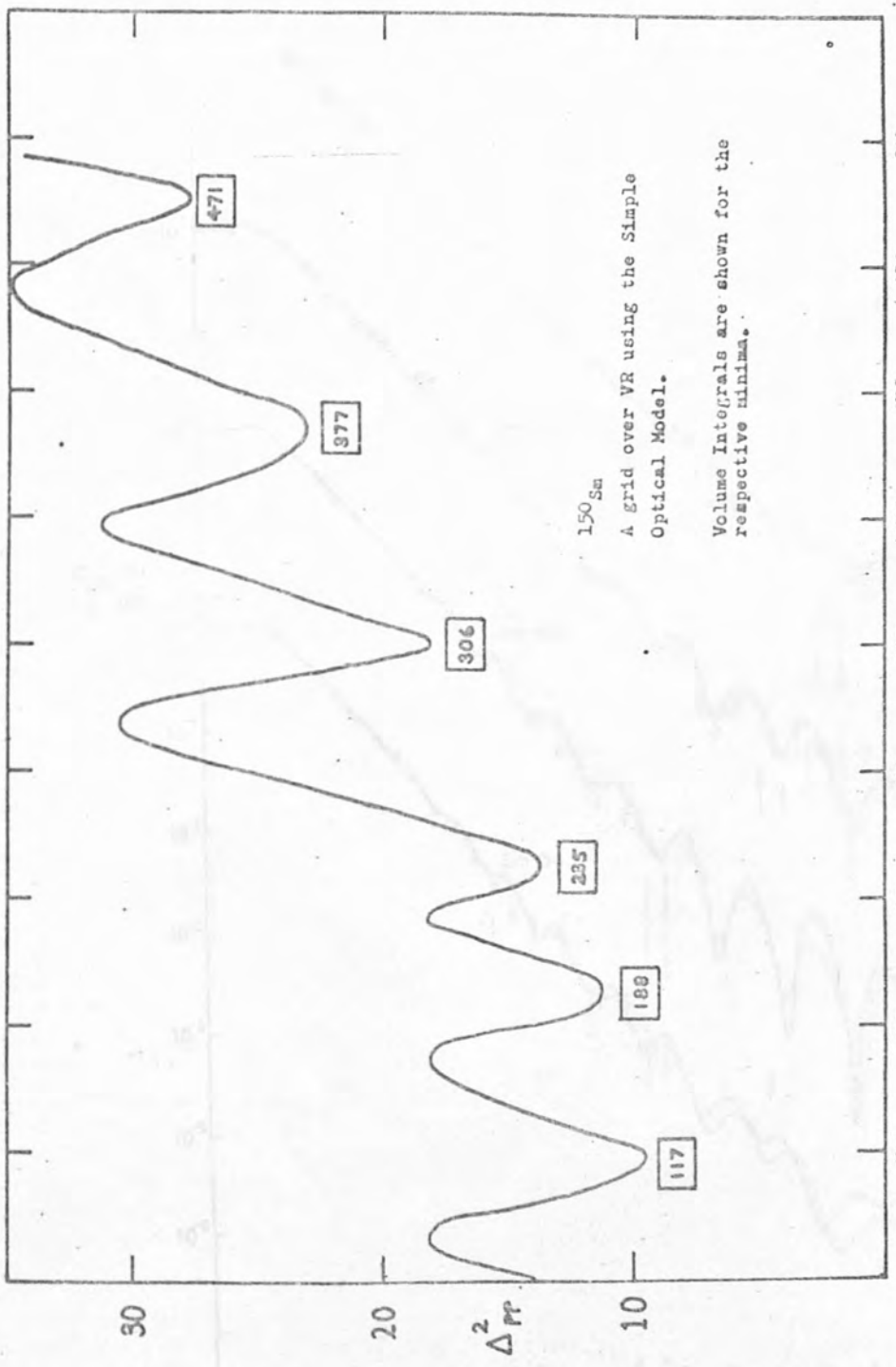

Fig 4.3 Grids over V_R for ^{150}Sm data

with r_R = 1.13 fm

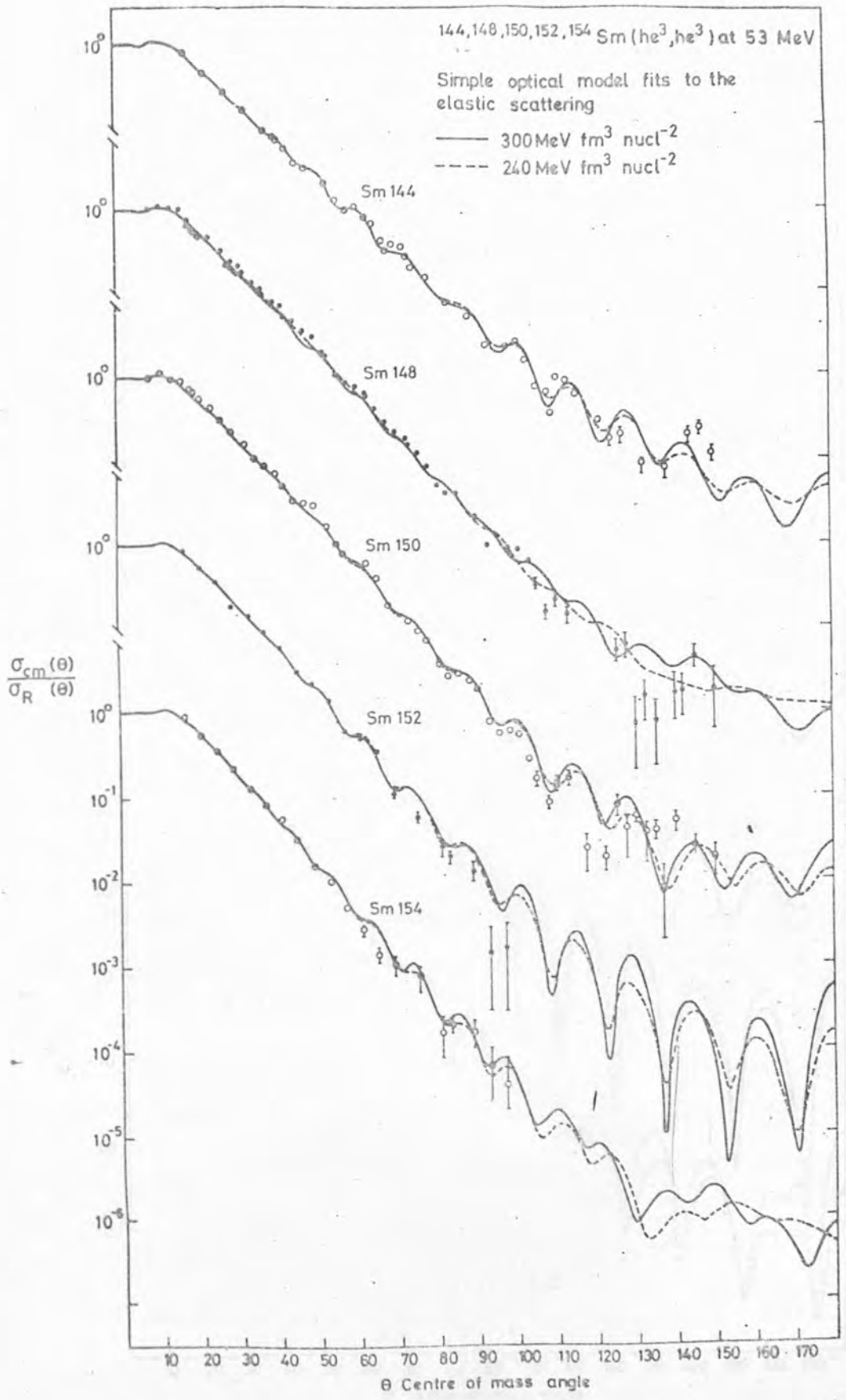

Fig 4.4 Simple Optical Model fits to ^{3}He elastic scattering from Samarium isotopes

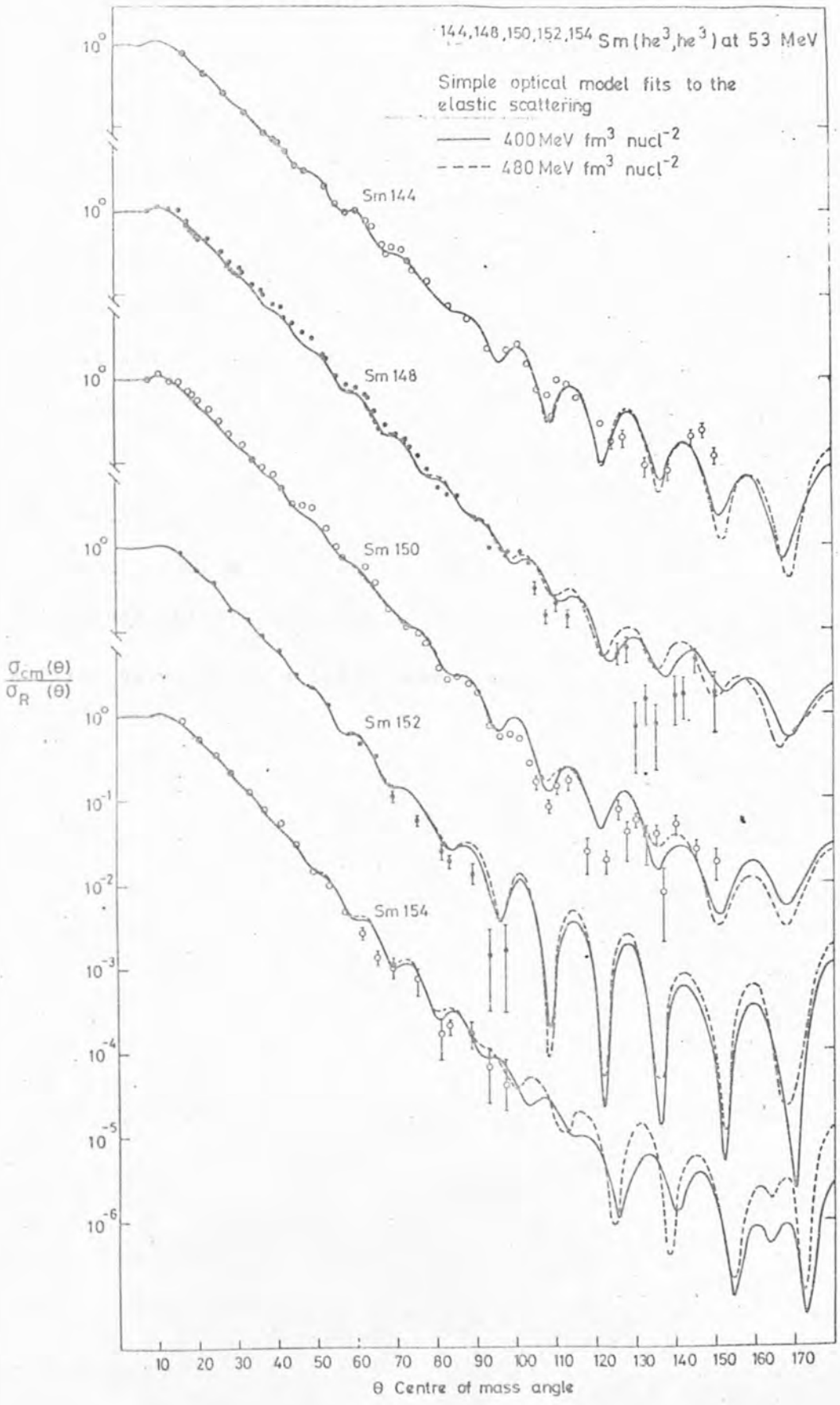

Fig 4.5 Simple Optical Model fits to ^{3}He elastic scattering from Samarium isotopes

Table 4.1

Optical model parameters for ^{3}He scattering from Samarium isotopes.

All depths in MeV

All lengths in fm

All volume integrals in MeV fm ^{3}

A fixed value of RR = 1.13fm was used.

		VR	AR	WD	RD	AD	$\langle r^2 \rangle_R^{1/2}$	$\langle r^2 \rangle_I^{1/2}$	JI	JR	Δ^2_{PP}
	^{144}Sm	107.7	0.849	23.8	1.223	0.823	5.568	7.216	98.1	259.8	8.2
200 MeV	^{148}Sm	84.1	0.763	21.6	1.110	1.067	5.428	7.266	98.9	195.6	25.6
potential	^{150}Sm	102.6	0.759	20.4	1.106	1.080	5.44	7.308	93.9	237.9	12.1
family	^{152}Sm	102.7	0.808	19.5	1.135	1.048	5.553	7.376	90.4	242.2	5.4
	^{154}Sm	102.7	0.771	31.9	0.865	1.199	5.496	6.659	108.2	238.7	3.2
	^{144}Sm	140.9	0.802	28.3	1.185	0.832	5.470	7.059	111.2	333.8	7.8
300 MeV	^{148}Sm	134.6	0.754	32.2	1.020	1.023	5.412	6.779	120.8	312.3	31.4
potential	^{150}Sm	134.6	0.749	24.1	1.105	1.079	5.42	7.295	110.4	311.2	16.1
family	^{152}Sm	134.6	0.772	22.8	1.088	1.067	5.481	7.215	100.2	313.4	5.5
	^{154}Sm	134.6	0.723	35.5	0.794	1.264	5.406	6.582	112.7	307.7	4.3
	^{144}Sm	177.5	0.761	32.5	1.144	0.855	5.369	6.913	123.2	414.0	9.8
400 MeV	^{148}Sm	173.4	0.729	37.3	0.978	1.038	5.363	6.64	132.1	398.4	34.1
potential	^{150}Sm	169.4	0.741	28.7	1.076	1.079	5.405	7.171	125.6	390.6	20.4
family	^{152}Sm	170.3	0.742	26.3	1.040	1.090	5.423	7.064	108.9	392.2	6.2
	^{154}Sm	170.3	0.686	36.4	0.745	1.324	5.339	6.596	112.3	384.5	5.9
	^{144}Sm	217.7	0.723	36.4	1.093	0.896	5.317	6.771	133.9	500.6	12.7
500 MeV	^{148}Sm	216.8	0.707	43.1	0.934	1.064	5.322	6.522	145.1	494.4	39.1
potential	^{150}Sm	205.5	0.736	33.2	1.060	1.079	5.395	7.104	141.4	472.9	24.1
family	^{152}Sm	209.2	0.715	29.8	0.995	1.119	5.374	6.949	117.2	477.4	7.4
	^{154}Sm	209.2	0.662	36.4	0.731	1.356	5.296	6.644	112.8	468.6	7.8

excited states in the deformed nucleus.

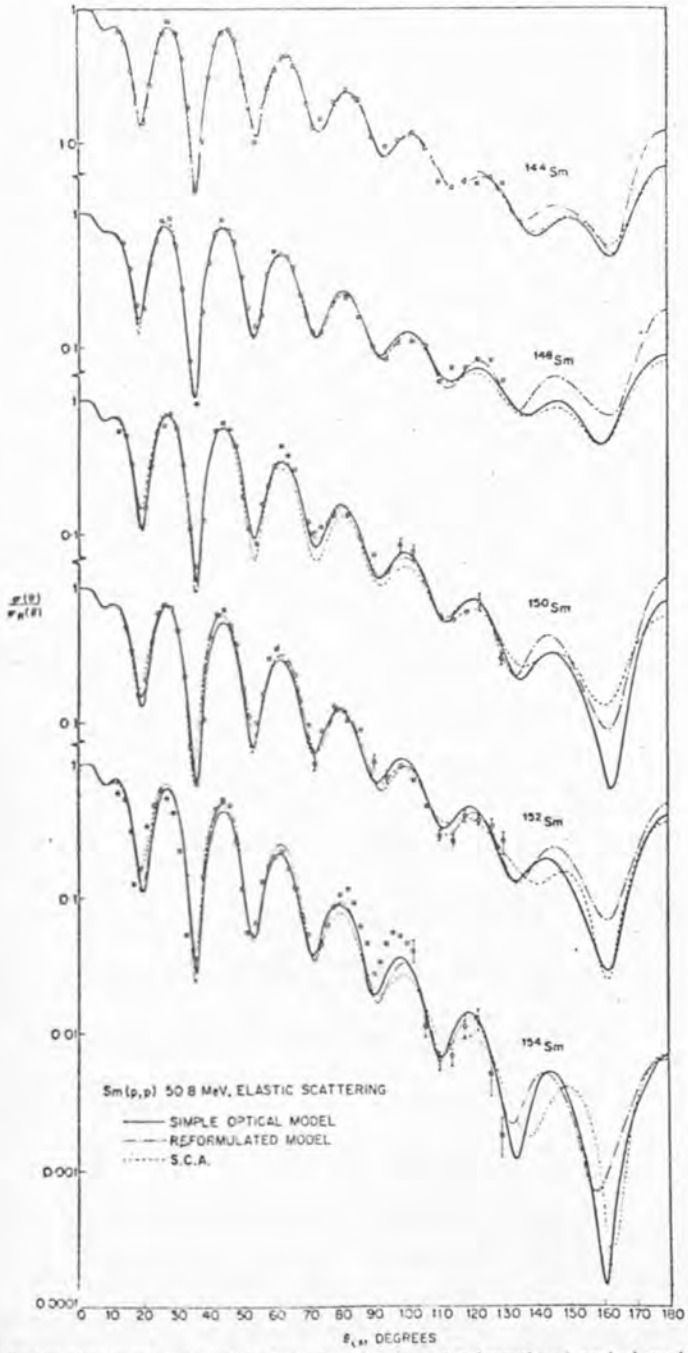

Fits to the elastic scattering data from the simple and reformulated optical models and the SCA. Errors bars are generally too small to be visible.

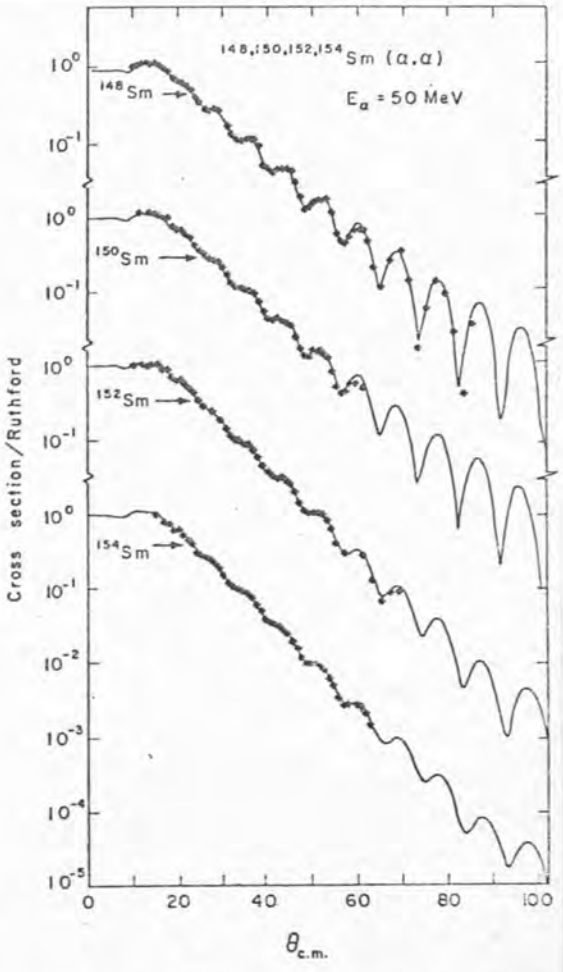

The elastic scattering of 50 MeV alpha particles from samarium isotopes which span the spherical ($A = 148$) to deformed ($A = 154$) region. Note the systematic trend to weaker oscillations and steeper slope of the envelope of maxima with increasing collectivity. Solid lines are elastic optical model calculations of the cross section.

DIFFERENTIAL CROSS-SECTIONS FOR PROTON AND ALPHA PARTICLE ELASTIC SCATTERING (Wo 10) (G1 03)

The proton elastic scattering cross-sections at 50.8 MeV (Fu 06) showed a difference in character from the alpha particle data, and even the 16 MeV proton data (St 20). There was no damping of the oscillations for the deformed nuclei; instead the oscillations were

more pronounced and the decrease of cross-section with angle was larger for the deformed nuclei.

This present work complements the work of Woollam et al (Wo 09) which studies the elastic scattering of 53.4 MeV ^{3}He particles from ^{144}Sm .

In the work of Woollam (Wo 06) a discrete ambiguity was mentioned which gave rise to a series of wavefunctions identical outside but having differing numbers of oscillations inside the nucleus. Because of the strong absorption present in ^{3}He scattering, the oscillations in the cross-sections are typically heavily damped, and the decrease in cross-section at back angles is very large. This lack of structure impedes the fitting procedure, but this can be remedied to some extent by taking data to a large angular range. A comparison of ^{3}He and alpha angular distributions shows that the damped structure in the former is not entirely due to Coulomb effects, but rather to the strong absorption occurring in the helium case which, because of the large binding energy, does not exist for alpha particle scattering.

It was shown by Urone et al (Ur 02) that the optical potential was valid for scattering cross-sections which are so small at back-angles by considering a range of cross-section data at about 37.7 MeV over a 1.3 MeV energy spread for a selection of targets. This data appears to show smooth variations with incident energy and target mass: necessary conditions for the validity of the optical model.

The ambiguities in the real potentials are also to some extent solved by theoretical considerations (Ab 01) where an upper limit of three times the nucleon value for the ^{3}He real optical potential has been derived. In fact, results show that for elastic scattering

of ^{3}He particles (Wo 09) and alpha particles (Ba 02) the real optical potential is always less than $V_p A$ where V_p is the real optical potential for proton elastic scattering (Wo 10) and A is the number of nucleons in the incident projectile. Thus, for example, Abul-Magd and El-Nadi obtained

$$V_{^3He}(r) = \int \phi(r,p) \left[V_p(\underline{r}_1) + V_n(\underline{r}_2) + V_p(\underline{r}_3) \right] d\underline{r}\, d\underline{p}$$

where $\underline{r}_1$, $\underline{r}_2$, $\underline{r}_3$ are position vectors of the constituent nucleons.

The calculations of Abul-Magd and El-Nadi suggest that a potential having three times the nucleon strength is most realistic. Similar conclusions about the discrete ambiguities have been reached by other authors (Gi 01) where the potential to use has been shown to be the one having slightly less than three times the nucleon value. Binding energy effects reduce this value. The nucleon potential should be calculated for nucleons having an energy of one-third the incident helion energy. From global parameters (Be 05) the proton equivalent potential is 57.9 MeV . The helion potential should thus be about 165 MeV . This then could correspond to potentials having a volume integral of either 300 MeV fm^3 nucl^{-2} or 400 MeV fm^3 nucl^{-2} in the present work. Previous authors (Gi 01) have taken the 400 MeV fm^3 nucl^{-2} family, but Woollam et al (Wo 06), and recently Weisrose et al (We 03), have shown that the more realistic potential family is the one having a volume integral of $\sim$ 300 MeV fm^3 nucl^{-2} .

With particular reference to the optical model family ambiguity, Fulmer and Hafele (Fu 09) claimed that they resolved the ambiguity by taking high energy data. They concluded that the normalised volume integral of the real potential at $V \sim 130$ MeV is $J_R/A_i A_t \sim 330$ MeV fm^3 and $J_R/A_i A_t$ changes by $\sim$ 100 MeV fm^3 for

successive families. However, in the same work they demonstrate the A dependence of the optical model for helium-3 scattering, and suggest that J_R decreases by 0.5 MeV fm^3 per a.m.u. of increasing atomic mass. Their crucial point is the ^{144}Sm volume integral whose parameterisation is shown in table 4.2. A re-analysis of this data at 59.8 MeV gives, however, the second set of parameters in this table, and if this point were plotted on the graph of Fulmer and Hafele, the indications would suggest that there was no A dependence at all.

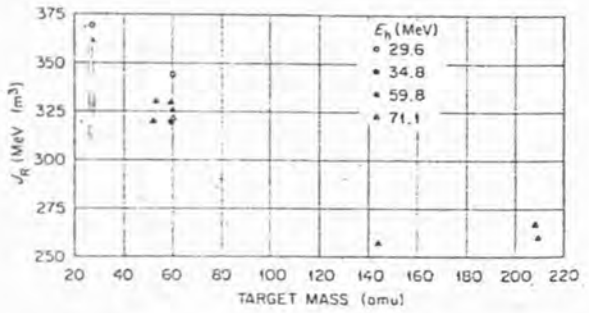

Values of the real well volume integral per particle pair as a function of target mass for helion-nucleus elastic scattering optical-model potentials with $V \sim 130$ MeV. Targets include ^{27}Al, ^{52}Cr, ^{53}Cr, ^{59}Co, ^{60}Ni, ^{144}Sm, ^{208}Pb, and ^{209}Bi.

The graph shown in the reference Fu 09.

Woollam (Wo 06), using a value of real radius parameter r_R of 1.13 fm and a value of real potential depth V_R of about 140 MeV, found that if grids were performed over r_R allowing V_R to reach a value to give a minimum Δ^2_{pp}, then, although large variations occurred in r_R and V_R, only small variations were found in the volume integrals. Thus the various potentials were unambiguously labelled by the values of the real integral.

	FULMER	PRESENT
VR	100.8	138.6
RR	1.15	1.13
AR	0.919	0.858
WD	23.6	28.0
RD	1.26	1.226
AD	0.809	0.840
$\langle r^2 \rangle_R^{\frac{1}{2}}$	5.782	5.587
$\langle r^2 \rangle_I^{\frac{1}{2}}$	7.366	7.262
JR/A_iA_t	261.76	335.43
JI/A_iA_t	101.15	118.72
Δ^2_{pp}	3.00	1.24

Table 4.2 Two analyses of the $^{144}Sm(^3He,^3He)^{144}Sm$ data at 59.8 MeV.

Depths in MeV; lengths in fm;
Volume Integrals in MeV fm ^{3}

A grid was performed over r_R allowing all other parameters to vary to convergence. This did not produce any well-defined value of r_R and hence a value of 1.13 fm corresponding to previous work was chosen. The ambiguities between V_R and r_R arise because three variables V_R, r_R and a_R are used to describe a system having only two well determined quantities, $J_R/A_i A_t$ and $\langle r^2 \rangle_R$.

4.1.2 The Imaginary Potential

The data of ^{3}He scattering from Samarium lies considerably below the scattering from a pure Coulomb potential having a Saxon-Woods charge distribution in the region $40^\circ < \theta < 90^\circ$. This demonstrates the strong absorption occurring in this angular region which is to be accounted for by the imaginary part of the nuclear potential.

For all data sets, combinations of volume and surface absorption potentials were investigated, with coupled geometries. This might be expected to yield a better fit because of the introduction of an extra parameter in the simple optical model. However, it was found that the best fit was obtained when $W_V = 0$, and only a surface imaginary term was considered. This has been found by previous authors when analysing ^{3}He scattering, showing that the incident ^{3}He particle interacts only with the tail of the nuclear potential at 53 MeV. Although the helium-3 data pick out $W_D \neq 0$, $W_V = 0$, the alpha data is ambiguous in this respect and many analyses use $W_V \neq 0$ and $W_D = 0$.

The surface imaginary term W_D was found for each set of potential families and was found to increase corresponding to increasing values of V_R for one particular isotope.

4.1.3 The Spin Orbit Potential

The fits shown in figs. 4.3 and 4.4. do not include spin orbit terms. Theoretical estimates (Ab 01) predict a spin-orbit well depth between 2 and 3 MeV for ^{3}He, although many previous attempts to measure the strength of this interaction have suffered from serious ambiguities. Fulmer and Hafele (Fu 08) determined the spin-orbit term by performing parameter searches for ^{3}He elastic scattering data at successive fixed values of V_s . Resulting plots of Δ^2/N vs V_s showed consistent minima for the 13 data sets used. The Δ^2/N vs V_s plots for all the even mass targets had minima at values of V_s between 2.0 and 3.0 MeV . One of these data sets was ^{3}He scattering off ^{144}Sm at 59.8 MeV . Woollam (Wo 06), however, decided that although he achieved a minimum Δ^2/N for V_s at 2 MeV , the minimum was not well-defined and was probably only due to the inclusion of the three extra parameters V_s , r_s and a_s . The spin-orbit grids performed by these two authors are shown in fig. 4.6.

Cohler (Co 08) using the theoretical formulations of Abul-Magd and El-Nadi (Ab 01), and using the spin-orbit parameters obtained by Woollam (Wo 06) for proton scattering from Samarium 144, has calculated the spin-orbit form factor for helium-3 scattering from Samarium 144. Fitting this form factor with a derivative Saxon-Woods form factor by varying the geometry parameters led to the following

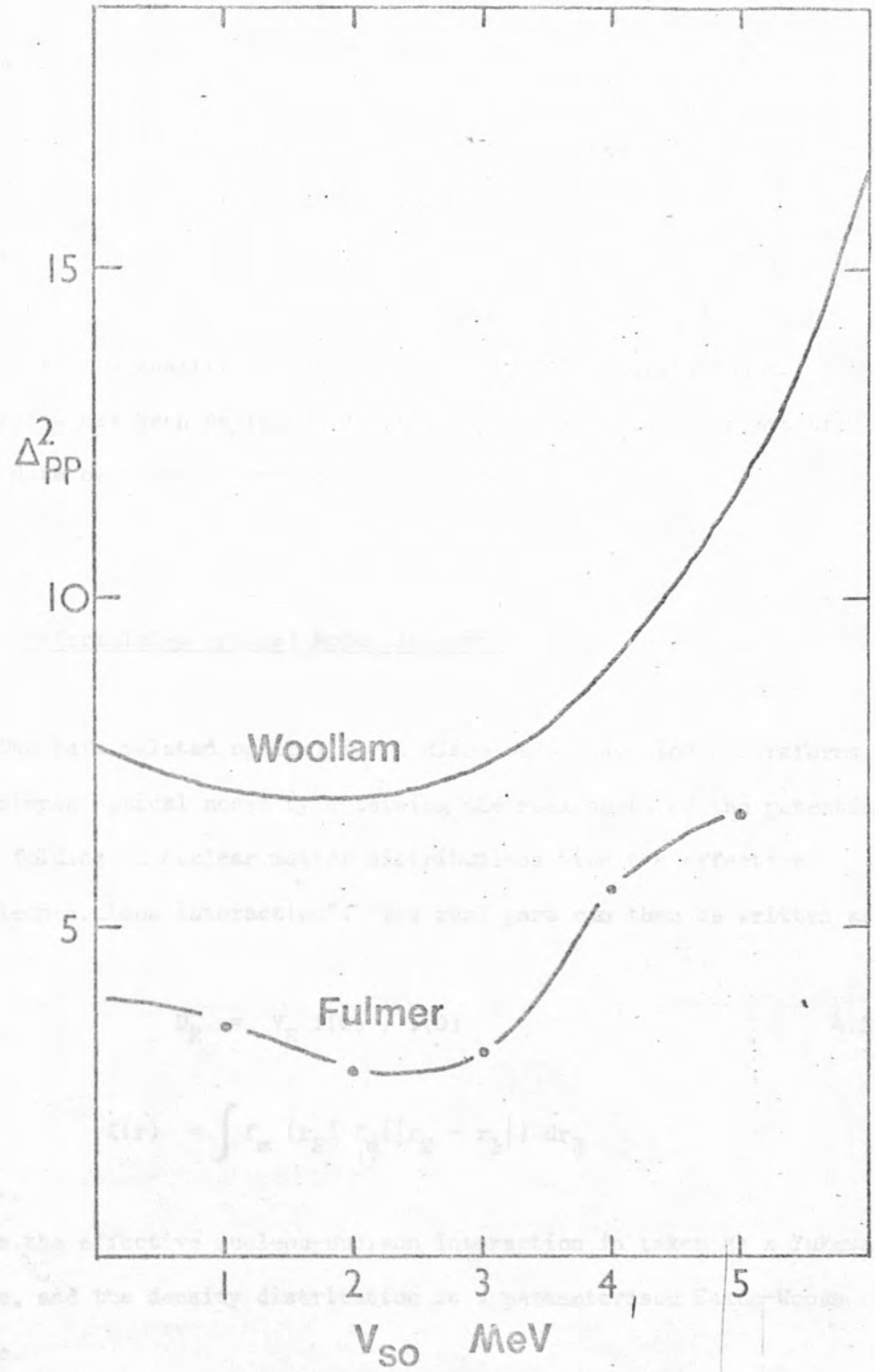

Fig 4.6 Determination of Spin Orbit Potential for $^{144}Sm(^3He,^3He)$

set of parameters:- V_s = 2.07 MeV; r_s = 1.063 fm; a_s = 0.926 fm . These form factors are shown in fig. 4.7.

With the present work, a grid performed over V_s for values up to 3 MeV gave a worse fit than that obtained for $V_s = 0$. The need for good quality ^{3}He polarisation data is evident, and an apparatus has been designed and built by Clarke (Cl 07) to measure this data by a double scattering technique.

4.2 Reformulated Optical Model Analysis

The reformulated optical model discussed in section 2.2 reforms the simple optical model by obtaining the real parts of the potential from folding in nuclear matter distributions with the effective "nucleon-nucleon interaction". The real part can then be written as

$$U_R = V_R \, I(r) / I(0) \qquad 4.2.1$$

with

$$I(r) = \int f_m(r_2) \, f_d(|r_2 - r_1|) \, dr_2$$

where the effective nucleon-nucleon interaction is taken as a Yukawa shape, and the density distribution is a parameterised Saxon-Woods shape.

Assuming that the msr of the internucleon potential and the nuclear matter distribution will not depend on the incident particle, then for ^{3}He scattering from the Samarium isotopes, we have

$$\langle r^2 \rangle_R = \langle r^2 \rangle_m + \langle r^2 \rangle_{t.b.} + \langle r^2 \rangle_{^3He} \qquad 4.2.2$$

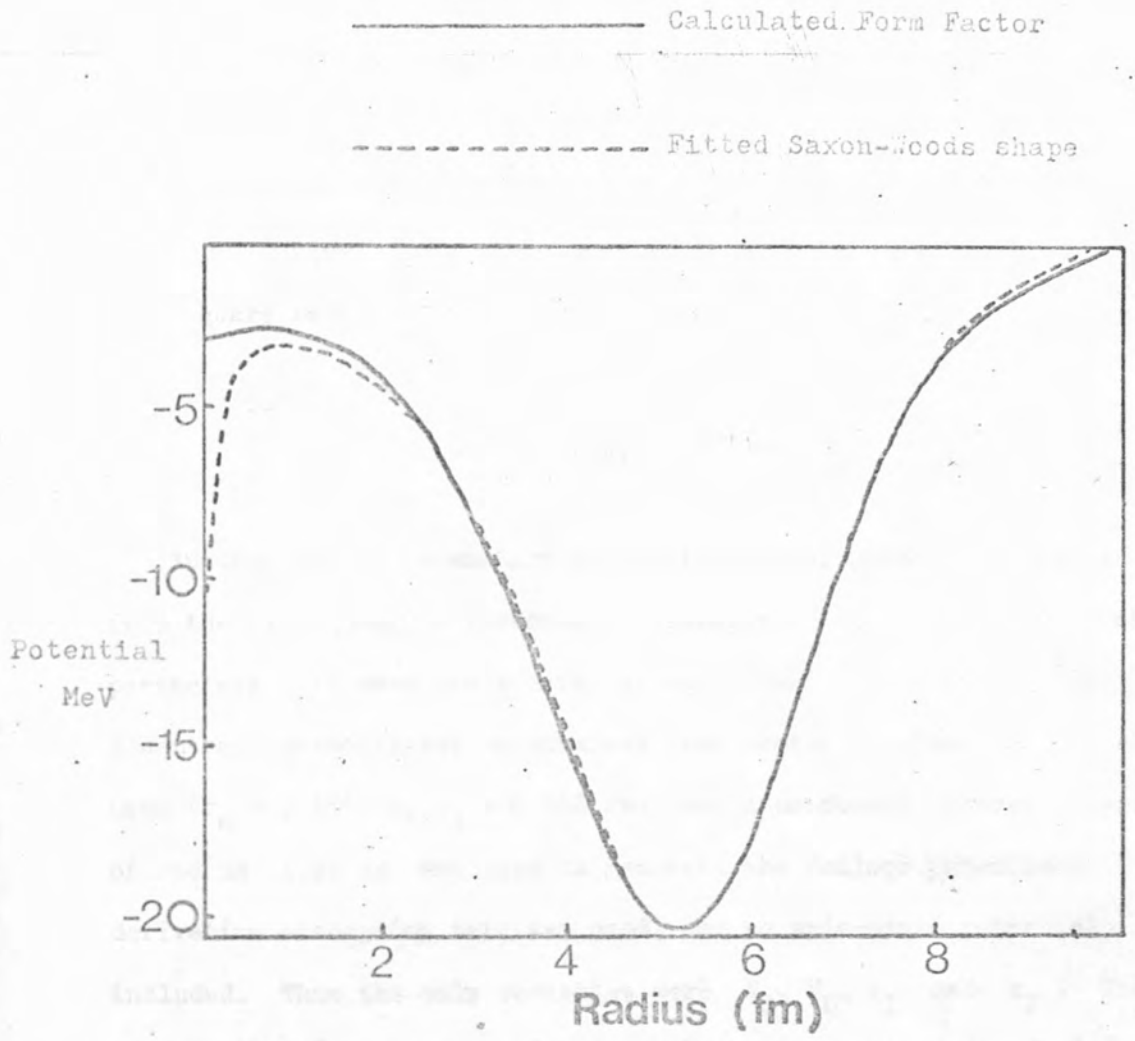

	VS	RS	AS
Proton Spin Orbit (Wo06)	6.21	1.075	0.833
Calculated ^{3}He Spin Orbit	2.07	1.063	0.926

Fig 4.7 The theoretically calculated Spin Orbit Potential

where $\langle r^2 \rangle_{^3He}$ is the msr of the ^3He particle. Under these conditions the msr of the ^3He particle could be determined. However, Woollam (Wo 06) decided there was little or no size dependence in helion scattering. Thus the relationship between the msr of the helion and the msr of the two-body potential cannot be uniquely determined, and hence a new quantity, the mean square radius of the overall two-body interaction, was defined

$$\langle r^2 \rangle_d = \langle r^2 \rangle_{t.b.} + \langle r^2 \rangle_{^3He} \quad . \qquad 4.2.3$$

Nuclear matter parameters were obtained for proton scattering from the even Samarium isotopes. Initially, these matter distribution parameters were used and a grid was made over $\langle r^2 \rangle_d$ for ^{150}Sm. A neutron parameterisation obtained from proton analyses (Wo 06) was used (r_n = 1.186 fm, a_n = 0.768 fm) and a uniformly charged sphere of radius 1.25 fm was used to generate the Coulomb potential. A derivative absorption term was used, and no spin-orbit potential included. Thus the only variables were V_R, W_D, r_I and a_I. The grid over $\langle r^2 \rangle_d$ is shown in fig. 4.8 where no well-defined minimum occurs for $\langle r^2 \rangle_d$.

Subsequently grids were performed over $\langle r^2 \rangle_d$ allowing the neutron parameters to vary, to see if similar results to those of Woollam et al (Wo 06) could be obtained where a well-defined minimum was obtained by allowing variations of the reformulated optical model parameters, including the matter distribution parameters, in a grid over $\langle r^2 \rangle_d$.

The results shown for $^{148,150,152}Sm$ isotopes are shown in figs. 4.9, 4.10, 4.11 where very shallow, undefined minima occur. The fits obtained were very similar to those obtained from the simple

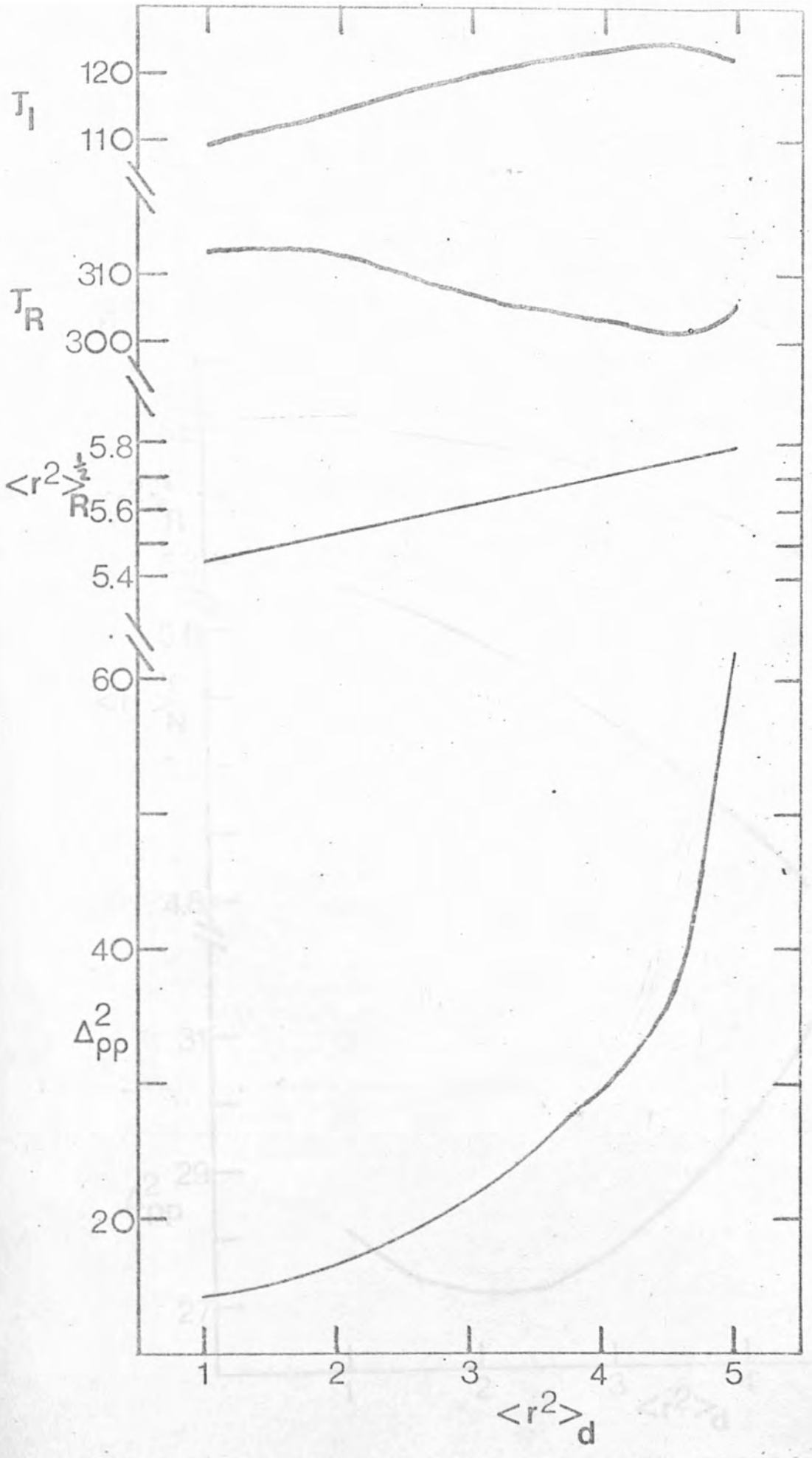

Fig 4.8 Grid over the msr of the two body force for ^{150}Sm with fixed matter distribution.

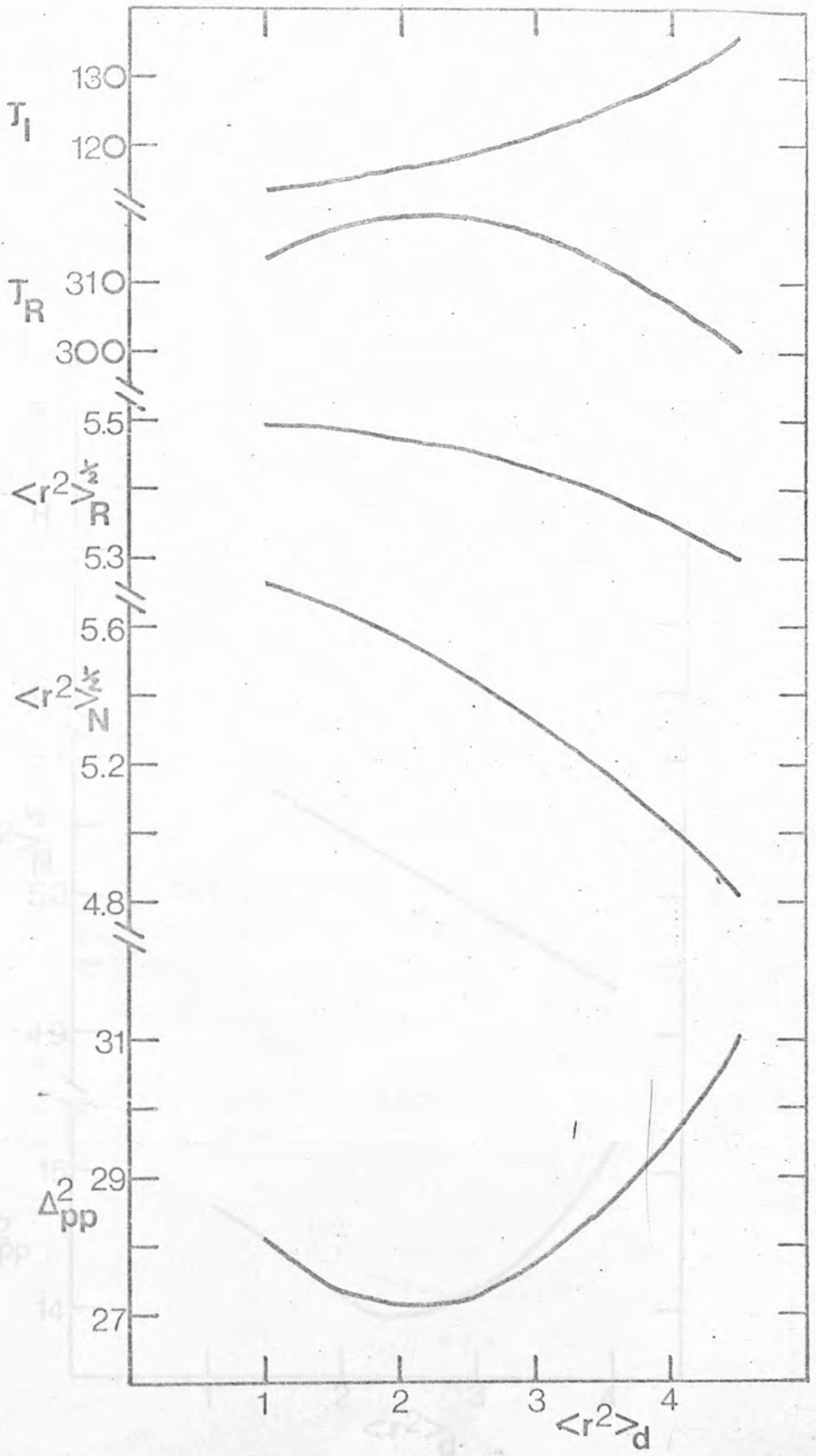

Fig 4.9 Grid over the msr of the two body force for ^{148}Sm allowing the matter distribution to vary

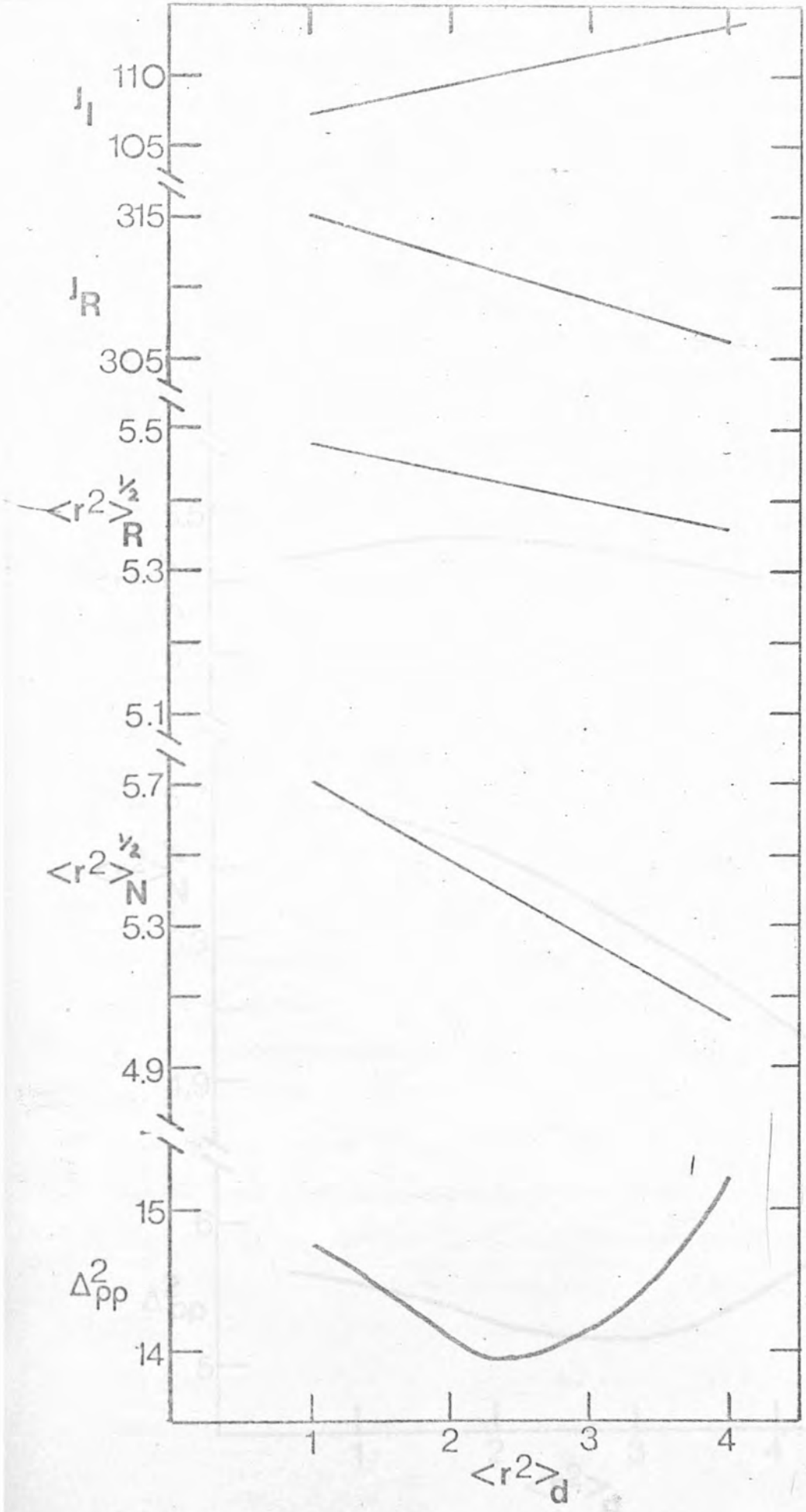

Fig 4.10 Grid over the msr of the two body force for ^{150}Sm allowing the matter distribution to vary

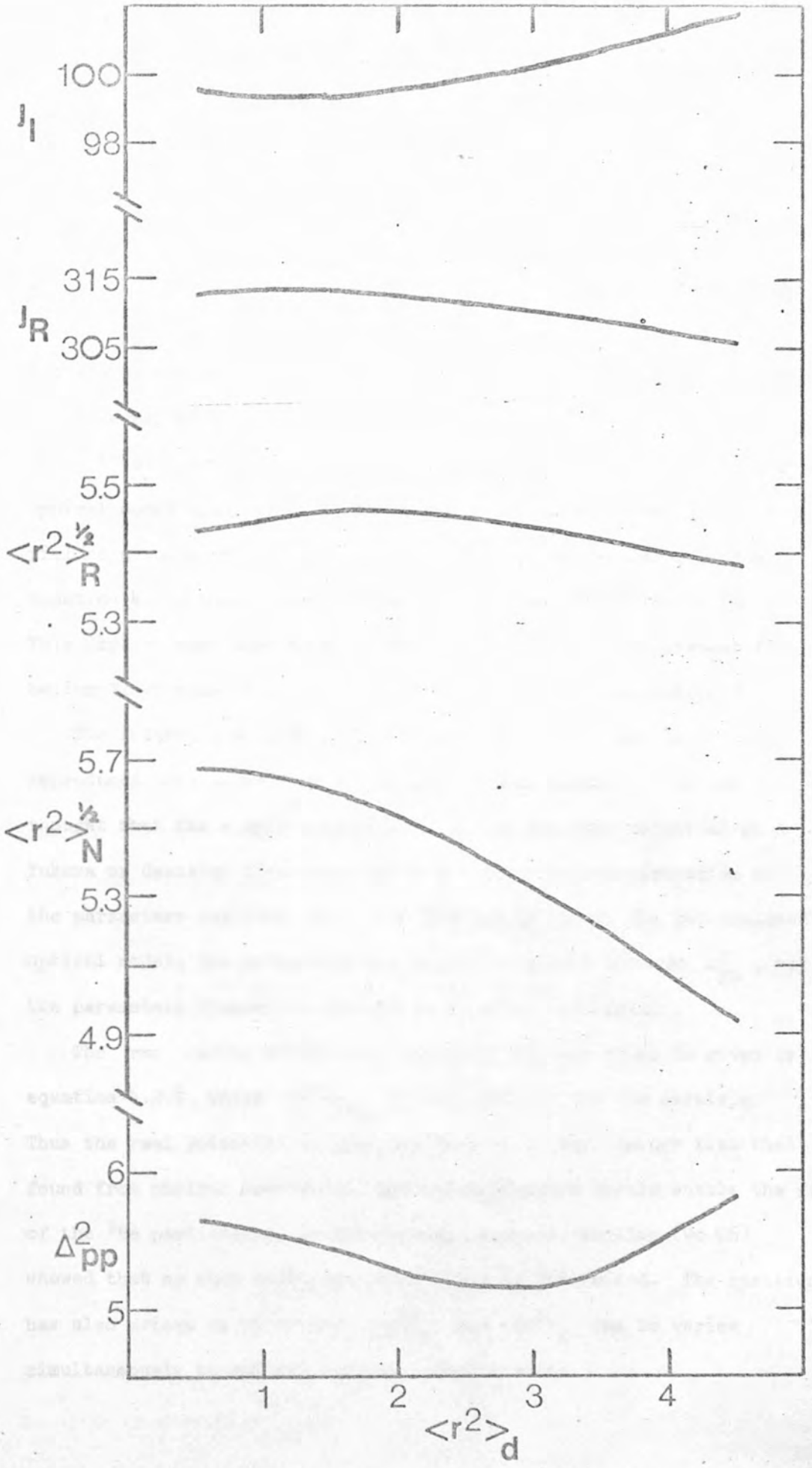

Fig 4.11 Grid over the msr of the two body force for ^{152}Sm allowing the matter distribution to vary

optical model analysis. However, there is some doubt as to the value of such an analysis since the values of $\langle r^2 \rangle_m$ and $\langle r^2 \rangle_d$ may combine to give a value for $\langle r^2 \rangle_R$, which produces a minimum in Δ^2_{pp}, but their values may not be meaningful, and it could be merely fortuitous that their combination gives an $\langle r^2 \rangle_R$ which produces a minimum Δ^2_{pp}.

However, if these minima are accepted then the value for $\langle r^2 \rangle_d$ for ^{148}Sm is $\sim$ 2.2 fm, whereas that obtained from the reformulated optical model analysis of proton elastic scattering from ^{148}Sm yielded a value of $\langle r^2 \rangle_d$ = 2.1 fm. This seems to indicate from equation 4.2.3 that there is little or no size effect for helium-3. This implies that some kind of saturation effect is not present for helium-3, whereas it is necessary for heavy ions, see section 5.2.3.

The reformulated model of Greenlees (Gr 08) has not in general reproduced data as well as the simple optical model. It is now thought that the simple parameterisation of the real potential as a Yukawa or Gaussian force does not yield accurate representation of the parameters involved, i.e. when fitting data with the reformulated optical model, the parameters may adjust to give a minimum Δ^2_{pp}, but the parameters themselves are not necessarily meaningful.

The rms radius of the real potential in this model is given in equation 4.2.2, where $\langle r^2 \rangle_{^3He}$ is the msr of the ^{3}He particle. Thus the real potential is expected to have a msr larger than that found from nucleon scattering, and the difference should enable the size of the ^{3}He particles to be determined. However, Woollam (Wo 06) showed that no such size dependence could be determined. The question has also arisen as to whether $\langle r^2 \rangle_m$ and $\langle r^2 \rangle_d$ can be varied simultaneously to achieve any meaningful results.

4.3 D.W.B.A. Analysis

The Distorted Wave Born Approximation was performed using the computer code DWUCK (Ku 03), which is applied to a distorted nucleus by assuming an axially symmetric non-spherical surface for the optical model given by

$$R(\theta) = R_0 \left[1 + \sum_L \beta_L Y_L^0(\theta) \right].$$

The coupling between the ground state and the excited levels is assumed weak so that an expansion in terms of the distortion parameters β_L becomes, for the first 2^+ level,

$$V(r - R(\theta)) = V(r - R_0) - \beta_2 Y_2^0(\theta) \frac{dV}{dr}$$

where $V(r - R_0)$ is the optical potential for elastic scattering. The inelastic scattering is accounted for by the radial derivative of the elastic scattering optical potential.

The D.W.B.A. analysis was performed using the parameters shown in table 4.1 for the 200, 300 and 400 MeV fm^3 families. The differential cross-sections produced by DWUCK are related to the data by equation 2.5.2.

$$\frac{d\sigma}{d\Omega} = C \sum_L \beta_L^2 \sigma_L(\theta) \quad .$$

Theoretical predictions were normalised to the experimental data to give the values of the deformation parameters. The fits thus obtained are shown in figs. 4.12 and 4.13, and the corresponding quadrupole and octupole deformation parameters are shown in table 4.3. The quality of the fits is very good, except in the extreme forward angle region where

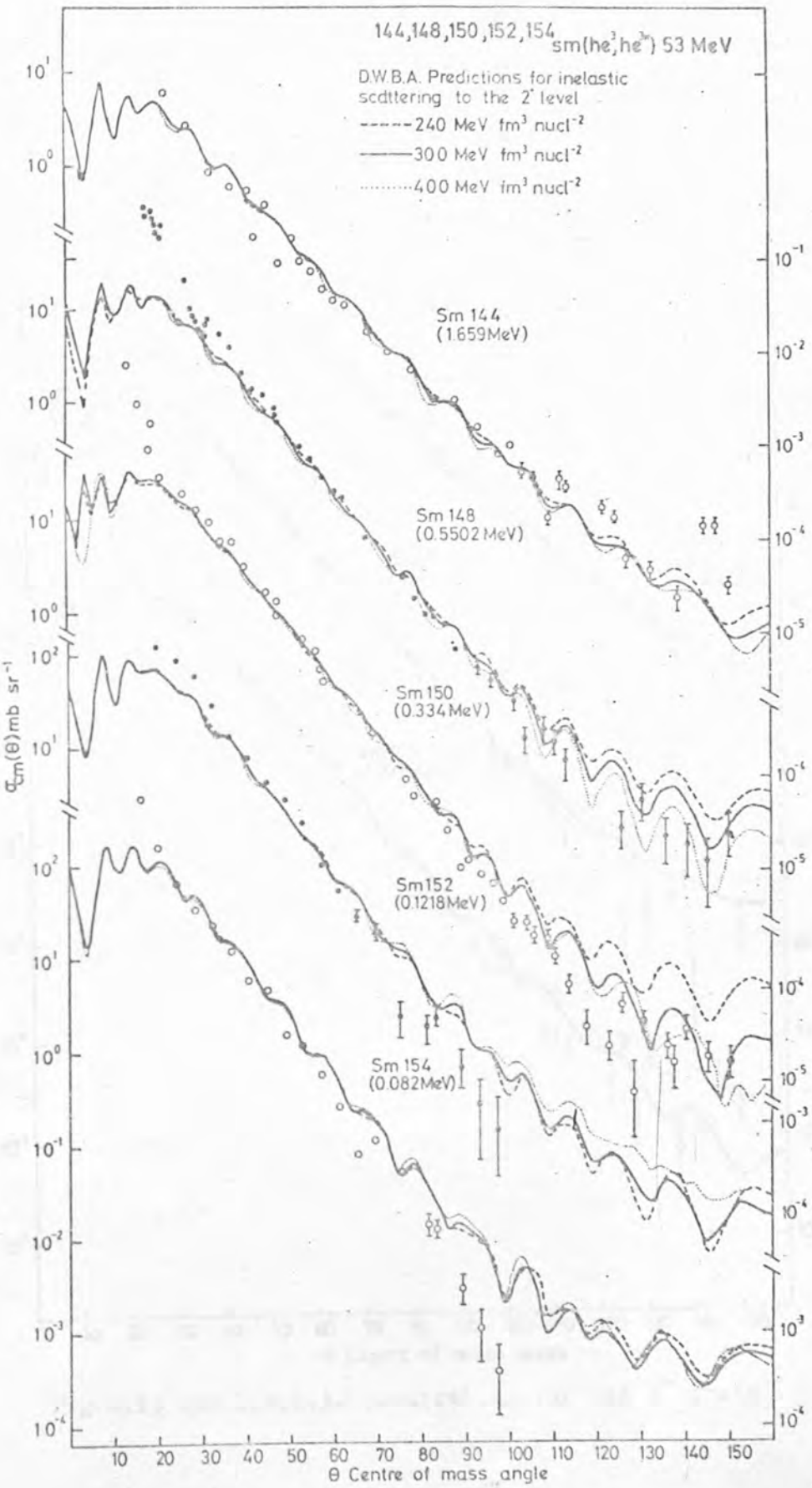

Fig 4.12 The D.W.B.A. predictions for the 2^+ state

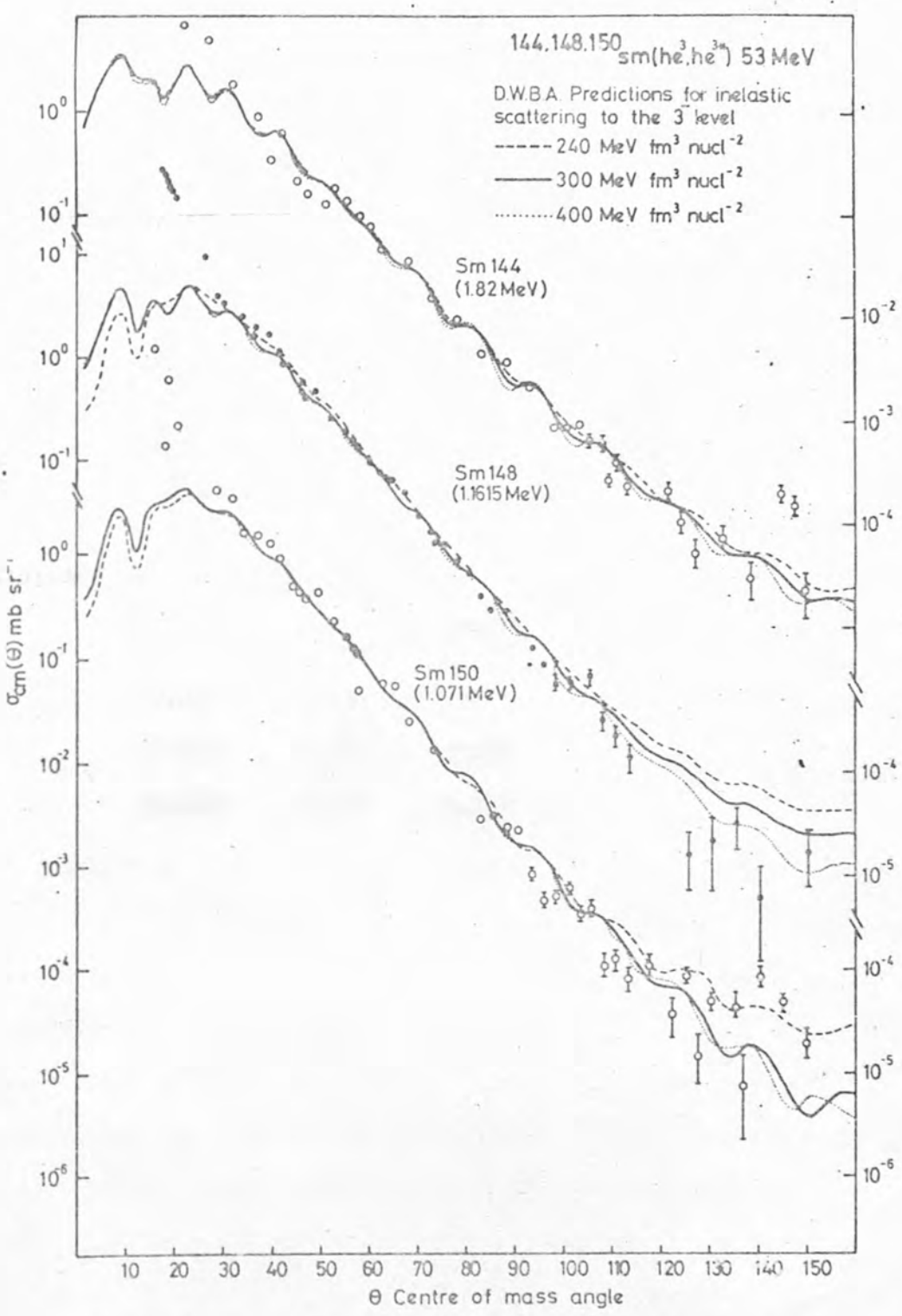

Fig 4.13 The D.W.B.A. predictions for the 3^- state

Table 4.3

The Quadrupole and Octupole Deformation Parameters obtained from D.W.B.A. analysis using three sets of parameters from the Simple Optical Model analysis.

Quadrupole Deformation Parameters

	^{144}Sm	^{148}Sm	^{150}Sm	^{152}Sm	^{154}Sm
A	0.099	0.136	0.169	0.287	0.369
B	0.075	0.128	0.176	0.276	0.367
C	0.095	0.137	0.168	0.277	0.380

Octupole Deformation Parameters

	^{144}Sm	^{148}Sm	^{150}Sm
A	0.115	0.139	0.136
B	0.114	0.155	0.129
C	0.114	0.156	0.136

the theory predicts oscillations but the cross-sections increase. This could be due to a limitation of the programme for very heavy nuclei. The computer code DWUCK allows as many as 100 partial waves to be used. The back angle oscillations are in general not well fitted.

Table 4.4 compares the β_2 values obtained from previous sources to those obtained from the present work. The β_2 values were calculated from B(E2) values using equation 2.3.17, and assuming that

$$\overline{R} = 1.25\, A^{\frac{1}{3}} .$$

The values given in this table compare well with those obtained in the present work.

The octupole deformation parameters obtained from the D.W.B.A. analysis seem to indicate that the 3^- state of the ^{148}Sm nucleus is more deformed than that for the ^{150}Sm nucleus.

One of the major reasons for selecting the Samarium isotopes as a subject of study was an attempt to resolve the question concerning the status, vibrational or rotational, of the ^{150}Sm isotope. Woollam (Wo 10) in his proton elastic scattering analyses found that the data for ^{152}Sm and ^{154}Sm showed a pronounced decrease of large angle elastic scattering cross-section compared to that of ^{144}Sm and ^{148}Sm, and that the data of ^{150}Sm was more like that of the heavier deformed Samarium isotopes than that of the lighter spherical Samarium isotopes. In contrast, the angular distribution of inelastic scattering to the lowest 2^+ level for ^{150}Sm looked more like that of ^{148}Sm than that of ^{152}Sm .

Table 4.4

Comparison of β_2 values for different analyses.

A	144	148	150	152	154
DWBA [a]	0.057	0.108	0.146	0.260	0.323
SCA [a]	0.055	0.107	0.139	0.262	0.294
(α,α') [b]		0.11		0.257	0.279
(p,p') [c]		0.12			0.250
B(E2) [d]		0.132	0.179	0.277	
DWBA [e]	0.073	0.128	0.176	0.276	0.367

a) (Wol0)

b) (He03) (Gl03)

c) (Brl1)

d) (Ch05)

e) Present Work

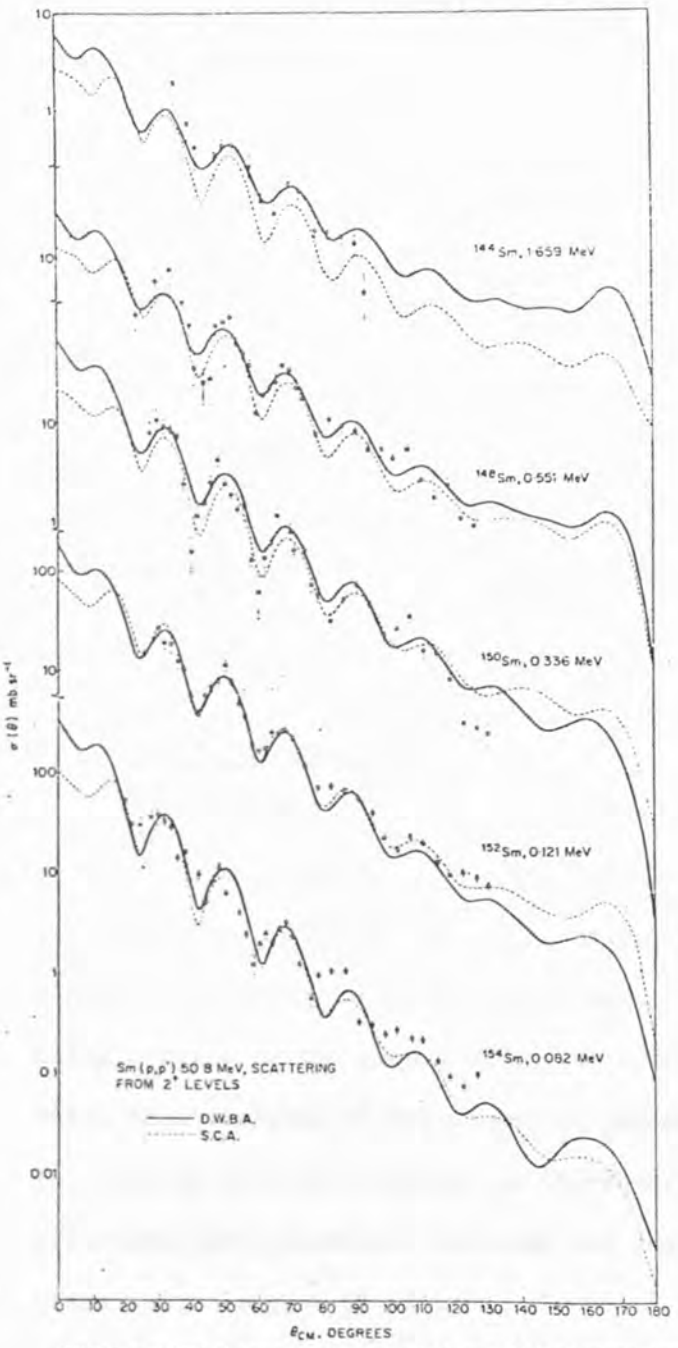

DWBA and SCA fits to scattering from the lowest 2^+ level of each isotope.

PROTON INELASTIC SCATTERING FROM THE SAMARIUM ISOTOPES.

Ref Wo 10

The alpha particle elastic scattering from the Samarium isotopes, however, only show a systematic trend to weaker oscillations and steeper slope of the envelope of maxima with increasing A number.

The data for the 2^+ levels in the present work shows that the Samarium 150 data exhibits a similar property to the rotational nuclei in its tendency to decrease strongly in cross-section at backward angles, whilst the vibrational isotopes data oscillates about a less steep

gradient. It is difficult to compare the elastic scattering data of the Samarium 150 to that of the rotational isotopes because of their lack of angular range, but nevertheless, the size of oscillations of the Samarium 150 data is more in the style of the vibrational nuclei than that of the rotational. This disagrees with the conclusions of Woollam et al. for proton scattering, but the evidence for ^{150}Sm behaving in the same style as the vibrational Samarium isotopes is shown in its energy level structure.

4.4 The S.C.A. Analysis

The strong coupling approximation analyses were performed using the search code JUPITOR (Ta 02). Optical model parameters, for the elastic scattering and deformation parameters for each of the states being coupled to the ground state, were fed into this programme which then searched on any number of parameters. The convergence of this search to a good minimum in chi-squared was very fast, generally after only one iteration, although the computing time for this was often quite long, $\sim$ 30 minutes. However, the search routine was particularly sensitive to the starting values of the parameters. Due to the large amount of computing time involved some approximations had to be made. The method for fitting the data for the strong coupling approximation was therefore as follows.

Two sets of starting parameters were taken. Firstly, the optical model parameters which fitted the elastic scattering for each respective Samarium isotope, and secondly, the parameters obtained by Woollam (Wo 09) for the S.C.A. analysis of ^{144}Sm (^{3}He,^{3}He) ^{144}Sm. The quadrupole deformation parameter from the DWBA analysis was assumed,

and in the first instance the 2^+ level for each isotope was coupled to the ground state and the real and imaginary depths were searched upon. The 3^- level, as well as the 2^+ level, was then coupled to the ground state and, using the potential depths obtained from the previous search, the octupole deformation parameter, β_3, was varied until a good fit to the data was obtained.

The fits obtained from the method are shown in figs. 4.14, 4.15 and 4.16. No 3^- data was available for the ^{152}Sm and ^{154}Sm isotopes. The parameters which produced these fits are shown in table 4.5.

Before discussing the general trends of the parameters throughout the isotopic range, the immediately noticeable peculiar effect is the ability to fit the ^{144}Sm data with almost the optical model parameters. This is a direct contradiction of the work of Woollam, who found that the real and imaginary potentials were smaller and the real diffuseness parameter was much larger than those obtained from the simple optical model analyses. However, the other Samarium isotope's data were fitted using the S.C.A. geometries found by Woollam.

The general trend of the real potential depth is to decrease with increasing target mass, whilst the imaginary depth remains at more or less a constant value, apart from the value of the surface absorption term for ^{154}Sm.

It is expected that the absorption due to the coupling of the levels in the S.C.A. will be taken into account explicitly, and that the only absorption term will be that which is required to account for coupling to all the other levels which have not been considered. Comparison of the absorption depths in table 4.5 to those in table 4.1

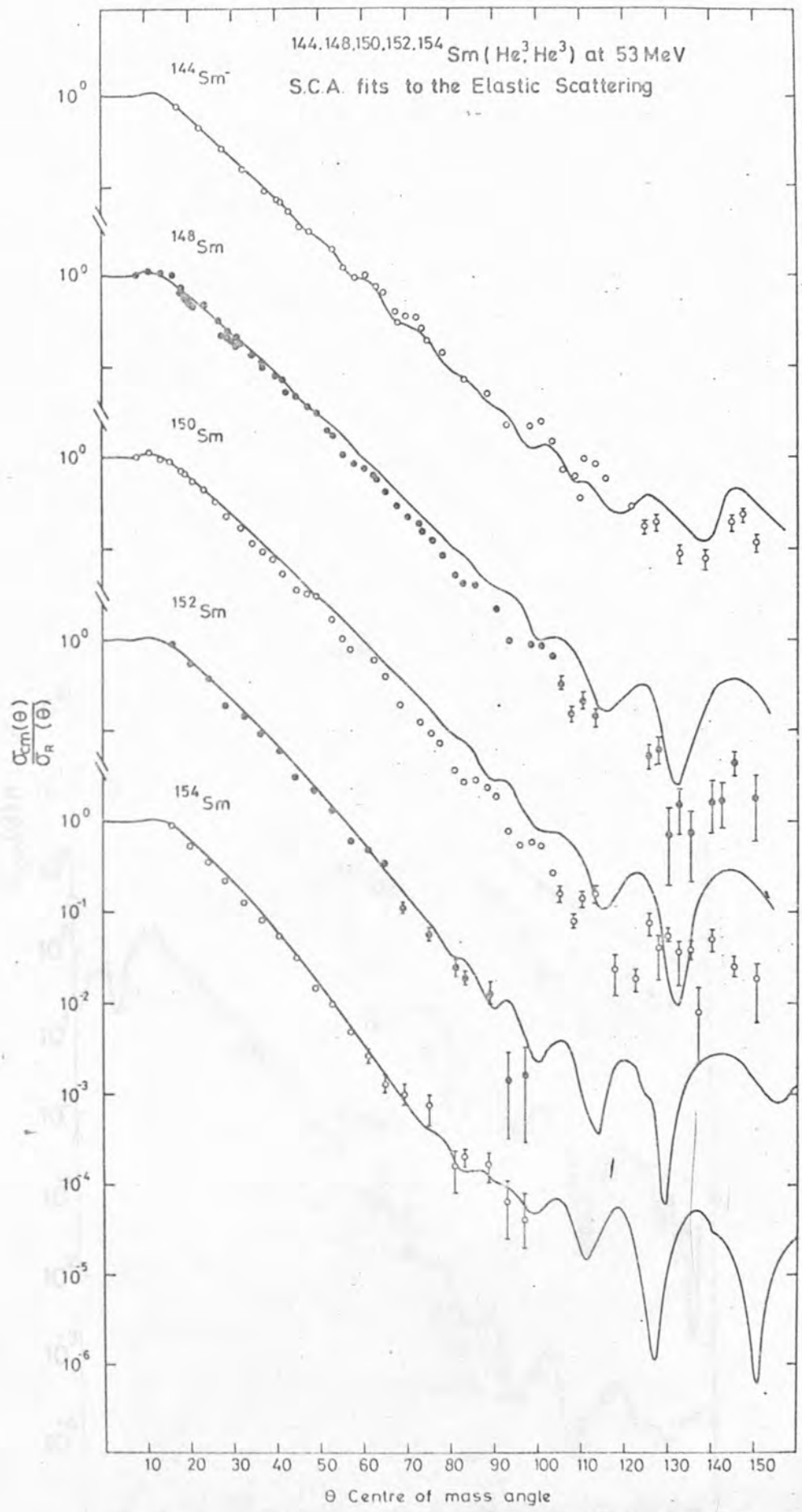

Fig 4.14 The S.C.A. analysis of the elastic scattering data.

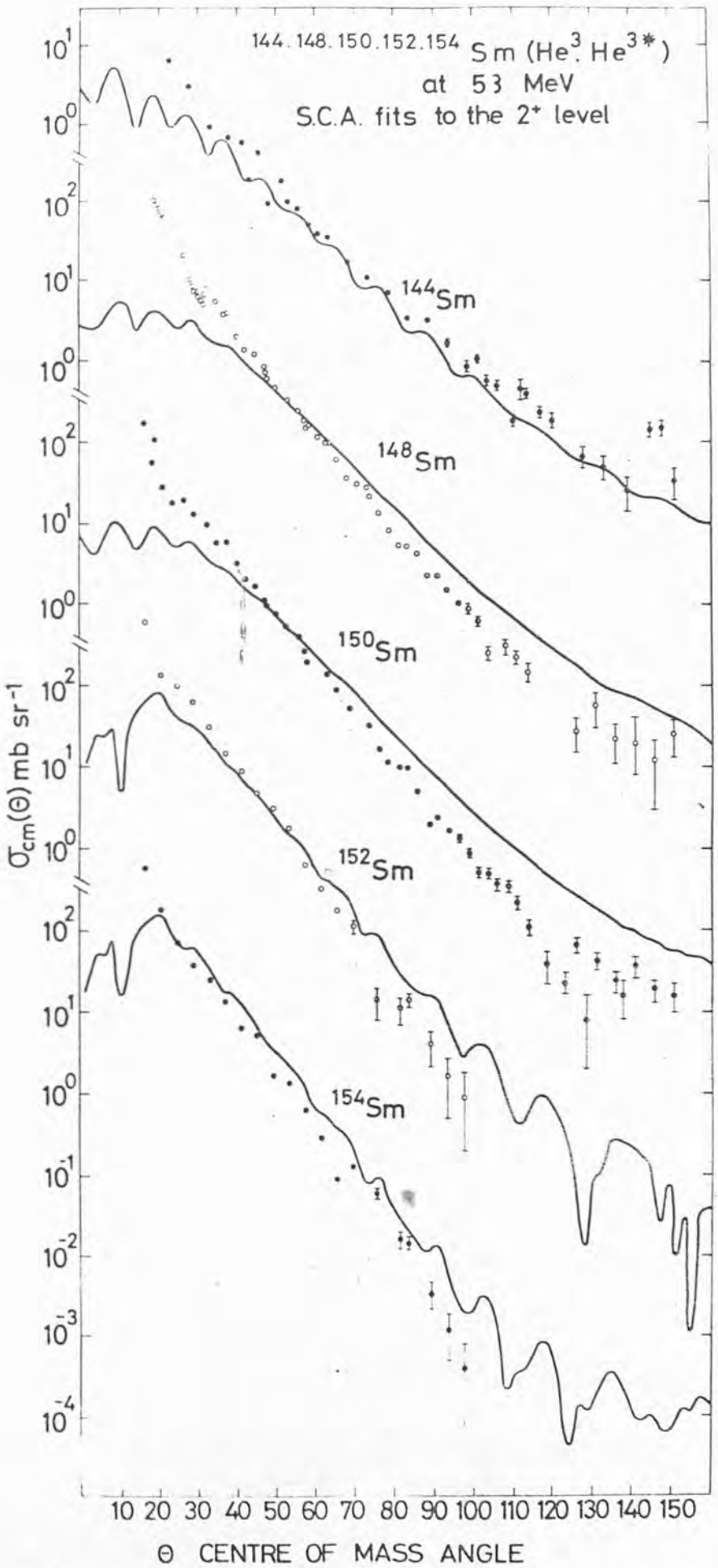

Fig 4.15 SCA analysis of inelastic scattering data for the 2^+ state

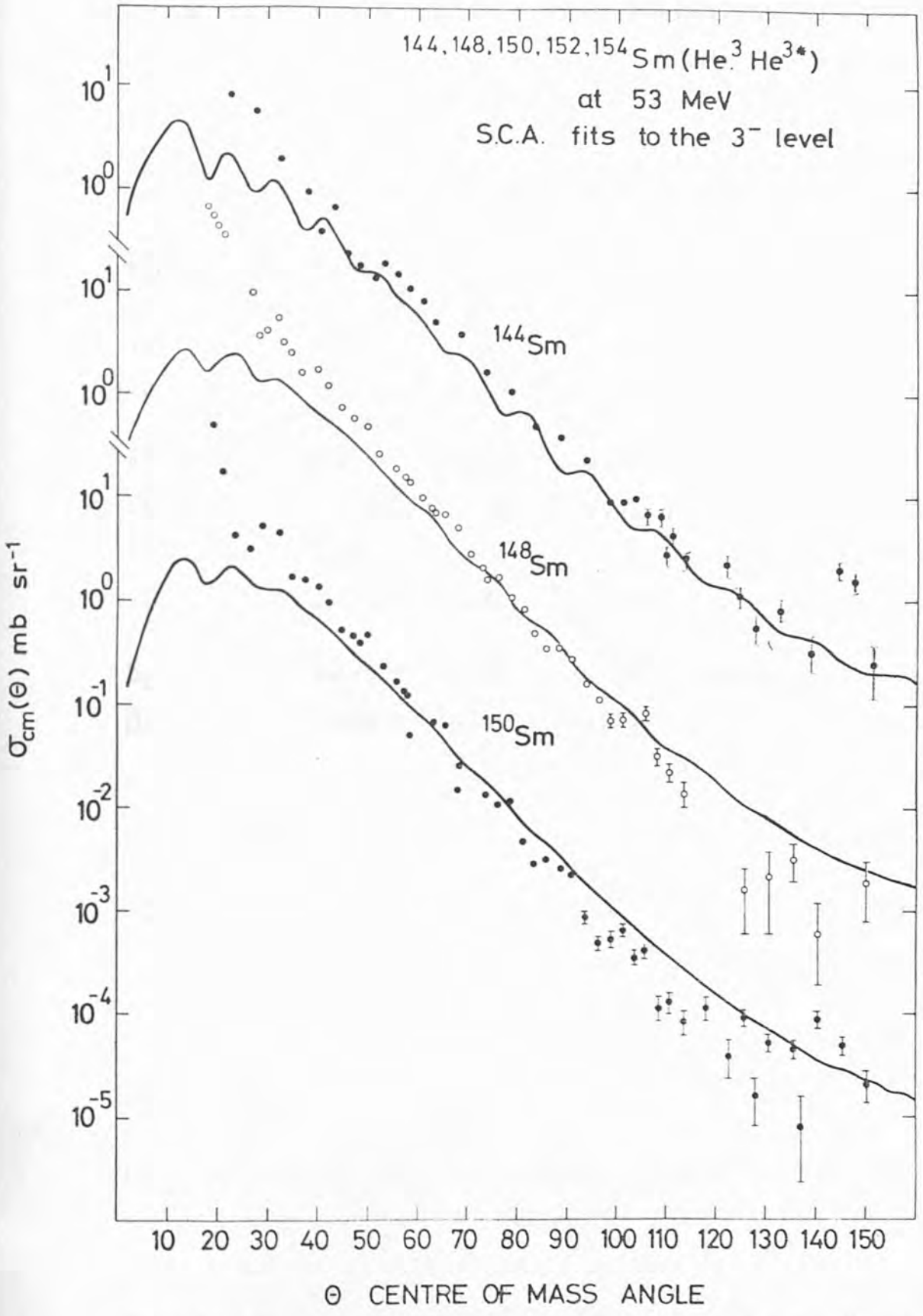

Fig 4.16 SCA analysis of inelastic scattering data for the 3^- state

Table 4.5

Parameters obtained from S.C.A. analyses.

A	144	148	150	152	154
Coupling Scheme	$0^+-2^+-3^-$	$0^+-2^+-3^-$	$0^+-2^+-3^-$	0^+-2^+	0^+-2^+
VR	141.1	126.12	121.29	113.9	85.6
WD	27.67	25.97	27.57	27.75	18.11
AR	0.802	0.682	0.682	0.682	0.682
AI	0.832	1.006	1.006	1.006	1.006
RR	1.13	1.136	1.136	1.136	1.136
RI	1.185	1.080	1.080	1.080	1.080
β_2	0.073	0.128	0.176	0.276	0.367
β_3	0.089	0.108	0.105		

for the 300 MeV potential family show that the numerical values of WD increase for the isotopes ^{150}Sm and ^{152}Sm.

Glendenning et al (Gl 03) in their S.C.A. treatment of alpha particle scattering from Samarium isotopes, found that a single potential gave rise to good fits to the elastic scattering data of all the isotopes as long as the strongly collective states were treated explicitly. They claim that the expression for the optical potential can be split into two parts, consisting of the sum over non-collective states and the sum over the low-lying collective states which couple strongly to the ground state. Having thus taken these states explicitly into account they reason that the optical potential for the non-collective states should be constant over a wide mass range. Woollam (Wo 10) in his S.C.A. analysis of proton scattering from Samarium isotopes found that the parameters which best fitted the elastic scattering varied very slightly, and there were no general trends of increasing or decreasing depths through the isotope range. One of the features of both these analyses was that the S.C.A. analysis of the rotational nuclei considered both the 2^+ and 4^+ states, and in the case of Glendenning et al. the 6^+ state, as strongly collective states, whereas in the present analysis only data for the 2^+ state was available.

The present analysis, therefore, actually agrees with the work of Glendenning et al (Gl 03) who found that the single optical potential which fitted the elastic scattering from the Samarium isotopes when the coupled channels were included, was very similar to the optical potential which just described the elastic scattering from a vibrational nucleus. However, the real potential depth for rotational isotopes which did not take into account the coupled channels was half that of this single potential, although the imaginary depth was almost the same as that of the single potential.

Therefore it seems that failure to include all the strongly coupled channels in the rotational isotopes' S.C.A. analysis yields smaller real potential depths.

From table 4.5 the β_3 value for the ^{148}Sm isotope is similar to that for the ^{150}Sm isotope. The D.W.B.A. predictions gave greater octupole deformation parameters for ^{148}Sm than for ^{150}Sm. The fits to the 3^- data obtained from the S.C.A. analysis show that the size of the oscillations decrease with increasing target mass. The shapes of the angular distributions of the ^{148}Sm and ^{150}Sm data and theoretical fits are extremely similar, which seems to confirm the conclusion of section 4.3, where the ^{150}Sm isotope was concluded to behave more like a vibrational isotope than a rotational isotope.

CHAPTER 5

The Microscopic Optical Model

Introduction

This chapter presents the results of the analyses of helium-3 scattering from Samarium isotopes in terms of the three parameter ^{3}He-nucleus optical model developed by Sinha, Duggan and Griffiths (Si 15), and the nucleus-nucleus model developed by Sinha (Si 13) (Si 16).

The real and imaginary form factors were produced from both models and used to fit the data. No spin-orbit forces were used. The ^{3}He-nucleus three-parameter model produced poor fits to the data, and the reason for this is discussed in terms of the effective interaction used and the method for reformulating the nucleon microscopic optical potential to a composite particle microscopic optical potential. The validity of the estimation of the second-order real term is also discussed.

The nucleus-nucleus model is much more successful in fitting the data and shows clearly the need for saturation effects when considering the scattering of composite particles. This model, which does not estimate any second-order real term, also displays the problems associated with the discrete ambiguities found in the simple optical model analysis.

5.1 The ^{3}He - 3-parameter Model

This model, whose theory is developed in section 2.2, folds a Kuo-Brown effective interaction (Ku 04) with the target nuclear density to produce first and second order real terms and an imaginary potential, using the frivolous model approach for a proton potential. The Kuo-Brown interaction has been used to fit proton scattering data (Si 10). The test of the Samaddar et al. (Sa 01) calculation of the optical potential of a composite projectile as a function of the optical potentials of its constituent nucleons has not yet been performed adequately.

The proton and neutron density distributions were calculated from the parameters obtained from reformulated optical model analyses (Gr 08) of proton scattering from the Samarium isotopes (Wo 06), where these densities have a Saxon-Woods shape and are normalised to the central density ρ_0 using the expressions

$$Z,N = \int \rho_{p,n}(r)\, d^3r$$

and

$$\frac{J_R}{V_R} = \frac{Z}{\rho_0}$$

hence

$$\rho_{0\ p,n} = \frac{Z,N}{(\frac{4\pi R^3}{3})(1 + \frac{\pi^2 a^2}{R^2})} \quad \text{nucleons fm}^{-3} .$$

Densities obtained from shell model calculations (Ho 07) were also used in the calculations for Samarium 144 , although these did not prove to be a crucial factor in the analysis.

The ^{3}He - 3-parameter model calculates the direct interaction due to the Kuo-Brown force for protons and neutrons, and adds the

exchange term due to antisymmetrisation of the nucleons in the nucleus. The real and imaginary form factors for a helium-3 nucleus are then produced. The potentials obtained for the "two proton" part of the helium-3 projectile are shown in fig. 5.1. The ^{3}He-nucleus model uses a Blin-Stoyle prescription (Bl 10) to calculate the spin-orbit form factor. However, since the phenomenological analysis of the helium-3 scattering from the Samarium isotopes showed little evidence for the need of a spin orbit force, no spin orbit force was included in these analyses.

The microscopic real and imaginary form factors generated by the ^{3}He - 3-parameter model are shown in figs. 5.2 and 5.3. It is seen that the imaginary depth increases with increasing A number, and that the real depth does likewise apart from ^{154}Sm . An interesting feature of the shape of the imaginary potentials is that they show a volume absorption shape, as opposed to the surface shape obtained from the phenomenological optical model analysis.

A comparison of the potentials generated from the microscopic optical model for ^{144}Sm using both the densities obtained from the reformulated optical model analysis of the proton data, and those obtained from shell model calculations, and the potentials obtained from a simple phenomenological optical model analysis are shown in figs. 5.4 and 5.5. The volume integrals per particle pair, integrated numerically, and the mean square radii of the real potential calculated from the form factors are presented in table 5.1. The volume integral for the real part shows no change with increasing A number, although the volume integrals of the imaginary part as well as the mean square radii of real and imaginary terms increase slightly with increasing A number. A particularly interesting feature of fig. 5.4 is the fact that all the

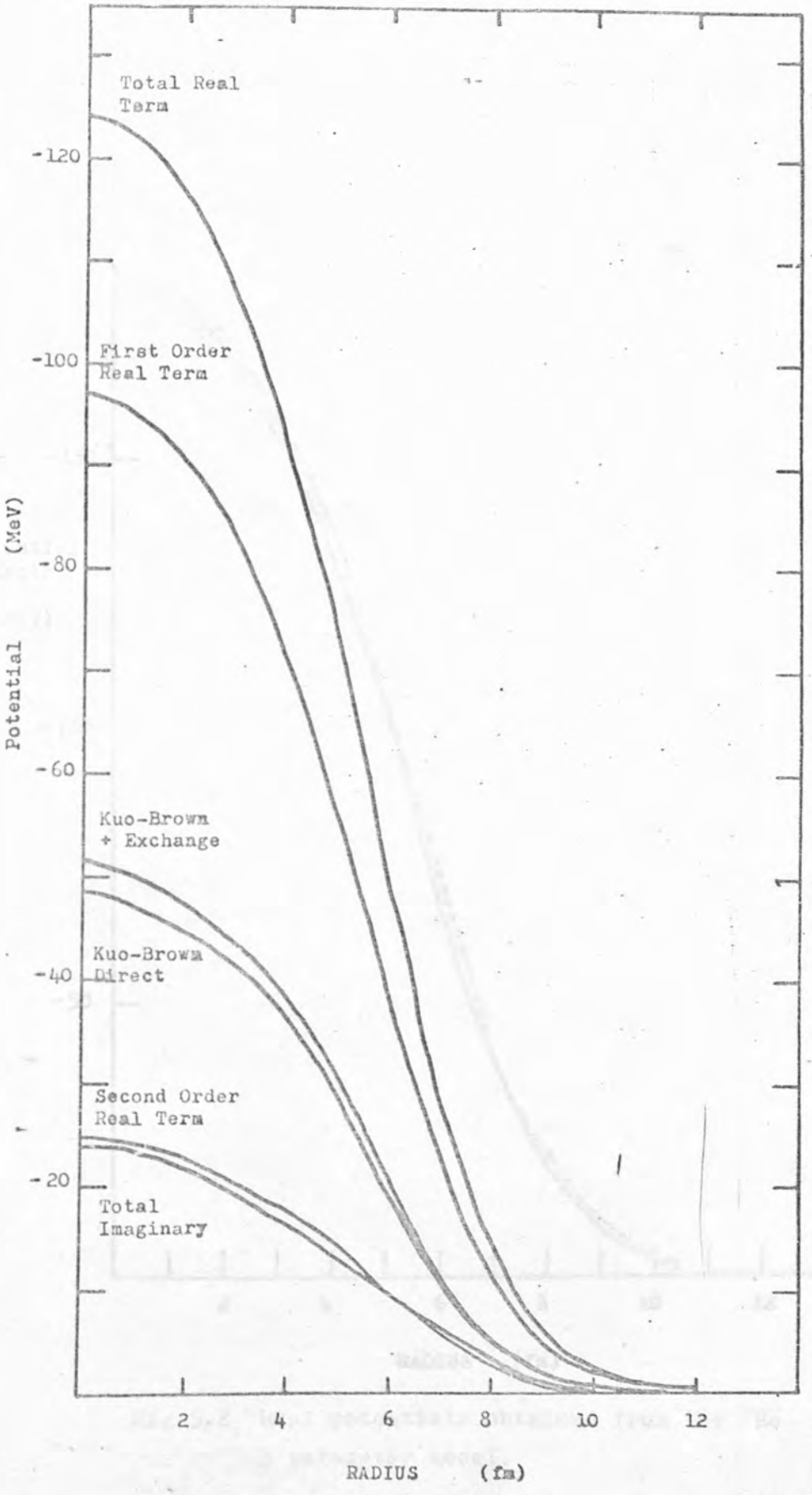

Fig 5.1 The 'two proton' contribution to the nuclear potential form-factor of the ^{3}He 3 parameter model.

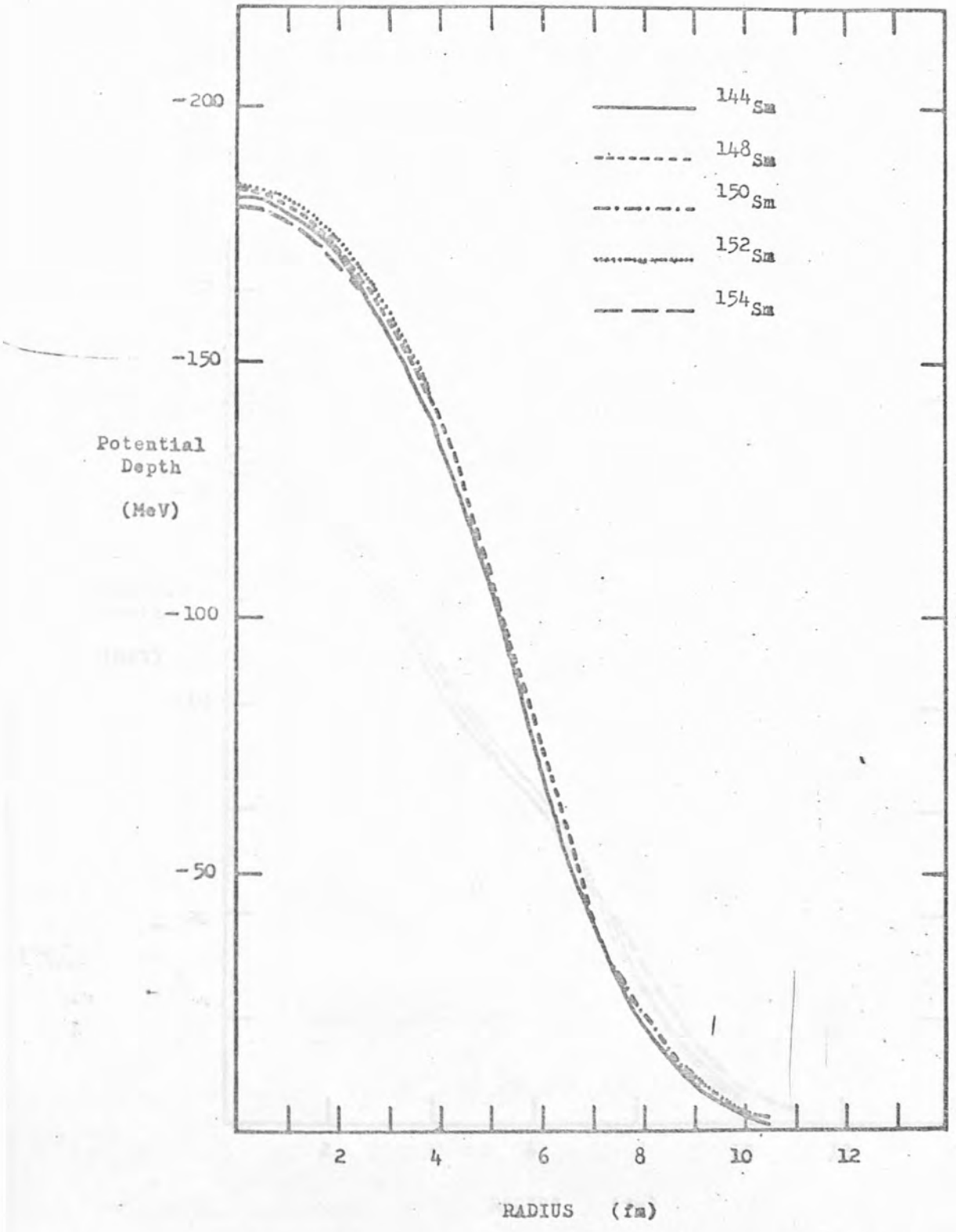

Fig 5.2 Real potentials obtained from the ^{3}He 3 parameter model.

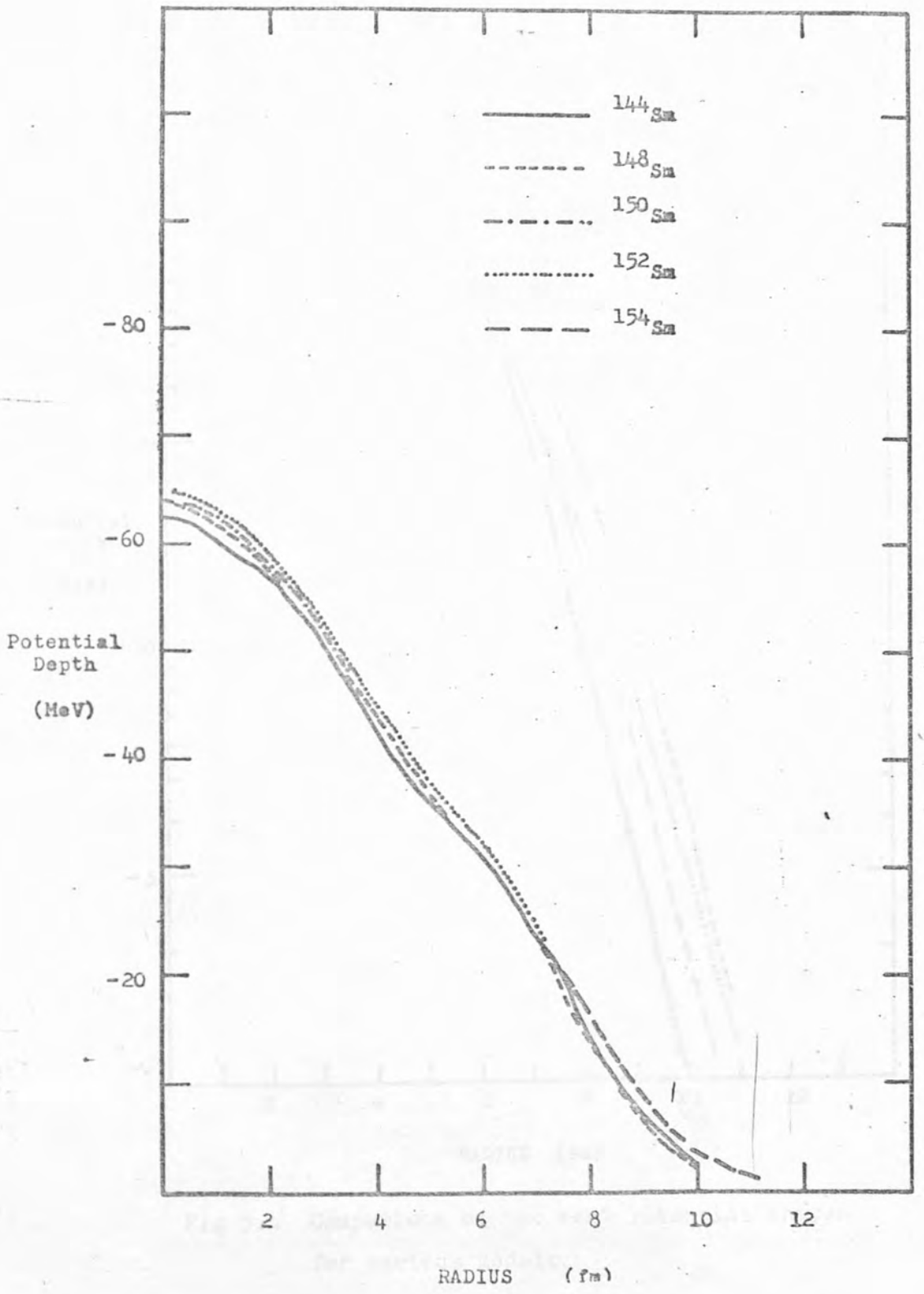

Fig 5.3 Imaginary potentials obtained from the ^{3}He 3 parameter model

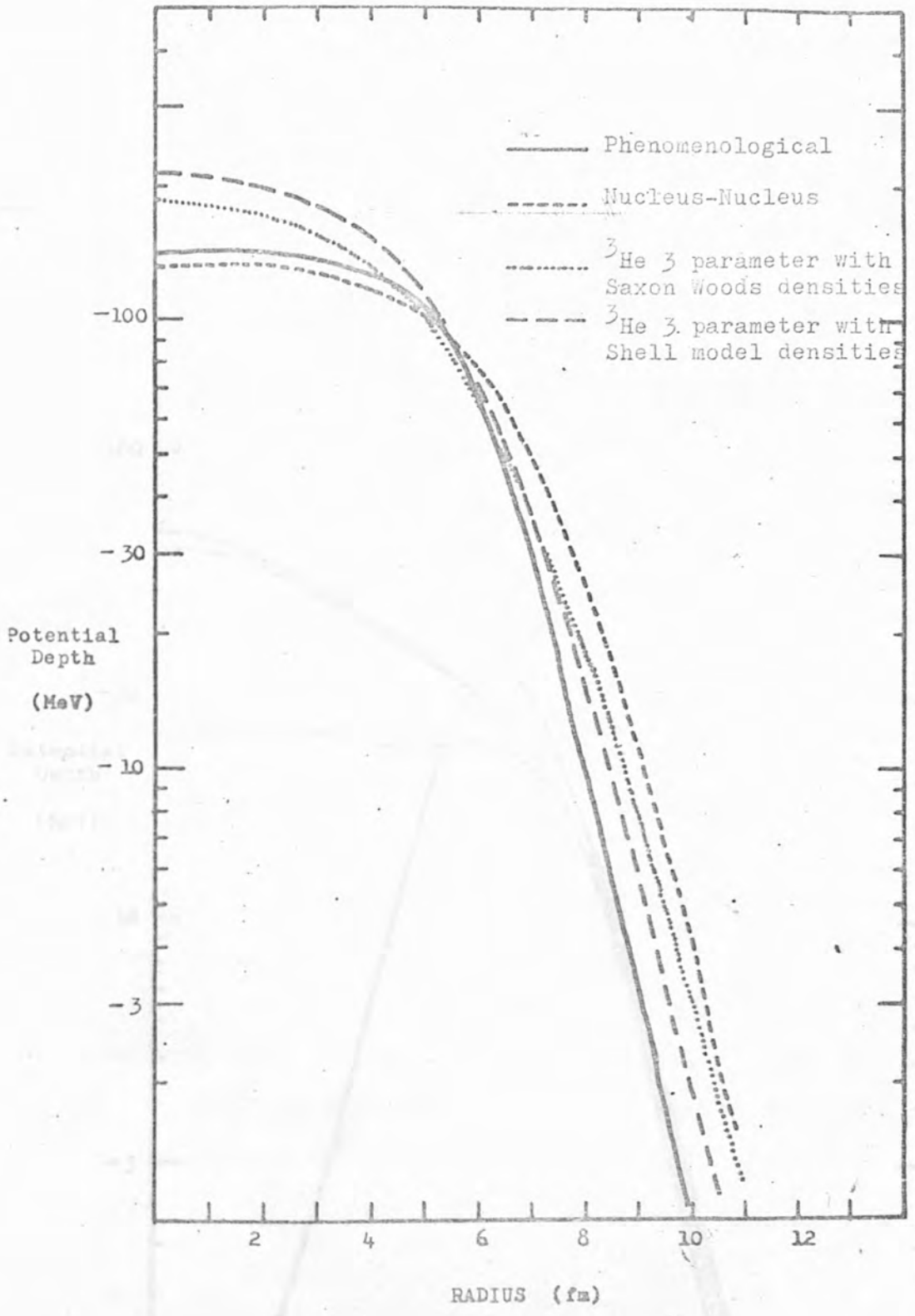

Fig 5.4 Comparison of the real potential shapes for various models.

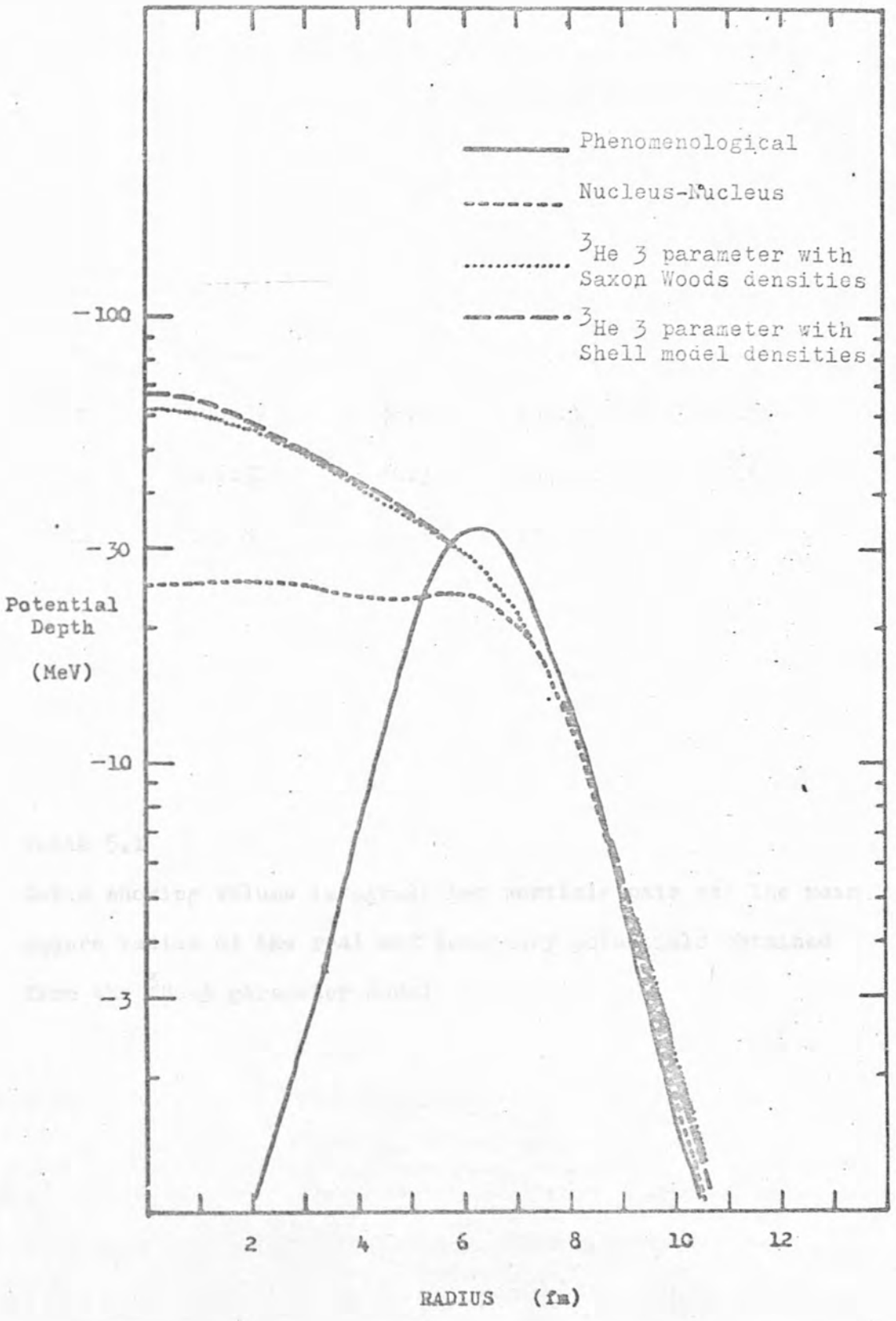

Fig 5.5 Comparison of the imaginary potential shapes for various models.

	REAL		IMAGINARY	
	J_R/A_iA_t	$\langle r^2\rangle_R$	J_I/A_iA_t	$\langle r^2\rangle_I$
^{144}Sm	406.0	35.4	179.9	42.8
^{148}Sm	406.31	35.35	180.1	42.6
^{150}Sm	406.27	36.3	182.5	43.5
^{152}Sm	406.32	36.3	184.26	43.6
^{154}Sm	405.8	37.5	189.0	44.8

Table 5.1

Table showing volume integrals per particle pair and the mean square radius of the real and imaginary potentials obtained from the ^{3}He-3 parameter model

form factors cross over at a nuclear radius of 5.8 fm . Phenomenologically the radius of the ^{144}Sm isotope was $R = r A^{1/3} = 5.8$ fm . It is well-known that potentials that produce similar scattering cross-sections for strongly absorbed particles have to be similar near the strong absorption radius. The potentials shown in figs. 5.4 and 5.5 are plotted on logarithmic scales to emphasise their differences.

The real and imaginary potentials obtained from the ^{3}He - 3-parameter model were read into an amended version of RAROMP which read external form factors instead of generating its own Saxon-Woods form factors. The depths of the real and imaginary potentials were allowed to vary, and fits to the data were obtained as shown in fig. 5.6, where the data is clearly fitted to 90^{o} but peculiar effects occur at backward angles. To some extent, a poor fit at backward angles is expected since the model assumes a frivolous model approach, i.e. the absorption arises entirely from the forward angle scattering amplitude. However, it was shown by substituting a conventional imaginary potential that the backward angle problem was not caused by the assumptions of the frivolous model, but by some inherent feature of the real potential shape. The interesting feature about these fits is that the real depth decreased to about 50 MeV , with a real volume integral per particle pair of 110 MeV fm^3 . Fig. 4.3 shows that there is a deep chi-squared minimum corresponding to a real central depth of 50 MeV . This serious ambiguity problem could not be resolved by any adjustment of the depth parameters.

In order to investigate the effects of the microscopic form-factor shape, a Saxon-Woods form factor was produced whose shape was almost identical to the microscopic form factor. This was achieved by plotting $\log_e(\frac{V_0}{f(r)} - 1)$ against r in fig. 5.7, where $f(r)$ is the microscopic form factor and V_0 the central depth of that form factor. For a

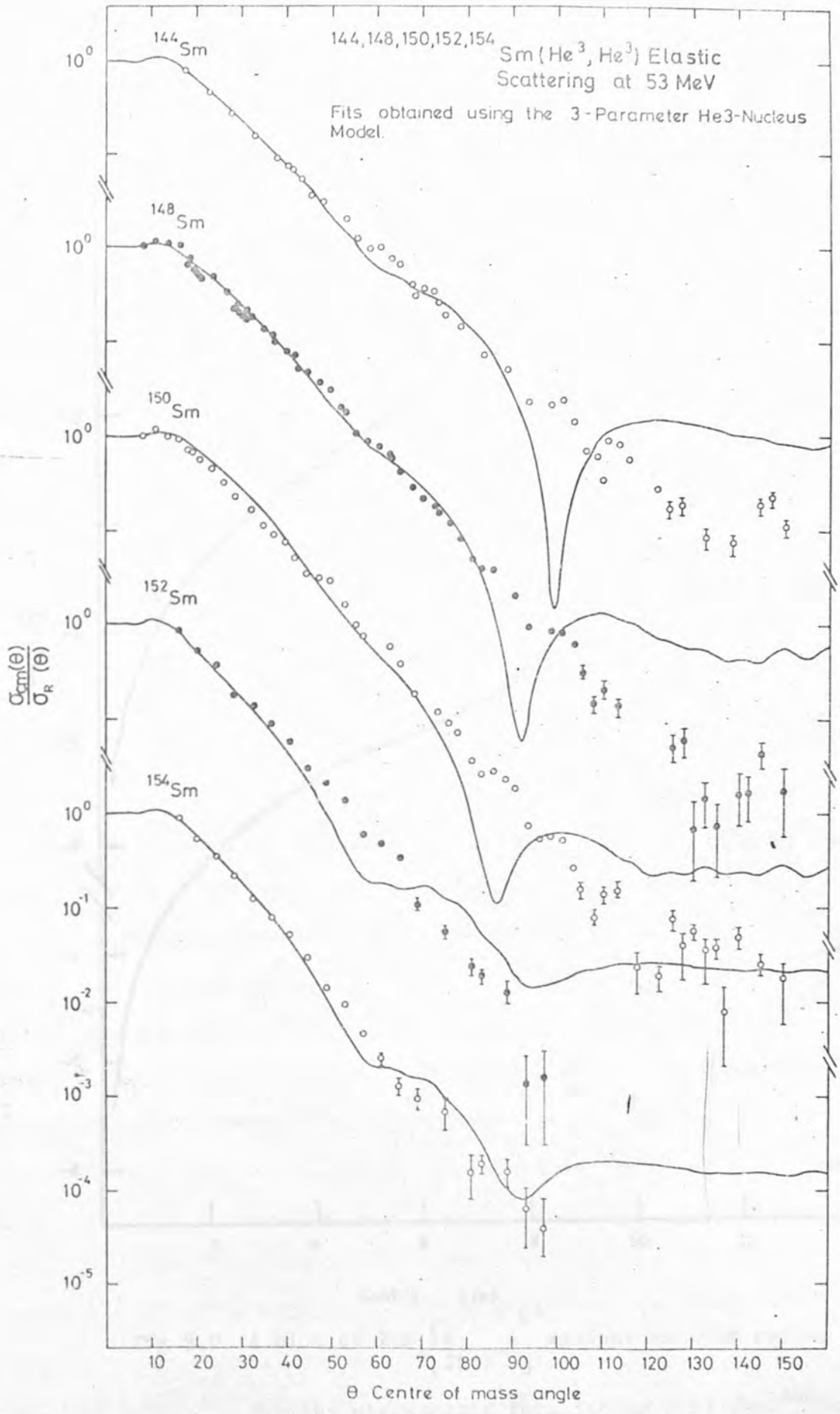

Fig 5.6 Fits obtained using the ^{3}He 3 parameter model

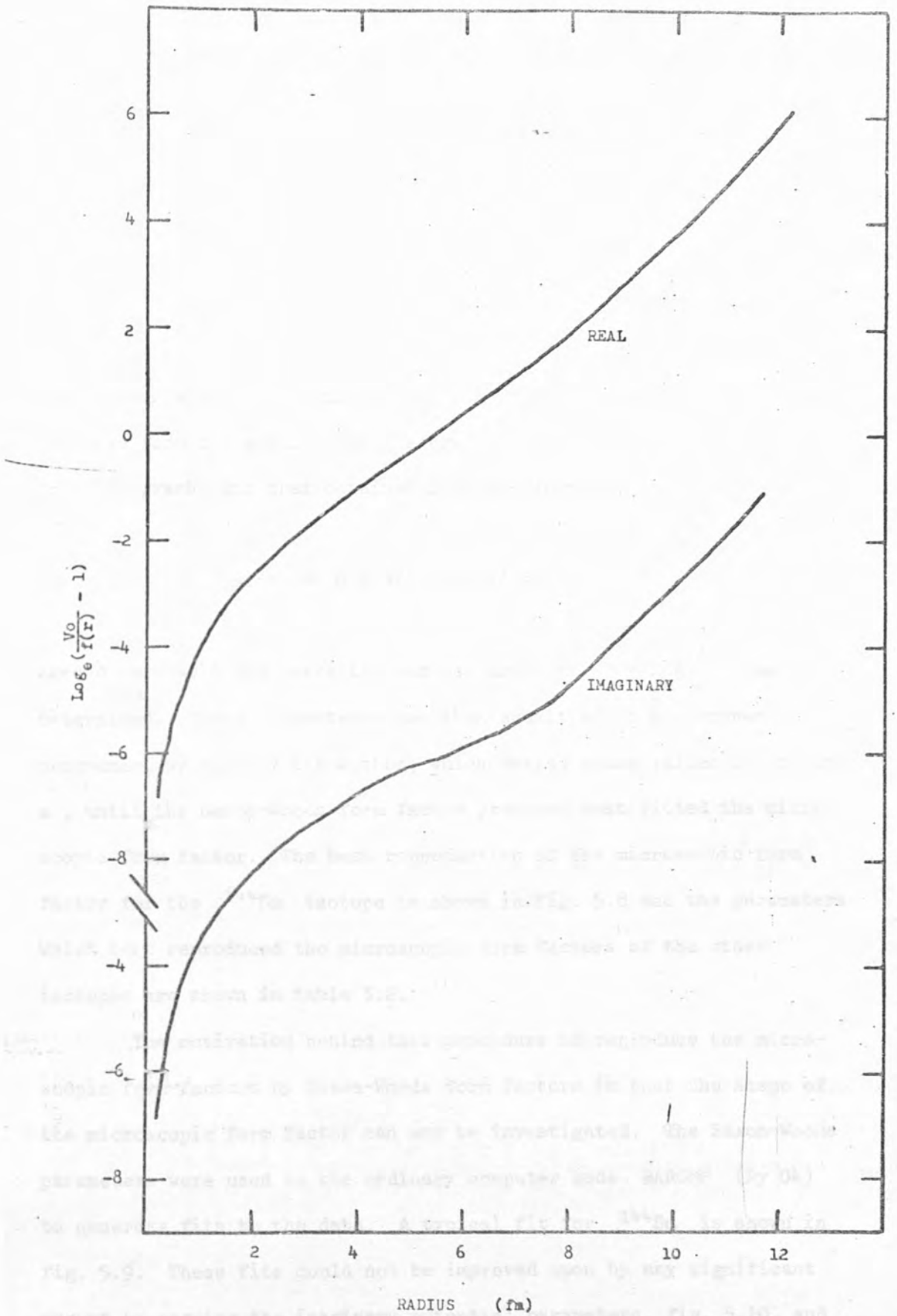

Fig 5.7 A plot of $\log_e\left[\frac{V_o}{f(r)} - 1\right]$ against nuclear radius - r for the microscopic form factor f(r) for ^{144}Sm

Saxon-Woods form factor,

$$\frac{r}{a} - \frac{R}{a} = \log_e \left(\frac{V_0}{f(r)} - 1\right)$$

and hence the graphs for ^{144}Sm in fig. 5.7 show that the surface region of the microscopic form factors do to some extent follow a Saxon-Woods shape. The value of the diffuseness parameter, a , was obtained from the gradient of the graph. The value of R obtained from the graph, and that obtained from the formula,

$$\langle r^2 \rangle = 0.6\, R^2 + 1.4\, \pi^2\, a^2$$

agreed very well and hence the radius parameter $r = R/A^{1/3}$ was determined. These parameters were then submitted to a computer programme, written by the author, which varied these values of r and a , until the Saxon-Woods form factor produced best fitted the microscopic form factor. The best reproduction of the microscopic form factor for the ^{144}Sm isotope is shown in fig. 5.8 and the parameters which best reproduced the microscopic form factors of the other isotopes are shown in table 5.2.

The motivation behind this procedure to reproduce the microscopic form factors by Saxon-Woods form factors is that the shape of the microscopic form factor can now be investigated. The Saxon-Woods parameters were used in the ordinary computer code RAROMP (Py 04) to generate fits to the data. A typical fit for ^{144}Sm is shown in fig. 5.9. These fits could not be improved upon by any significant amount by varying the imaginary potential parameters, fig. 5.10, and even a phenomenological surface imaginary or volume imaginary term made very little difference to the fit obtained. When the geometry

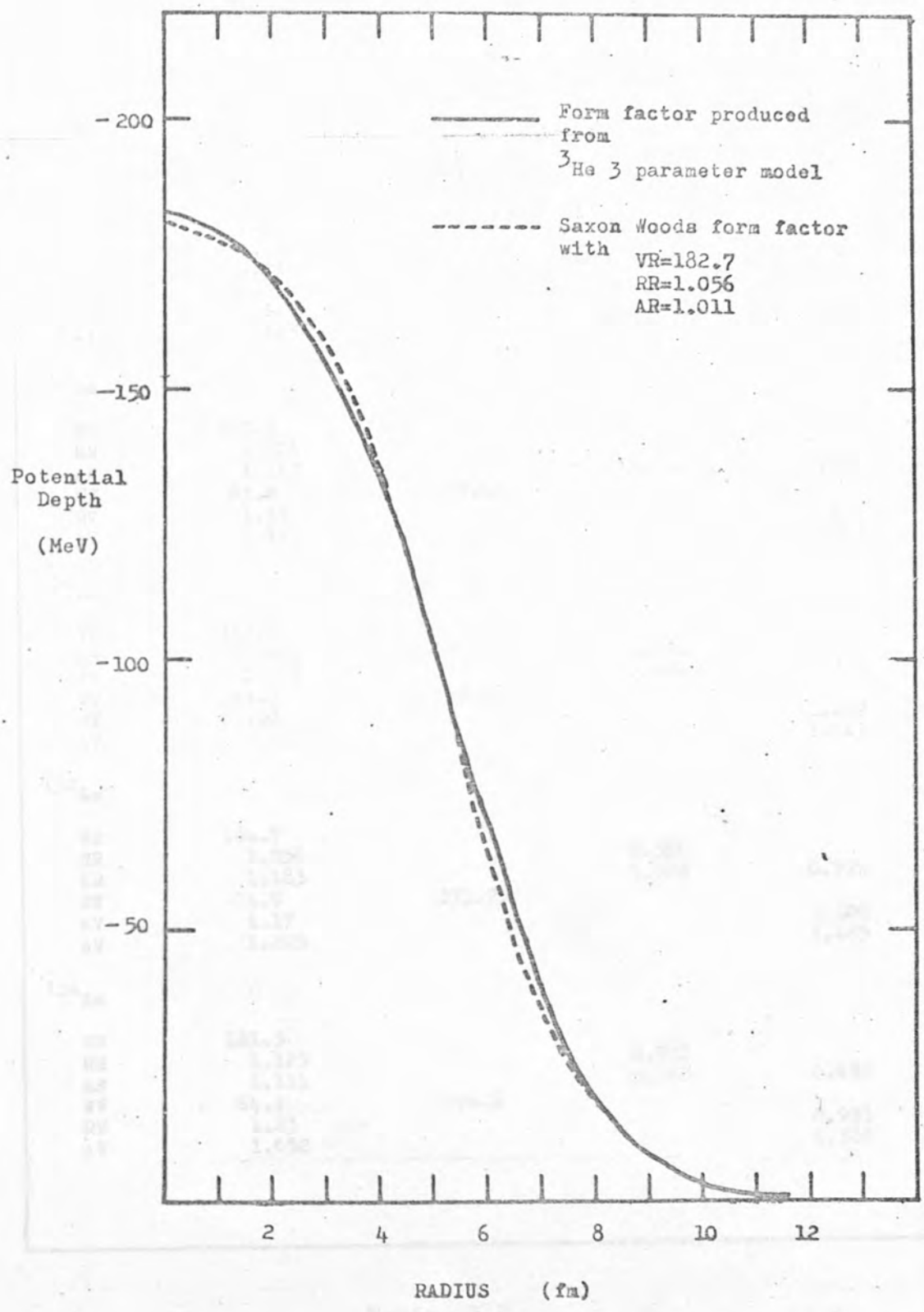

Fig 5.8 Comparison of the microscopic form factor, and Saxon Woods shape which best reproduces the microscopic form factor shape.

	Saxon-Woods parameters giving a similar shape to the ^{3}He 3 parameter model microscopic form factors	Effect of varying the imaginary central depth	Effect of varying the real geometry parameters	Effect of varying real and imaginary geometry parameters
^{144}Sm				
VR	182.7			
RR	1.006		1.368	
AR	1.211		0.566	0.877
WV	62.2	51.34		
RV	1.111			1.270
AV	1.125			0.841
^{148}Sm				
VR	183.8			
RR	1.026		1.296	
AR	1.112		0.648	0.730
WV	63.8	49.42		
RV	1.15			1.336
AV	1.129			0.963
^{150}Sm				
VR	183.6			
RR	1.037		0.638	
AR	1.161		1.028	0.748
WV	64.3	46.21		
RV	1.2			1.177
AV	1.143			1.043
^{152}Sm				
VR	184.7			
RR	1.056		0.566	
AR	1.183		1.028	0.772
WV	64.9	373.76		
RV	1.17			1.109
AV	1.205			1.105
^{154}Sm				
VR	181.5			
RR	1.125		0.911	
AR	1.111		0.960	0.682
WV	64.9	246.5		
RV	1.23			0.953
AV	1.052			1.300

Table 5.2

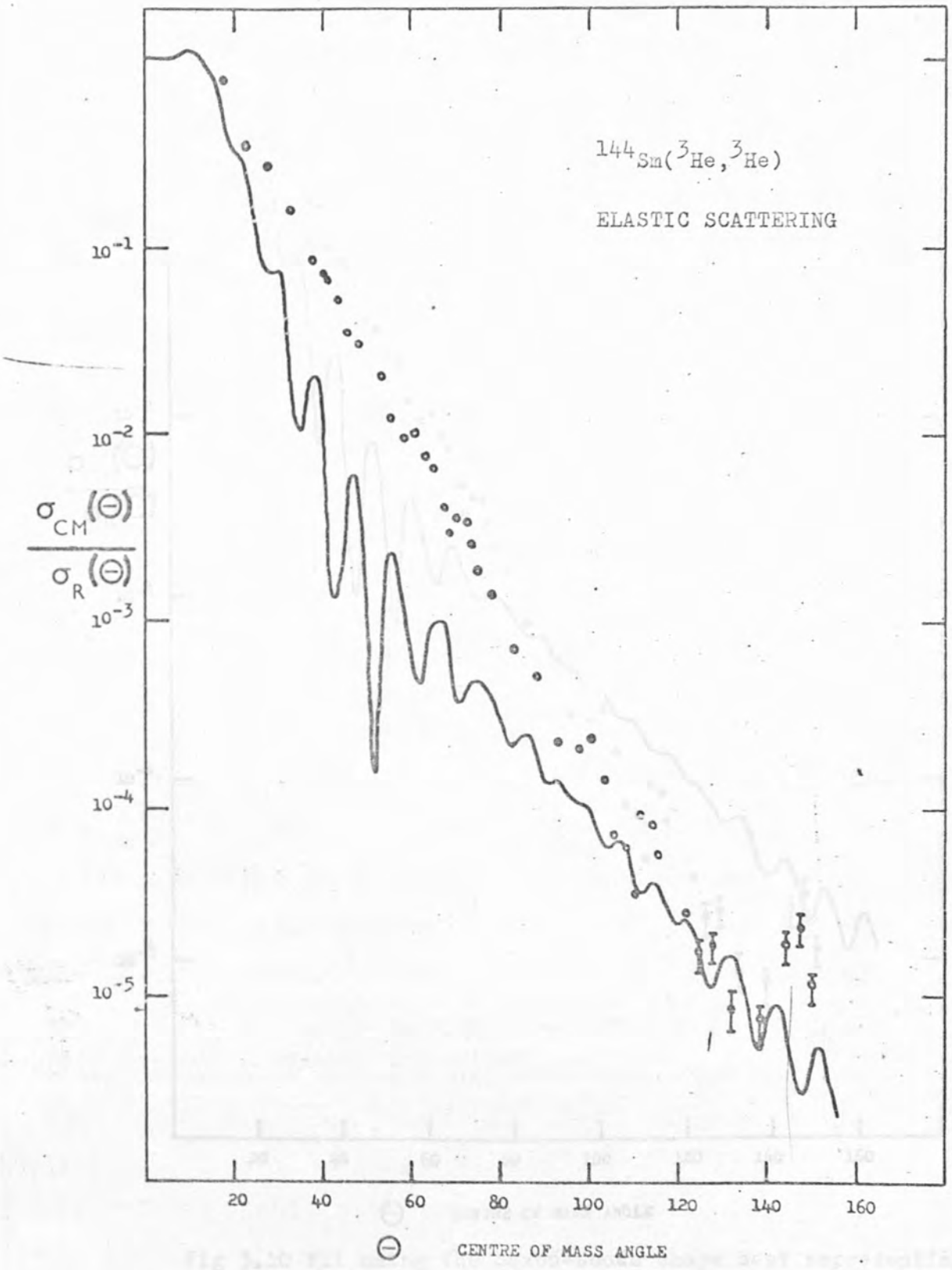

Fig 5.9 Fit using the Saxon-Woods shape best representing the microscopic form factor produced by the ^{3}He 3 parameter model.

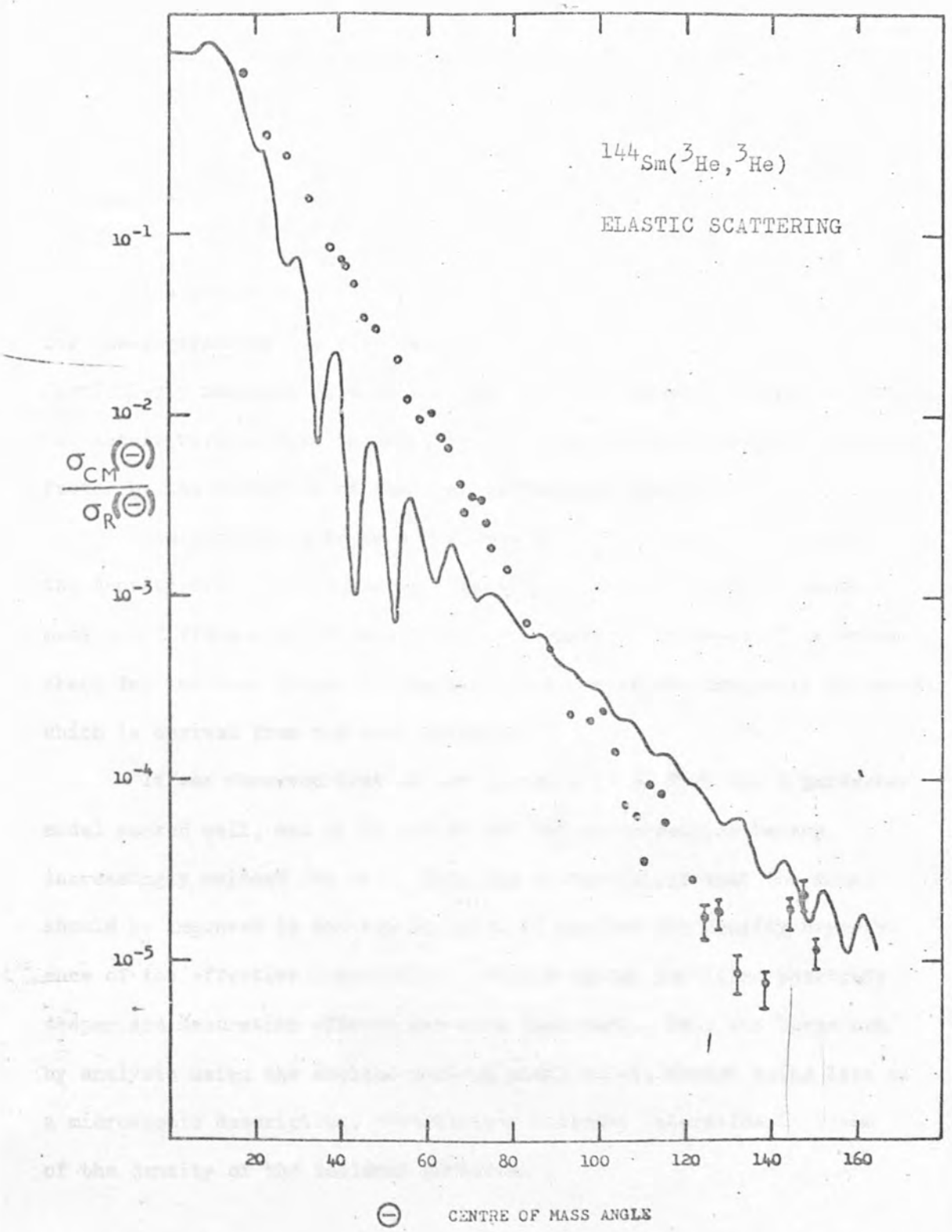

Fig 5.10 Fit using the Saxon-Woods shape best representing the microscopic form factor produced by the ^{3}He 3 parameter model and allowing the imaginary depth to vary

parameters of the real depth were allowed to vary, good fits to the data were obtained, fig. 5.11, but the effect was for the diffuseness parameter to be reduced. A better fit, fig. 5.12, was obtained by allowing the real diffuseness parameter and the imaginary geometry parameters to vary. The resultant parameters used to obtain the fits to the data as shown in figs. 5.9, 5.10, 5.11 and 5.12 are shown in table 5.2.

The effect on the shape of the microscopic potential of allowing these parameters to vary is shown in figs. 5.13 and 5.14. Particularly noticeable, when the real diffuseness and imaginary geometry parameters were allowed to vary, was the sharpening of the real form factor by the reduction of the real diffuseness parameter.

The conclusion to be drawn from this investigation was that the density distribution was satisfactory, but that the model produced much too diffuse a potential to fit the experimental data. This wrong shape for the real potential was also included in the imaginary potential, which is derived from the real potential.

It was observed that at low energies (< 30 MeV) the 3-parameter model worked well, but at 50 and 80 MeV the discrepancies became increasingly evident (We 02). This led to the belief that the model should be improved in the way in which it handled the density dependence of the effective interaction. Higher energy particles penetrate deeper and saturation effects are more important. This was borne out by analysis using the nucleus-nucleus model which, though being less of a microscopic description, nevertheless includes saturation in terms of the density of the incident particle.

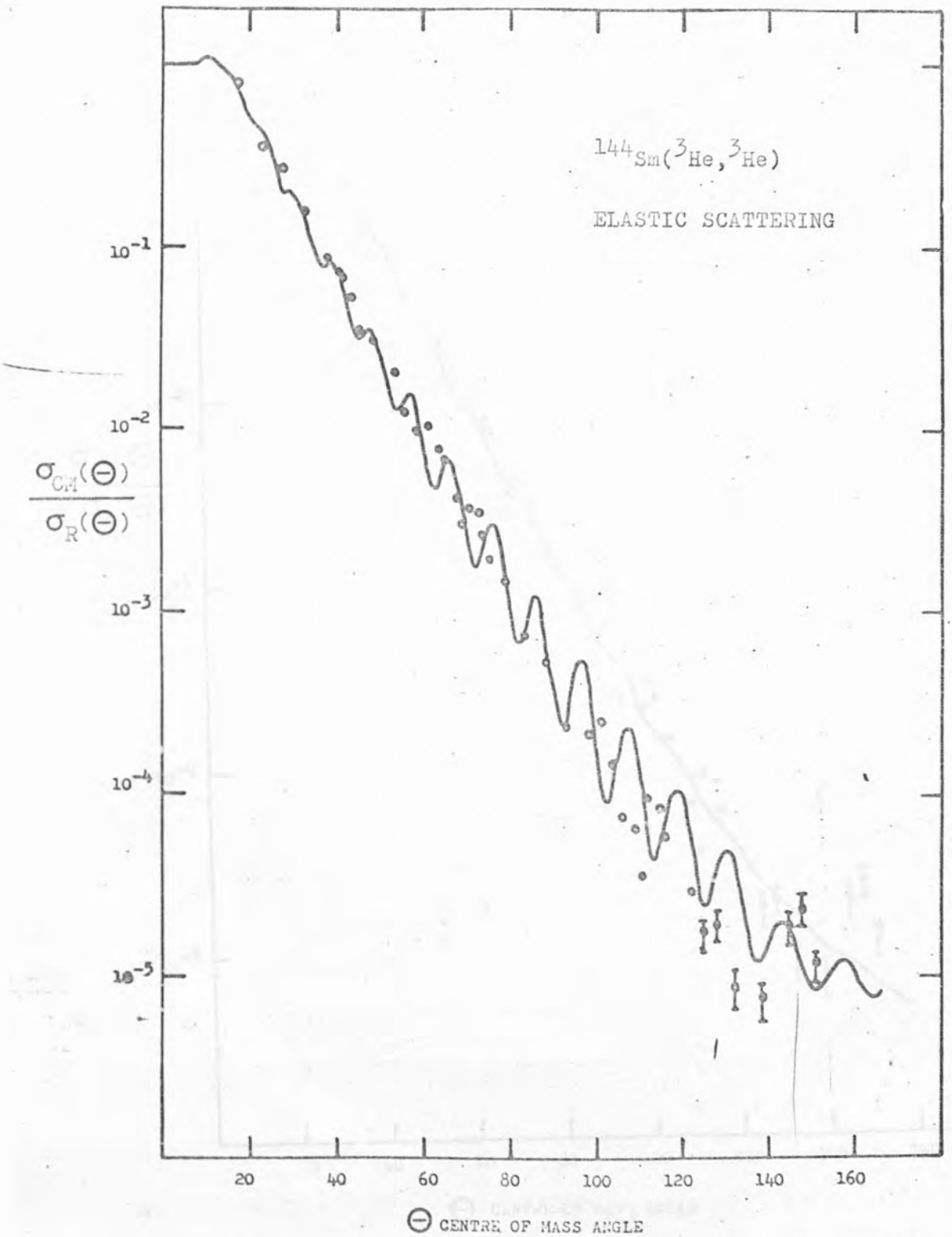

Fig 5.11 Fit using the Saxon-Woods shape best representing the microscopic form factor produced by the ^{3}He 3 parameter model and allowing the real geometry parameters to vary

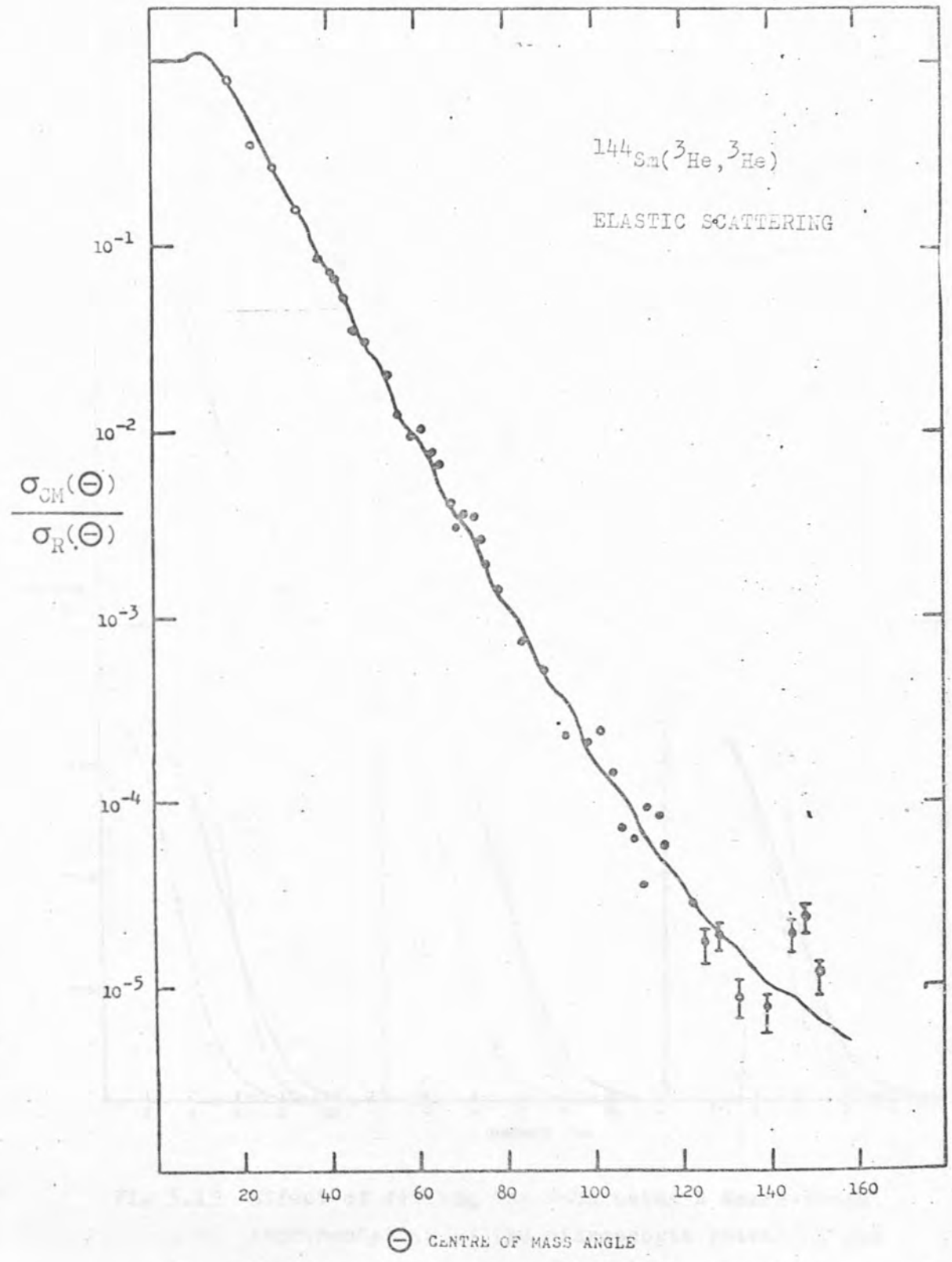

Fig 5.12 Fit using the Saxon-Woods shape best representing the microscopic form factor produced by the ^{3}He 3 parameter model and allowing the real diffuseness and imaginary geometry to vary

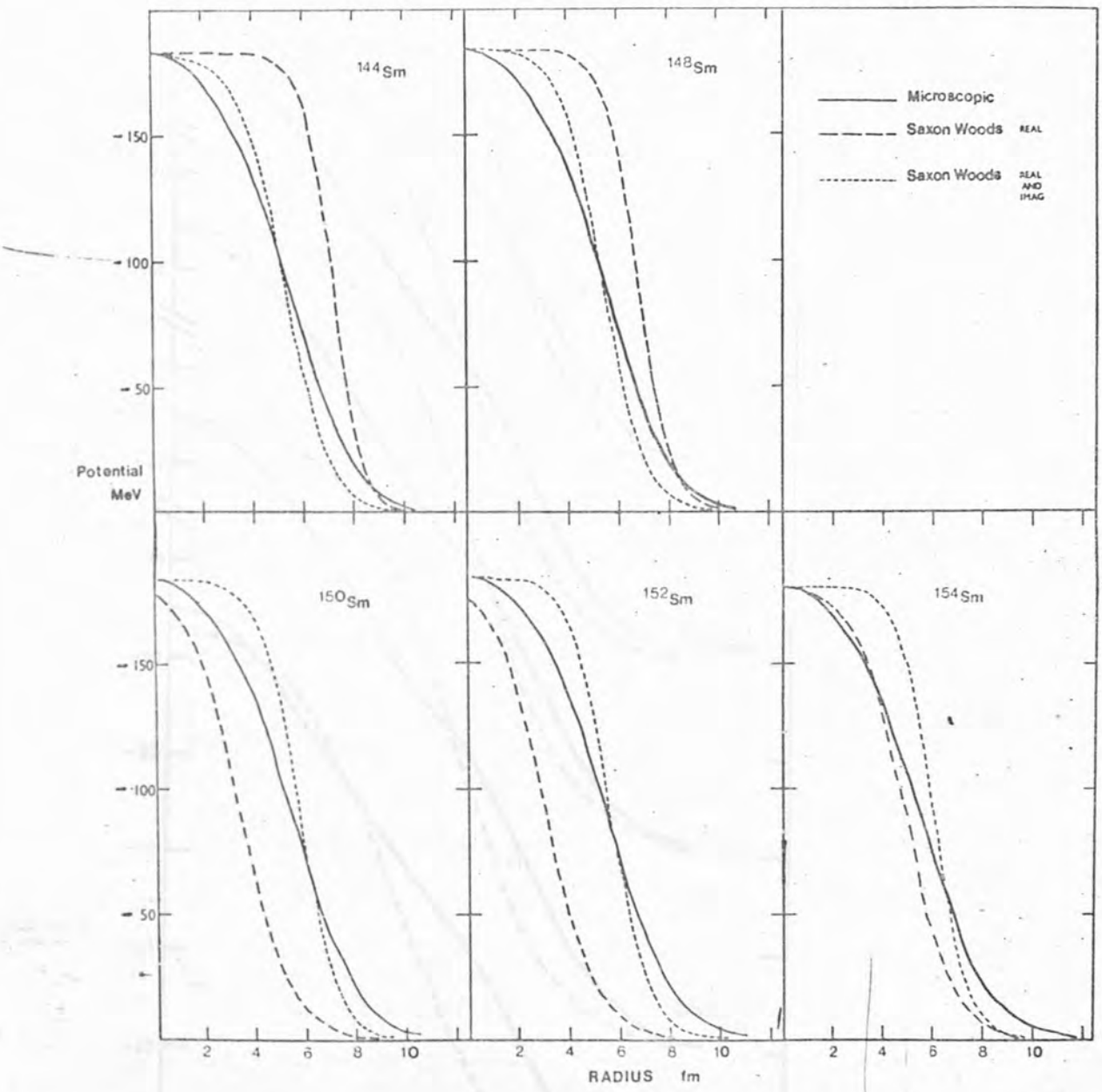

Fig 5.13 Effect of fitting the data using a Saxon-Woods representation of the microscopic potential and allowing the geometry parameters to vary

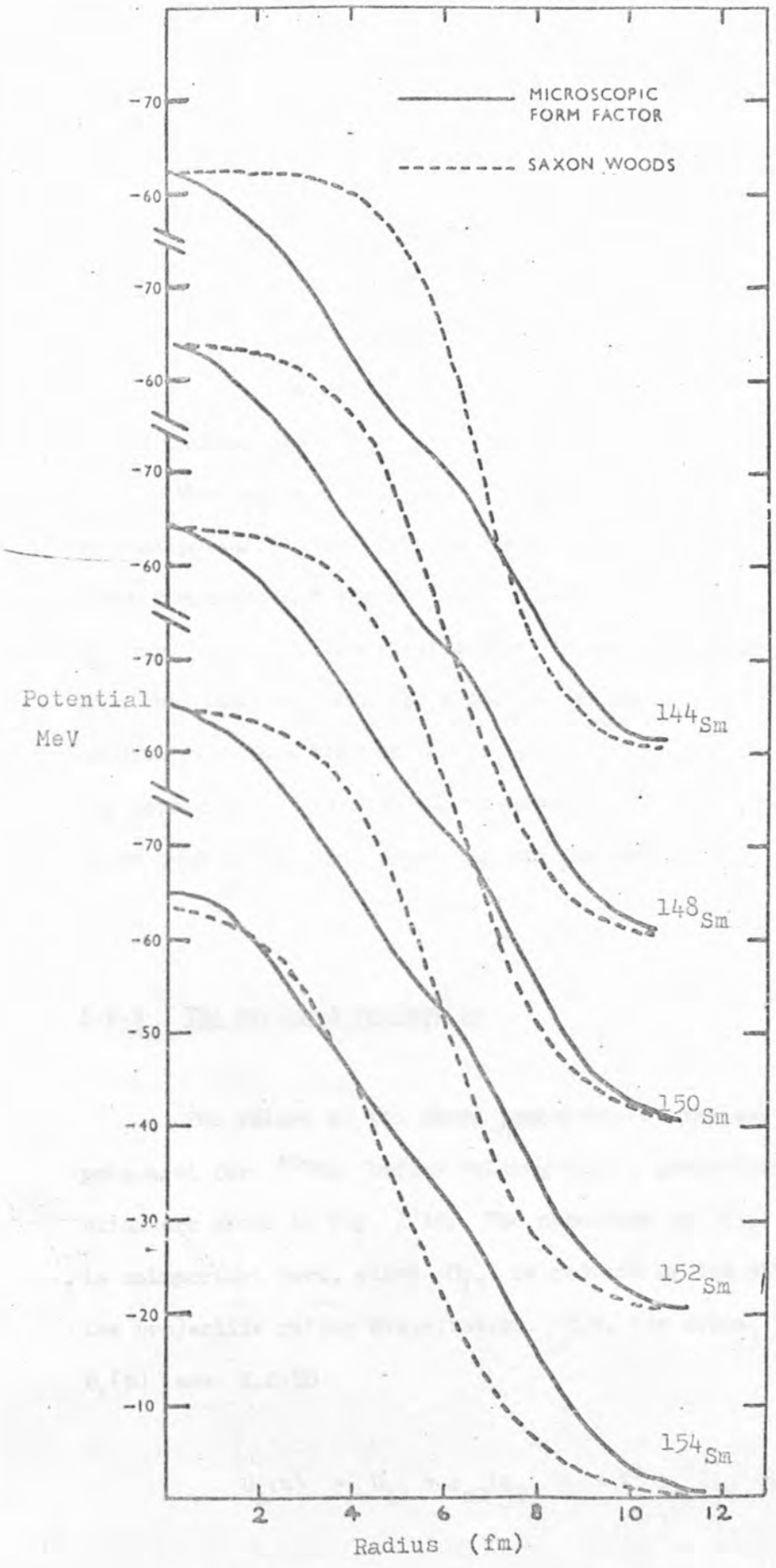

Fig 5.14 Effect of fitting the data using a Saxon-Woods representation of the imaginary potential and allowing the geometry parameters to vary

5.2 The Nucleus-Nucleus Model

The basic theoretical development of this model has been given in 2.2.3. The model itself, developed by Sinha (Si 13), possesses the interesting quality that the one-body optical potential for the target nucleus may be evaluated for a particular nucleus without reference to any particular projectile.

The computational techniques used to calculate the nucleus-nucleus optical potential fall into two parts. The first section calculates the three components of the one-body optical potential $U_1(t)$, i.e. U_{11}, U_{12} and U_{13} , before folding with the projectile matter distribution. Once this has been done for a particular nucleus, these values may be used to calculate the optical potential for any incident projectile. The second part folds the matter density of the projectile into these three components, thus producing the nucleus-nucleus optical potential.

5.2.1 The Helium-3 Projectile

The values of the three components of the one-body optical potential for ^{144}Sm before folding with a projectile matter distribution are shown in fig. 5.15. The magnitude of U_{12} relative to U_{11} is unimportant here, since U_{12} is reduced by the effect of folding in the projectile matter distribution. N.B. the actual components of $U_1(t)$ are 2.2.50

$$U_1(t) = U_{11} + \rho_{m2}(\underline{\xi}_2)\, U_2 + \nabla^2 \rho_{m2}(\underline{\xi}_2)\, U_{13} \quad .$$

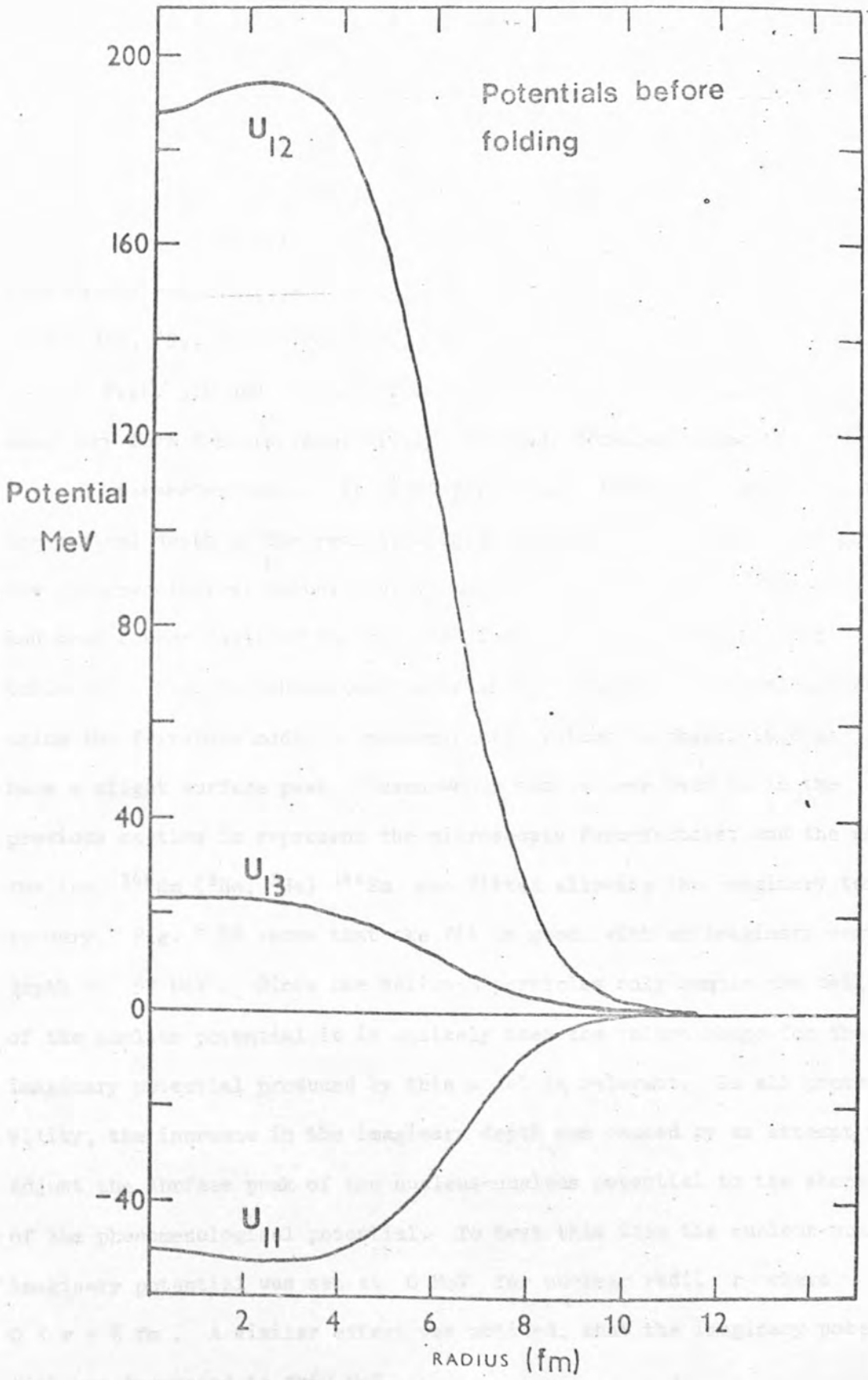

Fig 5.15 The three components of the one body optical potential for 144Sm

However, it can be seen that the sign of U_{12} is opposite to that of U_{11}, indicating the reduction in the one-body optical potential arising from the density-dependent part of the two-body interaction. $\nabla^2\rho_{m2}(\underline{\xi}_2)$ is usually negative, so that the U_{13} component behaves as a small attractive potential. Folding in these equations with the helium-3 projectile density, assumed to be a Gaussian shape (Sc 04) with a mean square radius of 3.5 fm^2 gave the optical potential for the ^{144}Sm (^3He, ^3He) ^{144}Sm reaction.

Figs. 5.4 and 5.5 also compare the shape of the real and imaginary form factors respectively, to those obtained using the ^3He - 3 parameter model. It is of particular interest to notice that the central depth of the real term is ~130 MeV , which compares with the phenomenological value. The volume integrals per particle pair and mean square radii of the real and imaginary terms are shown in table 5.3. Fig. 5.5 shows that although the imaginary term calculated using the frivolous model is predominantly volume in shape, it does have a slight surface peak. Saxon-Woods shapes were used as in the previous section to represent the microscopic form-factors, and the data for the ^{144}Sm (^3He, ^3He) ^{144}Sm was fitted allowing the imaginary term to vary. Fig. 5.16 shows that the fit is good, with an imaginary central depth of 57 MeV . Since the helium-3 particles only sample the tail of the nuclear potential it is unlikely that the volume shape for the imaginary potential produced by this model is relevant. In all probability, the increase in the imaginary depth was caused by an attempt to adjust the surface peak of the nucleus-nucleus potential to the shape of the phenomenological potential. To test this idea the nucleus-nucleus imaginary potential was set at 0 MeV for nuclear radii r where $0 < r < 6$ fm . A similar effect was noticed, that the imaginary potential was increased to ~60 MeV .

	REAL		IMAGINARY	
	J_R/A_iA_t	$\langle r^2\rangle_R$	J_I/A_iA_t	$\langle r^2\rangle_I$
$(^3He,^3He)$ at 53.4 MeV	432.8	39.5	133.5	44.8
$(^4He,^4He)$ at 50.0 MeV	382.12	39.3	132.4	44.7

Table 5.3

Table showing the volume integrals per particle pair and the mean square radius of the real and imaginary potentials obtained from the Nucleus-Nucleus model for the ^{144}Sm target.

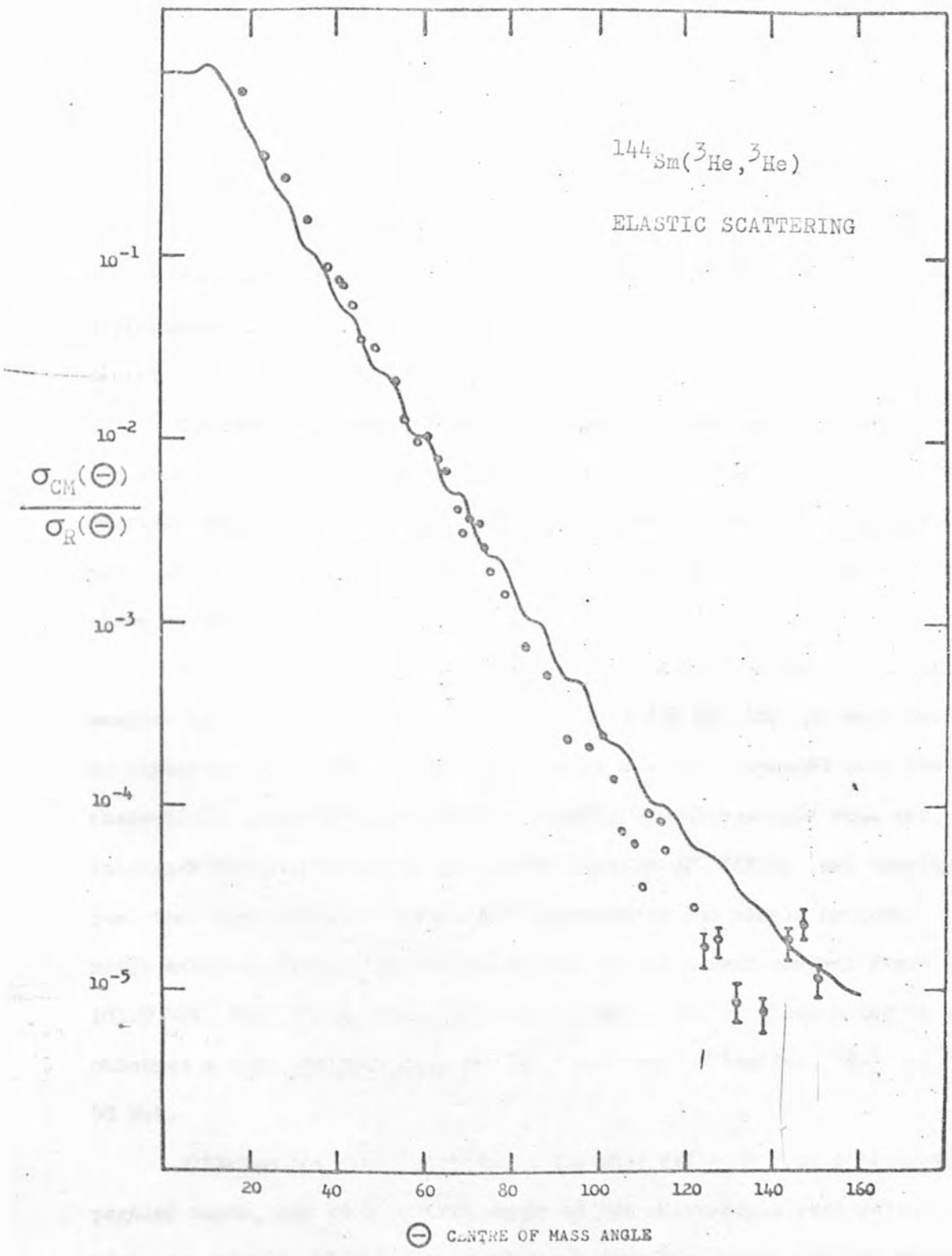

Fig 5.16 Fit to the $^{144}Sm(^{3}He,^{3}He)$ data using the Nucleus-Nucleus model.

The success of the nucleus-nucleus model and its applicability to heavier ions leads to its use to fit alpha data.

5.2.2 The Alpha Projectile

The projectile density distribution for an alpha particle was approximated by assuming it to be a Saxon-Woods phenomenological distribution (Ba 04).

The real and imaginary form factors for alpha particle scattering from ^{144}Sm are shown in fig. 5.17 where there is a well-pronounced surface peak in the imaginary term. The volume integrals per particle pair, and the mean square radii of the real and imaginary terms are shown in table 5.3.

The simple optical model parameters from the analyses of alpha scattering from Samarium isotopes at 50 MeV (Ba 02) (Gl 03) were used to reproduce the cross-section data, which was then compared with the theoretical predictions obtained by feeding the microscopic real and imaginary form factors into an amended version of RAROMP and varying just the real central depths. The features of the simple optical model analyses is that Barker and Hiebert obtain a real central depth of 185.0 MeV for ^{144}Sm (^{4}He, ^{4}He) at 50 MeV, whilst Glendenning et al obtained a real central depth of 65.5 MeV for $^{148}Sm(^{4}He, ^{4}He)$ at 50 MeV.

Although the fitting of the alpha data suffered from a lack of partial waves, the real central depth of the microscopic real potential was able to fit the data reproduced from the simple optical model analyses by either increasing to $\sim$180 MeV or decreasing to $\sim$ 60 MeV, with a correspondingly large increase in the microscopic imaginary

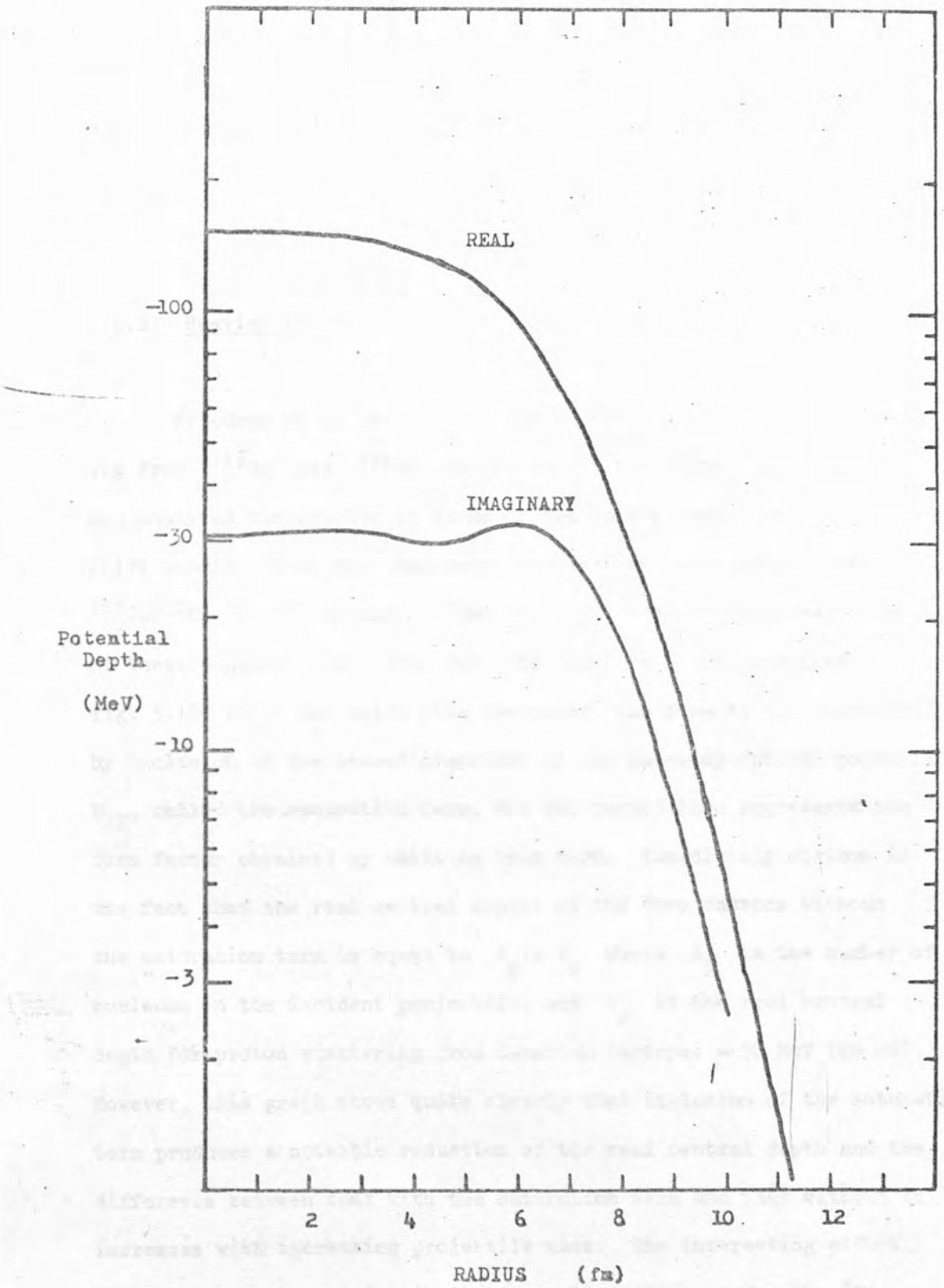

Fig 5.17 Nucleus-Nucleus model form factors for alpha particle scattering from ^{144}Sm at 50 MeV.

central depth.

The potentials generated from the model still suffer from the discrete ambiguity problem, but the saturation effects are well taken care of by this model.

5.2.3 Heavier Ion Projectiles

Friedman et al (Fr 05) have performed ^{12}C and ^{16}O scattering from ^{152}Sm and ^{154}Sm respectively at 118 MeV and 130 MeV and analysed the results in terms of the optical model and phase shift models. Real and imaginary form factors were produced for $^{152}Sm(^{12}C, ^{12}C)^{152}Sm$ and $^{152}Sm(^{16}O, ^{16}O)^{152}Sm$ and the real terms of these together with those for ^{3}He and ^{4}He are presented in fig. 5.18, where the solid line represents the form factor produced by inclusion of the second component of the one-body optical potential U_{12}, called the saturation term, and the dashed line represents the form factor obtained by omitting this term. Immediately obvious is the fact that the real central depths of the form factors without the saturation term is equal to $A_p \times V_p$ where A_p is the number of nucleons in the incident projectile, and V_p is the real central depth for proton scattering from Samarium isotopes $\sim$ 50 MeV (Wo 06). However, this graph shows quite clearly that inclusion of the saturation term produces a noteable reduction of the real central depth and the difference between that with the saturation term and that without it increases with increasing projectile mass. The interesting effect, also shown by Sinha (Si 13), is the small difference for the ^{3}He incident projectile between the optical potential obtained with and

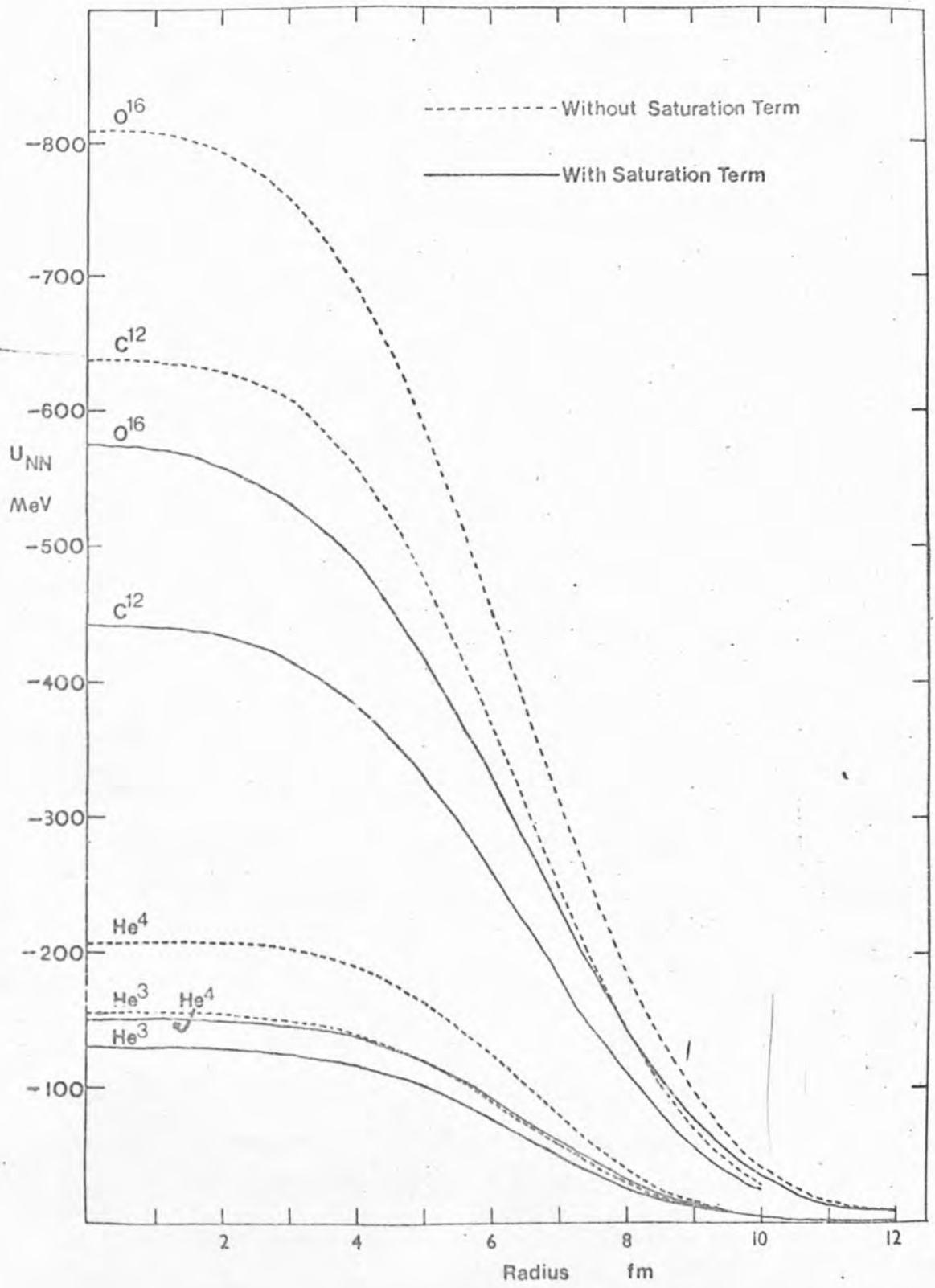

Fig 5.18 Real form factors for the reactions:-

$^{144}Sm(^{3}He,^{3}He)$; $^{144}Sm(^{4}He,^{4}He)$; and

$^{152}Sm(^{12}C,^{12}C)$; $^{152}Sm(^{16}O,^{16}O)$.

that obtained without the saturation term. This indicates the same conclusion as the conclusion obtained in section 4.2, i.e. that saturation effects are not so important for ^3He.

CHAPTER 6

Conclusions

6.1 Summary

The elastic scattering and inelastic scattering of ^{3}He ions to the lowest levels of ^{148}Sm and ^{150}Sm at 53.4 MeV and ^{152}Sm and ^{154}Sm at 53.1 MeV have been measured. The data at 53.4 MeV were obtained on the Variable Energy Cyclotron, Harwell, where a high beam intensity permitted the data to be taken to a large angular range (10^{o} - 150^{o}). The need to separate the first 2^{+} state at 82 keV from the elastic scattering to the ground state necessitated the use of the Oak Ridge Isochronous Cyclotron, Tennessee, where the spectrograph gave high resolution but a lower beam intensity, only permitting data to be taken to 100^{o} . This lack of back angle data for the rotational isotopes impeded some of the analyses which were performed.

The data completes the series of data of proton scattering at 50.8 MeV from the five even stable Samarium isotopes (Wo 10), proton inelastic scattering at 30 MeV (La 02) from ^{144}Sm, ^{3}He scattering at 53.4 MeV from ^{144}Sm (Wo 09), alpha scattering at 50 MeV from ^{144}Sm (Ba 02), and from the remaining four even stable Samarium isotopes at 50 MeV (Gl 03) (He 03) (Ha 02) . Apart from these data for light ion scattering from Samarium isotopes, Friedman (Fr 05) has measured ^{12}C and ^{16}O scattering from ^{152}Sm and ^{154}Sm isotopes at 118 MeV and 130 MeV .

The properties of the Samarium isotopes have been investigated, particularly within the context of the data now available. The increasing deformation with increasing target mass has been investi-

gated and the role of ^{150}Sm as a vibrational or rotational isotope has been studied.

6.2 The Elastic Scattering Analysis

The data for helium-3 elastic scattering from a range of Samarium isotopes has been used to test the A and N-Z dependence of the optical model, and also to test the reformulations of the optical model which replace the phenomenological optical potential with a potential obtained from folding the basic nucleon-nucleon two-body effective interaction into the target density.

The helium-3 scattering from Samarium isotopes at 53 MeV did not give a unique potential family, but the family corresponding to $V_R \sim 135$ MeV and $J_R/A_pA_t \sim 300$ MeV fm^3 per nucleon fitted the data as well as any other potential family. The potential families themselves occurred at intervals of ~ 70 MeV fm^3, corresponding to an increase in V_R of ~ 30 MeV from one family to the next. The root mean square radius of the real potential for all the families considered was fairly constant, ranging from 5.3 to 5.6 fm for all isotopes.

The isotope sequence was fitted with little variation of parameters, and without imposing any N-Z dependence on the parameters. The diffuseness parameter for all isotopes, except Samarium 144, was larger than that obtained by Woollam in his simple optical model analysis of helium-3 scattering from Samarium 144. The final values for the diffuseness and other parameters from these phenomenological analyses were very similar to the final parameters obtained by Woollam (Wo 09) in his S.C.A. analysis of the helium-3 scattering from Samarium 144.

The range of volume integrals within the preferred family was 310-330 MeV fm^3 . This is the family preferred from the analysis of helium-3 scattering from ^{60}Ni and ^{56}Fe at higher energies. At lower energies $\sim$ 30 MeV the correct volume integral to use has not yet been determined. Polarisation experiments are currently being performed to determine the spin-orbit depth for helium-3 interactions at 30 MeV and 50 MeV , and these results should enable an unambiguous volume integral to be obtained for these lower energies. It will be interesting to see if the volume integral for higher energies is also the correct one to use at lower energies. Although previous calculations (Fu 08) (Co 08) have predicted that there should be a spin orbit potential of between 2 MeV and 3 MeV , it was found that the inclusion of a spin orbit term into the simple optical model calculations did not improve the fit but rather worsened it. The need for good quality polarisation data for helium-3 is apparent.

Recent analyses of proton scattering from Samarium (Wo 10) and alpha particle scattering from Samarium (Ba 02) have used volume absorption terms, with smaller surface absorption terms in the case of the proton scattering. Nevertheless, no combination of volume and surface, or volume absorption term alone, gave a better fit than using a purely surface absorption term. This can be interpreted in terms of the greater penetrating power of protons compared with ^3He at a given energy. The use of a volume absorption potential for alpha particles is governed more by tradition than reason as only the tail of the potential is of importance in this case.

There was little A or N-Z dependence exhibited in the real volume integral over the small mass range of the Samarium isotopes.

Moreover, in the wider context of the A dependence of the optical model for helium-3 scattering as performed by Fulmer and Hafele (Fu 09), the volume integral $J_R \sim 330$ MeV fm^3 is seen to vary negligibly over the range of isotopes ^{60}Ni (Fu 09) to ^{144}Sm (present work) for helium-3 scattering at 50 MeV . The N-Z and A dependences are certainly not observable over isotope sequences. The isospin potential problem needs (p,n) or (^{3}He,t) measurements or comparison of ^{3}He and t or p and n elastic scattering. However, intense n and t beams are difficult to obtain.

The elastic scattering data fitted with the 330 MeV fm^3 family showed increasing oscillations with increasing A number, but the ^{150}Sm isotope oscillations were more in the style of the vibrational nuclei than that of the rotational nuclei. The need for backward angle data for the ^{152}Sm and ^{154}Sm isotopes is evident in order to make any detailed comparisons of the structure of the cross-sections. The largest difference between any set of cross-sections seems to occur between the ^{144}Sm and ^{148}Sm isotopes. This is puzzling, and has certainly not been the case for proton scattering and alpha particle scattering.

The three reformulations of the optical model which were tested were the Greenlees reformulation (Gr 08), in which the nucleon-nucleon force is represented by a Yukawa shape, and the density of the target nucleus is parametrised using a Saxon Woods shape. The ^{3}He - 3-parameter model (Si 15) uses a Kuo-Brown effective interaction folded into a target density which was obtained from shell model calculations, or taken from the Greenlees reformulation analyses. The helium-3 incident projectile as opposed to a single nucleon as projectile is taken into account using the Samaddar et al (Sa 01) formalism. The nucleus-nucleus model (Si 13) is a so-called double folding model in

which the Kallio-Kolveit interaction is folded with the target density, which is then folded with the incident projectile density. The particular virtue of this model is the self-consistent approach to the calculation of the elastic scattering of any nucleus from any nucleus. Unlike the previous model it neglects the anti-symmetrisation of the incident nucleons with respect to the target nucleons, and does not attempt to calculate a second-order term for the real potential.

The reformulated model due to Greenlees was found by Woollam (Wo 07) in his analysis of the elastic scattering of protons on ^{148}Sm to give unique values for the mean square radius of the effective interaction and the matter distribution parameterisation, although no other analyses have given similar results. In this present work it has been found that when gridding over $\langle r^2 \rangle_d$, the m.s.r. of the effective interaction, and allowing the matter distribution to vary, a minimum in chi-squared space occurs for $\langle r^2 \rangle_d \simeq$ 2.2 fms . If, however, the matter parameterisation, as obtained by Woollam, is used in this analysis and a grid performed over $\langle r^2 \rangle_d^{\frac{1}{2}}$, then no minimum is found. From the relation,

$$\langle r^2 \rangle_R = \langle r^2 \rangle_m + \langle r^2 \rangle_{t.b.} + \langle r^2 \rangle_{^3He}$$

one might assume that it should be possible to determine the mean square radius of the helium-3. However, the analysis of the proton scattering data yielded a value of $\langle r^2 \rangle_d$ of 2.1 fm . This present analysis suggests a value of 2.2 fm and hence there appears to be no helium-3 size dependence in this model. Our studies with the inclusion of the saturation term in the effective interaction shows that the reason for this effect could be that the repulsive effect of saturation

reduces the size of the potential and compensates for the increase in the size of the potential by the size of the helion. This emphasises that the simple folding procedure covers some important physical features in its approximation.

The ^{3}He - 3-parameter model produced real and imaginary form factors, the real being the sum of first and second-order terms, and the imaginary calculated according to the frivolous model, i.e. the absorption is due to the forward angle scattering amplitude. These form factors were used to fit the Samarium data and were found to produce poor fits. The question then is whether the effective interaction is inadequate to explain this situation, or whether the Samaddar et al (Sa 01) approach to the optical potential for the elastic scattering of ^{3}He calculated in terms of the optical potentials of nucleons forming the projectile is inadequate. The Kuo-Brown interaction has been used in the microscopic optical model analyses of the elastic scattering of protons from other nuclei with great success. Representing the form-factors obtained from this model by Saxon-Wood shapes, and putting their respective parameters into the standard optical model code RAROMP (Py 04) enabled the shape of the form factors to be investigated. Variation of the parameters led to the conclusion that the shape of the real term was too diffuse, although some sharpening of the imaginary term was also needed in order to obtain a good fit. The imaginary term calculated by the ^{3}He - 3-parameter model has a volume shape as opposed to the surface term used in the phenomenological analyses. The results of varying the Saxon-Woods parameters, which best represent the imaginary form factor produced by this model, until a good fit was obtained to the data, was to obtain a shape which in the surface region followed the shape of the phenomenological imaginary term. In the 3-parameter model the imaginary potential is derived from the real potential so

the too diffuse shape of the real potential is also reflected in the wrong shape for the imaginary potential. It is interesting that similar microscopic calculations performed by Rook also produce a potential with too diffuse a surface. This may well be due to the formulation of the second-order terms which play an increasingly important role as the projectile mass increases.

The nucleus-nucleus model was used to predict elastic scattering cross-sections of helium-3 scattering from Samarium isotopes. The real and imaginary form factors obtained from this model were used to fit the data varying only the potential depth's scaling parameter. A good fit was obtained, but with an imaginary depth larger than expected. However, the shape of this imaginary form factor was predominantly volume, with a small surface peak. The increase of the imaginary depth could then be accounted for by assuming that the depth had been adjusted until the tail of the imaginary potential followed the expected surface shape.

The nucleus-nucleus model was also used to calculate the real and imaginary form factors of the elastic scattering of alpha particles from Samarium 144. In this case the imaginary term was still predominantly volume, but with a much larger surface peak. It was found that the discrete ambiguity problem was unresolved since the microscopic form factor was able to reproduce alpha data by adjusting the real central depth scaling parameter until the real central depth was either $\approx$ 60 MeV or 170 MeV .

Calculations of the real form factor for ^{12}C and ^{16}O elastic scattering from Samarium isotopes have shown the need to include the saturation term (Si 13). The computer programme RAROMP which was used for the elastic scattering optical model fits had a maximum of 50 partial waves available. However, in order to analyse ^{16}O scattering from ^{152}Sm at 130 MeV , a programme with the facilities for about 200 partial waves is needed. This saturation term increases

in magnitude with increasing A of the incident projectile. The saturation term for the incident projectile helium-3 is very small, and the physical interpretation of this can be linked to the conclusion from the reformulated optical model due to Greenlees (Gr 08), i.e. that the helium-3 particle has a small size effect.

No N-Z, A or L.S dependence was observable from the elastic scattering from the isotopic sequence of Samarium isotopes, but the energy dependence has been explained by the exchange term in the microscopic optical model. These reformulated models including saturation use helium-3 and alpha data as testing ground and predict heavy ion potentials. However, these models do run into difficulties due to the importance of the second-order term as the projectile gets larger. The results presented in this thesis demonstrate these limitations.

A wide angular range of detailed cross-sections is vital to further work, which would require various particles scattering from Samarium isotopes over a range of energies. This work has shown that conclusions from single measurements can be misleading.

6.3 The Inelastic Scattering Analysis

The inelastic scattering data was fitted very well with three potential families having real volume integrals of 240, 300 and 400 MeV fm^3 , in the D.W.B.A. The β values derived from these calculations for the 2^+ levels increased as was expected for increasing A number, and these values compared favourably with previous results. Contrary to the elastic scattering data, the

angular distribution for the ^{150}Sm isotope shows a marked similarity to the rotational isotopes as opposed to the vibrational isotopes. This was exactly the opposite effect noticed by Woollam (Wo 10) in his analysis of proton scattering from Samarium nuclei. However, the similar level structures of the ^{144}Sm, ^{148}Sm and ^{150}Sm isotopes suggest that the ^{150}Sm is vibrational in structure. The need for higher energy data to a large angular range is apparent. The effect of the ^{150}Sm isotope behaving in some cases like a vibrational nucleus, and in others like a rotational nucleus, is to some extent further resolved by the S.C.A. analysis of inelastic scattering to the 3^- state. Here the shapes of the angular distributions of the data and the theoretical predictions for ^{148}Sm and ^{150}Sm are extremely similar. The general similarity of cross-sectional shapes is therefore not entirely a reliable guide to the character of target nuclei and more attention should be taken of excitation energies and distortion parameters.

The D.W.B.A. calculations for the 2^+ and 3^- states have predicted the data very well for all the families concerned. However, these calculations have not provided a critical test of the D.W.B.A., and this would probably be provided by D.W.B.A. analysis of the pickup reaction, ^3He, α, for the Samarium isotopes. Such an analysis was performed by Woollam and Griffiths (Wo 08) for the $^{144}Sm(^3He,^4He)^{143}Sm$ reaction where the apparent failure of the D.W.B.A. to describe the $\ell = 0$ transition strength in this reaction was discussed. They concluded that the discrepancy was due to the failure of the D.W.B.A. to account for this transition because it has a large momentum mismatch.

The strong coupling approximation calculations were performed with the computer code JUPITOR , but the problem of computing time prevented

a thorough analysis of all the data to be performed. The fits to the data showed definite interesting trends, particularly the decreasing value of the real central depth with increasing A number. The work of Glendenning et al (Gl 03) suggested that if all the low lying collective states were explicitly included in the S.C.A. analysis, then isotopes over a wide mass range could all be fitted with the same potential set. The parameters describing these potentials were similar to those parameters which described the elastic scattering only of the vibrational nuclei. They showed a need to include 2^+, 4^+ and 6^+ states in the rotational nuclei S.C.A. analysis, and that failure to do so resulted in a much smaller real central depth for these isotopes. Since in this analysis only data to the 2^+ level was available, it was expected that the real central depths should show a decrease with increasing A number, and this in fact is the case. Moreover, one would also expect a smaller value for the absorption depth in the S.C.A. analysis than for the simple optical model analysis since the low lying collective states which contribute strongly to absorption from the elastic scattering channels have been explicitly included in the calculations. This in general is also the case for the present analysis. The fits to the data from the Strong Coupling analysis are very good.

6.4 Conclusion

In this work the ambiguity problem for helium-3 particles has been investigated and partially resolved. The simple optical model analyses show that four potential families give equally good fits to the data, including the two favoured families 300 and 400 MeV fm^3 (Fu 09) (Ca 01).

The microscopic optical model analyses give volume integrals per particle pair of 400 MeV fm^3 for ^3He scattering from the Samarium isotopes. No evidence was found for the use of a spin-orbit term and a surface imaginary term yielded a much better fit than did a volume imaginary term, as was found by previous authors (We 02) (Wo 09).

A helium-3 potential has been formulated by folding the target density into a two-body effective interaction, and using the Samaddar et al. approach (Sa 01). The resulting real and imaginary form factors have been used to fit the data but the diffuseness, particularly of the real term, has been shown to be too large. The nucleus-nucleus model has been used to show that the saturation properties of heavy nuclei need to be included in an optical model calculation.

Open questions which still remain in optical model analyses are the energy dependence, and N-Z or A dependence and the correct shape for the microscopic potentials. The need for experimental data with heavy ions to test the nucleus-nucleus model is apparent. Good quality helium-3 data extending to backward angles on a range of isotopes, with even and odd nuclei between A = 50 to A = 70 has been obtained by Birmingham University and should enable any N-Z, N, A or N-Z/A dependence to be determined accurately. The spin orbit potential for helium-3 particles needs to be fixed by good quality polarisation experiments, now being actively performed at Birmingham University and King's College London. The optical model should reproduce the gross features of nuclei. The resolution of the discrete and continuous ambiguities in the real and imaginary potentials, the correct spin orbit force and the exact dependence of the potentials on various combinations of N, Z and A will enable an

accurate macroscopic prescription to be obtained. The future optical model must also include saturation for heavy ions and exchange for energy dependence. When a complete microscopic description is possible then the linking of the optical macroscopic potential with the effective nucleon-nucleon force will go a long way towards developing a comprehensive theory of the nuclei. This investigation has demonstrated that helium-3 and alpha beams produce a wealth of information in their interactions with nuclei. Many of the features of heavy ion reactions, such as Coulomb/nuclear interference, polarisation and target spin effects and coupling between elastic and inelastic scattering are dramatically apparent for the first time in helium-3 and alpha interactions. A complete understanding of the comprehensive information obtained in these studies will provide a sound basis for future studies with heavier ion beams.

REFERENCES

Ab 01 A Y Abul-Magd and M El-Nadi; Prog. Theor. Phys. 35 (1966) 788

Ac 02. H A Acker, G Backenstoss, C Dawn, J C Sens and S A Dewitt; Nucl. Phys. 87 (1966) 1

Ae 03 A E R E User Guide, Assembly type 1786D

Ae 04 A E R E User Guide 3008 Beam Monitoring Equipment, UG3008-1

Al 05 W D Allen; Nuc. Struc. (1967) 215

Ba 01 J B Ball; I E E E Transactions on Nuclear Science (1966)

Ba 02 J H Barker and J C Hiebert; Phys. Rev. C4 (1971) 2256

Ba 03 R H Bassel, G R Satchler, R M Drisko and E Rost; Phys Rev. 128 (1962) 2693

Ba 04 C J Batty, E Friedman and D F Jackson; Nucl. Phys. A175 (1971) 1

Be 05 F D Bechetti and G W Greenlees; Phys. Rev. 176 (1968) 1394

Be 06 H A Bethe; Phys. Rev. 47 (1935) 747

Be 07 H A Bethe; Z Physik 76 (1938) 293

Be 08 H A Bethe; Phys. Rev. 57 (1940) 1125

Be 09 H A Bethe, B H Brandow and A G Petschek; Phys. Rev. 129 (1963) 225

Bl 10 R J Blin-Stoyle; Phil. Mag. 46 (1955) 973

Bo 11 A Bohr and B R Mottelson; Dan. Mat. fys. Medd. 27 (1953) No 16

Br 12 P H Brown and P Stoler; Phys. Rev. C2 (1970) 765

Bu 13 B Buck; Phys. Rev. 127 (1962) 940

Bu 14 B Buck, A P Stamp and P E Hodgson; Phil. Mag. 8 (1963) 1805

Ca 01 M E Cage, A J Cole and G J Pyle; Nucl. Phys. A201 (1973) 418

Ch 02 D M Chase and F Rohrlich; Phys. Rev. 94 (1954) 81

Ch 03 D M Chase, L Willets and A R Edmonds; Phys. Rev. 110 (1958) 1080

Ch 04 P R Christensen, A Berinde, I Neamu and N Scintei; Nucl. Phys. A129 (1969) 337

Ch 05 A Christy and O Hausser; Nucl. Data Tables 11 (1972) 281

Cl 06 N M Clarke; King's College Report (unpublished)

Cl 07 N M Clarke; Nucl. Inst. and Meth. 97 (1971) 399

Co 08 M D Cohler; Private Communication

Dr 01 R M Drisko, G R Satchler and R H Bassel; Phys. Lett. 5 (1963) 347

Fa 01 J Fannon; Ph.D. thesis, University of London (unpublished)

Fe 02 E Fermi, Nuovo Cimento (1954) 407

Fe 03 H Feshbach; Ann. Phys. 5 (1958) 357

Fe 04 H Feshbach; Ann. Phys. 19 (1962) 287

Fr 05 A M Friedman, R H Siemssen and J G Cuninghame; Phys. Rev. C6 (1972) 2219

Fu 06 C B Fulmer, F G Kingston, A Scott and J C Hafele; Phys. Lett. 32B (1970) 454

Fu 07 C B Fulmer and J C Hafele; Phys. Rev. C5 (1972) 1969

Fu 08 C B Fulmer and J C Hafele; Phys. Rev. C7 (1973) 631

Fu 09 C B Fulmer and J C Hafele; Phys. Rev. C8 (1973) 172

Gi 01 E F Gibson, B W Ridley, J J Kraushaar, M E Rickey and R H Bassel; Phys. Rev. 155 (1967) 1194

Gl 02 C M Glashausser; Ph.D. thesis, Princeton University Technical Report PUC-937-1965-174

Gl 03 N K Glendenning, D L Hendrie and O N Jarvis; Phys Lett. 26B (1968) 131

Go 04 D A Goldberg and S M Smith; Phys. Rev. Lett. 29 (1972) 500

Go 05 C D Goodman, C A Ludeman, D C Hensley, R Kurz and E W Anderson; I E E E Transactions on Nuclear Science NS-18 No 1 (1971)

Gr 06 A M Green; Phys. Lett. 24B (1967) 384

Gr 07 A E S Green, T Sawada and D S Saxon; The Nuclear Independent Particle Model (1968) Academic Press

Gr 08 G W Greenlees, G J Pyle and Y C Tang; Phys. Rev. 171 (1968) 1115

Gr 09 R J Griffiths; Private Communication

Ha 01 T Hamada and I D Johnston; Nucl. Phys. 34 (1962) 382

Ha 02 B G Harvey, D L Hendrie, O N Jarvis, J Mahoney and L Valentin; Phys. Lett. 24B (1967) 43

He 03 D L Hendrie, N K Glendenning, B G Harvey, O N Jarvis, H H Duhm, J Saudinos and J Mahoney; Phys. Lett. 26B (1968) 127

Ho 04 P E Hodgson; Advan. in Phys. 15 (1966) 329

Ho 05 P E Hodgson; Advan. in Phys. 17 (1968) 563

Ho 06 P E Hodgson; Nuclear Reactions and Nuclear Structure, Oxford University Press (1971)

Ho 07 P E Hodgson; Private Communication

Hp 08 H P R P Private Communication

Ja 01 D F Jackson; Nuclear Reactions, Methuen and Co. Ltd. (1970)

Jo 02 R R Johnson and R J Griffiths; Nucl. Phys. A117 (1968) 273

Ke 01 A K Kerman, H McManus and R M Thaler; Ann. of Phys. 8 (1959) 551

Ki 02 K Kicuchi and M Kawai; Nuclear Matter and Nuclear Reactions, North Holland (1968)

Ku 03 P D Kunz; University of Colorado report COO-535-606

Ku 04 T T S Kuo and G E Brown; Nucl. Phys. 85 (1966) 40

La 01 A Lande, A Molian and G E Brown; Nucl. Phys. A115 (1968) 241

La 02 D Larson, S M Austin and B H Wildenthal; Phys. Rev. C9 (1974) 1574

La 03 J D Lawson; NIRL/R/85 report

Le 04 R E Le Levier and D S Saxon; Phys. Rev. 87 (1952) 40

Li 05 B A Lippman and J Schwinger; Phys. Rev. 79 (1950) 469

Ma 01 C J Marchese, R J Griffiths, N M Clarke, G J Pyle, G T A Squier and M E Cage; Nucl. Phys. A191 (1972) 627

Ma 02 C J Marchese, N M Clarke and R J Griffiths; Phys. Lett. 29 (1972) 660

Ma 03 C J Marchese; King's College report (unpublished)

Ma 04 P Marmier and E Sheldon; Physics of Nuclei and Particles, Vol 2, Academic Press (1970)

Me 05 M A Melkanoff, T Sawada and J Raynal; Methods in Computational Physics, Vol 6, Academic Press (1966)

Mo 06 S A Moskowski and B L Scott; Ann. Phys. 11 (1960) 65

Ne 01 J W Negele; Phys. Rev. C1 (1970) 1260

Ni 02 S G Nilsson; Kgl. Danske. Videnskab. Selskab, Mat-Fys. Medd. 29 (1955)

Nu 03 Nuclear Data Sheets; Academic Press

Nu 04 Nuclear Data 2200-8192 User Guide

Nu 05 Nuclear Data, Systems Analyser, 2200 User Guide

Nu 06 Nuclear Data System Power Supply, 2200/2201 User Guide

Os 01 M Ostrofsky, G Breit and D P Johnson; Phys. Rev. 49 (1936) 22

Ow 02 L W Owen and G R Satchler; Phys. Rev. Lett. 25 (1970) 1720

Pa 01 V R Pandharipande; Nucl. Phys. A166 (1971) 317

Pe 02 F G Perey; Phys. Rev. 131 (1963) 745

Pe 03 F G Perey and G R Satchler; Phys. Lett. 5 (1963) 212

Py 04 G J Pyle; University of Minnesota report C00-1265-04

Ra 01 J Rainwater; Phys. Rev. 79 (1950) 432

Re 02 H Rebel and G W Schweimer; Report KFK (1971) Kernforschungszentrum Karlsruhe

Rh 03 R H E L report, P L A User Guide, PLA/NP/17

Sa 01 S K Samaddar, R K Satpathy and S Mukherjee; Nucl. Phys. A150 (1970) 655

Sa 02 G R Satchler; Phys. Lett. 33B (1970) 385

Sa 03 T K Saylor, J X Saladin, I Y Lee and K A Erb; Phys. Lett. 42B (1972) 51

Sc 04 L I Schiff; Phys. Rev. 133 (1964) B802

Sc 05 G W Schweimer; Arbeitbericht No 29 and 35 (1970) des Syklotron-Laboratoriums Karlsruhe (unpublished)

Sc 06 N E Scott, J W Cobble and P J Daly; Nucl. Phys. A119 (1968) 131

Sh 07 A M Shahabuddin; Ph.D. thesis, University of London (unpublished)

Si 08 P P Singh and P Schwandt; Phys. Lett. 42B (1972) 181

Si 09 B C Sinha, V R W Edwards, E J Burge and W H Tait; Nucl. Phys. 183 (1972) 401

Si 10 B Sinha and F Duggan; Phys. Lett. 47B (1973) 389

Si 11 B Sinha; Nucl. Phys. A203 (1973) 473

Si 12 B sinha and F Duggan; Nucl. Phys. A226 (1974) 31

Si 13 B Sinha; Phys. Rev. Lett. 33 (1974) 600

Si 14 B C Sinha; King's College Report (unpublished)

Si 15 B C Sinha, F Duggan and R J Griffiths; Nucl. Phys. (to be published)

Si 16 B Sinha (to be published)

Si 17 R R Silbar and M M Sternheim; Phys. Rev. D6 (1972) 3117

Sl 18 D Slanina and H McManus; Nucl. Phys. A116 (1968) 271

St 19 P H Stelson and L Grodzins; Nucl. Data A1 (1965) 21

St 20 P Stoler, M Slagowitz, W Makofske and T Kruse; Phys. Rev. 155 (1967) 1334

Ta 01 T Tamura; Rev. Mod. Phys. 37 (1965) 679

Ta 02 T Tamura; ORNL Report No 4152 (1967)

Te 03 P W Tedder and B C Sinha; (to be published)

Te 04 Tennelec TC203BR User Guide: Amplifier

Te 05 Tennelec TC446 User Guide: Crossover Picloff

Te 06 Tennelec TC445 User Guide: Timing SCA

Te 07 Tennelec TC252 User Guide: Biased Amplifier

Te 08 Tennelec TC930 User Guide: Preamplifier Power Supply

Te 10 Tennelec TC164 User Guide: Preamplifier

Th 11 G L Thomas; Ph.D. thesis, University of London (unpublished)

Th 12 G L Thomas, B C Sinha and F Duggan; Nucl. Phys. A203 (1973) 305

Ur 01 P P Urone, L W Put, B W Ridley and G D Jones; Nucl. Phys. A167 (1971) 383

Ur 02 P P Urone, L W Put and B W Ridley; Nucl. Phys. A186 (1972) 344

We 01 C J Webb; Ph.D. thesis, Queen's University, Belfast (unpublished)

We 02 S A Weisrose; Ph.D. thesis,University of London (unpublished)

We 03 S A Weisrose, N M Clarke and R J Griffiths; Journal of Phys. G (to be published)

Wi 04 C Wilkin; Phys. Lett. 45 (1973) 203

Wo 05 R D Woods and D S Saxon; Phys. Rev. 95 (1954) 577

Wo 06 P B Woollam; Ph.D. thesis, University of London (unpublished)

Wo 07 P B Woollam, R J Griffiths, J F Grace and V E Lewis; Nucl. Phys. A154 (1970) 513

Wo 08 P B Woollam and R J Griffiths; Phys. Lett. 37B (1971) 13

Wo 09 P B Woollam, R J Griffiths and N M Clarke; Nucl. Phys. A189 (1972) 321

Wo 10 P B Woollam, R J Griffiths, F G Kingston, C B Fulmer, J C Hafele and A Scott; Nucl. Phys. A179 (1972) 657

Ze 01 B Zeidman, B Elbeck, B Hershind and M C Oleson; Nucl. Phys. 86 (1966) 471

Ze 02 M W Zemansky; Heat and Thermodynamics, McGraw Hill (1957)

Acknowledgements

I wish to thank my supervisor, Dr. N. M. Stewart for his advice and constant interest in all stages of this work. I also wish to acknowledge the indefatigable efforts of Dr. R. J. Griffiths from King's College, and also the help from the remainder of the King's College Nuclear Physics Group for their assistance on data taking runs and advice with problems of analysis. Particularly, I would like to thank Dr. N. M. Clarke for his experimental expertise and many valuable discussions, and Dr. B. C. Sinha who has greatly aided me in the understanding of the principles of the recent reformulations of the optical model. I also thank Dr. C. B. Fulmer of the Oak Ridge National Laboratory, Tennessee and his colleagues for their help in obtaining the data for these analyses, particularly the helium-3 scattering from the rotational Samarium isotopes. I am grateful to Mr. C. M. Freer for his technical guidance and for building the back angle detector mounts. I wish to thank Professor H.O.W. Richardson and Professor E. R. Dobbs of Bedford College, Professor W. C. Price of King's College and Dr. C. J. Batty of the Rutherford High Energy Laboratory for extending to me the facilities of their establishments. I also acknowledge the directors of the University of London Computing Centre and the Rutherford Laboratory for the large amount of time used on their computers. I am grateful to Mr. K. McIlroy and his staff of the V.E.C. Harwell, for their cooperation during the data taking run. A tutorial research studentship at Bedford College is gratefully acknowledged. I am indebted to Jacqueline for her constant encouragement. Finally I wish to pay tribute to the careful and efficient manner in which Jill Heathcote has typed my thesis.